Trends in Material Science & Mechanical Engineering-Proceedings of ICMSME 2023

Book · March 2025

DOI: 10.5281/zenodo.15104824

3 authors:

Pabitra Pabitra Maji
University of Engineering & Management
1 PUBLICATION **0** CITATIONS
SEE PROFILE

Rahul Kanti Nath
National Institute of Technology Agartala
19 PUBLICATIONS **315** CITATIONS
SEE PROFILE

Sabyasachi Mukherjee
Regent Education and Research Foundation(RERF), Kolkata - 700121, India
16 PUBLICATIONS **24** CITATIONS
SEE PROFILE

Trends in Materials Science & Mechanical Engineering

OrangeBooks Publication

1st Floor, Rajhans Arcade, Mall Road, Kohka, Bhilai, Chhattisgarh 490020

Website: **www.orangebooks.in**

First Edition, 2025

ISBN: 978-93-6554-959-1

Price: Rs. 665.00

Printed in India

TRENDS IN MATERIALS SCIENCE & MECHANICAL ENGINEERING

PROCEEDINGS OF ICMSME 2023

DR. PABITRA MAJI, DR. RAHUL KANTI NATH,
MR. SABYASACHI MUKHERJEE

OrangeBooks Publication
www.orangebooks.in

Trends in Materials Science & Mechanical Engineering

Proceedings of ICMSME 2023

Dr. Pabitra Maji

Associate Professor
Institute of Engineering and Management (IEM)
University of Engineering and Management Kolkata
Kolkata, West Bengal, India
Former Assistant Professor
Regent Education and Research Foundation Group of Institutions
Barrackpore, West Bengal, India

Dr. Rahul Kanti Nath

Research Scientist
HuT Lab
Amrita Vishwa Vidyapeetham, Amritapuri
University in Vallikavu, Kerala, India
Former Assistant Professor
Regent Education and Research Foundation Group of Institutions
Barrackpore, West Bengal, India

Mr. Sabyasachi Mukherjee

Assistant Professor
Department of Mechanical Engineering
Regent Education and Research Foundation Group of Institutions

Preface

This book is a collection of articles presented in the International Conference on Materials Science and Mechanical Engineering (ICMSME 2023) organised by Mechanical Engineering Department, Regent Education and Research Foundation, Kolkata. It represents the recent advancements in the field of materials synthesis and properties, manufacturing processes, design and fabrication of materials and thermo-fluid science. The chapters in the book are group of the articles in the relevant areas.

Chapter 1 is named as Design and Manufacturing which is a collaboration of articles on numerical simulations for some product design, specifications of engineering materials and fabrication of different products. Chapter 2 is Materials and Manufacturing which deals with synthesis and characterization of engineering materials as well as different manufacturing techniques such as Additive manufacturing, Coating and Welding. Chapter 3 is Thermo-Fluid which represents the thermal and fluid properties of materials used in engineering applications. Last but not the least, Chapter 4 is Biomaterials which illustrates the innovation and applications of various biomaterials.

With the coverage of wide aspects of materials science and mechanical engineering, the book is helpful for students, researchers, teachers and industry professionals to get an idea on the trends in the respective fields.

We are grateful to the authors of the articles presented in the conference. We also want to take this opportunity to acknowledge our deepest gratitude to the reviewers Dr. Raja Kumar, Dr. Kiran Kumar Billa, Dr. Ganesh Prasad Shukla, Dr. Rupak Roy, Mr. Carlos Rafael Silva de Oliveira, Mr. Afonso Henrique da Silva Júnior, Dr. Suman Dey, Dr. Tanmoy Medhi, Dr. Dipankar Biswas, Mr. Barun Routh, Dr. Anil Katarkar and Dr. Abhijit Biswas as well as the technical session chairs Dr. Swapnila Roy, Dr. Subrata Kumar Ghosh, Dr. Dipankar Kakati and Dr. Abhijit Banik for their invaluable contribution for scientific evaluation of the articles.

Kolkata, West Bengal, India — Dr. Pabitra Maji
Amritapuri, Kerala, India — Dr. Rahul Kanti Nath
Barrackpore, West Bengal, India — Mr. Sabyasachi Mukherjee

About the Editors

Dr. Pabitra Maji completed his bachelor's degree (B.Tech) in Mechanical Engineering from MCKV Institute of Engineering (Affiliated to WBUT, now MAKAUT), Howrah, West Bengal, India in 2014. He completed his masters (M.Tech) and Ph.D from National Institute of Technology Agartala, Tripura, India in 2016 and 2023 respectively. His areas of interests are materials processing, manufacturing techniques, mechanical, tribological and chemical properties of materials. Dr. Maji has published 20 articles in various reputed SCI and Scopus indexed journals, presented papers in a number of national and international conferences and holds 2 patents. He is also an academic editor of a Scopus indexed journal namely 'The Scientific World Journal'. He has worked as an Assistant Professor in the Department of Mechanical Engineering at Regent Education and Research Foundation Group of Institutions. Presently, he is working as an Associate Professor at University of Engineering and Management Kolkata.

Dr. Rahul Kanti Nath is currently working as Research Scientist at HuT Lab, Amrita Vishwa Vidyapeetham, Amritapuri, Kerala, India. He has formerly worked as an Assistant Professor at the Department of Mechanical Engineering, Regent Education and Research Foundation, Kolkata. He obtained his B.Tech. (Mechanical Engineering) from Vel Tech Dr. RR & Dr. SR Technical University, Chennai in 2014. He received his Master's and Ph.D. degrees from the National Institute of Technology Agartala in 2016 and 2023, respectively. His major areas of research interests include welding, additive manufacturing, numerical modeling, materials characterization and optimization of manufacturing processes. He published more than 15 papers in various peer-reviewed journals and conferences along with 1 patent. He received Young Scientist Award in the International Scientist Awards on Engineering, Science and Medicine, held on 2021, Goa, India. He serves as an editorial or advisory board member in BOHR Journal of Material Sciences and Engineering (BJMSE). He is also an associate member of the Institution of Engineers (India) [IEI].

Mr. Sabyasachi Mukherjee is an Assistant Professor at the Department of Mechanical Engineering at Regent Education and Research Foundation Group of Institutions in Kolkata, since 2017. Previously, he worked as lecturer in a diploma college. Mr. Mukherjee is having above 8 years of teaching experience. He has obtained his B. Tech degree in the field of Mechanical Engineering from Vel Tech Dr. RR & Dr. SR Technical University, Chennai. He has completed his Master's degree in Engineering Design (Mechanical) from Anna University, Chennai. Currently, he is pursuing his PhD from North Eastern Regional Institute of Science & Technology, Arunachal Pradesh, India. The core areas of his research study consist of Composite Materials and Non-

conventional Manufacturing. He has published research papers in various peer-reviewed journals and has presented several research articles in various National as well as International conferences. Noticeably, he is having patents (Indian and German) in the domain of science and technology.

Contents

Design and Manufacturing

On the application of the Mean-field Homogenization for transversely Isotropic Matrix

Mayank Lakhera, Rahul Agarwal, Deepjyoti Dhar, Atul Jain

Abstract

Mean field homogenization methods are used to determine the effective response of heterogeneous materials. There are many mean-field homogenizations formulations; among them, the most common is the Mori-Tanaka formulation. However, these methods are almost exclusively developed for isotropic matrices. Materials are often extruded to control the alignments of the fibres, which can sufficiently change the properties of the matrix and make the matrix behave in a transversely isotropic manner. Consequently, it becomes imperative to study this anisotropy's effect on the composite material's overall properties. This paper aims to apply Mori-Tanaka to a transversely isotropic matrix[1] to find the effective properties and average stress in the inclusions and the matrix. The solutions are then compared to 3-D finite element models of the composite material for different cases. The quantities compared are C_{11} and C_{22} of the overall composite and average phase stresses (S_{11} and S_{22}) both in the inclusions and the matrix.

Mori-Tanaka and the FE results were very close to each other for a low aspect ratio of the fibres and a low modulus mismatch between fibres and the matrix. At a higher aspect ratio and higher modulus mismatch, there was substantial variation in the results of FE and the Mori-Tanaka scheme. Still, Mori-Tanaka quite nicely predicted the results for effective properties and average stresses for a wide range of cases. It was concluded that Mori-Tanaka is an excellent mean field-field homogenization scheme for a transversely isotropic matrix when the axis of anisotropy of the matrix is the same as the semi-major axis of the ellipsoidal inclusions.

Keywords: Mean field homogenization; Mori-Tanaka; Finite Element Analysis; Eshelby tensor; Anisotropy; Transversely isotropic.

1. Introduction

Composite materials are increasingly used in every industry, be it automotive, aerospace, chemical, or energy. The development of composite material is very time and money-consuming owing to the tests it has to undergo for estimating the properties of the newly

[1] ✉ Mayank Lakhera
connectmayankk@kgpian.iitkgp.ac.in

Department of Mechanical Engineering, Indian Institute of Technology, Kharagpur, India-721302

formed material and to make sure it is best suited for the application for it has been designed. But they are still underused because of the inability to estimate the effective properties correctly. There are analytical methods available to determine the effective properties of the material, but this field is still new and unexplored. Thus, leaving the problem of validating these methods. If done, this can save a lot of time and money. Modern engineering applications require the material to be strong in a particular direction. This can be achieved with the help of short fiber composite material with different young's modulus and fiber orientation to tailor the properties for special loading conditions. Hence with the increasing demand for the short-fiber composite material, it becomes essential to understand the effect of short fibers and matrix properties on the overall properties of the composite material.

Homogenization schemes are at the core of finding the effecting properties of a composite material. Numerous pieces of literature are available describing various homogenization schemes. A basic idea of different homogenization schemes can be found in literature [1,2]. Mean field homogenization schemes and their application to various cases have been further described in detail in the literature[3]. The widely used homogenization scheme was developed by Mori and Tanaka[4]. Multi-step Mori-Tanaka, which overcomes the shortcomings of Mori-Tanaka, has also been discussed in the literature[5].

In 1957, Eshelby[6] first derived the results for elastic field within and outside the ellipsoidal inclusion for an isotropic matrix. He showed that the elastic field remains uniform within an ellipsoidal inclusion, which is also true for anisotropic mediums. A number of papers have been devoted to the study of matrix transverse isotropy. Some notable mentions are Sevostianov[7], Withers[8], and Chiang[9]. All these papers focused on deriving the elastic properties of the composite when the matrix medium is anisotropic. In this paper, we focus on predicting the abilities of Mori-Tanaka applied to the transversely isotropic matrix and verify it with finite element calculations for a wide number of cases. Results are compared for a number of cases as a function of modulus mismatch between fibers and the matrix. All the fibers are aligned in the same direction, but their distribution is uniformly random.

For microstructure generation, various algorithms are there in the literature. The RSA algorithm (Schneider et al.[10]) is the most commonly used algorithm for generating random packings. In its simplest form, the RSA algorithm generates packing with a volume fraction of up to 30%. Segurado and Llorca[11] proposed an improved version of the RSA algorithm. The modified RSA allows denser packing than RSA with around 50% volume fraction for identical spherical inclusions. Lubachevsky and Stillinger[12,13] proposed an algorithm based on molecular dynamics. This approach was proven to be better than the RSA algorithm as high-volume fractions can be reached within a short period of computational time. Ghossein et al[14] successfully created a microstructure with

high-volume fractions with less computational time. He also managed to generate microstructure with aspect ratios > 10 (up to 40), which were not present in the literature before him. The final microstructure generated by Ghossein's algorithm is completely random.

2. Theory and Mathematical Modelling

2.1 Mean field homogenization

For a heterogenous medium, establishing the relation between average stress and average strain in the heterogenous medium is called homogenization of the heterogeneous medium. The stress-strain relation for a linear elastic material is given by:

$$\langle \sigma_{ij} \rangle = C_{ijkl} * \langle \varepsilon_{kl} \rangle \tag{1}$$

where, $<\sigma_{ij}>$ is Average stress in the material, C_{ijkl} is Stiffness matrix of the material and $< \varepsilon_{kl}>$ is Average strain in the material.

2.2 Representative volume element (RVE)

An RVE is a volume element of the material which is small yet large enough to describe the structure and behaviour of the entire composite material. If experiments are performed on this elemental volume, the results will correspond to the behaviour of the whole material. For a homogeneous material, this is just a unit repeating cell; however, in the case of heterogenous materials, this becomes quite complicated. In the case of composite materials, the RVE should contain a sufficient number of inclusions for the properties to be independent of the applied traction and strain and similar across multiple realizations.

2.3 Eshelby tensor

Eshelby[6] derived an expression for relating the strain in the fibre to the Eigen strain. Eigen strain is the strain developed in the material when allowed to expand freely.

$$\langle \varepsilon_{ij} \rangle = S_{ijkl} * \langle \varepsilon_{kl} \rangle \tag{2}$$

Where the fourth-order tensor S_{ijkl} is known as Eshelby Tensor. Eshelby considered a particular case where the inclusion is embedded in an infinite matrix phase and then subjected to far-field stress or strain. Also, Eshelby derived his results for a special case of ellipsoids as inclusions. But from his solutions, solutions for all other special cases such as cylinders, spheres, and spheroids can be derived.

Eshelby tensor for an ellipsoid is obtained by integrating Green's function over the surface of the ellipsoid. Explicit expressions for the Eshelby tensor for the anisotropic medium are unavailable because of the difficulty in calculating these integrals. For the transversely isotropic case, the Eshelby tensor has been calculated by Withers8 and Chiang9. These expressions have been directly used in this paper.

2.4 Mori-Tanaka applied to the matrix and the inclusions

Eshelby method is applicable for inclusions far from each other so that the effect of one inclusion on the other can be neglected. Mori-Tanaka were the first to show that the elastic field in any inclusion is affected by the elastic field of the surrounding inclusions through the perturbed stress and strain fields in the matrix surrounding the inclusions. The expression for dilute strain concentration tensor for any individual fibre is:

$$A_m^\alpha = [(I + S^\alpha (C^m)^{-1}(C^\alpha - C^m)]^{-1} \tag{3}$$

Where I is identity matrix, S^α is Eshelby tensor for that fiber, C^m is the stiffness matrix of the matrix material and C^α is the stiffness matrix of that fiber. The strain concentration tensor, which considers the effect of strain fields of surrounding inclusions also, is given by:

$$A_r^\alpha = A_m^\alpha (v_m I + \sum_{\beta=1}^{m} v_\beta A_m^\beta)^{-1} \tag{4}$$

v_i denotes the volume fraction of the different phases. Then, strain in any r^{th} inclusion is given by:

$$\varepsilon_f^r = A_r^\alpha * \varepsilon^0 \tag{5}$$

where, ε^0 is the applied strain. And average stresses in the fiber are calculated as:

$$\sigma_f^r = C_f^r * \varepsilon_f^r \tag{6}$$

The strain concentration tensor for the matrix is calculated as:

$$A_m = \frac{(I - A_f v_f)}{v_m} \tag{7}$$

where, A_f is the weighted average of the strain concentration tensor of all the fibers. Then, strain in the matrix is given by:

$$\varepsilon_m = A_m * \varepsilon^0 \tag{8}$$

Similarly, average stresses in the matrix are calculated as:

$$\sigma_m = C_m * \varepsilon_m \tag{9}$$

Finally, the overall effective stiffness matrix of the composite is calculated as:

$$C_{eff} = C^m + \sum_{\alpha=1}^{m} v_\alpha (C^\alpha - C^m) A^\alpha \tag{10}$$

2.5 Microstructure generation

A MATLAB code was developed to generate the microstructure. Two different microstructures with fiber aspect ratios 3 and 10 were generated. The code generated

isotropic matrix and fibers. Matrix properties were later changed in the ABAQUS GUI to make it transversely isotropic. For our study, all the fibers are aligned in one direction.

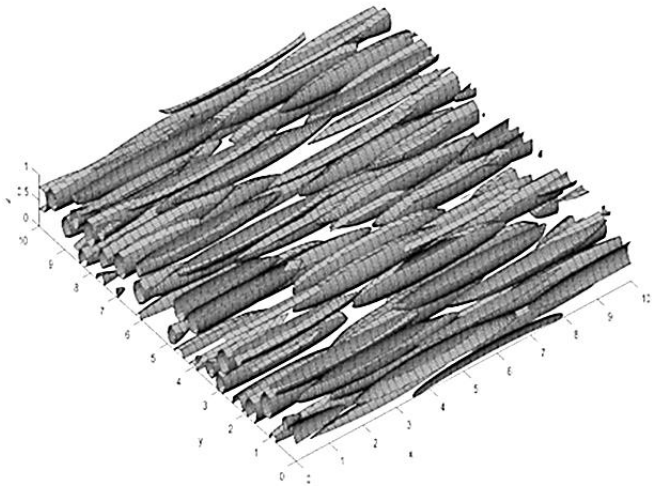

Fig. 1 Microstructure generated for aligned and uniformly distributed fibers.

3. Methodology

3.1 Mori-Tanaka applied to the transversely isotropic matrix

A MATLAB code and finite element models were developed to predict the accuracy of Mori-Tanaka applied to a transversely isotropic matrix. Fibers were randomly distributed in the FE model since fiber position does not affect the effective properties of the overall composite. Although fiber position can be controlled we have restricted this paper to the study of only randomly distributed fibers aligned in one direction. To the MATLAB code, the effective stiffness matrix of the matrix material, the aspect ratio of the fibers, young's modulus, and Poisson's ratio are fed as input. The MATLAB code calculates the overall effective stiffness matrix of the whole composite, average stresses in the fibers, and phase average stresses in the matrix which were then compared to the values obtained by the FE simulation.

For simplicity, we have considered the axis of anisotropy of the matrix material to be in the same direction as the semi-major axis of the ellipsoidal inclusions which is the same as the global x-direction.

3.2 Finite element model generation

To predict the accuracy of Mori-Tanaka applied to a transversely isotropic matrix, FE simulations were performed on a number of FE models which were generated with the help of MATLAB code. We limited our analysis to two aspect ratios, 3 & 10. The fiber volume fraction was chosen to be 0.25. For aspect ratio 3, quality mesh was obtained using ABAQUS. Hence, the number of fibers was chosen to be 40 but for aspect ratio of 10, quality mesh is not possible in ABAQUS. For this reason, number of fibers in higher aspect ratio was kept at 20.

3.3 Matrix and inclusion material

Fibers are isotropic. Young's modulus of the fibers is varied from 50 GPa to 1000 GPa, and results are plotted. Poisson's ratio of fibers is 0.22. Zinc is a transversely isotropic material and was chosen as the matrix material for analysis whose properties are as follows. All values are in GPa.

$$C = \begin{bmatrix} 159 & 32.3 & 32.3 & 0 & 0 & 0 \\ 32.3 & 62.1 & 48.2 & 0 & 0 & 0 \\ 32.3 & 48.2 & 62.1 & 0 & 0 & 0 \\ 0 & 0 & 0 & 6.95 & 0 & 0 \\ 0 & 0 & 0 & 0 & 40 & 0 \\ 0 & 0 & 0 & 0 & 0 & 40 \end{bmatrix}$$

Stiffness matrix for Zinc (Zn)

1-axis is the axis of anisotropy which is parallel to the x-axis in ABAQUS and the semi-major axis of the ellipsoidal inclusions.

3.4 Loading conditions

To calculate C_{11} of the composite material, 1% strain was applied as a loading condition in the x-direction. Rest all faces were fixed in their respective normal directions. Average phase stress in the matrix and the inclusions were calculated. Then, average stress overall composite is given by:

$$\sigma_{avg} = v_f \sigma_f + v_m \sigma_m \tag{11}$$

To calculate C_{22} of the composite material, 1% strain was applied as a loading condition in the y-direction. Rest all faces were fixed in their respective normal direction.

4. Results

This section compares Mori-Tanaka results and FE results for inclusion stress, phase average stress and effective stiffness matrix.

4.1 Mori-Tanaka applied to fibers with aspect ratio 3

When the aspect ratio of the fibers is three and young's modulus of the isotropic fibers (E) is 50 GPa, and C_{11} of the matrix material is 159 GPa, the values of C_{11} of the composite predicted by Mori-Tanaka and FE were 129.6 GPa and 128.32 GPa respectively. The inclusion average stress (S_{11}) values predicted by MT and FE were 664 MPa and 696 MPa, respectively (**Fig. 2**).

Similarly, for E = 100 GPa, the values predicted by MT and FE for C_{11} of the composite were 147 GPa and 146.93 GPa, respectively. The inclusion average stress (S_{11}) values predicted by MT and FE were 1198 MPa and 1210 MPa respectively. The values of S_{22} predicted by MT were slightly off from FE results. Even for higher values of young's modulus of fibers such as E = 1000 GPa, the values predicted by both MT and FE were significantly close (**Fig. 3**).

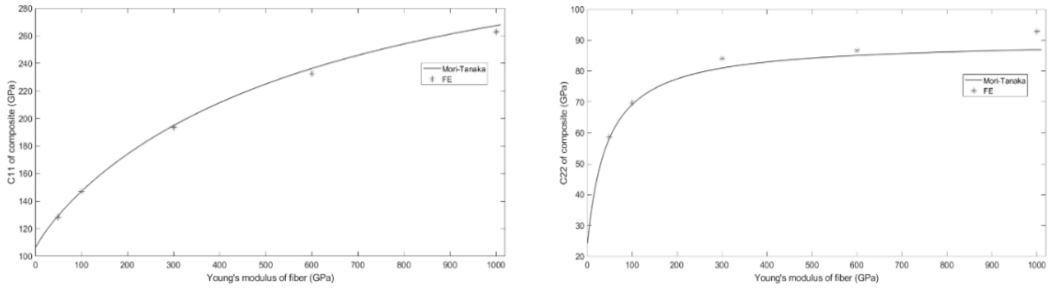

(a) (b)

Fig. 2 For AR3 (a) C_{11} and (b) C_{22} of the composite as a function of modulus mismatch between matrix and fibers.

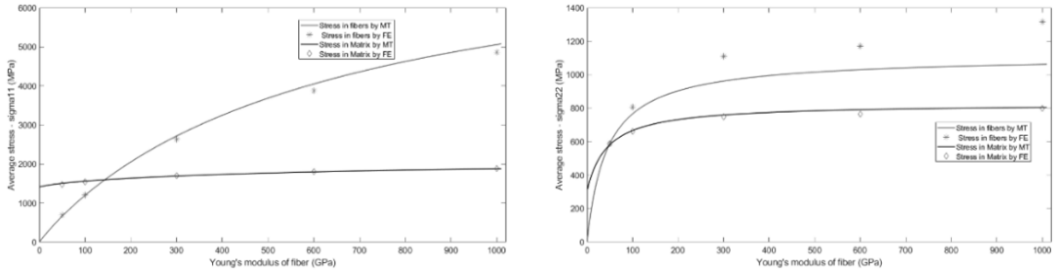

(a) (b)

Fig. 3 For AR3 (a) average stress (S_{11}) in the fiber and the matrix for loading in the x-direction (b) average stress (S_{22}) in the fiber and the matrix for loading in the y-direction.

4.2 Mori-Tanaka applied to fibers with aspect ratio 10

When the aspect ratio of the fibers is 10 and young's modulus of the isotropic fibers (E) is 100 GPa and C_{11} of the matrix material is 159 GPa, the values of C_{11} of the composite predicted by Mori-Tanaka and FE were 147.6 GPa and 147.46 GPa respectively. The inclusion average stress (S_{11}) values predicted by MT and FE were 1153 MPa and 1171 MPa respectively (**Fig. 4**).

Similarly, for E = 300 GPa, the values predicted by MT and FE for C_{11} of the composite were 199.2 GPa and 197.66 GPa respectively. The inclusion average stress (S_{11}) values predicted by MT and FE were 3054 MPa and 2930 MPa respectively. The values of S_{22} predicted by MT were slightly off from FE results (**Fig. 5**).

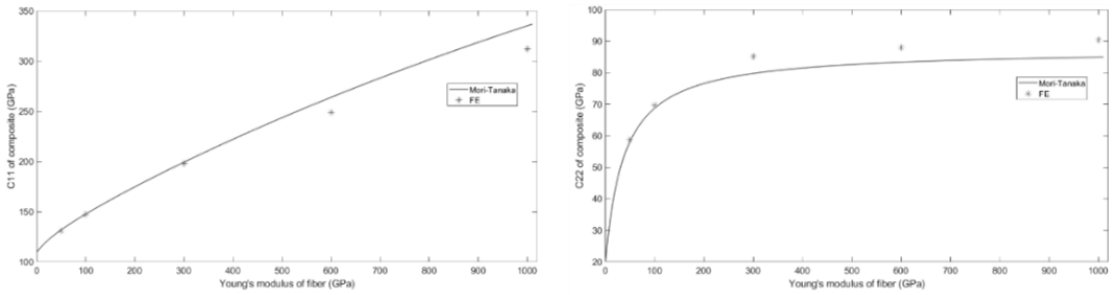

(a) (b)

Fig. 4 For AR10 (a) C_{11} and (b) C_{22} of the composite as a function of modulus mismatch between matrix and fibers.

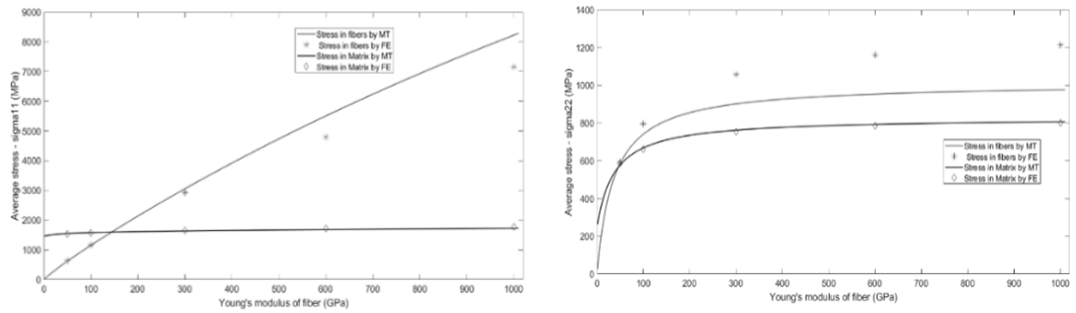

(a) (b)

Fig. 5 For AR10 (a) average stress (S_{11}) in the fiber and the matrix for loading in the x-direction (b) average stress (S_{22}) in the fiber and the matrix for loading in the y-direction.

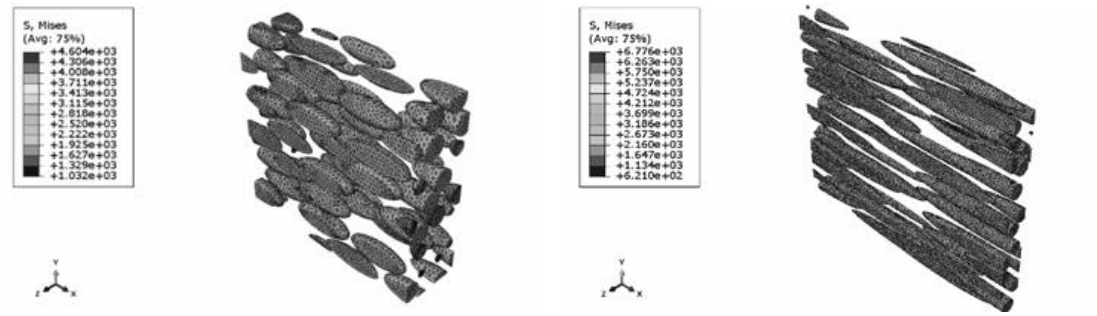

(a) (b)

Fig. 6 Average stress (S_{11}) distribution in the fibers for (a) E = 300 GPa and AR = 3 and (b) E = 300 GPa and AR = 10

Fig. 6 shows the average stress S11 in each fibre for loading in the x-direction. It can be seen that stress is not same in every fibre. Average stresses in **Fig. 3** & **Fig. 5** are plotted as the volume average of stresses in all the fibres.

5. Conclusions and Further Scope

Comparisons were made for effective stiffness values, average stress values in the fibers, and phase average stress in the matrix for a number of cases. Results were plotted as a function of modulus mismatch between the fiber and the matrix. It was seen that if the modulus mismatch is not too high and the aspect ratio is 3, the values predicted by both MT and FE were in excellent agreement with each other. At higher modulus mismatch for lower aspect ratio, there was a slight variation in the predicted values with Mori-Tanaka under-predicting the values in the case of effective stiffness matrix and over-predicting the average stress values in the inclusions.

For aspect ratio 10, at low modulus mismatch, the values predicted for effective stiffness values, average stress values in the fibers, and phase average stress in the matrix were in close agreement with each other. At higher modulus though, the variation was quite significant. Variation was seen in the values of S_{22} for both aspect ratios. The observed trend is similar to that observed during previous benchmarking exercises for the isotropic matrix.

Thus, we can safely say that Mori-Tanaka is an excellent mean-field homogenization scheme in the case of a transversely isotropic matrix when all the fibers are aligned in the same direction and the axis of anisotropy of the matrix is the same as the semi-major axis of the ellipsoids.

Further work can be done in this area where the volume fraction of the fibers can be varied, and results can be compared. Also, the axis of anisotropy of the matrix can be changed and results can be studied when it is not aligned in the direction of the semi-major axis of the ellipsoids.

References

1. A Jain, SV Lomov, Y Abdin, I Verpoest, W van Paepegem. Compos. Sci. Technol. 2013; 87:86-93.
2. B Klusemann, B Svendsen, B Klusemann, B Svendsen. Eur. J Mech. A-Solid. 2012; 34: 21-37.
3. A Jain. Mater. Today Commun. 2019; 21.
4. T Mori, K Tanaka. Acta Metall. 1973; 21(5): 571-574.
5. D Swaroop, D Dhar, A Suriyan, A Jain. Mech. Mater. 2022; 174: 104447.
6. JD Eshelby. Proc. R. Soc. London, Ser. A. 1957; 241(1226): 376-396.
7. I Sevostianov, N Yilmaz, V Kushch, V Levin. Int. J Solids Struct. 2005; 42:455-476.
8. PJ Withers. Philosophical Magazine A. 1989; 59:759–781.
9. CR Chiang. Acta Mech. 2017; 228:1819-1833.

10. K Schneider, B Klusemann, S Bargmann. Adv. Eng. Softw. 2016; 99:177-188.

11. J Segurado, J Llorca. J. Mech. Phys. Solids. 2002; 50(10): 2107-2121.

12. BD Lubachevsky, FH Stillinger, EN Pinson. J Stat. Phys. 1991; 64:501-524.

13. BD Lubachevsky. J. Comput. Phys. 1991; 94(2):255-283.

14. E Ghossein, M Lévesque. J. Comput. Phys. 2013; 253:471-490.

Effect of Length of Cut-off Wall on the Seepage Characteristics of a Non-Homogeneous Earth Dam using Finite Element based Software Geo-Slope

Imran Arshad[a], Irfan Ahmed Shaikh[a], Shakeel Hussain Chattha[b], Zaheer Ahmed Khan[b]

Abstract

The water impounded in earth dam maybe seeped through its body or abutments which has significant importance in the stability of dams. The core zone, which serves as an impermeable zone, is where embankment dams are weak. Zonal core embankment dams are a composite of several material characteristics. When water leaks through such dams it causes many problems. Thus, it warrants proper assessment of storage headworks. But the field investigations are cumbersome and expensive and cannot always be carried-out. The way-out is to simulate the seepage invoking calibrated numerical models. In this study three geometric models of a non-homogenous earth dam depict along with three different scenarios i.e. (i) original design, (ii). Dam with a partial cut-off wall, (iii). Dam with a full cut-off wall was numerically analysed by using Geo-Slope (SEEP/W) software. The results indicate that the cut-off wall at its original shape and design performs better as the overall minimum seepage value of order 2.2117 x 10^{-4} ft^3/sec/ft, with an exit gradient of 0.099 and minimum seepage velocity 1.0020 x 10^{-6} ft/sec, at EL 270 ft reservoir level. Any increment in the length of cut-off wall will be uneconomical as it does not make much difference to minimize seepage flux, seepage velocity, and exit gradient. For the majority of flow characteristics, the cut-off wall's length plays a very limited role therefore, it can be said that the Hub Dam has operated efficiently since its construction in accordance with its original form and design.

Keywords: SEEP/W model; Phreatic-line; Cut-off wall; Finite element analysis; Hub dam

1. Introduction

The dam is an impermeable barrier in front of the water flow that is mainly used to store or divert the flow direction. Earth dam is one of the oldest constructional establishments that man has used in agricultural fields and provision of potable water for his primitive needs **[1]**. Faulty design, improper construction, poor maintenance practices, and poor[2] quality materials using may cause fail for engineering structures like earth dams. Seepage problems are seen in all types of dams**[2]**. It may not affect the stability of the dam if the exit gradient is under unity. Dams may fail due to some criteria such as piping, overtopping, and seepage the foundation under the barrier, etc.**[3]**.

[2] ✉ Imran Arshad

engr_imran1985@yahoo.com

[a]Department of Irrigation and Drainage, Sindh Agriculture University Tandojam, Sindh, Pakistan

[b]Department of Farm Structures, Sindh Agriculture University Tandojam, Sindh, Pakistan

Piping and leakage may cause to fail in natural dams because they may have high porosities and they have not undergone systematic compaction[4]. These failures are variable according to dam type. For instance, failure rates vary between cemented dams and earth-fill dams. The cutoff wall and filter are an efficient way for seepage controlling through a dam foundation[5]. The slurry wall is structural foundation instrument constructed underground for controlling slurry fluid, including bentonite, pulverized clays and concrete mixed with water, for supporting the field walls of an excavation and later backfilled which may be increase enhanced with a steel cage, precast panel or steel beams[6]. Each side of the wall alignment to supply horizontal and vertical alignment control for the excavation and reinforced elements to be inserted in the excavated unit. Cut-off walls with various thickness and depths were suggested as another alternative for seepage remediation[7].

Researchers around the globe have proposed a various range of remedies to decrease the failure caused by seepage. A zonal earth dam's supply of a clay core, clay blanket, and chimney filter can control the seepage through the dam body[8]. A common practice around the world is to provide a cutoff wall made of an impermeable substance to lower the seepage through the foundation. Installation of a cutoff wall or sheet pile can be used to control the reduction of exit gradient and seepage flux[9]. A thorough study is still absent, even though numerous studies have been considered so far to decrease seepage utilizing vertical cut off walls[10]. To analyze the seepage flow, exit gradient, and maximum seepage velocity through the body and the foundation of a non-homogeneous earth dam, detailed numerical research has been carried out in this study.

2. Materials and Methods

2.1 Location of the Dam

The present research work is undertaken for seepage modeling of the (Hub dam) earth dam, which located on the Hub River 35 km, northwest of Karachi city, Sindh-Pakistan. The height of the dam 154 ft. with a base width of 866 ft., and total length of 15,640 ft. respectively. The elevation of crest was EL 352 ft, while the ground elevation level was in between EL 220 ft to EL 250 respectively. The maximum, normal and minimum reservoir level was located at an elevation EL 346, EL 339, and EL 270 respectively. The profile of the dam axes is elaborated in **Fig. 1**[11].

2.2 Numerical Model

For numerical analysis, three geometric models of a non-homogenous earth dam (Hub dam) depict along with three different scenarios i.e. (i) original design, (ii). Dam with a partial cut-off wall, (iii). Dam with a full cut-off wall respectively. The numerical model was created using Geo-Slope (SEEP/W) software and the steady state analysis was selected to simulate the hydraulic conditions beneath the dam foundation[12]. The geometry of the dam in the SEEP/W model is presented in (**Fig. 2.a–c**). The model's sections were

divided into segments (elements) using a quad and triangle meshing method. A mesh of 957 nodes, 901 elements, and an approximate global element area size of 20ft. was created. These meshing approaches select to give accurate analysis for the soil elements

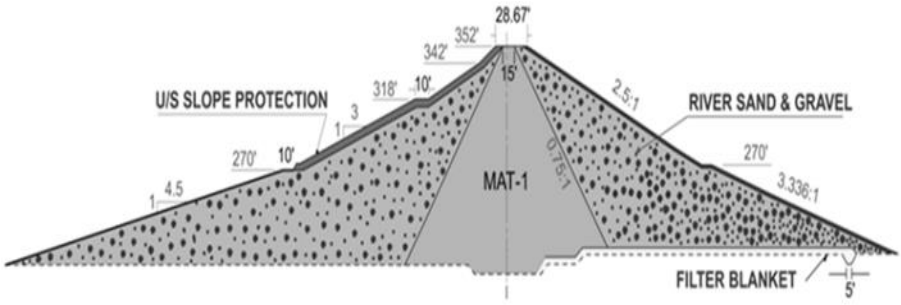

Fig. 1 Cross-section of non-homogeneous section of hub dam[11].

underneath dam foundation[13]. A saturated case was selected for the model in regards to construction and soil materials; it was chosen because it was ideal for a steady state analysis and was a domain that would remain saturated for the duration of the simulation[14].

a.

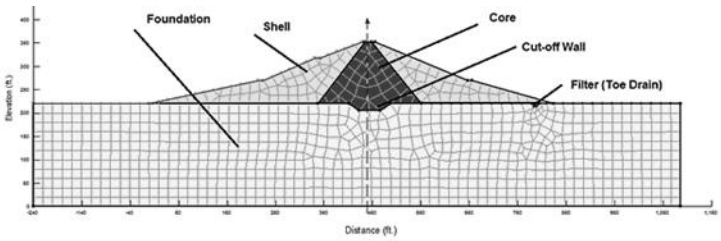

b.

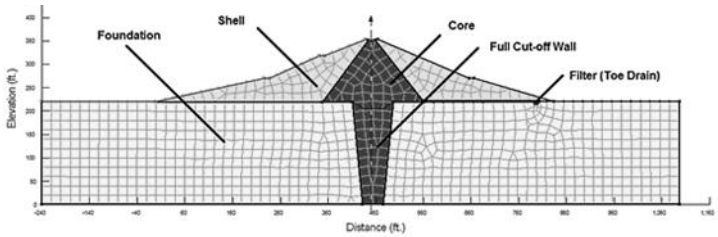

c.

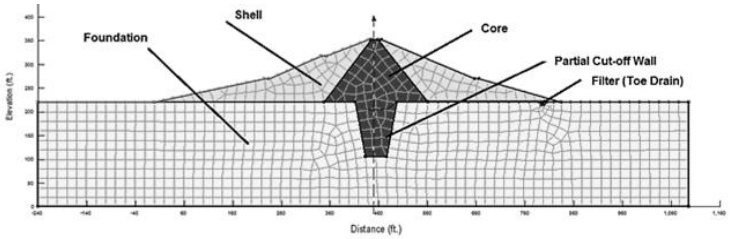

Fig. 2 The SEEP/W mesh (a) original design, (b) with partial cut-off wall, (c) with full cut-off wall.

In order to formulate the model various coefficient and parameters were entered into the software respectively. The interface materials used for hydraulic conductivity equaled zero (the dam structure and cutoff wall). A Dirichlet and Neumann boundary node was assigned on the upstream and downstream slope of the dam[15]. Free water means the upstream side are open and the increasing in water quantity are expected. The performance of dam was studied for three different scenarios i.e. (i) original design, (ii). Dam with a partial cutoff wall, (iii). Dam with a full cutoff wall at various reservoir levels i.e. minimum water level EL 270 ft., normal water level EL 339 ft., and maximum water level EL 346 ft., respectively. The comparison of numerical simulations is discussed for cutoff wall accordingly[16]. **Fig. 2(a)** represents an earth dam at its original shape and design. **Fig. 2(b)** represents an earth dam with a partial cutoff wall and **Fig. 2(c).**

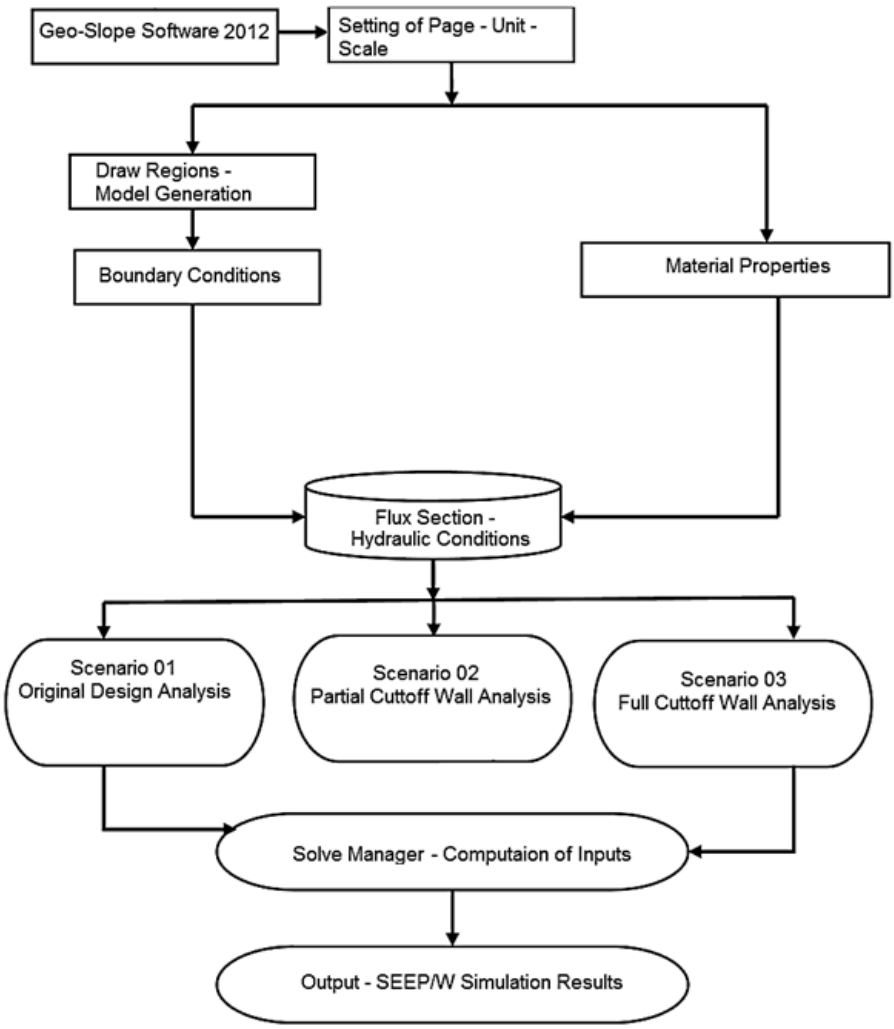

Fig. 3 Flowchart for finite element modelling using Geo-slope software.

represents an earth dam with a full cutoff wall. The core of the dam comprised of a silt-clay and the foundation of the dam consists of fine sand, coarse sand, gravel, and impervious rock respectively[17]. The cutoff wall was also filled with the same material as of a clay-core respectively. For analytical purposes, in this study only the saturated condition of the earth dam is considered and studied. **Fig. 3** represents the flowchart of the finite element modeling procedure.

Table 1 and **Table 2** contains the hydraulic conductivities of materials and geological parameters of Hub dam. The calibration values of the material used was obtained through a trial-and-error method by using the hydraulic conductivities values as a guess value at the time of construction respectively. All the cases, mentioned above, are performed separately.

Table 1 Hydraulic conductivities used for modelling.

Type of material used in modelling	**Hyd. conductivity (ft/sec)**	
	***Guess values**	**Calibrated values**
Foundation	1×10^{-6}	3.315×10^{-6}
Shell	1×10^{-6}	2.155×10^{-5}
Core	1×10^{-7}	2.155×10^{-8}
Cutoff wall	1×10^{-7}	2.000×10^{-8}
Filter Drain	1×10^{-2}	3.825×10^{-2}

*Source: Water and Power Development Authority: Pakistan[11]

Table 2 Geological parameters.

S. No	**Material Type**	**Unit Weight *p* (kN/m^3)**	**Cohesion c (kpa)**	**Friction Angle φ (degree)**
1	Foundation	20	275	45^0
2	U/S Shell	19	0	45^0
3	Core	19	0	35^0
4	Cutoff wall	19	0	35^0
5	Filter Blanket	18.5	0	30^0

2.3 Governing equations used by SEEP/W software

The following partial differential equations (PDE) are the basic equations used to model the SEEP/W program:

$$\frac{\partial}{\partial x}\left(k_x \frac{\partial H}{\partial x}\right) + \frac{\partial}{\partial v}\left(k_y \frac{\partial H}{\partial v}\right) + Q = \frac{\partial \theta}{\partial t} \quad (1)$$

where, H is total head, k_x is horizontal conductivity and k_y is vertical conductivity and Q is flux. Equation 1 is a 2D second-order nonlinear partial differential equation and describes the transient flow conditions; Its extraction includes Darcy's basic constitutional law on groundwater flow, which is given below:

$$q = Aki \quad (2)$$

$$v = \frac{q}{A} = ki \quad (3)$$

and where, q is specific discharge, A is cross-section area, k is permeability and i is hydraulic gradient.

2.4 Basic Finite Element Equation

The basic finite element equation (i.e., the general finite element method) should be applied to SEEP/W simulation models as follows.

$$[k]\{H\} = \{Q\} \quad (4)$$

where, k is node's material properties, H is node's total head and Q is water flow at a node.

SEEP/W formulates in terms of total head, and boundary conditions are specified according to this value. This parameter should be calculated as follows.

$$H = \frac{u}{rw} + h \quad (5)$$

where, H is total head, u is pressure head and h is elevation head.

3. Results and Discussion

Flow-net, equipotential lines, phreatic line, and velocity vectors

The SEEP/W program is utilized for seepage analysis for a hub dam embankment and its establishment for various reservoir level situations to obtain invasive information[18]. For this reason, utilizing the product flow net has been drawn to the chosen area and for various rises as appeared in (**Fig. 4** – **Fig. 6**). The performance of dam was studied for three different cases i.e. (i) original design, (ii). Dam with a partial cutoff wall, (iii). Dam with a full cutoff wall at different reservoir levels i.e. maximum EL 346 ft., normal EL 339 ft., and minimum EL 270 ft., respectively. The comparison of numerical simulations is discussed for cut-off wall[19]. The flow net includes streamlines, equipotential lines, speed. Vectors representing prevailing land stream (seepage) and phreatic line representing the Hub dam's seepage behavior. It is evident from the results that seepage is occurring through the dam foundation, so a proper remedial measure is required to minimize the seepage through the dam body.

Case I: Non-homogeneous section at original shape and design

The behavior of the dam at the time of its construction for different scenarios i.e. reservoir level EL 270 ft., EL 339 ft., and EL 346 ft., the phreatic line and flow direction of the water shows a non-linear behavior. The results revealed that there is no longer any risk of piping or internal erosion due to seepage for all the scenarios as the exit gradient value (i.e., less than 1.0) and maximum seepage velocity are within allowed limits. However, the velocity increases exponentially when the water level in the upstream area rises. This is due to the laminar flow which is initially being linear, but when the water level rises in the reservoir, the flow is now laminar but non-linear.

In addition to showing the location of the flow, velocity vectors are helpful. SEEP/W uses the magnitude of the true velocity in its estimation of the vector's size to show where the velocities are high or low visually. The average x- and y-velocities of each element are calculated from the Gauss point velocity measurements, and the results are then vectorially summed. This creates an average velocity vector for each element. The tail of this average velocity vector is shown on the plot alongside the center of the element. In accordance with the element velocity in relation to the maximum velocity, all other vectors are drawn.

The phreatic line (blue color line) after passing the central core suddenly drops where the filter drain is provided. The seepage flux of order 2.2117×10^{-4} $ft^3/sec/ft.$, 5.6064×10^{-4} $ft^3/sec/ft.$, and 5.9361×10^{-4} $ft^3/sec/ft.$, with an exit gradient of 0.099, 0.188, and 0.317 was observed for a reservoir levels corresponding to EL 270 ft., EL 339 ft., and EL 346 ft., respectively. Likewise, the maximum seepage velocity at various reservoir levels i.e. EL 270 ft., EL 339 ft., and EL 346 ft., was found 1.002×10^{-6} ft/sec., 2.4900×10^{-6} ft/sec., and 3.0240×10^{-6} ft/sec respectively. At different water levels, the pore water pressure decreased almost linearly, indicating that steady state flow takes place in all parts of the dam body i.e. shell, core, foundation of the dam. Water level fluctuations affected the upstream of the dam more rapidly and reduction of pressure Soccurred at a higher rate. Due to the low velocity of water drainage inside the clay core materials, the least change in the amount of pore water pressure occurred within the core[20].

a.

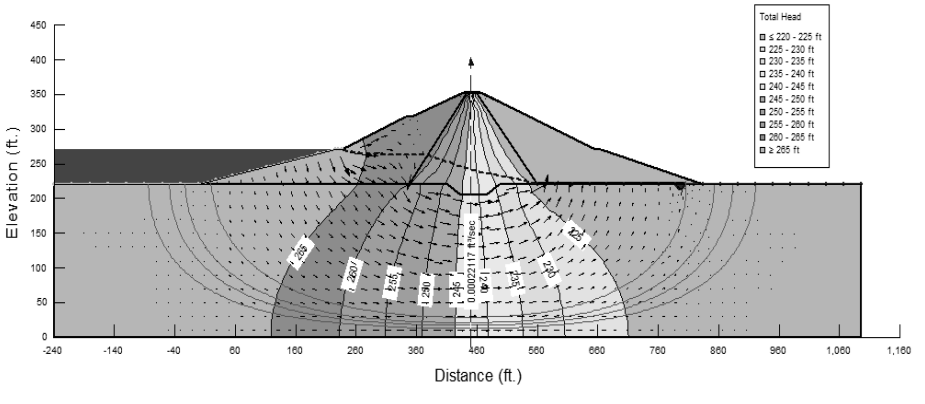

b.

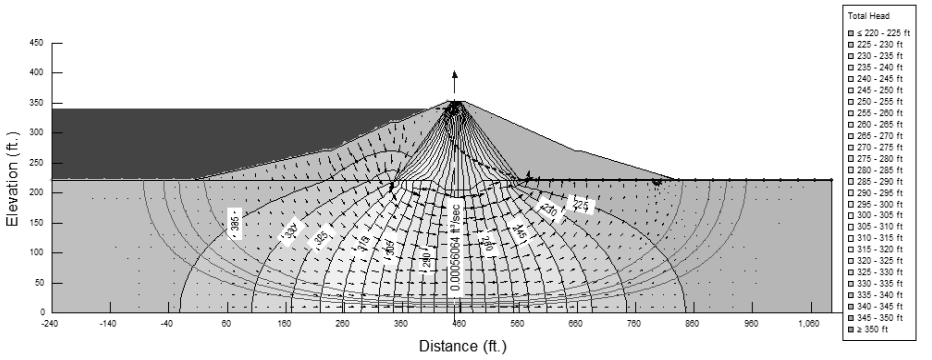
Total Head
≤ 220 - 225 ft
225 - 230 ft
230 - 235 ft
235 - 240 ft
240 - 245 ft
245 - 250 ft
250 - 255 ft
255 - 260 ft
260 - 265 ft
265 - 270 ft
270 - 275 ft
275 - 280 ft
280 - 285 ft
285 - 290 ft
290 - 295 ft
295 - 300 ft
300 - 305 ft
305 - 310 ft
310 - 315 ft
315 - 320 ft
320 - 325 ft
325 - 330 ft
330 - 335 ft
335 - 340 ft
340 - 345 ft
345 - 350 ft
≥ 350 ft
Elevation (ft.)
Distance (ft.)
0.00056064 ft³/sec

c.

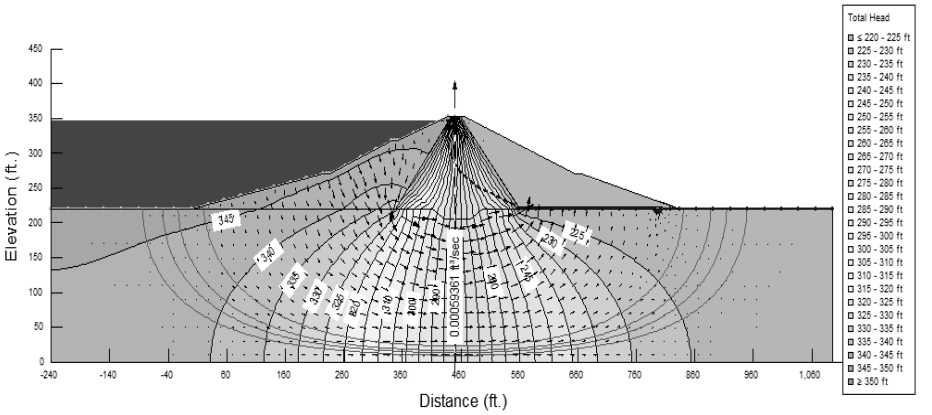
Total Head
≤ 220 - 225 ft
225 - 230 ft
230 - 235 ft
235 - 240 ft
240 - 245 ft
245 - 250 ft
250 - 255 ft
255 - 260 ft
260 - 265 ft
265 - 270 ft
270 - 275 ft
275 - 280 ft
280 - 285 ft
285 - 290 ft
290 - 295 ft
295 - 300 ft
300 - 305 ft
305 - 310 ft
310 - 315 ft
315 - 320 ft
320 - 325 ft
325 - 330 ft
330 - 335 ft
335 - 340 ft
340 - 345 ft
345 - 350 ft
≥ 350 ft
Elevation (ft.)
Distance (ft.)
0.00059361 ft³/sec

d.

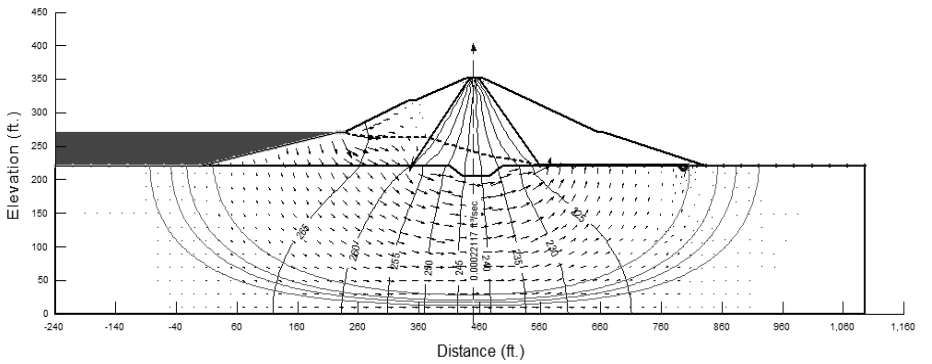
Elevation (ft.)
Distance (ft.)
0.00022117 ft³/sec

e.

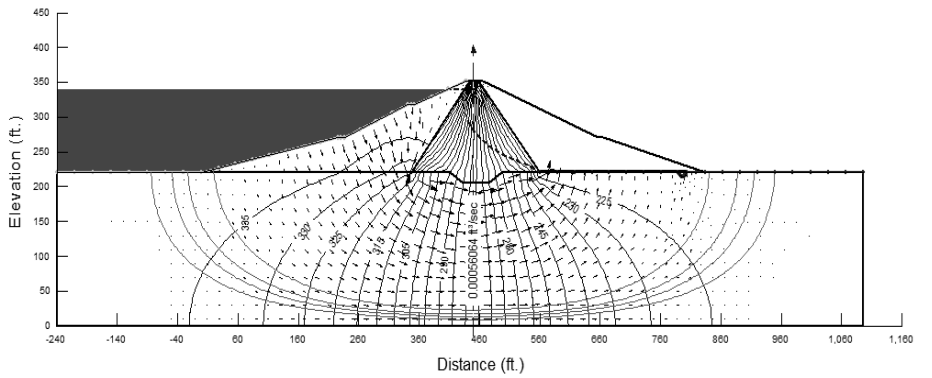
Elevation (ft.)
Distance (ft.)
0.00056064 ft³/sec

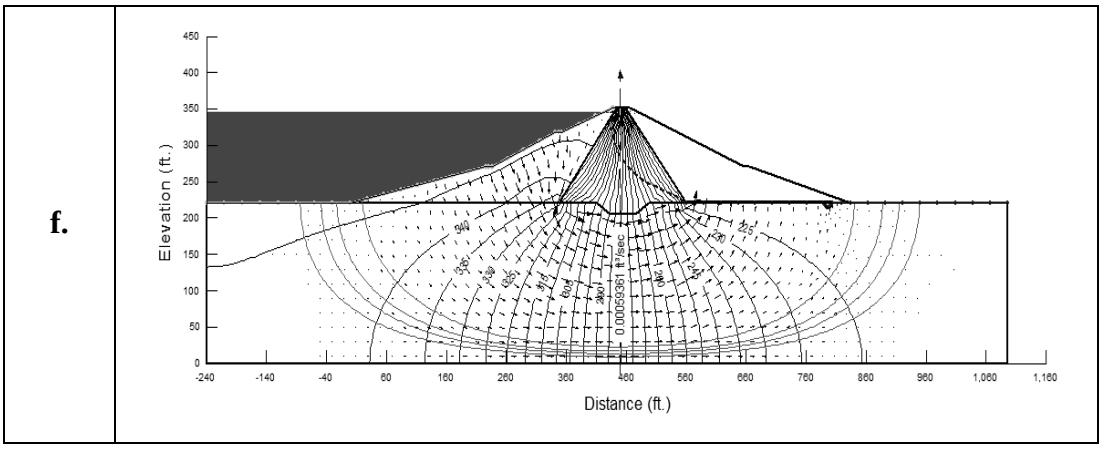

Fig. 4 (a-c) SEEP/W model results and (d-f) Phreatic Line behavior for original design. (a,d) Reservoir height = EL 270 ft, (b,e) Reservoir height = EL 339 ft, (c,f) Reservoir height = EL 346 ft.

The obtained results were consistent with the studies of Aasma et al.[21]. At all points in the downstream slope, the exit hydraulic gradient was less than unity therefore; the dam is safe against piping. The different color contours represent that the total head will be same at any node. The flow paths (green color lines) are an imaginary droplet of water which follows from the entrance to exit accordingly[22]. The amount of flow was seen to be the same between each flow line in a flow net, indicating that each flow channel experiences the same amount of flow. **Fig. 4** describes the SEEP/W simulated results for the case (I) at different reservoir levels.

Case II: Non-Homogeneous Section with a partial cut-off wall

Likewise, the seepage analysis was performed for a non-homogeneous section with a partial cutoff wall under steady-state condition for a different water reservoir levels. The results showed that for each water reservoir level EL 270 ft., EL 339 ft., and EL 346 ft. the seepage flux of order 1.5441×10^{-4} ft^3/sec/ft., 3.8143×10^{-4} ft^3/sec/ft., and 4.0387×10^{-4} ft^3/sec/ft., with an exit gradient 0.089, 0.157, and 0.299 was observed respectively. Likewise, the maximum seepage velocity at various reservoir levels i.e. EL 270 ft., EL 339 ft., and EL 346 ft. were found 0.911×10^{-6} ft/sec., 2.251×10^{-6} ft/sec., and 2.899×10^{-6} ft/sec respectively[23]. (**Fig. 5**), describes the SEEP/W simulated results for the case (II) at different reservoir levels.

Case III: Non-homogeneous section with a full cut-off wall

Similarly, the seepage analysis was performed for a non-homogeneous section without cutoff wall and a filter drain under steady-state condition for a different water reservoir level. The results showed that for each water reservoir level EL 270 ft., EL 339 ft., and EL 346 ft., the seepage flux of order 0.20689×10^{-4} ft^3/sec/ft., 0.49549×10^{-4} ft^3/sec/ft, and 0.52464×10^{-4} ft^3/sec/ft., with an exit gradient 0.081, 0.141, and 0.285 was observed respectively. Likewise, the maximum seepage velocity at various reservoir levels i.e. EL

270 ft., EL 339 ft., and EL 346 ft. were found 0.7899 × 10^{-6} ft/sec, 1.859 × 10^{-6} ft/sec, and 2.353 × 10^{-6} ft/sec, respectively. (**Fig. 6**), describes the SEEP/W simulated results for the case (III) at different reservoir levels.

Table 3 The SEEP/W model results of Hub dam for different water levels in reservoir

Parameters	**Upstream Reservoir levels**								
	Original design			**Partial cut-off wall**			**Full cut-off wall**		
	270 ft.	*339 ft.*	*346 ft.*	*270 ft.*	*339 ft.*	*346 ft.*	*270 ft.*	*339 ft.*	*346 ft.*
Seepage flux × 10^{-4} (ft^3/sec/ft)	2.2117	5.6064	5.7477	1.5441	3.8143	3.9105	0.2069	0.4955	0.5246
Exit gradient	0.0990	0.1880	0.3170	0.0890	0.1570	0.2990	0.0810	0.1410	0.2850
Max. Seepage velocity × 10^{-6} (ft/sec)	1.0020	2.4900	3.0240	0.9110	2.2510	2.8990	0.7899	1.8590	2.3530

The comparison of all three scenarios showed that partial and full cutoff wall does not make much difference to minimize seepage and exit gradient respectively. Therefore, it indicates that there is no possibility found for a downstream slope failure[24]. In addition to this, the seepage flow line behavior for all the scenarios were found normal as it passes the core and falls into the filter drain respectively. Similar results were obtained by[25] for the case non-homogeneous earth dam.

a.

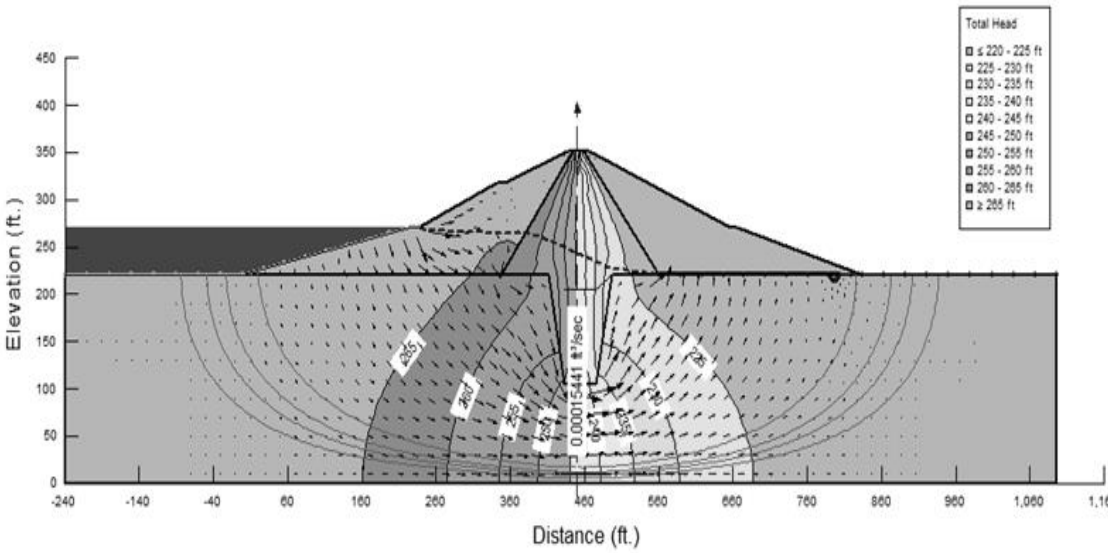

b.

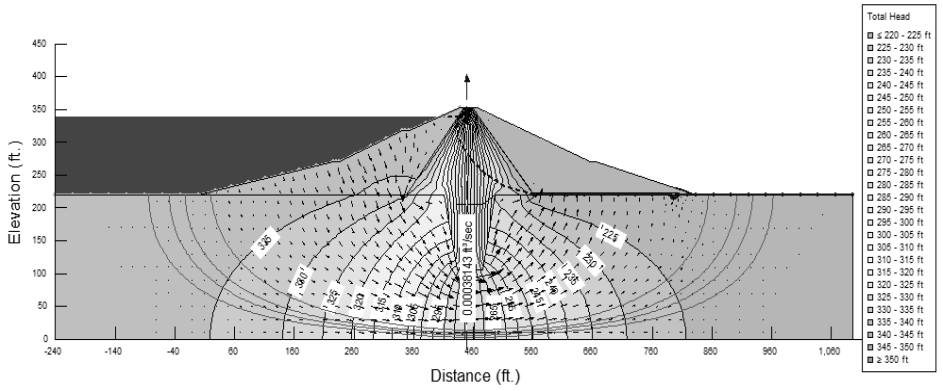
Total Head
≤ 220 - 225 ft
225 - 230 ft
230 - 235 ft
235 - 240 ft
240 - 245 ft
245 - 250 ft
250 - 255 ft
255 - 260 ft
260 - 265 ft
265 - 270 ft
270 - 275 ft
275 - 280 ft
280 - 285 ft
285 - 290 ft
290 - 295 ft
295 - 300 ft
300 - 305 ft
305 - 310 ft
310 - 315 ft
315 - 320 ft
320 - 325 ft
325 - 330 ft
330 - 335 ft
335 - 340 ft
340 - 345 ft
345 - 350 ft
≥ 350 ft
Elevation (ft.)
Distance (ft.)
0.0003814 ft²/sec

c.

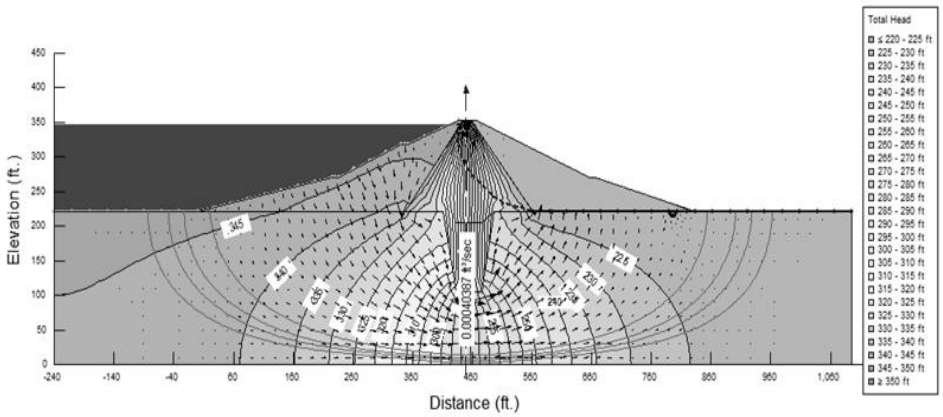
Total Head
≤ 220 - 225 ft
225 - 230 ft
230 - 235 ft
235 - 240 ft
240 - 245 ft
245 - 250 ft
250 - 255 ft
255 - 260 ft
260 - 265 ft
265 - 270 ft
270 - 275 ft
275 - 280 ft
280 - 285 ft
285 - 290 ft
290 - 295 ft
295 - 300 ft
300 - 305 ft
305 - 310 ft
310 - 315 ft
315 - 320 ft
320 - 325 ft
325 - 330 ft
330 - 335 ft
335 - 340 ft
340 - 345 ft
345 - 350 ft
≥ 350 ft
Elevation (ft.)
Distance (ft.)
0.0004038 ft²/sec

d.

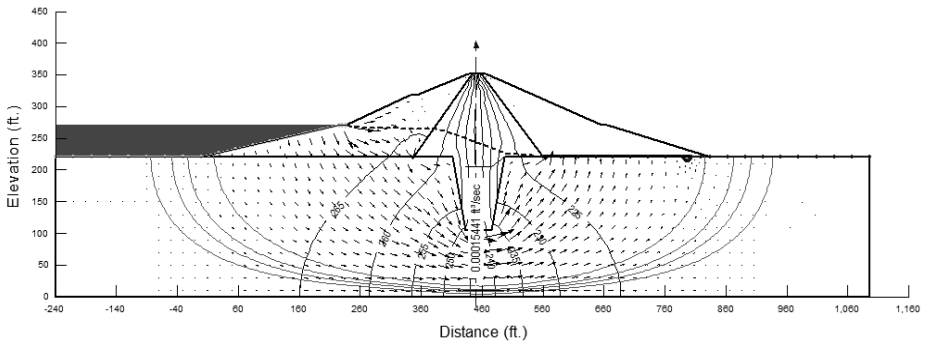
Elevation (ft.)
Distance (ft.)
0.0001544 ft²/sec

e.

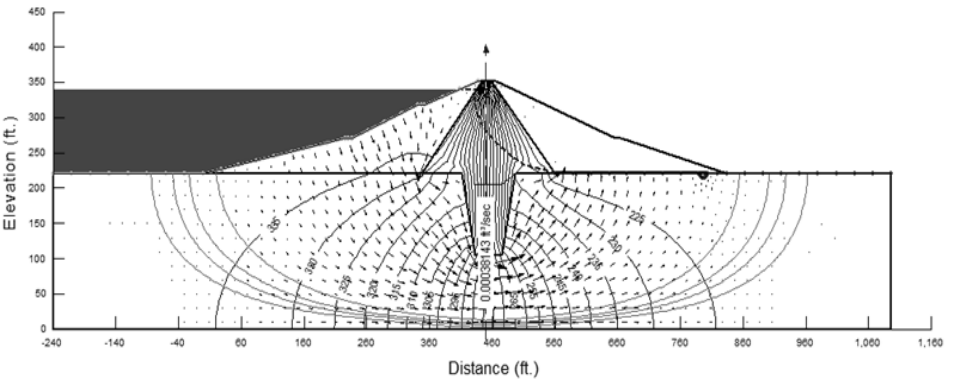
Elevation (ft.)
Distance (ft.)
0.0003814 ft²/sec

f.

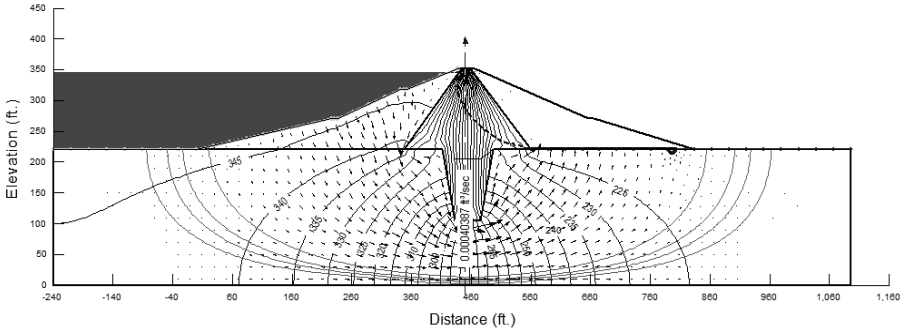

Fig. 5 (a-c) SEEP/W model results and (d-f) Phreatic Line behavior for dam with partial cut-off wall. (a,d) Reservoir height = EL 270 ft, (b,e) Reservoir height = EL 339 ft, (c,f) Reservoir height = EL 346 ft.

a.

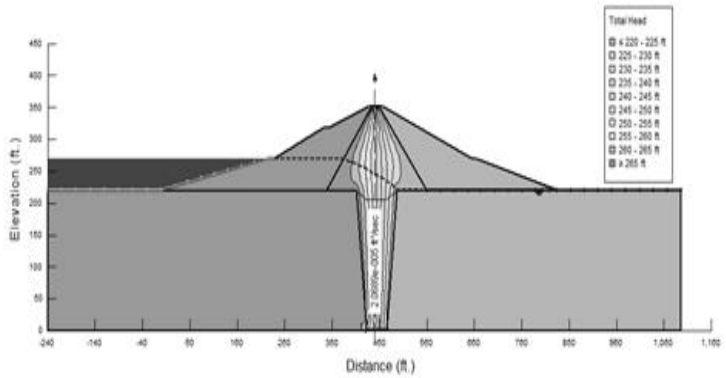

b.

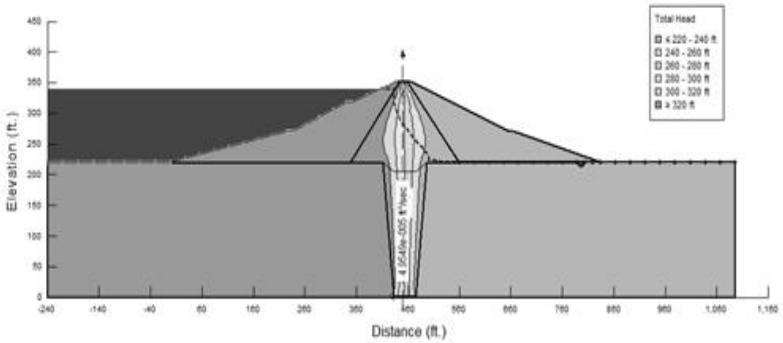

c.

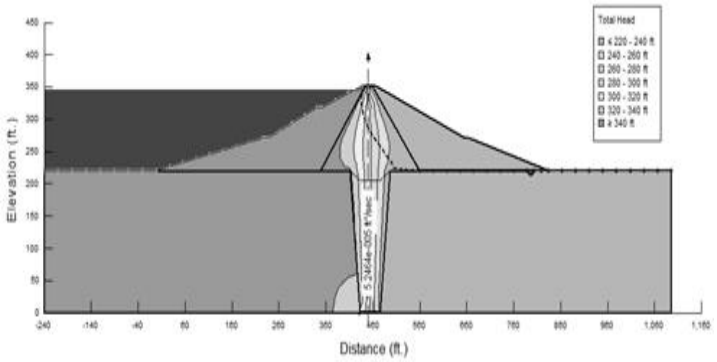

d.

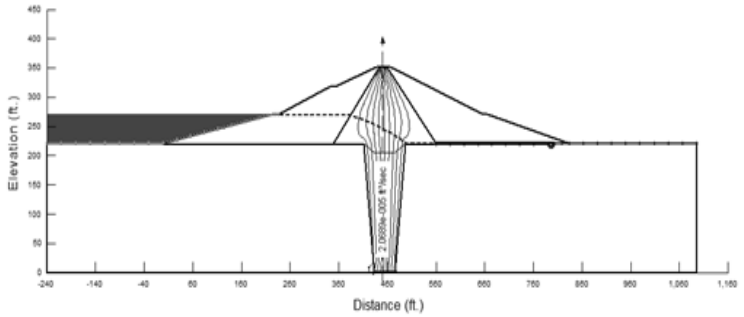

e.

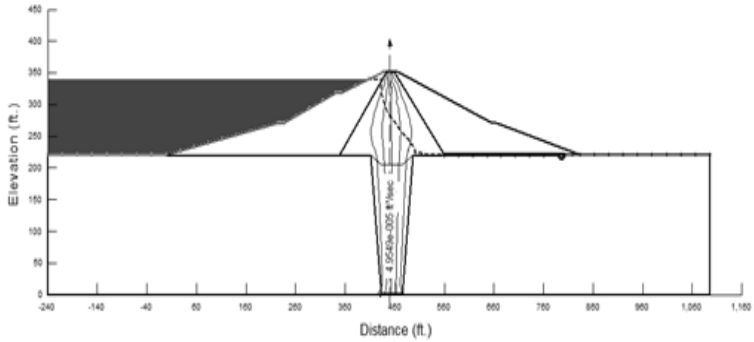

f.

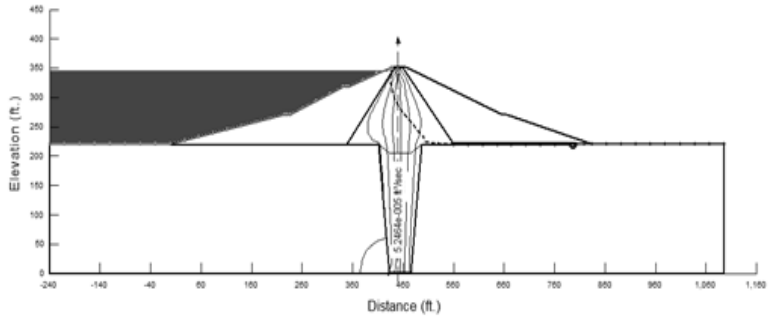

Fig. 6 (a-c) SEEP/W model results and (d-f) Phreatic Line behavior for dam with full cut-off wall. (a,d) Reservoir height = EL 270 ft, (b,e) Reservoir height = EL 339 ft, (c,f) Reservoir height = EL 346 ft.

For the current case it seems that partial cutoff wall and full cutoff wall doesn't make much difference in lowering the seepage and exit gradient as the same trend was observed for all the scenarios. **Fig. 7** explains a graphics relation for seepage flux, exit gradient, and maximum seepage velocity as a function of elevations, respectively.

a.	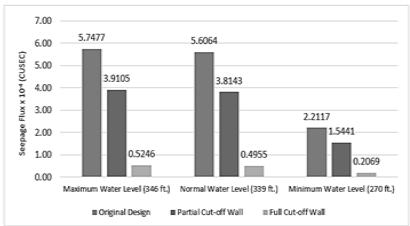

b.	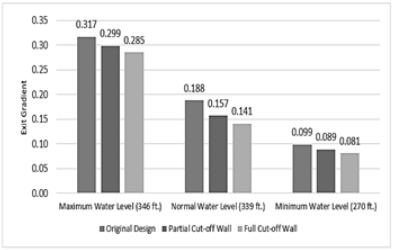
c.	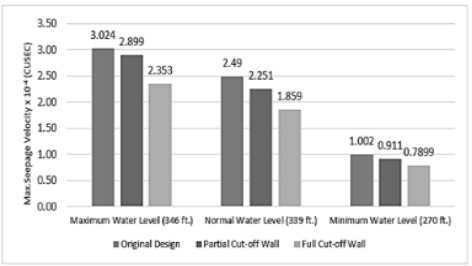

Fig. 7 Relationship of water level in reservoir with (a) seepage flux, (b) exit gradient and (c) Maximum Seepage Velocity for various scenarios.

4. Conclusions

As seepage is a problematic issue in earth dams therefore, this study attempted to investigate seepage effect on an earthen dam (Hub dam) for three different scenarios i.e., (i) original design, (ii). Dam with a partial cut-off wall, (iii). Dam with a full cut-off wall respectively. The analysis is carried out by using SEEP/W, a sub program of Geo-Slope software. Simulated results were obtained after using the hydraulic conductivities of different materials used for the dam construction. The results showed that the cut-off wall at its original design performs better as the overall minimum seepage value of order 2.2117×10^{-4} ft^3/sec/ft, with an exit gradient of 0.099 and minimum seepage velocity 1.0020×10^{-6} ft/sec, at EL 270 ft reservoir level. The results included the seepage flow paths and flow patterns together with the velocity vectors, as well as pore-water pressure results. The existence of a cut-off walls will reduce the uplift pressure under the foundation and the exit gradient downstream of the structure, which reduces the required volume of the super structure and the length of the downstream protection, respectively. The comparison of all three cases showed that the length of the cut-off wall plays an essential role to protect the dam from the seepage problem. Use of partial cut-off and full cut-off wall may not contribute much to lower the various flow parameters respectively. According to the simulated results it is an evident that the imperviousness of the foundation material is predominant over that of the shell material in the case of the Hub dam, it is discovered that the installation of an impervious cut-off wall has little impact on reducing the amount of seepage. Therefore, the role of the length of the cut-off wall is almost negligible for most of the flow parameters. The numerical methods give deep

understanding for hydraulic and geotechnical problems. Hence, it can be concluded that Hub dam performed effectively since its construction at its original shape and design.

Acknowledgement

The authors wish to express their gratitude to ACE Pakistan (Associated Consulting Engineers), WAPDA Pakistan (Water and Power Development Authority) officials deputed at Hub dam, and all other individuals who have been source of help throughout the research period.

References

1. A Kamanbedast, A Delvari. World App. Sci. J 2012; 17(9):1087-1094.
2. OA Al-Damluji, M Fattah, RA Al-Adthami. J Eng. Tech. 2004; 23(12):750-766.
3. I Arshad, MM Babar, CA Vallejera. PSM Biol. Res. 2019; 4(1):40-50.
4. RZ Moayed, VR Rashidian, E Izadi. Civ. Eng. Dept. Imam Khomeini Int. Uni. Qazvin, Iran. 2012.
5. A Malekpour, D Farsadizadeh, AH Dalir, J Sadrekarimi. Turk. J Eng. Environ. Sci. 2012; 36(2):139-152.
6. HKT Alnealy, NOS Alghazali. Amer. J Civ. Eng. 2015; 3(4):116-124.
7. B Mansuri, F Salmasi. J Civ. Eng. Urban. 2013; 3(3): 114-121.
8. SO Osuji, SA Adegbemileke. Asian J Sci. Tech. 2015; 6(5):1447-1454.
9. A Parsaie, AH Haghiabi. J Civ. Eng. 2018; 4(2):143-151.
10. I Arshad, MM Babar, N Javed. PSM Biol. Res. 2017; 2(1):13-20.
11. WAPDA. 4th Periodic Inspection Report of Hub Dam. Published by ACE – WAPDA. 4th ed. Karachi: Pakistan 2009.
12. I Arshad. Int. J Altern. Fuels. Energy. 2018; 2(1):01-13.
13. TD Stark, NH Jafari, JSL Zhindon, A. Baghdady. J Geotech. Environ. Eng. 2017; 143(2):112-121.
14. SAA Khattab Al- Rafidain Eng. J. 2010; 18(1):95-102.
15. I Arshad, MM Babar. Finite Element Analysis of Seepage through an Earthen Dam by using Geo-Slope (SEEP/W) software. Int. J. Res., 2014; 1(8): 612-619.
16. S Baghalian, F Nazari, SS Malihi. Int. J Eng. App. Sci. 2012; 4(3):49-56.
17. S Nasim. M.Sc. Thesis, Collage of Engineering, University of Kufa, Iraq. 2007.
18. I Arshad, MM Babar. Int. J Res. 2014; 1(7):67-79.

19. D Doherty. Design and Construction of Earth Dams: A Primer on Dam Design. 5th ed. New York: Longman 2009.

20. OE Omofunmi, JG Kolo, AS Oladipo, PD Diabana, AS Ojo. J App. Sci. Tech. 2017; 22(5):1-11.

21. AJJ Aasma. Diyala J Eng. Sci. 2016; 9(2):83-94.

22. I Arshad, MM Babar, CA Vallejera. Int. J Altern. Fuels. Energy. 2019; 3(1):1-12.

23. AA Jamel. Diyala J Eng. Sci.,2016; 9(2):38-49.

24. R Issam, B Bachir, R Abdelaziz, I Arshad. PSM Biol. Res. 2020; 5(4):137-146.

25. RH Irzooki. Eng. Tech. J. 2016; 34(3):430-440.

Review of Specifications of Structural Steels

Asim Kumar Samanta[a], Kishore Debnath[a], Arpan Kumar Mondal[c]

Abstract

Steel is very important material as it is used in many applications. Structural steel is used to construct infrastructure such as Buildings, Bridges and Stadiums etc. needed for development, which is about 50% of total steel consumed. However, quality of steel is a matter of concern. If the strength of steel increases, steel structure becomes lighter. However, increasing strength of steel creates difficulty in welding as well as elongation, which are also equally important required properties. Specifications of steel produced in India are compared with respect to the specifications of steel produced in advanced countries like USA, Europe and Australia. It has been observed that specifications of structural steel in India are not advanced enough compared to the specifications in advanced countries.

Keywords: Structural; Steel; Yield Strength; Weldability; Elongation; Alloy Steel.

1. Introduction

Steel is the most versatile material mankind has ever developed so far. No other material can find so many applications. Steel is used to manufacture a small item like pin. It is used to construct a big application like bridge. The reasons for its wide-ranging applications of steel are versatile properties, steel can exhibit. Every application needs particular properties to make it suitable for application.

Steel is an alloy of iron and carbon. The raw materials of steel are generally Hematite (Fe_2CO_3) and Magnetite (Fe_3CO_4). Pig Iron (maximum 4% Carbon) is produced in blast furnace or in similar furnaces using raw materials. Pig Iron is converted to steel in steel smelting furnace by controlling the impurities and adding required elements to achieve desirable properties needed for a particular application. Then steel is rolled to different plates / shapes in rolling mills to make it suitable for fabrication. Properties are improved through different thermo-mechanical processes.

2. Classification of Steel

Steel is an alloy material. It consists of iron, carbon, manganese, silicon, sulphur and phosphorous. Carbon content is limited to 2% maximum in steel. The alloying elements

✉ Asim Kumar Samanta

p19me019@nitm.ac.in

[a] Department of Mechanical Engineering, NIT Meghalaya, Shillong 793003, India

[b] Department of Mechanical Engineering, NITTTR Kolkata, Kolkata 700106, India

such as copper, molybdenum, nickel, and vanadium etc. are also added in pre-determined quantity to achieve some application related properties in steel.

According to EN 10020 - 2000 (Definition and classification of grades of steel)[1], Steel is classified by chemical composition as alloy steel and non-alloy steel. However, classification of steel as per its usage is also common practice. The term “Structural steel” is one of such practices.

3. Structural Steel

Structural steel contains maximum 0.25% of carbon. Structures such as bridges, buildings and stadium etc. are the facilities constructed using structural steels in our society to facilitate easy and improved life of human beings. About 1950 MT steel was produced in 2021 worldwide. Approximately 50% steel is used in construction of structures. Every application of steel needs some specific properties.

Following are the important properties of structural steels.

- **a.** Yield strength
- **b.** Tensile strength
- **c.** Elongation
- **d.** Impact strength
- **e.** Weldability
- **f.** Corrosion resistance
- **g.** Fire resistance
- **h.** Fatigue resistance
- **i.** Elastic modulus
- **j.** Poisson's ratio
- **k.** Shear strength
- **l.** Co-efficient of thermal expansion

Specifications of structural steel are standardized worldwide in different codes and standards elaborating the required properties. Mechanical properties such as yield strength, tensile strength, elongation and impact strength are mentioned in every standard. Weldability, corrosion resistance, fire resistance and fatigue resistance are determined from the chemical composition as well as the manufacturing processes. Other properties are physical and cannot be changed.

4. Classification of Structural Steel

Based on chemical compositions, structural steel is classified mainly in three broad categories. Such as carbon steel (Manganese <1.20%), carbon-manganese steel

(Manganese >1.20%) and structural alloy steel containing many alloying elements mentioned in EN 10020 – 2000[1].

Structural steel can be graded based on mechanical properties mainly by minimum yield strength, some time by minimum tensile strength. Structural steel having less than 235 MPa yield strength is understood to be low strength structural steel whereas structural steel having yield Strength from 235 MPa to 350 MPa is understood to be medium strength structural steel and high strength structural steel has yield strength more than 350 MPa.

5. Important Properties

Tensile properties such as yield strength and tensile strength are the most important properties of structural steel because members in structure are required to carry/withstand loads. However, the idea of more yield strength of steel will result into comparably lighter structure may not be true always.

Normally, members of the structure are subjected to three types of loads. These are tension, compression and bending loads. Increased yield strength will definitely make the structure lighter if the member is subjected to tensile loads. However, if the member is subjected to compression, yield strength has no role to play. Member will buckle under compression. Buckling resistance ($P_{cr} \propto EI/L^2$) proportional to moment of inertia (I) which is the geometrical properties of the member and independent of yield strength. When the member is subjected to bending, the member will be subjected to both tension and compression and it will create deflection. In this case, increased tensile properties may be helpful but limit in deflection may not permit the member to be under tension to the maximum limit. Deflection is proportional to (ML/EI), dependant on moment of inertia (I) and independent of yield strength. May be, this is the reason that steels of medium strength are mostly used in structure.

However, from construction technology point of view, welding is one of the important properties. During fabrication, welding is a preferred method of joining owing to its several advantages. Strength of steel is increased by adding carbon and manganese etc. but it reduces the weldability. Instead of content of carbon, carbon equivalent of steel is the terminology which indicates the weldability or relative weldability – more correctly. Following formulae of carbon equivalent recommended in section H5.1 of AWS D1.1 – 2020 (Structural welding code—steel)[2] is accepted worldwide to calculate carbon equivalent (CE) of structural steel.

$$CE = C + \frac{Mn}{6} + \frac{Cr+Mo+V}{5} + \frac{Ni+Cu}{15} \quad (1)$$

Based on formulae of carbon equivalent mentioned above, the 'Welding Technology Institute' of Australia has provided the information (**Table 1**) on weldability of structural

steel in its technical note no.1 titled "The Weldability of Steels"[3]. It shows that how welding becomes difficult with the increasing of carbon equivalent.

Table 1 Weldability with respect to carbon equivalent.[3]

Carbon Equivalent	Weldability
Below 0.40	Any welding process with any electrode is satisfactory
Between 0.40 – 0.50	Hydrogen controlled electrodes with semi-automatic processes are recommended. Rutile or other electrodes maybe used
Between 0.50 – 0.60	Hydrogen controlled electrodes or semi-automatic or automatic processes are essential.
Between 0.60 – 0.80	Hydrogen controlled electrodes or semi-automatic or automatic processes are essential. However, slow cooling from welding or preheat temperature is recommended. Post-weld heat treatment is suggested for stress relief, particularly where severe service conditions apply to the component
Above 0.80	Welding is not recommended

From serviceability / durability of structures point of view, another three important properties are resistance to corrosion, fatigue and fire. Corrosion is a natural phenomenon for degrading steel and hence resisting corrosion is important. Though many methods to prevent corrosion are available, resistivity of steel to corrosion by virtue of its chemical composition is important. Index of corrosion resistance is given in ASTM G 101 - 2015 (Standard guide for estimating the atmospheric corrosion resistance of low alloy steel)[4]. The formula is known as Legault-Leckie Equation. The equation is given below:

$$I = 26.01\,(\%\ of\ Cu) + 3.88\,(\%\ of\ Ni) + 1.20\,(\%\ of\ Cr) + 1.49\,(\%\ of\ Si) + 17.28\,(\%\ of\ P) - 7.29\,(\%\ of\ Cu)(\%\ of\ Ni) - 9.10\,(\%\ of\ Ni)(\%\ of\ P) - 33.39\,(\%\ of\ Cu)^2 \quad (2)$$

Another two resistances (fire and fatigue) of structural steel, though important, are not included in this paper to keep it simple for understanding.

There are many products of structural steel. Hence, there are many codes / standards. However, codes related to manufacturing of hot-rolled plates and shapes (angle, beam and channel) are included here for discussion. Related codes published in USA, Europe and Australia are referred to here for comparison.

In this context, it may be noted that the structural steel having more than 450 MPa yield strength or having less than 15% elongation is not considered for design of structure for many reasons as recommended by standards for designing structures of many countries including India.

6. Structural Steel Specifications in India

Bureau of Indian Standards (BIS) is the statutory authority in India to publish codes & standards. It has published four standards for manufacturing structural steels. These are described here briefly.

IS 15911 - 2010 (Structural steel (ordinary quality) — specification)[5] is the standard for producing low strength structural steels. It specifies three grades of steel having minimum yield strength of 165 MPa, 170 MPa and 215 MPa. Normally alloying elements are not added. These steels are not used where minimum impact strength is required. Big structures are not constructed with these steels as structure will heavy owing to its low strength.

IS 2062 - 2011 **(**Hot rolled medium and high tensile structural steel — specification)[6] is the most important code for producing structural steels. IS 800 - 2007 (General construction in steel - code of practice)[6] directly recommends to use steel produced as per IS 2062 - 2011 having up to 450 MPa yield strength and minimum elongation of 15%, though the code specifies steels from 250 MPa to 650 MPa yield strength. It specifies the steels into four sub-grades based on the requirement of impact strength. However, mixing of alloying elements is optional.

1S 11587 - 1986 (Specification for structural weather resistant steels)[7] specifies steel of two strength levels (480 MPa and 500 MPa). It may be noted that the strength level mentioned in this code is not yield strength as convention. Rather it is minimum tensile strength. Yield strength is in the range of 325 – 355 MPa. A number of alloying elements are added to the steels to make these corrosion resistant. However, steel is not produced as per this code in India as it is not directly recommended by the design code (IS 800 – 2007) and users are used to protect steel from corrosion by other methods such as painting and thermal spraying etc.

IS 15103 - 2002 (Fire resistant steel – specification)[8] is also a code made to produce fire resistant steels. It specifies steel of two strength levels (410 MPa and 490 MPa). However, similar to corrosion resistant steel, the strength mentioned here is maximum tensile strength. Yield strength of steels specified here is in the range of 240 – 350 MPa. In this case too, a number of alloying elements are added to the steel to make it fire resistant. However, steel is not produced as per this code in India as it is not directly recommended by the design code (IS 800 - 2007) and users are used to protect steels from fire by other conventional methods.

7. Structural Steel Specifications in USA

The USA (United States of America) is considered to be the most advanced country in terms of technological advancement. Production of steel and its applications are no exception. Many societies / associations published codes and standards. However, standards published by ASTM (American Society of Testing Materials) related to steel is

very popular and adopted not only in USA but also in many other countries. ASTM has published several standards specifying many grades of steel. In this context, it may be noted that AISC 360–2016 (Specification for structural steel buildings)[9] is an important code for designing steel buildings. It recommends the steel produced as per ASTM standards. Following are the few standards for manufacturing structural steels.

ASTM A 36/A 36M - 2019 (Standard specification for carbon structural steel)[10] is a standard used for manufacturing of structural steel of 250 MPa (minimum yield strength) to be used for all structural applications. The steel has no specific micro-alloying element. However, copper of minimum 0.20% may be added if specified.

ASTM A 529/A 529M - 2019 (Standard specification for high strength carbon manganese steel of structural quality)[11] is the standard specifying higher strength (345 MPa and 380 MPa minimum yield strength). The standard permits steels to have more than 1.20% manganese along with other micro-alloying elements such as copper, columbium, chromium, nickel and molybdenum etc.

ASTM A 242/A 242M - 2018 (Standard specification for high-strength low-alloy structural steel)[12] specifies structural steel of three grades (290 MPA, 315 MPA and 345 MPa minimum yield strength) to be used as structural members where durability is desired. The steels have alloying elements such as chromium, nickel, silicon, vanadium, titanium and zirconium in addition to minimum copper of 0.20%. The extended durability is achieved by making the steels corrosion resistant. It has Index of corrosion resistance more than 6.0 as per the predictive method based on the data of Larabee and Coburn as given in ASTM G 101 (Standard guide for estimating the atmospheric corrosion resistance of low alloy steels)[4].

ASTM A 572/A 572M - 2021 (Standard specification for high-strength low-alloy columbium-vanadium structural steel)[13] is another standard specifying low alloy structural steel of five grades (290 MPa, 345 MPa, 380 MPa, 415 MPa and 450 MPa minimum yield strength). Obviously, these steels contain alloying elements in different combinations.

ASTM A 588/A 588M - 2019 (Standard specification for high-strength low-alloy structural steel with 345 MPa minimum yield point to 100 mm thick)[14] is also another standard specifying corrosion resistant steel of yield strength from 290 MPa to 315 MPa. The steels are used in light weight welded bridges and buildings where added durability is desired. The steels have index of corrosion resistance more than 6.0 as per 'Predictive method based on the data of Larabee and Coburn' as given in ASTM G 101 (Standard guide for estimating the atmospheric corrosion resistance of low alloy steels)[4].

ASTM A 709/A 709M - 2021 (Standard specification for structural steel for bridges)[15] is a standard where high performance steels of 345 MPa, 485 MPa and 690 MPa minimum yield strength intended to be sued in Bridges are specified. It has specifications of 250

MPa and 345 MPa with superior quality compared the similar steels specified in other standards.

ASTM A 913/A 913M - 2019 (Standard specification for high-strength low-alloy steel shapes of structural quality, produced by quenching and self-tempering process)[16] specifies the steels of higher strength (345 MPa, 415 MPa, 450 MPa and 485 MPa). The steels are produced by Quenching and Self-Tempering Processes. The steels used to make steel shapes (angle, beam and channels).

8. Structural Steel Specifications in Europe

EN 10025 (Hot rolled products of structural steels) is the specification of structural steel produced in Europe. Different qualities of steel are specified by its several parts which are described below. EN 10025 (Part 1) - 2004 (Hot rolled products of structural steels: General technical delivery conditions)[17] describes the general requirements of producing steel specified other parts of EN 10025.

EN 10025 (Part 2) - 2019 (Hot rolled products of structural steels: Technical delivery conditions for non-alloy structural steels)[18] specifies the structural steels of five strength levels (235 MPa, 275 MPa, 355 MPa, 460 MPa and 500 MPa). Steel of each strength level is sub-divided into many grades based on impact strength requirement at room temperature (20˚C), 0˚C and -20˚C. It has also specified another three grades of steels (S185, S295 and S360) which do not require any impact test. Copper up to 0.55% are added to make steels resistant to corrosion. All specified grades of steel contain a number of micro-alloying elements (below the limit specified in EN 10020), hence described as non-alloy structural steels.

EN 10025 (Part 3) - 2019 (Hot rolled products of structural steels: Technical delivery conditions for normalized/normalized rolled weldable fine grain structural steels)[19] describes the specification of structural steel in four strength levels (275 MPa, 355 MPa, 420 MPa and 460 MPa minimum yield strength). All steels are normalized, fine grained and weldable, hence superior in quality compared to the steels specified in Part 2 of EN 10025. Copper up to 0.55% are added to make steels resistant to corrosion. All grades of steel are tested for impact strength at -20˚C and -50˚C.

EN 10025 (Part 4) - 2019 (Hot rolled products of structural steels: Technical delivery conditions for thermo-mechanical rolled weldable fine grain structural steels)[20] specifies steels of five strength levels (235 MPa, 355 MPa, 420 MPa, 460 MPa and 500 MPa). All steels are rolled by thermo-mechanical process (increased cooling rate with or without tempering but excluding direct quenching or quenching and tempering) to achieve some properties which are not possible by heat-treatment alone. All grades of steel are tested for impact strength at -20˚C and -50˚C. Steels are fine grained according to ISO 643 - 2003 (Steels – micrographic determination of the apparent grain size)[21].

EN 10025 (Part 5) – 2019 (Hot rolled products of structural steels: Technical delivery conditions for structural steels with improved atmospheric corrosion resistance)[22] specifies four steel grades (S235, S355, S420 and S460). All grades of steel are with improved corrosion resistance which are achieved by adding copper (0.25-0.55%), chromium (0.40-0.80%), nickel (0.65% maximum), molybdenum (0.30% maximum) and zirconium (0.15% maximum). All grades of steel are also tested for impact strength at 0˚C, -20˚C, -40˚C and -50˚C as per requirement.

EN 10025 (Part 6) - 2019 (Hot rolled products of structural steels: Technical delivery conditions for flat products of high yield strength structural steels in the quenched and tempered condition)[23] specifies seven grades (S460, S500, S550, S620, S690, S890 and S960) of steels which are fully killed and fine-grained. High Strength of Steels is achieved by quenching and tempering processes. Impact Strengths are tested at 0˚C, -20˚C, -40˚C and -60 ˚C as required.

It may be noted here that all the steel specified above are not suitable for every application. For selecting the appropriate grade of steel, related design standard should be referred to. For example, for steel buildings, steel having minimum elongation of 15% and strength up to 460 MPa yield strength with ratio of tensile stress to yield stress more than 1.10 as recommended in EN 1993-1-1-2005 (Design of steel structures: general rules and rules for buildings)[24].

9. Structural Steel Specifications in Australia / New Zealand

Specifications of structural steels produced in Australia and New Zealand are standardized by atandards Australia situated in Sydney, Australia. Important standards related to manufacturing of hot rolled plates and shapes are described briefly here.

AS/NZS 1594 - 2002 (Hot-rolled steel flat products)[25] specifies chemical composition and mechanical properties of hot rolled plates etc. It has specifications of five grades of steels (200, 250, 300, 350 and 400). Presence of micro-alloying elements like copper, nickel, chromium, niobium and vanadium make the quality of steels better. However, these steels are not tested for impact strength.

AS/NZS 3678 - 2016 (Structural steel - hot-rolled plates, floorplates and slabs)[26] is another standard for specifying steel plates of structural us when impact test is mandatory. Steel produced according to this standard have six strength levels (200, 250, 300, 350, 400 and 450 minimum yield strength). Micro-alloying elements like copper, nickel, chromium, aluminum, titanium, niobium and vanadium are added. Steels are tested for minimum impact strength at 0˚C, -15˚C, -20˚C and -40˚C as per requirement.

AS/NZS 3679 - 2016 (Structural steel - Part 1: Hot-rolled bars and sections)[27] is the standard of structural steels required to produce shapes (angle, beam and channel etc.). It specifies steels of two strength levels (300 and 350 MPa minimum yield strength). Though steels are described as carbon or carbon-manganese steels but presence of micro-

alloying elements like copper, nickel, chromium, molybdenum, niobium and vanadium in various proportions makes the steels quality better. Steels are tested for minimum impact strength at 0°C and -15°C.

AS/NZS 3679 - 2016 (Structural steel – Part 2: Welded I-sections)[28] is the standard specifying the manufacturing of I-sections using the hot rolled plates produced according to AS/NZS 3678 – 2016. It is to be noted that 'I-Section' (beam) is one of the most efficient sections (shape) in terms of its geometrical properties. Normally wide flange beams and columns are manufactured by welding.

In this context, it may be noted that the steel structures in Australia / New Zealand are designed by AS 4100 - 2020 (Steel structures)[29] which recommends steels of maximum yield strength of 450 MPa and more than 15% elongation should be used for construction of steel structures.

10. Review & discussion

Steel structure is designed to not only satisfy constructional requirement but also to ensure that the structure will survive for its entire long life (50-100 years) after resisting all the actions (loads). That is why not only strength but also resistance to corrosion and fatigue etc. are equally important properties of structural steels. By using increased strength of the steel, structures may not be lighter always as strength of members subjected to compression or bending depend of geometrical properties rather than yield strength. Most of the design codes worldwide recommend use of steels up to 450 MPa yield strength ensuring than it has minimum elongation of 15%. If the structure is exposed to cold weather, impact strength at lower temperature is another necessity. In view of above, all the specifications mentioned above are compared with respect to yield strength, weldability and resistance to corrosion.

Table 2 shows the range of strengths of structural steel produced in different countries. It has been observed that minimum yield strength of the steels produced is 165 MPa which is in India. Maximum strength is 960 MPa in Europe. Type of steels produced in India is either carbon steel or carbon-manganese steel. There is no specification of alloyed structural steel in India. However, it is interesting to note that the only specification off fire-resistant structural steel is IS 15103 – 2002 which is an Indian standard. No other country has specification of fire-resistant steel. In view of recommendations in design code (AS 4100), steels produced in Australia are of efficient categories. Specifications of Australia are very simple to understand.

Table 2 Minimum and maximum yield strength of steels specified in different countries.

Country	Standard	Minimum Yield Strength	Maximum Yield Strength
India	IS 15911 - 2010	165 MPa	215 MPa

	IS 2062 - 2011	250 MPa	650 MPa
USA	ASTM A 36 - 2019	250 MPa	-
	ASTM A 709 - 2021	250 MPa	690 MPa
Europe	EN 10025 (Part 2) - 2019	235 MPa	500 MPa
	EN 10025 (Part 6) - 2019	460 MPa	960 MPa
Australia / New Zealand	AS/NZS 1594 - 2002	200 MPa	400 MPa
	AS/NZS 3678 - 2016	200 MPa	450 MPa

Though the steel of specification up to 650 MPa is specified in IS: 2062 – 2011, it is not clear how the steel beyond 400 MPa minimum yield strength is to be produced. Specifications of advanced countries reveal that high strength steel is produced by "Quench-Tempering" processes. However, these high strength steels are not in regular production in India.

ASTM A 709 - 2021 is the only code specifying high performance steels (of 345, 485 and 690 MPa minimum yield strength) which exceed requirements of properties mentioned in other codes for similar strength levels.

Weldability is very important property of steel. It is mandatory requirement of construction and maintenance of structure. Relative weldability is assessed by its 'Carbon equivalent'. Carbon equivalent of steels of comparable strengths is shown in **Table 3**. It can be observed that steel having more than 400 MPa yield strength has Carbon equivalent more than 0.50 is difficult to weld. Difficulty in welding of structural steel has been reduced in other countries by adding alloying elements. But Indian standard does not specify adding of alloying elements. Though a few alloying elements are added on demands of purchaser but it can't solve weldability problems.

Table 3 Carbon equivalent and index of corrosion resistance of comparable grades of steels.

Standards	**Grades**	**Carbon Equivalent**	**Index of Corrosion Resistance**
IS 2062 - 2011	E 350 (A, BR, BO)	0.47	0.84
	E 450 (A, BR)	0.52	0.84

EN 10025 (P-2) - 2019	S 355K2	0.49	5.45
	S 450JO	0.49	5.54
EN 10025 (P-3) - 2019	S 355 N	0.45	8.42
	S 460 N	0.54	7.85
AS 3678 - 2016	350	0.48	7.17
	450	0.48	4.96
AS 3679 (P-1) - 2016	350	0.45	7.03
ASTM 709	HPS 345 W, HPS 485 W	-	7.30
Note: ASTM Codes does not provide any Carbon equivalent value in the standards. AWS D 1.1 (Structural welding code – steel) recommends welding procedure for each grade of steels separately.			

Corrosion is a natural phenomenon for degradation of steels. Corrosion is normally prevented/ reduced in the structure by coating (painting / thermal spraying) or any other method such as cathodic protection., However, inherent resistance to corrosion is desirable. Index of resistance to corrosion is evaluated by using Legault-Leckie equation as recommended by ASTM G 101 – 2015. The index calculated for different specification is given in **Table 3**. It is observed that steels produced in advanced countries have better resistance to corrosion.

11. Conclusions

Steel is preferred for constructing structures for its high strength to weight ratio. Durability and maintainability are few of the other properties for selecting steel for constructing structures. As strength of steels increases, structures become lighter consuming less amount steel. However, this idea may not be true in all the cases. Load bearing capacity of members in either compression or bending increases with the increase of moment of inertia (which is a geometrical property). It is not dependent of yield strength of the steel.

When the strength of the steel is increased, weldability is decreased. Weldability is a matter of concern for using high strength steel (more than 350 MPa yield strength). That is why structural steels of medium strength (250 MPa - 300 MPa yield strength) are mostly used / produced. Problems of weldability are reduced by adding alloying elements or by grain refining in advanced countries, which is not seen in India.

Similarly, index of corrosion resistance of the steel abroad is substantially higher compared to steel in India. Hence, performance of steel in structure is better in advanced countries. Obviously, steel produced in USA, Europe and Australia is costlier compared to that of steel produced in India.

References

1. EN 10020 - 2000, European Committee for Standardization, Brussels.
2. AWS D1.1 – 2020, American Welding Society, USA.
3. WTIA Technical Note No.1, Welding Technology Institute of Australia, Newington, Australia.
4. ASTM G 101 - 2015, American Society for Testing and Materials, USA.
5. IS 15911: 2010, Bureau of Indian Standards, New Delhi.
6. IS 2062 - 2011, Bureau of Indian Standards, New Delhi.
7. 1S 11587 - 1986, Bureau of Indian Standards, New Delhi.
8. IS 15103 - 2002, Bureau of Indian Standards, New Delhi.
9. AISC 360 – 2016, American Institute of Steel Construction (AISC), Chicago, USA.
10. ASTM A 36/A 36M - 2004, American Society for Testing and Materials, USA.
11. ASTM A 529/A 529M - 2005, American Society for Testing and Materials, USA.
12. ASTM A 242/A 242M - 2013, American Society for Testing and Materials, USA.
13. ASTM A 572/A 572M - 2007, American Society for Testing and Materials, USA.
14. ASTM A 588/A 588M - 2004, American Society for Testing and Materials, USA.
15. ASTM A 709/A 709M: 2009, American Society for Testing and Materials, USA.
16. ASTM A 913/A 913M - 2001, American Society for Testing and Materials, USA.
17. EN 10025 (Part 1) – 2004, European Committee for Standardization, Brussels.
18. EN 10025 (Part 2) – 2004, European Committee for Standardization, Brussels.
19. EN 10025 (Part 3) – 2004, European Committee for Standardization, Brussels.
20. EN 10025 (Part 4) – 2004, European Committee for Standardization, Brussels.
21. ISO 643 – 2003, International Organization for Standardization, Switzerland.
22. EN 10025 (Part 5) – 2004, European Committee for Standardization, Brussels.
23. EN 10025 (Part 6) – 2019, European Committee for Standardization, Brussels.
24. EN 1993-1-1-2005, European Committee for Standardization, Brussels.

25. AS/NZS 1594 – 2002, Standards Australia, Sydney, Australia.

26. AS/NZS 3678 – 2016, Standards Australia, Sydney, Australia.

27. AS/NZS 3679 – 2016 (Part 1), Standards Australia, Sydney, Australia.

28. AS/NZS 3679 – 2016 (Part 2), Standards Australia, Sydney, Australia

29. AS 4100 – 2020, Standards Australia, Sydney, Australia.

A State-of-art on Different Techniques Used in Tool Depreciation Method

Banarsi Pandey[a,b], Sachindra Mahto[a], Binit Kumar Jha[c]

Abstract

Surface roughness induced in machined components affects the quality of the products as well as the machining cost. Surface roughness has a significant role in tool wear management and this is one of the easiest methods to monitor the machine under various operating criteria. Surface roughness is directly involved in tool wear prediction. Here, the paper explores the different techniques regarding online wear monitoring. The wear measurement is of two types: direct measurement and indirect measurement methods. This paper includes several types of methods and techniques related to tool wear detection and surface roughness optimization. It may be interesting for researchers working on tool wear monitoring systems. Here, the phenomenon and criteria selection of the tool wear monitoring method in detail is discussed. The author has drawn several conclusions based on the comparative study of the reports that shows the utility of a wear detection setup in manufacturing and other industries. The sensors fusion method is used in online tool wear monitoring systems. The monitoring system where two or more two sensors of the same and different types are used and decisions are made based on the comparative study of the sensors, called as sensors fusion method.

Keywords: Tool Depreciation; Surface Roughness; Detecting Technique; Cutting Parameters

1. Introduction

The tool damages generally occur during the cutting process and directly affect the surface roughness. Thus, overall efficiency of the machine and economic efficiency is affected. Day by day many scholars research different types of methods that try to diminish tool defects. No one can completely diminish the tool defect problem. Here the researchers try to find out defects as earlier as possible so the major damages will be solved and safe the complete setup by changing the tool from time to time.[3]

A minimized tool defect shows the surface roughness is refined. By doing all these things researchers become successful to keep the production cost lower. Industry statistical reports reveal that tool failure is the most common factor causing any machine to break down. It is 20% to 30% during the total downtime of the CNC machine tool[1-3]. Research

[3] ✉ Banarsi Pandey
banarsi1983@gmail.com

[a] Department of Mechanical Engineering, North Eastern Regional Institute of Science and Technology, Itanagar, Arunachal Pradesh 791109, India

[b] School of Manufacturing Skills, Bhartiya Skill Development University, Rajasthan 302042, India

[c] Department of Mechanical Engineering, Regent Education and Research Foundation, Barrackpore, West Bengal 700121, India

reports also show that 75% of the downtime may be reduced if the machine is having tool wear measurement and detecting systems. Because of this productivity is increased by 10%~60% and machine utilization is raised to 50%[2,3].

American Kennametal Corporation's research study reveals that about 30% of the total processing fee can be saved if the CNC monitoring system is used[3,4]. Hence, it is essential, to develop a new process from time to time in the wear-detecting system that improves the surface roughness, which is due to tool wear phenomena. So that, the machine runs smoothly without any disturbance for a long period. Wear-detecting techniques are grouped into two categories[3,5,6].

1. Direct wear detecting technique and
2. Indirect wear-detecting technique

The direct wear measurement technique is the monitoring process based on the direct contact method. The direct wear measurement technique contains current discharge, optical fiber observations, coating microscope properties, resistance analysis technique, ray calculation technique, and image processing technique[5]. The implementation of this technique in practice is not so easy because this is having two drawbacks, firstly, it is very difficult to detect tool states in operational conditions, and secondly, it is impossible to check sudden damages in the operating state. Therefore, the indirect measurement method has become the most popular study for researchers. This uses the physical quantities that include the cutting process, like cutting force, torque, workpiece geometry, chip shape, and noise or vibration intensity. In the past few years, improvement and search for new techniques for tool wear-detecting setups and methods becomes a burning issue. This is all because it improves the overall efficiency of an industry.

The indirect tool wear-detecting techniques include various no of sensors depending upon the need; these may be either similar or dissimilar kind. The analysis done by controlling the unit of a sensor at the running time is called a real-time measurement technique sometimes; the prediction of tool depression is identified with a simulation method. Overall, this technique is classified into two categories[5].

1. On-line detecting technique, and
2. Simulation-based detecting technique.

On-Line Detecting Technique

Online tool wear-detecting technique is related to the sensor's behaviour and its application. These sensors take the input as physical properties like velocity, acceleration, force, etc., and transform this as electrical signals[7].

Simulation-Based Detecting Technique

Here, the tool depression is detected by the simulation 3D technique. An optimistic condition is developed that is closer to real working criteria in a computer with the help of the simulation 3D technique. After successful implementation, the same is validated on the real machine. This is also known as the offline tool depression method.

The paper generally described the various numbers of technical papers regarding improvement and search of different methods for online detecting techniques along with optimization of process parameters and, 3D simulation validation. The author tries to clarify many aspects regarding how a tool-detecting technique setup is developed, its method, and its application in brief. This paper also deals with 3D simulation, description of process variables on the response factor, different types of optimizations, and validation techniques. The paper aims to focus on the overall productivity increment of any machine by reducing the tool wear, increasing surface roughness, setting the optimum spindle speed, and taking care of process variables over the response factor.

2. The Indirect Method of the Tool Conditioning Monitoring

This system includes the sensors, data acquisition device, signal propagating & analysis device and processing unit, condition realization device, and a display unit. The block diagram of the Tool condition monitoring system is represented as shown in the **Fig. 1**. This paper describes the different types of tool condition monitoring techniques in brief. It also deals with the relationship among process variables, response face, and, tool depreciation for most of the TCM system. The general schematic diagram of the TCM system is shown in **Fig. 2**.

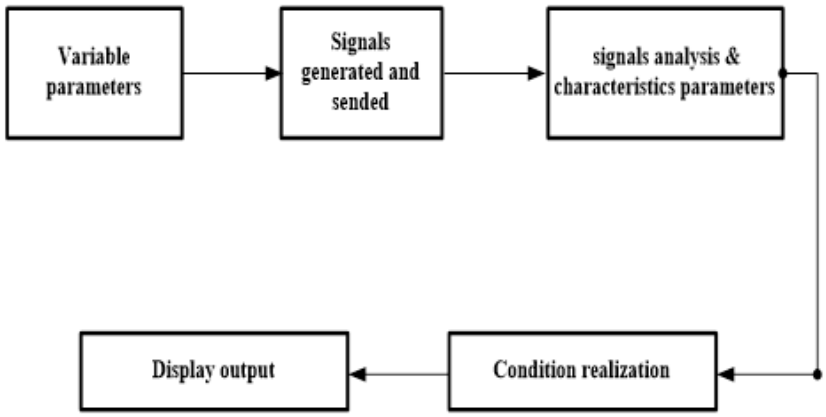

Fig. 1 Block Diagram of TCM Set-Up.

2.1 Tool Depreciation Detecting Technique on Cutting Force

Most of the scholars found that the cutting tool is engaged with the workpiece during the machining process. A dynamic motion is initiated because of residual stress. A force sensor takes this as an input signal in the form of an electric signal which is converted

into force in terms of volts. As the cutting force increases the rake face's contact area increases, as a result, the wear increases. Ordinary strain gauges, piezoelectric sensors, and dynamometers are used to detect the signals output from the systems.

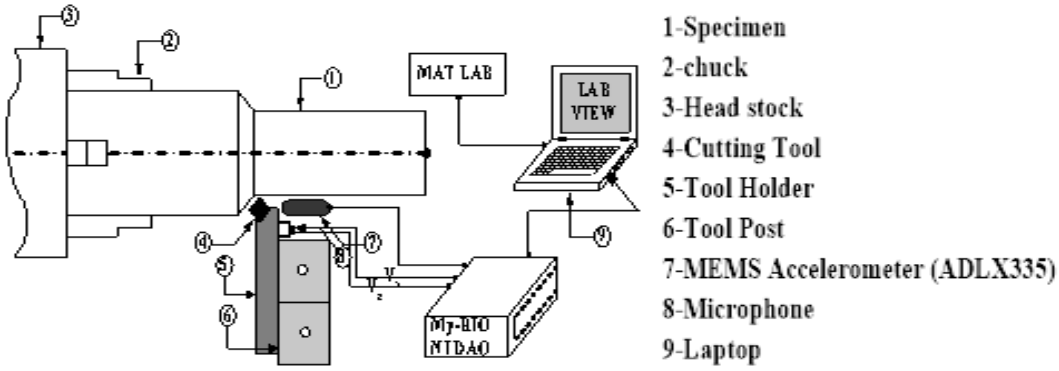

Fig. 2 Schematic Diagram of TCM.

The turning of UNS-A97075 in a dry environment requires increased spindle speed. Hence a great amount of friction is induced between the contact surface tool and the workpiece. As a result of this friction and vibration are induced and the tool is burned out[8]. The cutting force is directly proportional to the parametric variables (feed and depth of cut) and surface hardness. Studies revealed that surface roughness is inversely proportional to surface hardness. It is also observed that surface roughness is greatly affected by feed and surface hardness is inversely proportional to contact temperature[9]. A higher compressive residual stress is generated during the turning operation. Here, a small nose radius and PVD-coated insert are used in machining. In FEN analysis, it is revealed that thermal load is the mainstream for the generation of residual stress[10].

The tool wear increases as the cutting forces are increased[11]. In the validation of the Modified Taylor tool life equation, experiments are in the same sequences and conditions. The researchers reveal that workpiece hardness is the most significant factor follows by cutting speed and depth of cut. The coated tool has a higher tool life[11,12]. The researcher cast an MMC with the application of in situ method and analysed the effective performance parameters on their responsive factors and found that as cutting speed increased the height of BUE increased[13]. Dings et al. have discussed the main form of wear at cutting conditions[14].

In the end, the researcher concluded that all the process parameters affect the cutting force. Therefore, it is not easy to develop an exact and absolute TMC cutting force model. Comparison of force involved in tool breakage and damage of cutting edge is impossible. Measuring instruments like sensors etc. have installation, adjustments, and maintenance problems. Thus, this method is inconvenient in use.

2.2 Based on Vibration Analysis Monitoring Method

Here, the monitoring method includes the signal generating & processing unit, signal analyser & condition recognition unit, and an output display device. A vibration signal arises during the cutting operation having sufficient information about the tool conditions. The tool wear state is decided by selecting the refined vibration signal from the acceleration sensor and exploring the relevant index[15]. The monitoring setup consisting of an accelerometer sensor is fixed to the holder surface in such ways that the maximum signals are captured. Here, the reference threshold value is fixed and comparing the display data of the sensor. If the displayed data is a greater one, repeat again and again. Then the conclusion is drawn that the tool is damaged and needs to be changed immediately[16].

The tool wears analysis is studied through the time and frequency characteristic feature of vibration signals[17]. All the optimization work is done through the RSM method and found that feed rate is a significant factor that affects surface roughness, whereas the vibration is having low effect[16]. A 2D tuned mass damper is invented and applied in the milling machine to study out feature characteristics of both the tuned and the untuned milling machine and found that 10.8% less is reduced[18]. The experiment is carried out in varying lubrication oil quantity flow rate, feed, and types of surfaces developed on the workpiece, and found that surface roughness shows more vibrational condition at minimum flow rate and maximum feed[19]. A tool condition monitoring system method was developed and found that its accuracy is nearer to 97%. By application of this method, a low-cost monitoring system is made[20].

2.3 An Acoustic Emission Monitoring Method

Sound is the disturbance generated in terms of transient elastic waves traveling in the entire three mediums (air liquid and solid) and that can be hearable by the human ear. Tool wear and cracks can be easily separated by sound appearance. A lot of research papers and reports available show acoustic emission (AE) signals are used in tool wear monitoring. Monitoring based on acoustic signal emission requires an acoustic sensor or microphone to capture the sound emitted during cutting. The AE is generated in the cutting and chip formation mechanism. The time and frequency domain analysis of acoustic signals describes the stages of wear.

At the received sound natural frequency identification of stages became easy. Natural frequency is directly proportional to cutting levels which is also directly proportional to wear[20]. A very wide range of bandwidth of the AE sensor (10 kHz-1MHz) shows that this sensor is the most sensitive. A fined calibrated sensor is used at the perfect location along with the proper filter. AE sensors are mostly used in sensor fusion tool detection techniques. Characteristic analysis of AE signals is performed for face milling and found that is very sensitive technique. The correlation among characteristic phenomena is easily established. A Cutting tool wear monitoring method is established to find out coated tool

life via pattern recognition method. This classified the tool life into three stages[21]. In multi-point milling, Fiber-Optic Interferometer gave a better result than a conventional piezoelectric sensor[22]. Here, the involvement of scuffing in the sliding surface is examined by the featured analysis of acoustic emission. A wavelet packet is taken for signal filtering. The energy band theorem classified the stage of percentage involvements of scuffing. The accuracy is found about 88%[23]. The tool geometry and chip structure affect the tool condition. The chip form and tool geometry width of cut. The tool wear on the cutting edge influence the frequency and the amplitude of chatter RMS AE signal during cutting[24]. The grinder wheel burning is examined by a statistical study of AE signals. There is more variation shown in constant false alarm rate, power ratio, mean value variance, kurtosis, and skewness than RMS of AE[25].

Lab View is used to filter the noise signals. At the workpiece's natural frequency, tool wear increases as the flank wear increases[20,25,26]. The tool monitoring of 3-axes of CNC milling and drilling with the use of AE signals is possible along with force analysis[27-29]. The author developed a low-cost online tool depreciation technique. Here, Mems accelerometer and microphone are used to record the vibration and sound signal separately. A NI MY RIO DAQ is used to filter the signal data. MAT LAB GUI toolbox is used to control the tool wear condition and IV block[30]. The sound signal is captured through two microphones only used to find out the vessel's liquid level. This recorded signal is examined and validated. Different characteristics feature study shows sound emitted during bubbling at different vessel levels[31]. The wind turbine noise annoyance is cross-examined for audio and audio-visual on human beings and find human being is most irritated in audio-visual conditions[32].

Using the sound mapping technique lob diagram is examined and validated for a milling operation. A huge data collection is needed. Handling and analysis of huge data is the main drawback of this method. Since it takes more time and is expensive. So, this is not a proper method to develop a TCM[33]. Elastic characteristics of AE are studied. The frequency-domain analysis is compared to STFT's spectroscope and based on numerical simulation results are concluded[34]. An AE-sensing method is a burning topic to develop an intelligent tool wear condition monitoring system, signal analysis, and its feature extraction is done precisely. An amalgamation of characteristics with other sensors is a fruitful technique to produce TCM[35]. Based on the above study, several conclusions are drawn related to the advantages of tool wear condition monitoring via acoustic emission monitoring. They are as follows:

- Because of its high-frequency level, it is easy to filter the high-pass of the non-disturbance signals.
- An acoustic emission sensor can be easily attached to a machine affecting the process.

- During signal processing, a higher signal-to-noise ratio is taken because a wear zone is avoided[6].
- The AE sensor reacts very fast with high responsiveness**.**

AE has a favorable feature in comparison with the other two monitoring techniques. Hence this is widely used TCM irrespective of the above two methods.

2.4 Monitoring Method Based on Electric Current Measurement

This is a new prominent technique utilized in the online monitoring system based on motor current signals. Here, the condition of the tool is identified via cutting force signals. The characteristic of this signal is directly controlled by motor output torque. The involvement of motor power is affected by motor output torque and the current supply to the motor[17]. Resistance is used as a measuring device when the tool touches the workpiece. As the intermediate surface on the flank face of the tool increased resistance value increased. The setup is easy in comparison to other methods and has great accuracy[36].

Based on the above investigation we can say that this method gives better accuracy than other processes. Their installation is easy and obtained results are almost free from other existing parameters like EMF etc. It also reduces the cost of the online tool monitoring method.

2.5 Multi-Sensors or Fused Sensors Monitoring Technique

As in all, sensors have their singularity and physical properties that come with the measurement only. Their properties fall in a limited range. These sensors are directly and indirectly affected by environmental noise. Because of this environmental noise, there is an error generated during the analysis period. So, a single sensor is not able to give the appropriate information. Hence, to overcome this error two or more sensors are used to collect the information. In this particular state, most scholars give focus on a new technique called the multi-sensors tool depreciation technique. This is also called as fusion sensor method. Here the scholar has used two or more similar and dissimilar sensors (like dynamometer sensors, accelerometer sensors, and acoustic sensors, etc.) to detect tool depreciation and diagnosis of surface texture.

Two sensors servo amplifiers and accelerometers are used to check the wearing condition of the flank in a CNC turning. This technique improves the accuracy of TCM[37]. A comparative study of FT-Welch's method and the HHT method gives ideas that the HHT method gives better results. Here, a dynamometer and accelerometer are used to develop an online tool monitoring setup. The nonlinearity and non-stationary properties are the main drawbacks of this setup. So, the analysis of online cutting is impossible[38]. The wave pocket transform method is used and validated in the proportional covariate model (PCM) for studying the reliably of the cutting tool. Here, vibration signals generated via accelerometer and 0.5 operational reliability thresholds for the cutting tool are taken[39].

A more reliable tool monitoring system is prepared with the use of acoustic and accelerometer sensors. The system is attached to the lathe. During the turning operation, analysis and validation of the Process parameter are taken out. The FFT Technique is used to time domain signals into the frequency domain[40]. Among five models such as RSM-LIN, REG-LIN, RSM-QUA, ANN-I, ANN-II, and Nested-ANN (nested artificial neural networks), a precise and accurate model is developed with the help of nested-ANN. Using the above model, optimistic process parameters might be selected to get the required surface texture[41]. A monitoring setup is developed using clustering methods. All the experiments are performed on a 3D milling machine. Here, an accelerometer, dynamometer, and acoustic sensor are used to capture vibration, and force, signals. The clustering method is applied to all recorded signals. After a brief analysis and validation, the author concludes that the clustering methods are durable, healthy, and relevant[42].

3. Conclusions

The online condition monitoring tool wear is a burning topic in advanced manufacturing technology through which the researchers have to improve production efficiency, reduced processing costs, and guarantee to give good surface quality. This paper also deals with the analysis and comparisons of the various tools and wear monitoring methods. After referring to several research papers related to condition monitoring, the multi-sensors monitoring method or fused sensors monitoring method is a better tool depression technique that identifies the tool stage. This may reduce successfully contradicted veracity with great soundness. This type of setup is suited to many of the machining operations to improve the profit to a great extent.

References

1. Y Ji, Shijiazhuang Vocational and Technical College. 2005; 17(6):35-37.
2. S Kurada, C Bradley. Comput. Ind. 1997; 34:55-72.
3. QG Feng. Master's Dissertation. Shanghai Jiao Tong University. 2004.
4. AG Rehorn, J Jiang, PE Orban, Int. J Adv. Manf. Technol. 2005; 26: 693-710.
5. R Raphael, S Rajappan. Glob. J Eng. Sci. Res. AIVESC-18: 8-11.
6. H Chen. in D Li, Y Liu, Y Chen (eds). Computer and Computing Technologies in Agriculture IV. 2011; 347: 215-220.
7. A Keshri. PhD Thesis. Università Degli Studi di Napoli Federico II. 2011.
8. YH Li. PhD Thesis. Shanghai Jiao Tong University. 1999.
9. K Jemielniak. Proc. Inst. Mech. Eng., Part B. 2006; 220(2): 163-170.
10. G. Byrne, D. Dornfeld, I. Inasaki, G. Ketteler, W. König, R. Teti. Annals CIRP Ann. 1995; 44(2): 441-567.

11. B de Agustina, C Bernal, AM Camacho, EM Rubio. Procedia Eng. 2013; 63: 694-699.

12. S Chinchanikar, KS Choudhury. Int. J Refract Metals Hard Mater. 2013; 38: 124-133.

13. VB Magdum, VR Naik. IJETT. 2013; 4(5): 1564-1568.

14. SL Ding, R. Izamshah RA, J Mo, QS Liu. KEM. 2010; 458: 355-361.

15. Z Zhuang. PhD Thesis. Shanghai Jiao Tong University. 2009.

16. Z Hessainia, A Belbah, MA Yallese, T Mabrouki, JF Rigal. Meas. 2013; 46: 1671-1681.

17. F Han, F Xie. IOP Conf. Series MSE. 2017; 220: 1-5.

18. Y Yang, W Dai, Q Liu. J Sound Vib. 2015; 335: 78-88.

19. D Carou, EM Rubio, CH Lauro, JP Davim. Meas. 2016; 94: 338-343.

20. P Gierlak, A Burghardt, D Szybicki, M Szuster, M Muszyńska. Mech. Syst. Signal Pr. 2017; 89: 14-26.

21. AA Fikri, AA Permanasari. AIP Conf. Proc. 2016; 1778: 030066.

22. T Moriwaki, M Tobito. J Eng. Ind. 1990; 112(3): 212-218.

23. TA Carolan, DP Hand, JS Barton, JDC Jones, P Wilkinson, RL Reuben. J Manuf. Sci. Eng. 1996; 118(3): 428-433.

24. F. Saeidi, SA Shevchik, K Wasmer. Tribology International. 2016; 94: 112-117.

25. RY Chiou, SY Liang. Int. J Mach. Tool. Manuf. 2000; 40: 927-94.

26. PR Aguiar, PJA Serni, FRL Dotto, EC Bianchi. J Braz. Soc. Mech. Sci. 2006; 28(1): 118-124.

27. P Huo, M Zhang, L Gao, R Li. IJAST. 2014; 4(4): 202.

28. C XiaoQi, Z Hao, D Wildermuth. SIMTech Technical Report. AT/01/014/AMP, 2001.

29. P Gokul, T Karthikeyan, RK Kumar, S Malini. IOSR-JECE. 2013; 5(4): 21-30.

30. I Marinescu, DA Axinte. Int. J Mach. Tool. Manuf. 2008; 48(10): 1148-1160.

31. B Pandey, BK Jha, S Mahto. in B Das, R Patgiri, S Bandyopadhyay VE Balas. Modeling, Simulation and Optimization. 2021; 206: 87-99.

32. S Singh, AR Mohanty, Appl. Acoust. 2018; 129: 248-257.

33. M Szychowska, H Hafke-Dys, A Preis, J Kociński, P Kleka. Appl. Acoust. 2018; 129: 190-203, 2018.

34. G Quintana, J Ciurana, I Ferrer, CA Rodríguez. Int. J Mach. Tool. Manuf. 2009; 49: 203-211.

35. A Papacharalampopoulos, P Stavropoulos, C Doukas, P Foteinopoulos, G Chryssolouris. Proc. CIRP. 2013; 8: 426-431.

36. X Li. Int. J Mach. Tool. Manuf. 2002; 42: 157-165.

37. M Trejo-Hernandez, RA Osornio-Rios, RDJ Romero-Troncoso, C Rodriguez-Donate, A Dominguez-Gonzalez, G Herrera-Ruiz. Sensors. 2010; 10: 3373-3388.

38. A Gouarir, S Kurokawa, T Sajima, M Murata. IJAT. 2016; 10(5): 767-772.

39. T Kalvoda, YR Hwang. Sensor. Actuat. A-Phys. 2010; 161: 39-45.

40. G Cai, X Chen, B Li, B Chen, Z He. Sensors. 2012; 12: 12964-12987.

41. MSH Bhuiyan, IA Choudhury, M Dahari. J Manuf. Syst. 2014; 33: 476-487.

42. AJ Torabi, MJ Er, X Li, BS Lim, GO Peen. IEEE Syst. J. 2016; 10(2): 721-732.

Design and Analysis of an Arduino based Heart Rate Monitoring System using Photoplethysmography (PPG) Sensors with MATLAB Signal Processing and IOT Applications

M. Ganguly[a], R. Das[a], S. Bhattacharya[b]

Abstract

In this paper the design and fabrication of a low-cost "Heart rate monitoring system" using an Arduino Uno microcontroller and the Photoplethysmography (PPG) principle is investigated to determine the heart beats per minute (BPM). This PPG signal is derived from changes in blood flow, specifically from changes in blood volume. An IR sensor is used to detect the variation in blood volume caused by the pulse rate. An active bandpass filter is cascaded using control system analysis to reduce noise from the circuit. The practical model was constructed by connecting the "Heart beat sensor (PPG module)" with an Arduino Uno board responsible for calculating the beats per minute and displaying the result in a 16×2 LCD display after suitable simulation in PROTEUS software. The Arduino IDE (Integrated development environment) provides a tabular and graphical representation of the output signal through serial driving and serial plotting. Raw data processing and analysis can provide a variety of graphical accessories with the help of MATLAB and R, respectively. In addition, this study investigates some amazing IOT-based applications for serial data transmission (wireless communication protocol) using Bluetooth or WiFi-enabled equipment. As a result, any specific person or remote doctor can view the transmission of HR values from a wearable device through an Android application as well as the transmission of HR values and graphical figures remotely with the aid of the worldwide system of communication (GSM). In addition, this study investigates how to analyse data effectively using the R programming language after receiving BPM information from the microcontroller to create a logical and statistical representation of the heart rate monitoring system.

Keywords: Photoplethysmography (PPG); Heart beat sensor; Arduino; PROTEUS; MATLAB; R programming

1. Introduction

Technological advances in biomedical instruments are being rapidly gained for fitness tracking in today's life due to the growing health worries, in which heart rate plays an important role. The wireless mobile health monitoring systems that can continuously[4] monitor patients while using minimal power is another result of modern technology

[4] ✉ M. Ganguly

ray_madhabi@yahoo.co.in

[a] West Bengal Stat University, Barasat, West Bengal 700126, India

[b] Abacus Institute of Engineering and Management, Hooghly, West Bengal 712148, India

advancement. Instead of using the laborious manual ECG method, a person's heart rate can be calculated by using the PPG methodology. Additionally, wireless HR monitoring systems that employ the PPG approach significantly contribute to the diagnosis of health in hospitals, clinics, and homes.

This paper focuses on making improvements to healthcare monitoring technology so that patients can be observed easily at home or at work. The pulse is the most accurate approach to determine the HR number, as the pulse follows the rhythmic expansion and contraction of the heart with the cardiovascular system.

In this study, an optical pulse rate sensor and an Arduino Uno board are utilised to determine the heart rate using the PPG approach. The PPG sensor gives the voltage level of PPG impulses, which sometimes can be affected by background noise, respiration, and physical movement. To distinguish between the noise free PPG output and the noisy signal, many filters have been used. Mathematical modelling of the circuit provides the frequency and time domain analysis of the entire system. Equivalent simulation circuit has been done by proteus software and the complete signal processing, signal generation, noise removal, analysis has been done in MATLAB. The heart rate values are then sent from the PC via the USB cord to the Arduino Uno board. These values, which were obtained on the Arduino UNO board, are transmitted through bluetooth to the mobile device. The bluetooth module HC-05 data transmission hardware is used to do this. The bluetooth connection must be established between the HC-05 bluetooth module and the mobile phone bluetooth. The user receives the heart rate value in their mobile phone once the connection is established. The values that the mobile phone's application receives may then be forwarded to a distant location through the GSM communication network included into the mobile phone. The specific cell phone number to whom the information has to be sent must be put into the application in order to accomplish this. The information is then turned into a text message and remotely transmitted to that particular number. A remote physician may be able to monitor and assess the patient's condition based on the information they have access to.

Due to non-invasiveness and ease of use for heart rate detection, the PPG approach has been widely employed for the measurement of heart rate signals. The ECG is the most frequently used method to measure heart rate[1,2], but in order to obtain accurate electrical signals from the heart, electrodes must be physically placed to the body at various places with the help of a special gel. PPG, especially wearable devices, provides a good option because it only requires to be kept on the finger or wrist to measure the heart rate. There are several works involving the PPG signals for heart rate analysis and detection.

Moraes et al.[3] claim that numerous approaches and developments in PPG signal analysis are explored, and conclusions are also taken from it. The techniques, including frequency domain analysis and time domain analysis employing statistical and geometric indices, were described. It also concluded that the PPG approach is preferred over the ECG and

that its advantages outweigh those of the latter method's body-attached electrodes. A review of the PPG literature over the previous 20 years is also included. By estimating pulse transit time, Janjua et al.[4] proposed a chest-worn blood pressure monitoring device that evaluates arterial stiffness (PTT). In another investigation[5], the NIELVIS-II+ was employed as a DAQ board to link PCG and PPG devices with the PC for the purpose of signal acquisition, which was then passed to MATLAB for additional processing and heart rate extraction. Canale et al.[6] created a MATLAB technique for adaptive noise cancellation that extracts the HR frequency. A wearable PPG wristband, an STM32F407VG micro-controller, and an embedded three axis accelerometer are used for data collecting. Fast Fourier transform was used to estimate the frequency spectrum (FFT). Johnson et al.[7] estimated the BP and HR using two PPG signals. The PPG signal's noise was removed using a low pass filter. The threshold approach was used to determine the number of peaks. The pulse transit time (PTT) was calculated using LabVIEW utilizing the peak location, peak time, and peak time difference. Several researchers claimed that PPG de-noising gave substantial accuracy and the analysis of the clean PPG signal for medical inference produced higher performance efficacy[8,9]. PPG segments were subjected to several forms of analysis, including feature extraction for the dissimilarity measure, outlier detection for the identification of noisy segments, and clinical utility assessment for the detection of CAD. Previously a few attempts have been made to fabricate, a portable data acquisition system that was created for the gathering of PPG signals through USB interface was used for PPG signal capture and preliminary level analysis[10-12].

2. Methodology

Nowadays, optical monitoring is a more practical way to assess heart rate than electrical approach and it is necessary to identify the initial technology employed to measure the pulse. The use of an IR led and photo sensor together is a cost-effective method of monitoring the pulse. The optical technique takes advantage of the fact that tiny subcutaneous blood vessels (capillaries) in any patch of skin (fingertip, ear lobe, etc.) furnished with a good blood supply, alternately expand and contract in time with the heartbeat. In this work, we created a two segment IR controlled PPG based ADC circuit[13] in order to develop and construct a pulse rate sensor with suitable mathematical modelling which has two segments – i) IR sensor segment and ii) an active bandpass filter. The workflow is presented in **Fig. 1**. A. PPG Signal Acquisition.

The sensor (infrared sensor) consists of an IR light emitting diode transmitter and an IR photo detector acting as the receiver (**Fig. 2**). An ordinary infrared LED photodiode pair can sense the rhythmic change as small but detectable variations in skin contrast. This method uses both transmittance and reflectance principles. A particular light sensor is used by infrared sensors to identify a particular light wavelength in the infrared (IR) spectrum. The intensity of the received light is examined in reflectance mode by using an

LED that emits light at the same wavelength as what the sensor is looking for. Then combine an ADC circuit which is developed with an active band pass filter. Then, we have suggested a system integrating two SEN-11574 ready-made pulse rate sensors with an Arduino interface. Additionally, we created an ADC circuit using light sources with different wavelengths, namely 560 nm and 910 nm (green and infrared LEDs), and performance was evaluated over the finger. Green light (560 nm) has a lower depth of tissue penetration than red (660 nm) and NIR light (900 nm). The epidermal-dermal junction and papillary dermis are therefore accessible to green light. Instead of using an IR signal, we can record a PPG signal in order to analyse volumetric variations in the blood flow of the microvasculature by using Green Light(560nm). Such a PPG sensor can detect signals from vessels with modest diameters at a depth of about 1 mm.

There are three stages in the developed system.

1. To determine the volumetric change in blood, the sensor first detects the pulse through the fingertip or wrist.
2. The signal is delivered for amplification, filtering, and digitization in the second phase.
3. In the third and final phase, the Arduino Uno receives the digitized signal via serial port communication, calculates the heart rate, and displays the BPM reading as a result.

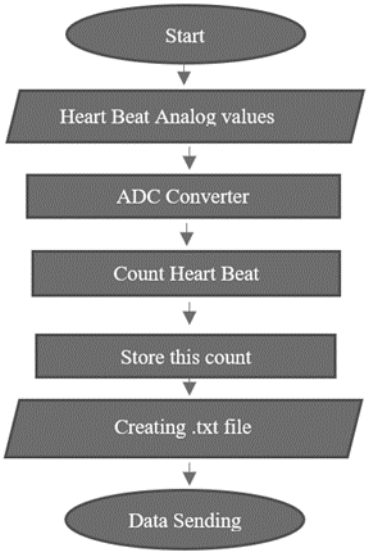

Fig. 1 Algorithm of Arduino based HRM.

2.1 Signal Amplification and filtering

The noise that affects the PPG signals[13] that the sensor receives comes from DC components, which are caused by outside light sources that interfere with the light from the LED shining on the photodiode of the PPG sensor and some body movements that are

present while the measurements are being taken. These light sources and movements are combined with the original signal, and making it impossible to extract the necessary information. As a result, the raw, noisy PPG data that was obtained from the sensor needs to be processed. So, the signal is then thoroughly filtered by a series of signal processing circuits via a quad OP-AMP LM358N. The signal is first passed through a RC high-pass filter (HPF) to get rid of the DC component. The cut-off frequency of the HPF is set to 0.7 Hz. The next stage is an active low-pass filter (LPF) that is made of an Op-Amp circuit. The gain and the cut-off frequency of the LPF are set to 101 and 2.34 Hz, respectively. Thus, the combination of the HPF and LPF helps to remove unwanted DC signal and high frequency noise including 50 Hz mains interference, while amplifying the low amplitude pulse signal (AC component) 101 times (**Fig. 3**).

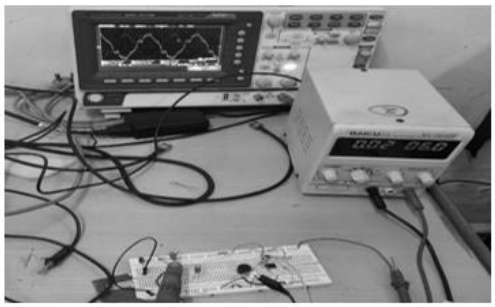

Fig. 2. Demonstration of PPG Model.

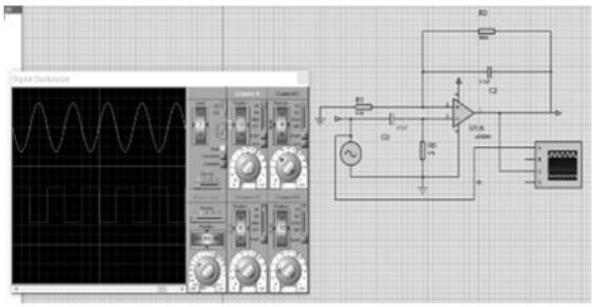

Fig. 3. Filtered PPG signal in Proteus.

2.2 Control System Analysis of Filter using MATLAB

Cycles per second and Hertz are equivalent terms. 75 beats/60 seconds = 1.25 beats per second which can be expressed as 1.25 Hz. Therefore, in order to control frequency range, we must design a filter circuit with a cut-off frequency of almost 1.25. The high-pass filter is a simple first-order RC circuit with a lower frequency bound of $1/2\pi R_0C_0$ = 0.72 Hz. The high pass filter has a cut off at $1/2\pi R_1C_1$ = 2.34 Hz and amplifies $(R_1 + R_2)/R_2$ times. The steepness of the PPG pulse signal dictates that the high-pass and low-pass filter frequencies must be chosen to produce a band-pass filter that amplifies the 2Hz frequency. The transfer function of the system is presented below:

$$T(s) = \frac{V_0(s)}{V_{in}(s)} = \frac{(R_1R_2C_2S + R_1 + R_2)(R_0C_0S)}{(R_1R_2C_2S + R_1)(R_0C_0S + 1)} = \frac{S^2 + 19.23S}{S^2 + 19.23S + 66.57} = \frac{S(S + 1485}{(S + 14.7)(S + 4.5)} \quad (1)$$

Comparing equation with the general transfer function of 2nd order filter circuit $T(s) = (\alpha s^2 + \beta s + \gamma)/(s^2 + \omega_c/Qs + \omega_c^2)$, we get $\omega_c = 1/R_OR_2C_O$ = 8.15 rad/sec. So, the cut off frequency $f_c = \omega_c/2\pi$ = 1.25 Hz and the bandwidth of frequency spectrum = f_c/Q = 3.08 Hz. The circuit connection and the bode plot is shown in **Fig. 4** and **Fig. 5** respectively.

3. Results and Discussion

Using the collected PPG signals from different persons, the resting heart rate in bpm were then obtained. A person's heart beats normally between 60 and 100 times per minute. It is clear that younger people, those under the age of 20, have higher heart rates than people beyond the age of 20, and that the heart rate value decreases with age for those between the ages of 20 and 70. The heart rate value starts to increase again in those over 70. The measured heart rate for several people is displayed in **Table 1**.

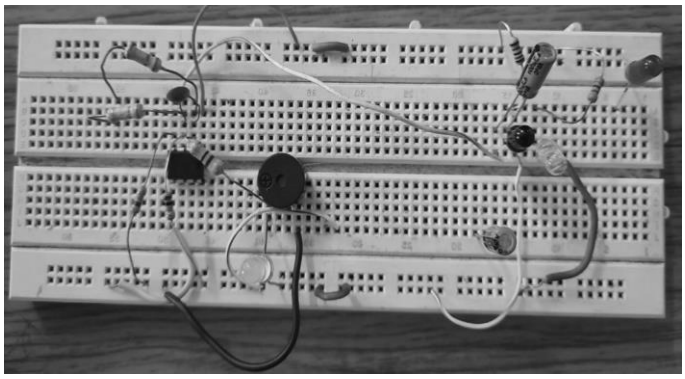

.

R_0 = 47kΩ
R_1=6.8 kΩ
R_2=680 kΩ
C_2 =0.1 µk
C_7=4.7 µK
R*= 10kΩ
R= 220Ω

Fig. 4 Circuit in bread board

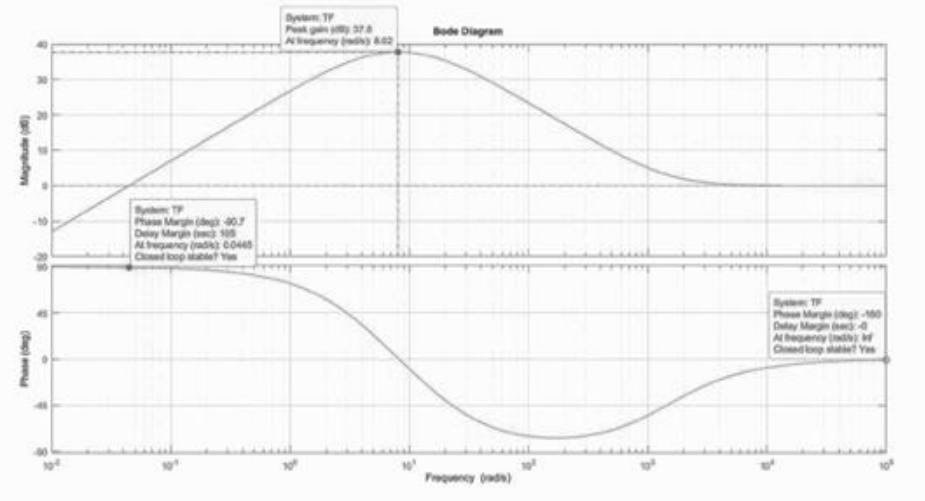

Fig. 5 Bode Plot of the system.

Table 1. Heart rate of Different Persons

Gender	Age	Measured Heart Rate (BMP)
M	21	74
M	45	82
M	30	80
F	22	88
F	28	80
F	45	84

These HRV are then transmitted to the Arduino UNO board through the USB cable connected to the PC (**Fig. 6a, b**). Through the bluetooth, these obtained values are transmitted to the mobile phone (**Fig. 6c**). Bluetooth module HC-05 data transmission hardware helps to do this. The user receives the heart rate value in their mobile phone once the connection is established. Once the connection is setup the value of the heart rate is received by the user in the mobile phone. For receiving information, application bluetooth terminal is used which has been specifically designed for this purpose. The values received by the mobile phone's application may subsequently be sent to a remote site through the GSM communication network. The specific cell phone number to whom the information has to be sent must be put into the application in order to accomplish this. The data is then converted into a text message and sent to that specific number of remote physicians who may be able to monitor and assess the patient's condition based on the information they have access to.

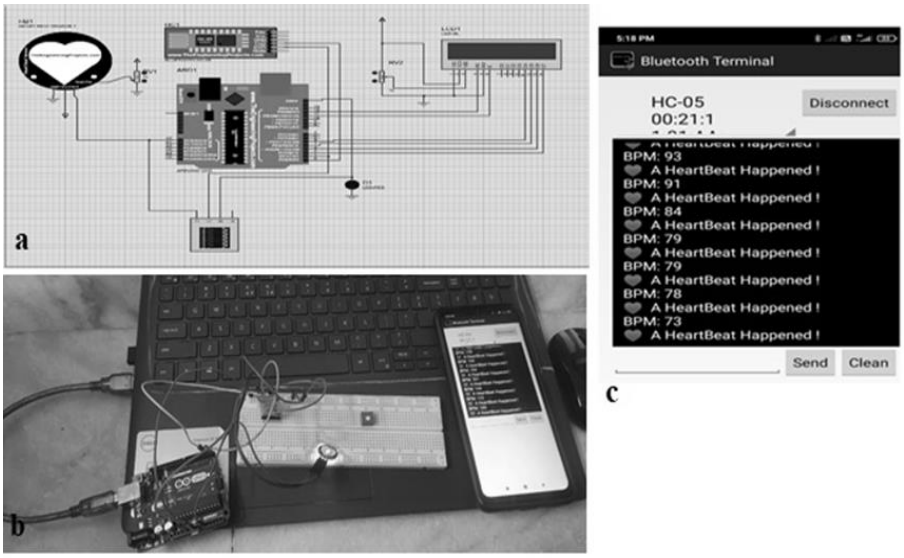

Fig. 6 a. Interfacing of HC-05 with Arduino in Proteus, b. Practical interfacing of HC-05 with Arduino, c. Monitoring of HR in bluetooth terminal.

4. Conclusions

A person's heart rate can be determined by this system consists of the inexpensive Arduino UNO board and pulse rate sensors (SEN-11574 pulse). The sensors are attached with the Arduino and then analogue sensor signal is converted into the digital form by programming the Arduino. Additionally, an IR-controlled heartbeat detecting circuit is constructed and, through an analysis of the control system, a filter is developed that aids in blocking the unnecessary frequency and allowing the necessary bandwidth. The Proteus simulator help to make this system virtually. The captured PPG signal can be used for peak detection to compute the heart rate and average peak intervals, for signal feature extraction, for spectral analysis and PSD estimate, and for PRV calculation. This study also investigates some amazing internet of things (IoT)-based applications that use serial data transfer (a wireless communication protocol) across a supported wireless network like bluetooth, E-SIM, or WiFi. Therefore, a person's or a distant physician's method of communication (GSM) can be presented for the transmission of HR values from a wearable device via an android application as well as the remote transmission of HR values and graphical figures with the help of a global system. This work will be of enormous help to anybody who want to work on PPG. By adding a large number of extra sensors to the system, we can also measure a wide range of additional physical characteristics, including body temperature, blood oxygen saturation, mean arterial pressure, total peripheral resistance, etc. Additionally, we can create a database or an application to store all previous data that will be useful for future therapy and to enable patient monitoring from anywhere in the world.

By using the Arduino UNO, pulse rate sensors, and bluetooth module, all of which are generally accessible for system development, this eliminates the need for the easily accessible data evaluation and transmission boards. Thus, this entire system presents a low-cost alternative to existing systems using embedded chips, which are pricey and made especially for the purpose with built-in sensors. It also provides a dependable way to deliver a message to a remote location utilising a mobile phone that is compatible with GSM and bluetooth to communicate HR information to a mobile app.

References

1. R Banerjee, A Sinha, AD Choudhury, A Visvanathan. IEEE Int. Conf. Acous. Speech Signal Proc. Florence, Italy, May 2014, pp. 4404–4408.
2. Q Zhu, X Tian, CW Wong, M Wu. IEEE EMBS Int. Conf. Biomedical Health Informatics (BHI), Chicago, IL, May 2019.
3. JL Moraes, MX Rocha, GG Vasconcelos, JEF Vasconcelos, VHC de Albuquerque, AR Alexandria. Sensor. 2018; 18(6): 1894.

4. G Janjua, D Guldenring, D Finlay, J McLaughlin. EMBC. 2017; 821-824.

5. AK Bhoi, KS Sherpa, JS Tamang, D Phurailatpam, AK Gupta. ICCSP. 2015; 62-65.

6. P Canale, A Fontanella, E Torti, G Danese, F Leporati. MECO. 2017; 1-4.

7. AM Johnson, R Jegan, XA Mary. ICEEIMT. 2017; 311-315.

8. A Ukil, S Bandyoapdhyay, C Puri, A Pal, K Mandana. IEEE Van. Comput. Cardio. Conf. 2016.

9. S Alam, R Gupta. CIEC. 2016; 178-182.

10. N Daimiwal, M Sundhararajan, R Shriram. Int. Conf. Comm. Signal Proc. 2014; 999-1002.

11. A Gaurav, M Maheedhar, VN Tiwari, R Narayanan. EMBC. 2016; 607-610.

12. G Angius, L Raffo. Comput. Cardi. IEEE. 2012.

13. J Allen. Physiol. Meas. 2007; 28: R1–R39.

Motorized Solar Scarecrow Birds Animal Repellent: A Review

Joydip Ray, Suhail Haider, Saptarshi Samanta, Trinath Barik, Soumyankar Sambhav

Abstract

Birds, which play a major role in pollination, can leave nuisance insects and rodents, causing their normal decline by eliminating crop yields, according to the report, called Agricultural Problems. Ants have rarely proven to be effective in keeping birds away from the fields, because birds may feel that they are not real humans because they do not move. To solve this problem, a manual solar powered carabiner is designed that automatically detects the sound of birds and uses a motor to scream to scare birds and animals. The system uses a controller, DC motors, batteries, solar panels, gears and connecting links along with poles and frame models for sound sensing microphones. Garak is installed in the field with the help of iron poles, which increases its versatility in terms of its installation location. Solar panels continue to charge the system during the day. The built-in microphone continuously monitors the sound level in the environment. As soon as there is an increase in the level of noise in the environment, this signal is monitored by the controller and begins to act. The DC motor rotates and is driven by the entire hand mechanism. It brings out modern solar guards to protect the garden from non-violent birds.

Keywords: Solar power and energy; Energy conservation; Economic losses

1. Introduction

All over the world, poultry is a major threat to agricultural crops, barns, and human life. Bird species damage crops at the planting, seed and maturity stages, causing economic losses for the farming community and causing losses in agriculture, says a report by the Committee for Doubling Farmers' Income (DFI). Birds cause extensive economic damage to crops during lean periods in various agro-natural areas of the country. "The damage caused by birds to any plant depends on several factors, including the proximity of the bird population to the area under the plant, the design of the area, the season and the physiological state of the bird," he said[1]. The most common domestic birds arecrows (Corvuscorone), magpie, sparrows (Passer domestics), starlings (Sturnus vulgaris) and blackbirds (Turdusmerula) in many countries in the world. A scarecrow is a decoy or mannequin, often in the shape of a human. Humanoid scarecrows are usually dressed in[5] old clothes and placed in open fields to discourage birds from disturbing and feeding on recently cast seed and growing crops. But these days' birds and animals are smart enough to notice that it is not an actual human as it doesn't move[2]. An automatic and motorized scarecrow or smart scarecrow is more efficient than a normal scarecrow. The smart crow

[5] ✉ Saptarshi Samanta
saptarshi27samanta@gmail.com

Department of Mechanical Engineering, Institute of Engineering and Management, Kolkata, West Bengal 700091, India

automatically provides constant security for plants from birds and animals. This affects day and night. It works automatically. Smart crows are automatically equipped with sensors, moving arms and scare devices that protect birds and animals in danger. It doesn't kill or eradicate birds from nature for the sake of crop protection, thereby maintaining the balance in the ecosystem[3]. We are implementing a sound box to emit a sound of frequency ranges between 1kHz – 8kHz which can deter the birds from roaming around the farmland. Addition of a manual water sprinkler may be incorporated with it, which gets activated with a sense of touch[4,5]. This will keep off the birds and also be beneficial for the crops which flourish in sprinkler irrigation.

2. Working Principle

The system uses microcircuits for sound sensing, DC motors, batteries, solar panels, gears and joints along with poles and frame models to develop the system (**Fig. 1**). Look, an iron pole is set in the field. It can be installed anywhere outside because it does not require an external power supply. Solar panels continue to charge the system during the day[6]. Built-in microphone continuously monitors the sound level in the environment. As soon as there is an increase in the level of noise in the environment, this signal is monitored by the controller and begins to act. The DC motor rotates and is driven by the entire hand mechanism. The rotation of the motor plug rotates the gear that drives the Linkage arm mechanism[7]. This mechanism allows humans to move in a standing-like

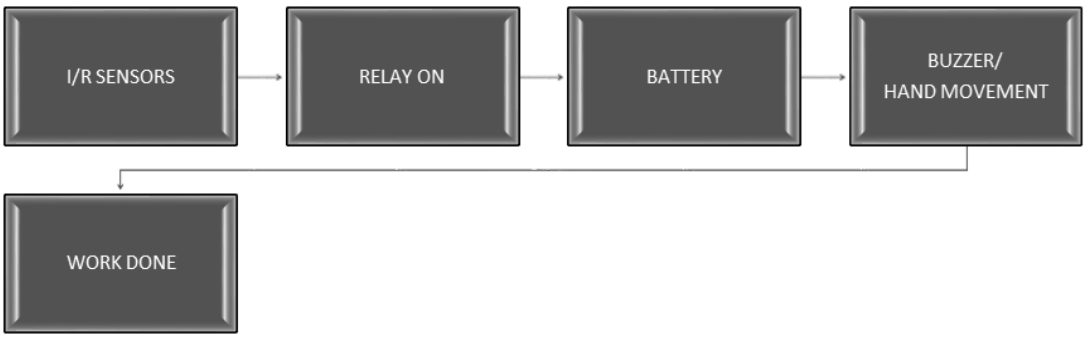

Fig. 1 Working principal of buzzer/ hand movement.

manner imitating human existence. In addition, the controller activates the speaker module to emit sound, so the hat near the field scares off the birds and animals as well. Therefore, the system produces a modern solar-powered crow to protect the farm from birds and animals[8].

Fig. 2a shows front view of proposed model which depicts the arm length, height of scarecrow and its approximate size. Dimensions of head and mounting board can also be visualized from the diagram. **Fig. 2b** shows side view of the same model, which shows details of the linkages and joints present in the proposed model.

a. Front view

b. Side view

Fig. 2 Pictorial view of the proposed model

3. Approach and Components Used

Experimental work was divided into two parts, one is working with mechanisms and the other is working with circuits. In the working mechanism, the spring mechanism is used to move the Karakov arm up and down. The crank rotates and is connected to the drive link by a connecting rod, which is connected by two arms to the drive link, which moves up and down. A T-shaped joint is used to support the mechanism. The system uses a controller, DC motors, batteries, solar panels, gears and connecting links along with poles and frame models for sound sensing microphones. Look, an iron pole is set in the field. It can be installed anywhere outside because it does not require an external power supply[9]. Solar panels continue to charge the system during the day. The built-in microphone continuously monitors the sound level in the environment. As soon as there is an increase in the level of noise in the environment, this signal is monitored by the controller and begins to act. The DC motor rotates and is driven by the entire hand mechanism. The rotation of the motor shaft rotates the gear connected to it, which drives the linked Arm Mechanism. This mechanism allows humans to move in a standing-like manner imitating human existence. The controller also activates the speaker module to make sounds, so birds and animals near the field are scared away[10,11]. Therefore, the system produces a modern solar-powered crow to protect the farm from birds and animals. We have divided our project into two parts, one is working with mechanisms and the other is working with circuits. In the working mechanism, the spring mechanism is used to move the prototype arm up and down. The crank rotates and is connected to the drive link by a connecting rod, which is connected by two arms to the drive link, which moves up and down[12,13]. A T-shaped joint is used to support the mechanism. In the operation of the circuit, the PIR

sensor detects the movement of birds and animals, sends a signal to the microcontroller (Arduino UNO), where the motor driver and battery are connected to the Arduino. The Arduino also sends a signal to the motor driver and the buzzer from the signal transmitter[14-16].

4. Conclusions

In this paper, the concept of a birdrepeller system such as a device and its design is introduced which applies astimulus to the wild birds as a control function. A motorized solar scarecrow is more efficient than normal scarecrow system which does the job of keeping the birds at bay by human like hand motions and emitting noise intolerable for the birds. Depending on the severity of the amount of damage done by the aves and other animals, farmers are free to choose a camera which can be mounted on the body of scarecrow. This gives the live images of the surroundings, captured by the feed and the same can be seen on the smartphones of the farmers. This may enhance the security of the hard-grown cultivated crops. Since, proposed model is driven by solar power, no external supply is needed, thus making it a net zero waste model.

References

1. C Saglam, F Onemli. J Tekirdag Agr. Facul. 2005; 2(1): 50-57.
2. W Abdelhakim. Int. J Heritage Tour. Hospit. 2020; 14(2): 42-51.
3. ML Avery, SJ Werner, JL Cummings, JS Humphrey, MP Milleson, CJ Carlson et al. Crop Protec. 2005; 24(7): 651-657.
4. M Bomford, PH O'Brien. Wild. Soc. Bull. 1990; 18: 411-422.
5. RW Summers. Crop Protec. 1985; 4(4): 520-528.
6. VR Suryawanshi. IJSR. 2015; 4(10): 1709-1711.
7. JW Thomas. J Acoust. Soc. Amer. 2002; 112.
8. A Nollkaemper. European J Inter. Law. 2015; 26(4): 957-964.
9. S Davies. Ear. Year. Edu. 2018; 20(4).
10. PS Dhake, SS Borde. IJATES. 2014; 02(03): 31-36.
11. R Scholten. ReNew: Technol. Sustain. Future. 2001; 75: 80.
12. S Nahatkar, A Gaur, TM Pattewa. IJARECE. 2012; 1(3): 187-191.
13. M Sathishkumar, S Rajini. IJARCET. 2015; 4(1): 70-74.
14. S Sivagamasundari, S Janani. Inter. J Comm. Eng. 2014; 06(6).
15. G Delanty. Irish Rev. 1991; 10.
16. E Hone. Sch. Sci. Math. 2010; 70: 322 - 326.

Manufacturing Techniques

Electrochemical Study of Graphitic Oxide and Reduced Graphene Oxide Emphasizing on their Defect Densities

Kumaresh Halder[a], Dibyendu Mandal[b], Abhishek Mallick[c], Sukhen Das[d], Arijit Roy[c]

Abstract

In this work, the functionalized reduced graphene oxide (rGO) was synthesized from commercial graphite flakes via graphitic oxide (GO) by means of cost-effective chemical treatment. Prepared samples were characterized by XRD, Raman spectroscopy, FTIR, FESEM and LCR meter. Using Raman spectra, samples were shown to be in the nanocrystalline zone with a low defect density of the order of 35×10^{10} /cm^2 only. Dielectric permittivity for rGO was found to attain a very high value (1.9×10^7) at 40 Hz frequency, referred to as colossal dielectric permittivity. The d.c. resistivity of rGO was found to be almost 14 times less than GO, revealing successful restoration of sp^2 network by removing the OH group from the GO structure to construct C-C and C=C bonds in rGO structure.

Keywords: Reduced Graphene Oxide (rGO); Oxidation; Chemical exfoliation; Defect density; Colossal dielectric permittivity

1. Introduction

Electronic devices now a days are becoming more and more complicated, necessitating demanding functionality with higher reliability. The electronic industry is constantly attempting to create materials that have exceptional electrical properties while being inexpensive. Keeping this scenario in mind, researches are going on to develop new graphene-based materials in composite or individual form that can offer increase package density, efficiency, flexibility, portability and durability[1,2].

Chemically modified graphene oxide has drawn sufficient attention among scientists for its innumerable applications like sensors, field effect transistors, energy storage devices etc. due to its excellent thermal, electrical and mechanical nature[3,4]. Graphene, one of the carbon allotropes has carbon atoms arranged in a planar monolayer manner into a two-dimensional honeycomb lattice, which consists of two equivalent sub lattices of carbon [6] atoms bonded together with σ bonds. The charged carriers, i.e., electron follow ballistic

[6] ✉ Kumaresh Halder

h.kumaresh89@gmail.com

[a]Department of BSH, Regent Education and Research Foundation, Barrackpore, India

[b]Department of Bio-Medical Engineering, JIS College of Engineering, Kalyani, India

[c]Department of Electronics, West Bengal State University, Barasat, India

[d]Department of Physics, Jadavpur University, India

motion in the 2D crystal lattice of graphene, which makes it highly conductive in nature despite of being organic[5]. Electrons present in graphene have no rest mass that contributes to some unique features like anomalous quantum hall effect, absence of localizations, high electron mobility at room temperature, and extraordinary thermal conductivity due to zero band gap[6].

There are various approaches to produce graphene, each with its own uniqueness and boundaries. Graphene produced by using mechanical approach as shown by Andre Geim and Novoselov, possesses purest form of graphene with compared to other methods, although the yield of production by their method is very less[7]. Chemical oxidation, on the other hand is an alternative method used to produce mass amount of graphene, which introduces functional groups (i.e., carbonyl, hydroxyl etc.) in between carbon layers of graphite that in turn weakens the Van-der-Walls bond between those carbon layers, which in turn initiates the possibility of low-cost synthesis, and the fabrication of large-scale samples[8].

In this work, we have measured the dielectric permittivity of both graphitic oxide (GO) produced via modified Hummer's method[9] and reduced graphene oxide (rGO) synthesized by treating by-product with strong reducing agent (e.g. hydrazine hydrate). All the electrochemical reactions involved during the preparation have been studied and discussed. An emphasis has given on defect densities found for both GO and rGO.

2. Experimental Procedure

2.1 Materials Used

Graphite fine powder (98%) was purchased from Loba Chemie Pvt. Ltd. (India). Hydrofluoric acid (40%), Sodium Nitrate ($NaNO_3$), Sulfuric acid (H_2SO_4, 98%), Hydrogen peroxide (H_2O_2, 30%), Hydrochloric acid (HCL, 37%) and Ethanol absolute were purchased from MERCK (India). Acetone (C_3H_6O), Potassium Permanganate ($KMnO_4$, 99.9%), Hydrazine hydrate ($N_2H_4.H_2O$, 80%) were purchased from Sisco Research Laboratories (SRL) (India).

2.2 Methods Involved and their Chemical Reactivity

There are four major stages are involved to produce Reduced Graphene Oxide from Graphite powder namely, purification of graphite flakes, graphitic oxide (GO) production from purified graphite flakes, graphene oxide synthesis from graphitic oxide (GO) and finally the reduction of graphene oxide to produce reduced graphene oxide (rGO).

Purification

Purification aims to reduce or remove impurities, which are intercalated between graphite planes, which in turn ensure maximum electrical conductivity of the material[10]. In order to purify, graphite powder was mechanical stirred with Hydrofluoric acid to accomplish a homogeneous mixture. After settling down for a sufficient time, acid was decanted and

distilled water was added to the residual flakes until pH became neutral. Then further decant of excess water has been performed followed by ultrasonication. Later Acetone was added and allowed the suspension to dry in oven at around 80°C temperature.

Preparation of GO

Graphitic oxide, a compound consists of carbon with functional oxide groups consists of stacked structure similar to graphite but with wider spacing as compared to graphite flakes. GO was artificially created by treating purified graphite flakes with strong oxidizer (e.g. sulfuric acid) which helps in removing an electron in chemical reaction known as redox in reaction with the graphite. At first graphite was treated with a mixture of sulfuric acid (H_2SO_4), sodium nitrate ($NaNO_3$) and potassium permanganate ($KMnO_4$). Potassium permanganate in reaction with concentrated sulfuric acid (98%) produces dimanganese-heptoxide (Mn_2O_7), reddish brown oil that has the ability to oxidize unsaturated aliphatic double bonds over aromatic double bonds. The chemical reactions associated with the formation of dimanganese-heptoxide are given in equations 1 and 2 below[11].

$$KMnO_4 + 3H_2SO_4 \rightarrow K^+ + MnO_3^+ + H_3O^+ + 3HSO_4^- \quad (1)$$

$$MnO_3^+ + MnO_4^- \rightarrow Mn_2O_7 \quad (2)$$

Graphene oxide from GO

Structurally the interplanar spacing between the individual atomic layers of graphene oxide caused is effectively larger than that of graphitic oxide. This increased spacing caused by oxidation process disrupts the sp^2 bonding network, which in turn decreases their conductivity drastically[12]. In order to turn graphitic oxide into graphene oxide one common step is to exfoliate via ultrasonication followed by vigorous stirring, which changes its stacked structure into few layered stacks.

From graphene oxide to rGO

For large-scale production in industrial applications such as energy storage industries, reducing graphitic oxide to produce graphene oxide (also referred to as rGO) is a crucial process due to the relative cost effectiveness and higher yield with desired quality levels. The reduction helps in restoring the π network predominantly responsible for good electrical conductivity. A common method of reduction is to treat GO with hydrazine hydrate and maintain the solution at 100°C for 24 hours. Hydrazine hydrate is preferred globally over the other reducing agent due to its non-reactive nature with water. The reduction in effective surface area caused by the heating procedure, which frequently causes damage to platelet structure, results in a significant decrease (almost 30%) in the mass of GO[13].

2.3 Investigating Instruments

The crystalline phases developed in the samples sintered at room temperature was analyzed by X-ray powder Diffractometer (model-D8, Bruker AXS, Wisconsin, USA.) using CuKα radiation- 1.5418 Å and operating at 40 KV with a scan speed of 1 s/step.

FTIR spectroscopy (FTIR-8400S, Shimadzu) was used to evaluate the characteristic stretching and bending modes of vibration of the chemical bonds in our samples with air as background in the wavelength range from 1200 to 400 cm^{-1}.

Raman and PL spectra were collected in a micro-Raman Spectrometer (Lab RAM HR, JobinYvon) equipped with Peltier-cooled CCD detector and 488 nm (Ar^{+} laser) as an excitation light-source. Raman spectra were also used to study the defects associated to GO and its derivative.

To study the morphology of the doped films Field Emission Scanning Electron Microscope (FESEM) (JSM 6700F, JEOL Ltd. Tokyo, Japan) was used.

Dielectric properties like dielectric permittivity (ε_r) and capacitance (C_p) of the samples were measured in the frequency ranges from 40 Hz–17 KHz using LCR meter (GWINSTEK LCR-8101G).

3. Results and Discussion

3.1. X-Ray Diffraction Analysis

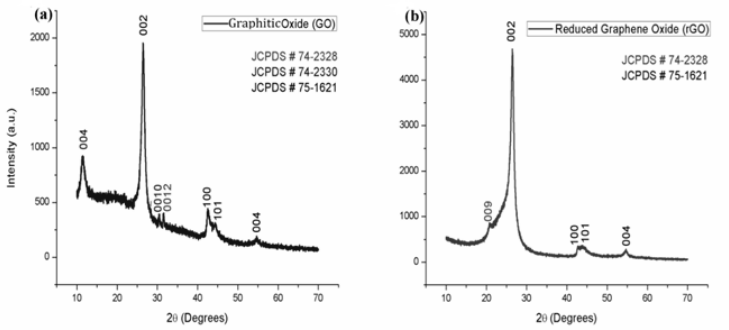

Fig. 1 X-ray diffraction pattern of (a) GO and (b) rGO.

Table 1 Parameters obtained from XRD analysis.

Sample	2θ (degrees)	h k l	d (nm)		Sample	2θ (degrees)	h k l	d (nm)
Graphitic Oxide (GO)	11.6	0 0 4	0.724		Reduced Graphene Oxide (rGO)	23.73	0 0 9	0.371
	26.47	0 0 2	0.339			26.47	0 0 2	0.339
	30.42	0 0	0.289			42.54	1 0	0.213

		10					0	
	31.98	0 0 12	0.278			44.31	1 0 1	0.204
	42.54	1 0 0	0.213			54.75	0 0 4	0.169
	44.31	1 0 1	0.204					
	54.75	0 0 4	0.169					

Fig. 1 represents the XRD pattern of (a) graphitic oxide (GO) and (b) reduced graphene oxide (rGO). From the figure it is visible that both GO and rGO exhibits a very sharp peak (002) at 2θ= 26.47° corresponding to the d spacing of 0.339 nm along with other characteristic peaks of carbon like (100) at 2θ= 42.54°, (101) at 2θ= 44.31° and (004) at 2θ= 54.75°, which are compatible with the literature data JCPDS # 75-1621. In case of GO three more or additional peaks (004) at 2θ= 11.6°, (0010) at 2θ= 30.42° and peak (0012) at 2θ= 31.98° compatible with the literature data JCPDS # 74-2328 were observed. The peak of rGO (009) at 2θ= 23.73° corresponding to the d spacing of 0.371 nm compatible with the literature data JCPDS # 74-2330. All the d spacing corresponding to associated planes with their 2θ values are listed in **Table 1**.

3.2 Raman Spectroscopic Analysis

Fig. 2 represents the Raman spectroscopy of (a) graphitic oxide (GO) and (b) reduced graphene oxide (rGO) respectively. From the figure, we can observe that the D, G, 2D and D+G bands of GO are obtained at 1350.92, 1579.04, 2709.10 and 2941.76 cm^{-1} respectively. While in case of reduced graphene oxide G, 2D and D+G peaks shifted towards 1568.47, 2698.53 and 1584 cm^{-1} respectively.

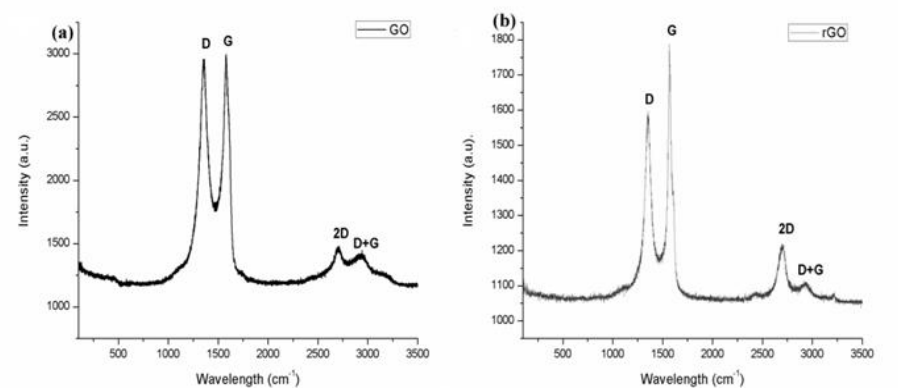

Fig. 2 Raman spectroscopic pattern of (a) GO and (b) rGO.

The ratio of two peak intensities I_D to I_G measures the amount of disorders associated with samples. In general, the defect density can be subdivided into two major categories: low defect density zone, which can be referred to as nanocrystalline graphite phase and

high defect density zone, which can be referred to as sp^2 amorphous carbon phase. These two zones are caused due to the two different areas around defect sites: an area within radius r_s and area within radius r_a, where r_s and r_a are radius corresponding to two circular areas: area of structurally disordered or 's' region and area of activated or 'a' region respectively, measured from the point of impact[16]. Depending on defect density regime, two empirical formulas are used to relate I_D/I_G and L_D.

In low defect density zone, the formula is:

$$\frac{I_D}{I_G} = \frac{C(\lambda)}{L_D^2} \tag{3}$$

whereas, in high defect density zone it becomes:

$$\frac{I_D}{I_G} = D(\lambda) \times L_D^2 \tag{4}$$

where L_D, $C(\lambda)$ and $D(\lambda)$ are the average distance between defects, a constant (depends on Raman excitation wavelength λ) and a parameter obtained by imposing continuity between two regimes respectively.

Normally I_G doesn't depend on disorders as G peak relates to the relative motion of sp^2 carbon atoms, but when $L_D < 3$nm, due to reduction in sp^2 domain and more distortion in hexagons of honeycomb lattice I_D decreases which in turn decreases the value of I_D/I_G, hence becomes proportional to L_D, so it is said to be in high defect density zone. Whereas, at $L_D > 3$nm, the value of I_D/I_G becomes inversely proportional to L_D, i.e. said to be in low defect density zone[17].

In **Table 2**, the peak position corresponding to bands associated are provided. In our case, the ratio of I_D to I_G becomes 0.992 for GO and 0.893 for rGO respectively, by fitting the value of I_D and I_G the value of L_D calculated for GO and rGO becomes 10.05 nm and 9.54 nm respectively, therefore the samples prepared can be well fitted in nanocrystalline zone with low defect densities[18,19]. Larger value of L_d is the signature of better material in terms of defect density. The defect densities ($n_d = 10^{14}/(\pi L_d^2)/cm^2$, L_d in nm) in GO and rGO were found to be less than 35×10^{10} /cm^2.

Table 2 Parameters obtained from Raman spectral analysis.

Parameters Measured (cm^{-1})	Graphitic Oxide (GO)	Reduced Graphene Oxide (rGO)
D band	1350.92	1350.92
G band	1579.04	1568.47
2D band	2709.10	2698.53
D+G band	2941.76	2931.94
I_D/I_G	0.992	0.893

3.3 FTIR Analysis

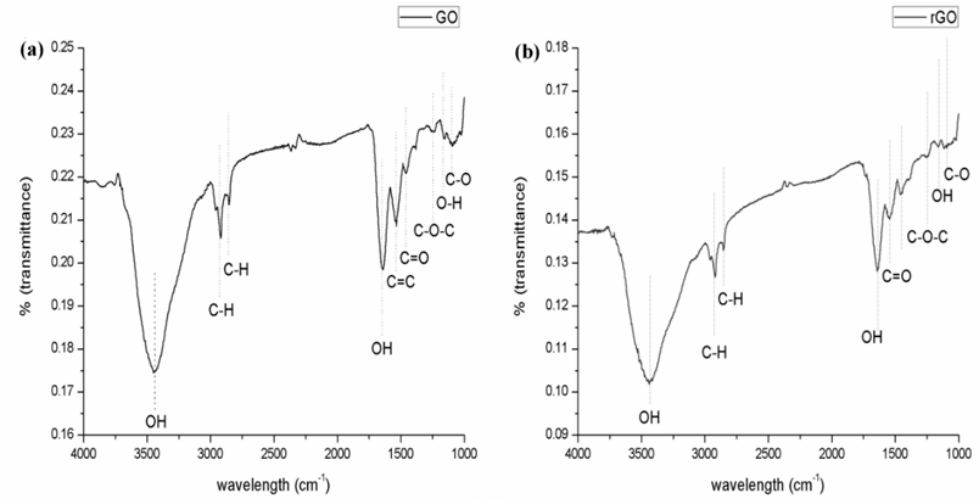

Fig. 3 FTIE spectrum of (a) GO and (b) rGO.

The FTIR spectra in the range of 4000-1000 cm^{-1} in **Fig. 3** was used for detailed investigation of the chemical structure of GO and rGO samples prepared. The spectrum showed strong peaks at 3438 cm^{-1} and 1632cm^{-1} for GO which attributed to OH stretching and bending vibrations respectively[20,21]. In case of rGO samples although the above-mentioned peaks are present, but are reduced in altitude. Hence, functional oxide groups are effectively reduced in rGO. The band observed at 1120 cm^{-1} was also due to OH vibrations[22]. The peaks observed at 2928cm^{-1} and 2859 cm^{-1} were due to C-H stretching vibrations of CH_2 groups. The peak at 1536cm^{-1} reflects the carbon skeletal vibration of graphene[23]. At 1500 cm^{-1} peak due to C=O vibration was observed because of exfoliation, which expanded CO_2 into graphene sheets during heating. Also, at 1080 cm^{-1} GO showed a peak due to C-O stretching confirms the presence of functional oxides[19]. Finally, the band corresponds to C-O-C was found to be at 1243 cm^{-1}.

3.4 FESEM Analysis

Surface morphology of both GO and rGO have studied with the aid of FESEM spectroscopy with two magnification ranges 25KX and 10KX and is shown in **Fig. 4**. From the micrographs shown in **Fig. 4a** and **4b**, we can observe disoriented clustered shapes of GO with open spaces, which are the result of oxidation. Whereas in case of rGO as shown in **Fig. 4c** and **4d**, the morphology obtained were modified to plate like structures similar to graphite. This is again the signature of successful reduction of rGO, which is evident from other characteristic studies too[24]. Minimum particle size found for the samples was 200 nm.

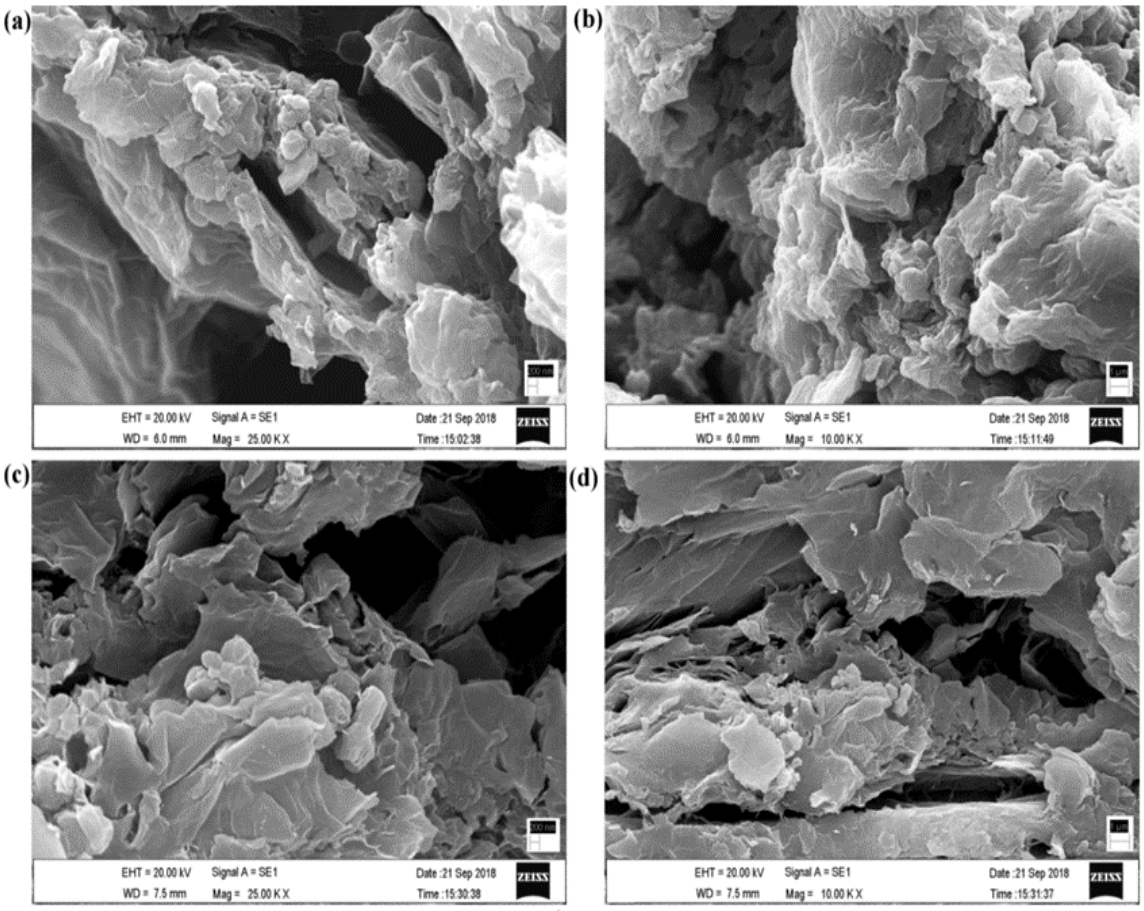

Fig. 4 FESEM morphology of (a) & (b) GO and (c) & (d) rGO.

3.5 Dielectric Analysis

Both GO and rGO samples have had their dielectric properties measured between the frequencies of 40 Hz and 1 MHz in a parallel plate capacitor configuration. Using a pelletizer, sample pellets of nearly uniform thickness were prepared, and two of the pallet's extreme surfaces were coated with silver paste to make them electrically conductive.

Dielectric permittivity (ε_r) of the samples was measured by using the following equation:

$$\varepsilon_r = \frac{C_p \times d}{A\varepsilon_0} \tag{5}$$

where, ε_r, C_p, d, and A respectively are the dielectric permittivity, capacitance, thickness and area of a given sample, and ε_0 is the free space permittivity (8.85×10^{-12} F/m).

Variation of dielectric permittivity (ε_r) in the frequency range 40 Hz to 1MHz has been studied for both GO and rGO samples. The plot in **Fig. 5** shows that the dielectric permittivity in both samples decreases with frequency and it approaches almost a constant value in the high frequency range. This characteristic results from the fact that the dipoles have enough time to rotate for alignment with the electric field at low frequencies, which causes a high value of dielectric permittivity. The dipole movement becomes affected and unable to keep up with the applied varying fields as the frequency rises, which causes a lag in the dipole oscillation behind the field. As a result, as frequency rises, the dielectric permittivity rapidly falls. The dipoles entirely fail to follow the pace of the field at extremely high frequency spectrum, achieving a constant value[25,26].

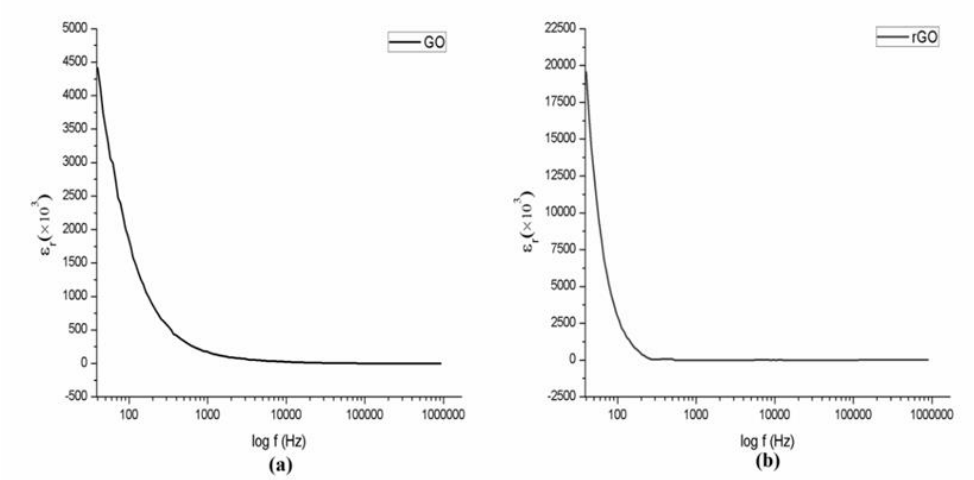

Fig. 5 Frequency response of dielectric permittivity (ε_r) of (a) GO and (b) rGO.

At low frequency (~ 40 Hz) GO attained the ε_r value of 4.4×10^6 which became 1.7×10^5 at a frequency of 1kHz and saturates thereafter, where rGO value for the same was 1.9×10^7at starting frequency (~ 40 Hz) and attained the value of 4×10^4 at 1 kHz. This extraordinary high value of dielectric permittivity is referred to as colossal dielectric permittivity and is attributed to the defects in the samples[27,28]. Since, the dielectric permittivity is found to be extremely high, our material has the potentiality to replace the conventional high k dielectric materials.

3.6 Measurement of Resistivity

Electrical resistivity (ρ_{total}) can be classified into two major categories: a.c. resistivity ($\rho_{a.c.}$ (ω)) and d.c. resistivity ($\rho_{d.c.}$). $\rho_{d.c.}$ is a dominant mechanism at lower frequency

where the frequency of the electric field remains constant over time and $\rho_{a.c.}$ (ω), in contrast, dominates the high frequency zone where the electric field varies[29,30] with time. Electrical resistivity for both GO and rGO have been measured at two frequency zones, which are listed in **Table 3**. The resistivity of GO became high as, after oxidation the interplanar spacing increases which in turn disrupt its sp^2 bonding network. In case of rGO resistivity value became almost 14 times less than GO, which indicates the successful restoration of sp^2 network by removing OH group from the structure to construct C-C and C=C bonds[22].

Table 3 The resistivity of graphitic oxide (GO) and reduced graphene oxide (rGO).

Samples	**d.c. resistivity ($\rho_{d.c.}$)**	**a.c. resistivity ($\rho_{a.c.}$ (ω))**
Graphitic Oxide (GO)	41.25	13.23
Reduced Graphene Oxide (rGO)	3.32	3.32

4. Conclusions

The pristine graphite flakes were primarily stirred with Hydrofluoric acid to achieve purification. Purified flakes were then oxidized with the help of a strong oxidizer following modified Hummer's method to produce graphitic oxide, which thereafter exfoliated in the presence of ultrasonicator and finally reduced in a condenser mantle by continuous stirring with hydrazine hydrate to achieve reduced graphene oxide. With the help of XRD crystal peaks corresponding to their plane with their d-spacing have been demonstrated. FESEM showed a significant change in morphology of GO after reduction. FTIR spectra confirmed the effective reduction of oxygen contained functional group which occurs due to intercalation of water molecules between graphite sheets. The intensities of D, G, 2D and D+G peaks obtained from Raman spectra were used to study defects. Colossal dielectric permittivity measured with LCR meter of rGO was to be almost 4.5 times larger than GO. Resistivity measurement leads to confirmation that rGO prepared by exfoliation and reduction was able to restore its sp^2 conjugated network. From the results we can conclude that the synthesized rGO could be a potential material for industries as a substitute of conventional high k dielectric material. In short, a cost-effective chemical synthesis of rGO was proposed. The various characterization techniques reveal that the properties and yield of the material were found to be very promising and not sacrificed due to the cost reduction in synthesizing the material.

This present work can be elaborated through the routes of medical research where the synthesized product can be amalgamated with biological substances to form the Bio-functionalized graphene biosensors for its utility in Medical science & Engineering. GO having a hydrophilic edge and hydrophobic central base, contribute to the non-covalent binding of biomolecule-graphene nanocomposites between GO and biomolecules

containing hydrophobic groups. The surfaces of GO and rGO being rich in oxygen-containing functional groups (carboxyl and hydroxyl), making them ideal substrates for immobilizing biomolecules (such as proteins, enzymes, antibodies, peptides, etc.) containing multiple functional groups. Also, the biomolecules containing numerous amino groups could form the stable amide bonds with carboxyl groups on GO or rGO surface, thereby making them the choice for the detection of bacterial and viral pathogens.

Acknowledgment

The authors would like to thank to Dr. Achintya Singha (J.C. Bose Institute, Kolkata India) for his assistance on Raman Spectroscopy.

References

1. C Tan, X Huang, H Zhang. Materials Today. 2013; 16:29-36.
2. X Cui, C Zhang, R Hao, Y Hou. Nanoscale. 2011; 3(5):2118-2126.
3. Y Huang, J Liang, Y Chen. Small. 2012; 8(12):1805-1834.
4. S Park, RS Ruoff. Nat. Nanotechnol. 2009; 4:217-224.
5. DAC Brownson, DK Kampouris, CE Banks. J. Power Sources. 2011; 196:4873-4885.
6. AK Geim. Science. 2009; 324:1530-1534.
7. AK Geim, KS Novoselov. Nat. Mater. 2007; 6:183-191.
8. P Zhu, M Shen, S Xiao, D Zhang. Physica B: Condensed Matter. 2011; 406:498-502.
9. WS Hummers Jr, RE Offman. J. Am. Chem. Soc. 1958; 80(6):1339-1339.
10. M Wissler. J. Power Sources. 2006; 156:142-150.
11. KR Koch, PF Krause. J. Chem. Ed. 1982; 59:973-974.
12. R Pasricha, S Gupta, AK Srivastava. Small. 2009; 5:2253-2259.
13. S Srnkovich, DA Dikin, RD Piner, KA Kohlhaas, A Kleinhammes, Y Jia et al. Carbon. 2007; 45:1558-1565.
14. A Shalaby, D Nihtianova, P Markov, et al. Bulg. Chem. Comm. 2015; 47(1):291-295.
15. Huh, S.H. Thermal Reduction of Graphne-Oxide, In: Physics and Applications of Graphene– Experiments, S. Mikhailov (Ed.), In: Tech Europe; 2002, p.73.
16. MM Lucchese, F Stavale, EHM Ferreira, C Vilani, MVO Moutinho, RB Capaz et al. Carbon. 2010; 48:1592-1597.

17. LG Cancado, A Jorio, EHM Ferreira, F Stavale, CA Achete, RB Capaz et al. Nano. Lett. 2011; 11:3190-3196.

18. F Tunistra, JL Koenig. J. Chem. Phys. 1970; 53(3):1126-1130.

19. A Kaniyoor, S Ramaprabhu. AIP Advances. 2012; 2:032163.

20. FT Thema, MJ Moloto, ED Dikio, NN Nwangiwe, L Kotsedi, M Maaza et al. J. Chem. 2012; 2013:1-6.

21. T Szabo, O Berkesi, I Dekany. Carbon. 2005; 43:3186-3189.

22. AV Murugan, T Muraliganth, A Manthiram. Chem. Mater. 2009; 21:5004-5006.

23. G Shao, Y Lu, F Wu, et al. J. Mater. Sc. 2012; 47:4400-4409.

24. L Meng, SJ Park. Bull. Korean Chem. Soc. 2012; 33:209-214.

25. K Halder, BK Paul, D Roy, A Bhattacharya, S Das.J. Mater. Sc.:Mater. Elec. 2015; 26(2):1172-1180.

26. K Halder, D Roy, S Das. Mater. Sc.:Mater. Elec. 2015; 26:5803-5811.

27. C Cheballah, Z Valdez-Nava, L Laudebat, T Lebey, P Bidan, S Diaham et al. J. Energy and Power Engg. 2013; 7(4):726-732.

28. S Sarkar, A Mondal, K Dey, R Ray. RSC Advances. 2015; 5(99):81260-81265.

29. K Halder, BK Paul, A Bhattacharya, S Das. J. Poly. Res. 2016; 23:133-143.

30. K Halder, BK Paul, B Bagchi, A Bhattacharya, S Das. J. Res. Updates Polym. Sc. 2014; 3:157-169.

Deposition of Electroless Co Film – A Review

Anurag Chakraborti, Surajit Patra, Amitava Ghatak

Abstract

Electroless coating is a type of uniform low thickness surface deposition of metals without electricity, on conducting or non-conducting surfaces through the path of chemical reduction, an attractive option among available surface coating techniques. Although, nickel plating via electroless route attracted majority of interests throughout the history of the development of this technology, electroless cobalt structures had their own niche of attention due to unique magnetic properties. Nowadays industrial drive to find alternative to hard chromium electroplating renewed focus on cobalt's promising anti corrosion properties. However, deposition rate and the efficiency of coating bath remain low. As a result, many researchers tried many different strategies in their quest to find optimum electroless Co bath which fulfils the stated purpose. In this article we tried to summarize different types of Co bath, their compositions and parameters influencing the bath as explored by researchers of the past and the present which in turn will serve as a useful guide for future studies in this field.

Keywords: Electroless; Cobalt; Protective coating; Anti-corrosion

1. Introduction

Protective surface coating over an exposed metal surface is used primarily to prevent corrosion and wear. For this purpose, many methods were developed in the course of the history of industrialization. Electroless coating is one of such coating techniques. It is steadily gaining traction since its inception by Brenner and Rindell[1] in 1947 due to homogenous thickness of surface coating even in intricate corners of the substrate, improved tribological properties and lower cost of instrumentation. Electroless coating or autocatalytic coating is a category of chemical process that deposits one or more metal layers by autocatalytic reduction of metal cations in a liquid chemical bath. Despite of rising popularity of electroless coating, electrolytic hard chromium (EHC) plating dominated industry as the most preferred anti-corrosion technology, although hexavalent chromium (Cr^{6+}) baths used for EHC plating is a well-known carcinogen to humans[2,3]. In 2007, US Environmental Protection Agency (US EPA) categorized Cr^{6+} containing baths[7] as unsuitable for environment and stressed on alternative approaches[4]. Thenceforth Ni and Co based electroless coatings are gaining renewed interest because of excellent corrosion resistant and anti-wear behaviour[4,5] in industrial applications.

[7] ✉ Anurag Chakraborti

anurag198924may@gmail.com

[a] Techno Engineering College Banipur, North 24 Parganas, West Bengal 743233 India

[b] Department of Mechanical Engineering, Techno India University Kolkata, West Bengal 700091, India

Quite a lot of Ni based binary (Ni-P, Ni-B, etc.) and ternary (Ni-W-P, Ni-Cu-P, Ni–Co–P, etc.) alloys, and composites (Ni-P-Al_2O_3, Ni-P-ZrO_2, Ni-P-SiC, Ni-P-TiO_2, Ni-P-ZrO_2-Al_2O_3, etc.) have been explored by researchers for high hardness, good corrosion and wear resistance[6]. Co (atomic number-27) and Ni (atomic number-28) have very similar physical and chemical properties. Despite the fact that electroless plating method for Co and Ni were developed almost at the same time, further advancement and application of Ni-based plating turned out to be more widely grown. Electroless Co initially was mostly investigated for its magnetic properties and potential use in magnetic recording medium[7–9]. Researchers developed various Ni based electroless coatings, but issues like poor adhesion and/or blistering, pitting, low deposition rate still persists. Hence nowadays electroless Co-based deposition has been starting to receive attention for its promising potential as corrosion and wear resistant metal.

The aim of the current review paper is to discuss about the influence of coating parameters for Co-based electroless deposition. The paper also includes the development of Co-based binary and ternary alloy coatings by researchers.

2. Electroless Co Bath Composition

The deposition process involves reduction of metal (M) cations in an aqueous solution of metal salt in the presence of a reducing agent (R) at the surface of a catalytic substrate. Deposition then continues due to the catalytic action of the deposited metal ions. Hence, the process is also named as autocatalytic. General chemical reaction for the electroless metal deposition process can be expressed as:

$$M^{z+} + ze^- \rightarrow M \quad (1)$$

$$R \rightarrow R^{z+} + ze^- \quad (2)$$

Physical and chemical properties of the resulting layer depend on microstructure and composition respectively. Catalysts play a very important role to initiate the process. Iron, nickel, cobalt, gold, palladium and aluminium substrates can act as catalyst,[1] while non catalytic substrates such as copper, magnesium, polymers, carbon, glass, etc. are activated using Pd^{2+} ions[1,10,11]. In an effort to find an activation process without using Pd^{2+}, Zhang et al. reported successful use of aluminium foil in conjunction with non-catalytic copper substrate[12].

The aqueous bath solution consists of (a) a cobalt salt as the source of cobalt ions, (b) a reducing agent to convert cobalt cations to cobalt atoms, (c) complexing agent, (d) pH regulator and (e) stabilizer.

2.1 Cobalt source

Cobalt chloride ($CoCl_2$) and cobalt sulphate ($CoSO_4$) are most preferred sources of cobalt ions for depositing Co-based electroless coatings. Brenner and Rindell reported that more than 0.17 M Co in the bath results in darkening of coating with significantly lower

deposition rate[1]. Consequently, usual practice is to keep the concentration of Co salt within 0.1 M.

2.2 Reducing agent

An effective reducing agent must contain two or more reactive hydrogen atoms as it is observed that Co^{2+} ions are reduced to cobalt atoms by autocatalytic dehydrogenation of the reducing agent[13]. In this regard, the role of sodium hypophosphite ($NaPO_2H_2 \cdot H_2O$) is widely investigated. Brenner and Rindell reported negligible Co deposition at hypophosphite concentration of 0.1 M or less. Increasing concentration of hypophosphite increases deposition rate[1]. Later, Tarozaite et al. observed that increase of hypophosphite concentration up to 0.5 M increases the deposition rate of Co on substrate. With further increase in concentration, deposition rate increases very slightly[14]. The deposited film contains small amount of elemental phosphorus (P) along with Co. P content in deposit increases from 2% to 6% with increase in hypophosphite concentration from 0.3 M to 1 M without changing pH of the solution.[14,15] **Fig. 1** shows the variation of P in as deposited film with hypophosphite concentration in the bath. The reduction process can be expressed by the following reactions

$$Co^{2+} + 5H_2PO_2^- \rightarrow Co + 3H_2PO_3^- + H_2 + 2P + H_2O \quad (3)$$

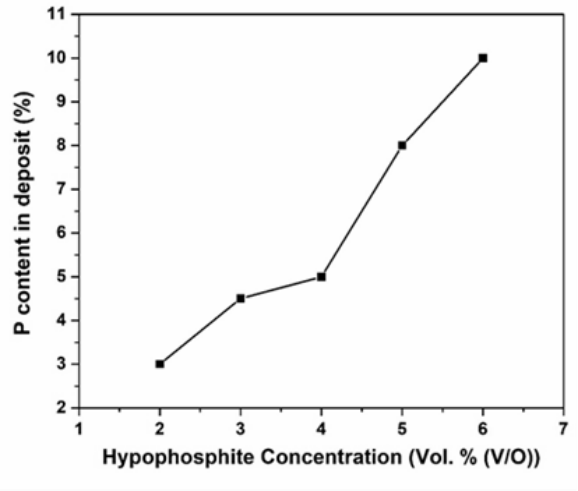

Fig. 1 Variation of P content with hypophosphite concentration[16].

During nucleation and subsequent growth of Co film on the substrate surface, P acts as growth inhibitor,[15,17] which can explain flattening of deposition rate at too much concentration of hypophosphite. Decreasing amount of P favours larger average crystallite size.[17] Dark field transmission electron micrograph[18] and EDS spectra analysis[19] suggest P tends to segregate at the grain boundaries and resists grain growth.

Brenner and Rindell observed that use of hypophosphite for Co deposition from acid bath seemingly not possible,[1] later it was found that in spite of the presence of other reducing agents, addition of hypophosphite resulted in rapidly decreasing deposition from acid

bath.[20,21] Pearlstein et al. in 1974 investigated the role of dimethylamine borane (DMAB) as reducing agent in acidic bath and found linear increase of deposition rate with DMAB concentration up to 0.07 M. The bath provides bright Co deposit containing elemental boron (B). Presence of more DMAB results in rapid bath decomposition.[20] Use of amines like diethylenetriamene as complexing agents can enable the bath to accommodate higher DMAB concentration.[22,23] Successful deposition of Co from alkaline bath is also reported using DMAB as reducing agent.[21] Morpholine borane acts in similar manner as a B containing reducing agent.[24] The reaction mechanism in almost neutral or weakly acidic bath can be presented as:

$$R_2NHBH_3 + 4H_2O + 1.5Co^{2+} \rightarrow 1.5Co + R_2NH^+ + B(OH)_4^- + 2H_2 + 3H^+ \quad (4)$$

where R is an alkyl group.

Instead of P or B containing agents, reduction using Hydrazine (N_2H_4) produces deposition of pure cobalt (>99.85%) with smooth and shiny appearance.[25,26] The reduction mechanism can be expressed as[25]:

Reaction in anode:

$$N_2H_4 + 4OH^- \rightarrow N_2 + 4H_2O + 4e^- \quad (5)$$

Reaction in cathode:

$$Co^{2+} + 2e^- \rightarrow Co \quad (6)$$

$$2H_2O + 2e^- \rightarrow H_2 + 2OH^- \quad (7)$$

Fig. 2 shows typical behaviour of deposition rate with reducing agent concentration. As addition of more reducing agent results in increased supply of electrons for metal ion reduction, the deposition rate increases.

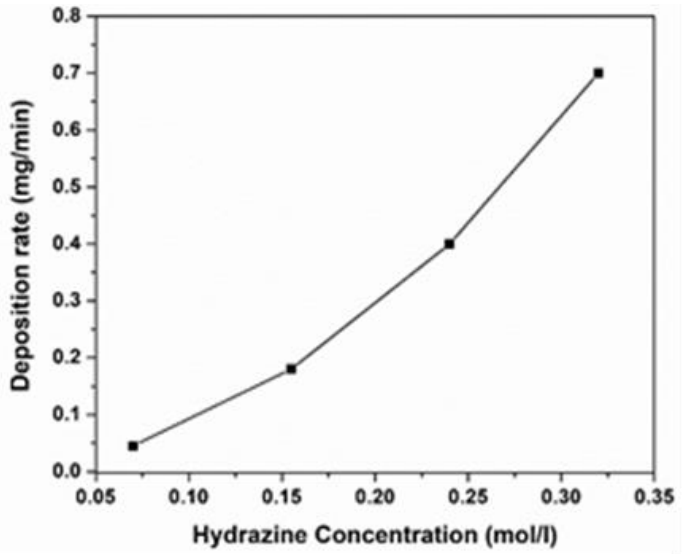

Fig. 2 Reducing agent (Hydrazine) vs. deposition rate[25].

2.3 Complexing Agent

A complexing agent used in electroless cobalt deposition is usually a salt of an organic acid (citrate, succinate etc.) or ammonia. It forms cobalt complex by replacing the water molecules which are coordinating with Co ion by ligands (**Fig. 3**). All ligands contain lone pair of electrons in outermost energy level, by donating this lone pair they can form co-ordinate bonds with metal ions. Thus it prevents Co ions to precipitate in the solution as phosphite salt and so resists rapid decrease of pH in the bath.[13]

Brenner and Rindell compared citrate and tartarate salts and concluded that the former produces superior and less porous film than the latter.[1] Pearlstein et al in 1974 showed successful use of succinate but more than 0.037 M was needed to ensure bath stability.[20] Sodium malonate or acetate [27] can also be used. Glycine in between 0.6 M - 0.8 M can be used to achieve directional growth, more than that retards the process.[24] Several amines (ethylene diamine, diethylene triamine, triethylenetetra amine etc.) are also reported to be useful as complexing agents.[23,28]

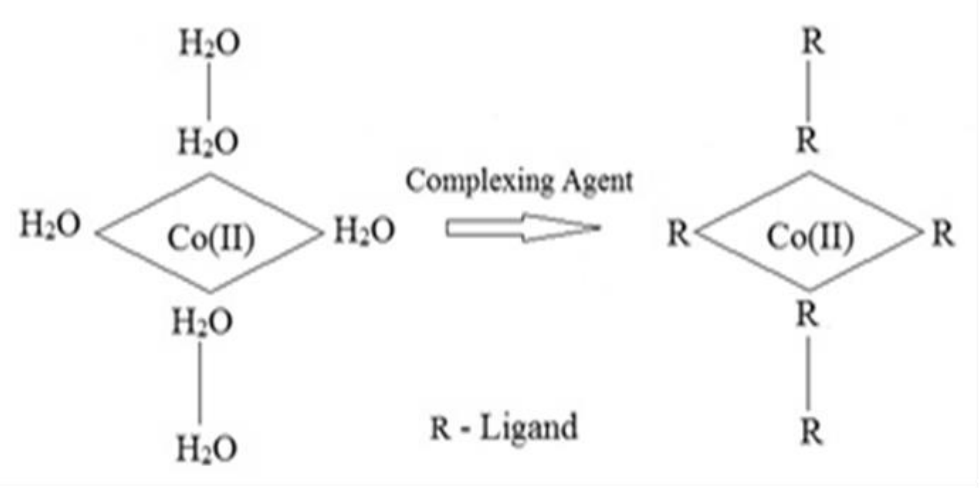

Fig. 3 Formation of Co (II) complex.

Addition of ammonium salts in electroless Ni baths doesn't bring forth any kind of significant change in the process or deposition rate however in Co bath it behaves differently. It was well observed from the beginning that presence of ammonia in the bath noticeably increases the quality of the deposit.

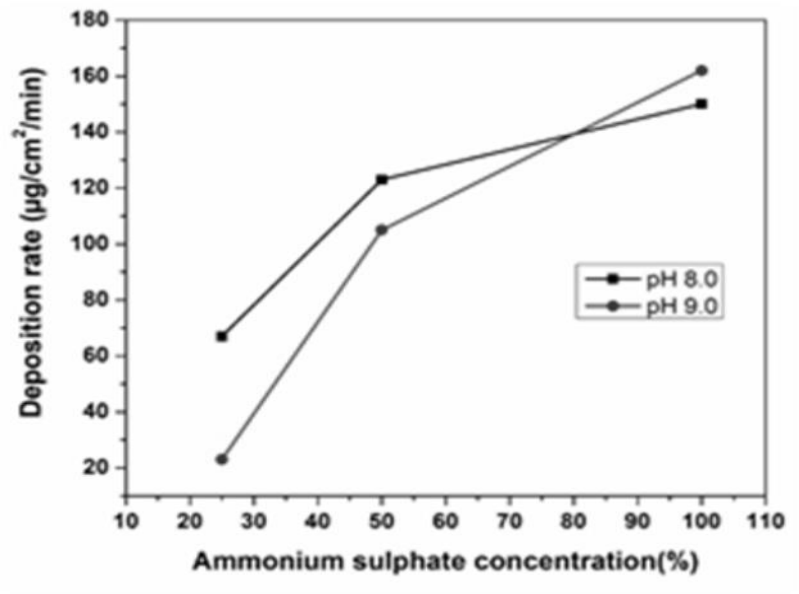

Fig. 4 Deposition rate vs. ammonium sulphate concentration[29].

Use of ammonium salt [e.g.,$(NH_4)_2SO_4$] in conjunction with organic stabilizers(citrate, succinate etc.) also increases Co deposition rate (**Fig. 4**).[1,29] Moreover, Djokic reported that at pH 12 or more presence of NH_4+ and $C_6H_5O_7^-$ both are important to resist bath degradation by rapid $Co(OH)_2$ precipitation.[25]

2.4 pH Regulator

Sodium, potassium or Ammonium hydroxides are used as pH regulators for alkaline baths[1,7,10,11] and H_2SO_4[20] or acetic acid[23] for acid baths. pH regulator is added continuously to maintain certain predetermined pH level throughout the process.

2.5 Stabilizer

A Co plating bath can be used over long period of time; however, it can spontaneously decompose at any time which is indicated by increased volume of hydrogen gas evolution. To prevent it from happening trace amount of stabilizer such as thiourea can be used, Addition of 0.3 mg/l increases deposition, more than that ensues rapid fall of deposition rate.[30] Addition of maleic or succinic acid also prevent bath decomposition.[31]

3. Electroless Co Bath Parameters

3.1 Temperature

Electroless deposition is possible at room temperature and with increasing temperature the deposition rate of metal ions increases almost linearly.[32,33] **Fig. 5** shows the plot of film thickness versus plating time in different bath temperature. While highest deposition rate is observed at 90 °C, maintaining pH at this bath temperature is very difficult.[32] Hence, 70-80 °C is found to be the ideal range of bath temperature for electroless

coating.[32,33] It is also observed that at higher temperature, P content seems to increase in deposited layer.[32]

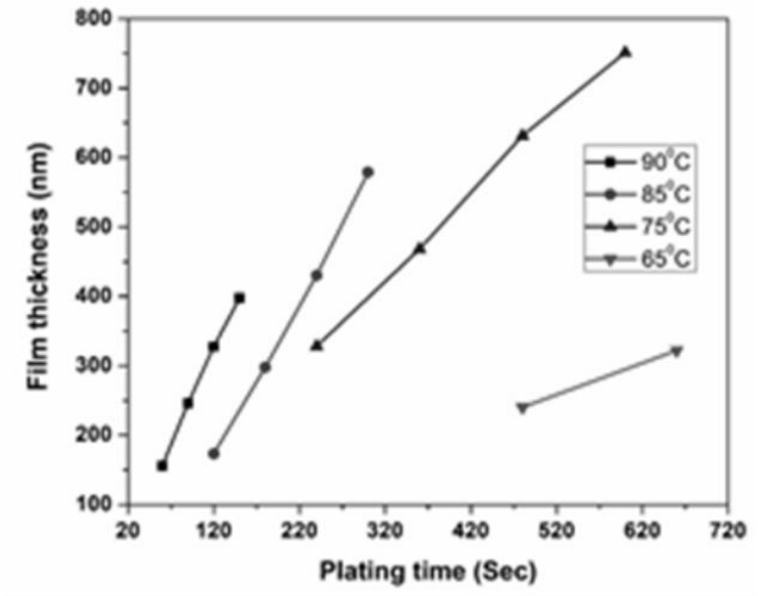

Fig. 5 Variation of film thickness with plating time.[34]

3.2 pH

In alkaline baths higher pH causes higher deposition rate[24] but lower average crystallite size in the film.[35] While for optimum deposition rate most of the studies recommend pH in between 8 and 9[11,32], values as high as 10 -12[25] are also used to get higher deposition rate. Increasing pH in case of an acid bath from 3.5 to 5 also significantly improves deposition rate although at pH 5.5 the bath quickly degrades.[20] P content in the deposit varies very slightly with pH in linear fashion but B content initially falls and then flattens as shown in **Fig. 6**.

3.3 Aging

Ammonia free alkaline cobalt baths do not show any decrease in deposition rate with aging.[37] However alkaline cobalt bath with ammonia has short span of deposition life due to dissolution of atmospheric oxygen. The bath ceases to provide significant deposition after 240 min of aging time. Continuous charging of nitrogen gas can prevent this kind of deterioration.[37] Homma and Noguchi showed hydrazine sulphate addition could extend bath life up to 10 days.[38] Thermally treating the bath by increasing its temperature to 20 °C higher than operating temperature, keeping there for 45 minutes and then cooling it back to operating temperature can also rejuvenate the solution.[39]

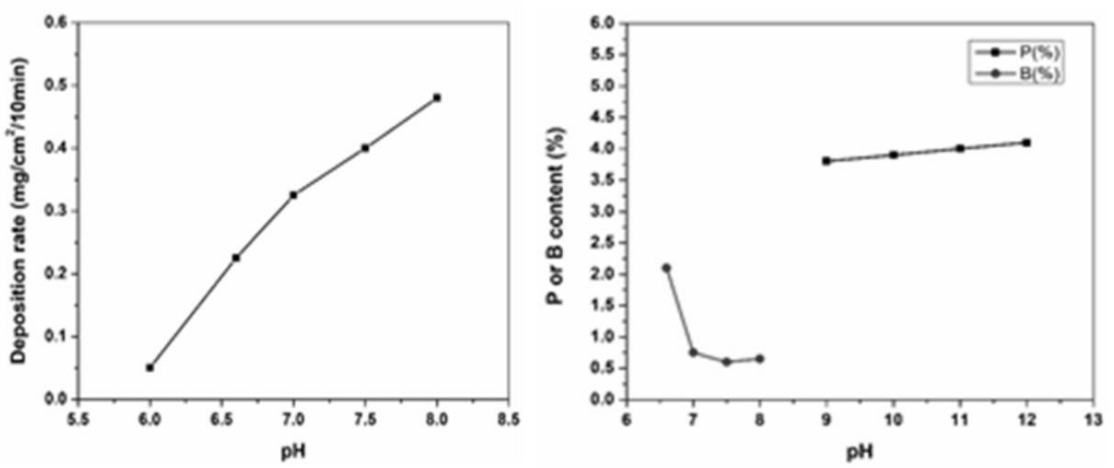

4. Alloying with Other Metals

Apart from hydrazine baths, all electroless Co deposits are binary alloys with either P or B depending on the reducing agent present in the bath. It is possible to produce cobalt alloys by adding other metal salts in the cobalt bath. Although addition of zinc (Zn^{++}) or stannate (SnO_3^{2-}) ions fail to produce zinc or tin alloy of cobalt, adding nickel, tungstate, rhenium or ferrous ions readily produces Ni, W, Re or Fe alloys of Cobalt.[40] But other alloys like Co-Re-P, Co-Fe-P are not as extensively studied as Co-Ni or Co-W based alloys. **Table 1** summarizes compositions of different kind of Co baths and **Table 2** summarizes various Co-alloy baths.

4.1 Alloying with Nickel (Ni)

Addition of Ni^{2+} salt in a typical cobalt bath produces Co-Ni-P[41–43] or Co-Ni-B[44–46] alloy depending on the reducing agent. While at pH range 8.0 - 9.0 rising pH seems to favour Ni content in the alloy,[41] pH 10 or more favour Co deposit.[42] Moreover using lactate [43] or tartarate [41] solutions as complexing agents along with sodium citrate results in higher deposition rate. Although bath pH has small effect in the composition of Co-Ni alloy, the most important driving factor is the metallic salt ratio [Co^{2+}/(Co^{2+}+Ni^{2+})].[40,41] It is noted that addition of even small amount of Ni salt doubles the deposition rate and in general favours Ni content in the deposit. For example, 1 wt% Ni^{2+} produces Co-6%Ni -P film as shown in **Fig. 7a**[36,4847].

4.2 Alloying with Tungsten (W)

Presence of sodium tungstate (Na_2WO_4) in Co bath produces Co-W alloy. While Use of hypophosphites as reducing agent produces Co-W-P alloys[4748], use of DMAB, borohydrides or borazens yields Co-W-B alloys[49] and using a mixture of hypophosphite and DMAB can result in Co-W-P-B alloy.[21] As can be seen in **Fig. 7b** unlike Ni, Tungsten concentration in the deposit shows weak dependence on the concentration of tungstate ions in the solution. [36,49]

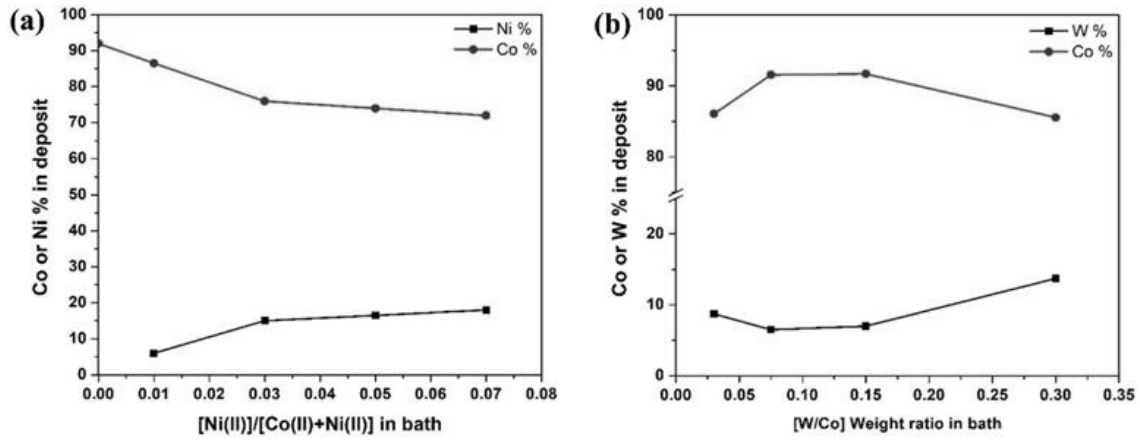

Fig. 7 Variation of (a) Ni[47], (b) W[36] in film with alloy metal salt concentration.

Table 1 Different kinds of electroless Co bath.								
Sl no.	**Co salt**	**Reducing agent**	**Complexing agent**	**pH**	**Temper-ature (°C)**	**Deposition rate**	**Deposit Composition**	**Ref.**
1.	CoCl2, 6H2O (7.5 g/l)	Sodium hypophosphite (3.52 g/l)	Tri-sodium citrate (17.9 g/l) + Ammonium chloride (12.5 g/l)	8.2	80	1.0 µm/hr	Co-P (4%)	11
2.	CoCl2, 6H2O (20 g/l)	Hydrazine (9.6 g/l)	Tri-sodium citrate (77.4 g/l) + Ammonium chloride (5.35 g/l)	12.1 - 12.6	60-70	6.1 µm/hr	Co (99.85%)	25
3.	CoCl2, 6H2O (25 g/l)	Dimethylamine borane (DMAB) (4 g/l)	Sodium succinate (25 g/l)	5	70	1.3 µm/hr	Co-B (1.7%)	20
4.	CoSO4, 7H2O (14g/l)	Morpholine borane (5.048 g/l)	Glycine (7.5 g/l)	7	30	0.46 µm/hr	Co-B (0.8-1%)	24

5.	CoSO4, 7H2O (30g/l)	Sodium hypophosphite (12 g/l)	Tri-sodium citrate (25 g/l) + Ammonium sulfate (50 g/l)	8.5	80	4.2 µm/hr	Co-P (~11%)	32

Table 2 Different kinds of electroless Co-alloy bath.

Sl no.	Co salt	Alloy metal source	Reducing agent	Complexing agent	pH	Tempe-rature (°C)	Deposit composition	Ref.
1.	Cobalt sulphate (0.05M)	Nickel sulphate (0.028M)	Sodium hypophosphite (0.23M)	Tri-sodium citrate (0.19M)	9	60	Co-Ni (29-30%)-P (9%)	50
2.	Cobalt chloride(0.1M)	Nickel chloride (0.1M)	Sodium borohydride (0.08M)	Glycene (0.6M)	10	25	Co-Ni-B (composition wt.% not reported)	45
3.	Cobalt sulphate(0.08M)	Na2WO4 · 2H2O (0.03M)	Sodium hypophosphite (0.169M)	Tri-sodium Citrate (0.492M)	9	85-95	Co-W (1.5–2.5 %) - P (8–10 %)	47
4.	Cobalt sulphate(0.1M)	Na2WO4 · 2H2O (0.6M)	DMAB (0.069M)	Tri-sodium Citrate (0.3M)	9.5 - 9.7	80-85	Co-W-B	21
5.	Cobalt sulphate(0.09M)	FeSO4 (0.07)	Sodium hypophosphite (0.3M)	Tri-sodium citrate (0.1M), Ammonium sulfate (0.05M)	10	90	Co-Fe (~30%) - P (1-2%)	51

5. Potential applications of Electroless Co film

Magnetic properties of electroless Co films, particularly coercivity, are extensively studied from the beginning. Coercivity is the ability of a ferromagnetic material to resist

external magnetic field without being magnetized. Tunable coercivity of electroless Co-P combined with ultra-thin nature of the deposited film make it a candidate of interest for high density magnetic recording medium.[8,9,10]

Co resists corrosion by forming passive oxide layer on its surface. Initially it was thought that formation of $Co(OH)_2$ is the main reason of passivation, but cyclic voltametric studies conclusively proved that it was actually CoO which causes surface passivity.[52] The formation reaction in moist environment is as follows:

$$Co + OH^- \rightarrow CoOH^+ + 2e^- \quad (8)$$

$$CoOH^+ \rightarrow CoO + H^+ \quad (9)$$

In initial study electroless Co layer showed reliable corrosion resistance even after 96 hr of salt-spray exposure and resisted edge corrosion more effectively than Ni coating.[20] It is also noticed that presence of Co (up to 8.2%) in electroless Ni-P film enhances corrosion resistance.[53] Co-P coating applied to magnesium alloy substrate reportedly showed better corrosion resistance behaviour than Ni-P.[54] Klingenberg et al. reported the micro-hardness (VHN) of Co-B to be 716 kg/mm^2 and of Co-P to be 883 kg/mm^2 after heat treatment at 350 $^{\circ}C$.[55] But there seems to be a lack of literature related to hardness and wear resistant properties of Co-P or Co-B alloy compared to magnetic properties.

In addition, electroless Co layer can provide effective barrier against the diffusion of conductor atoms (namely copper) into surrounding dielectric in microelectronics-based applications.[36]

6. Conclusions

The present review clearly demonstrates the ability of electroless process to deposit Co based coating ranging from pure Co to binary alloys like Co-P, Co-B or to ternary alloys like Co-Ni-P, Co-W-P, Co-W-B, Co-Fe-P etc on wide variety of base material surfaces, as well as by modifying composition and basic operating conditions of coating bath. Potential applications of such coatings encompass improved corrosion and wear prevention, magnetic information storage capability, barrier layer against Cu diffusion and many more waiting to be explored. This article hopes to provide a fundamental understanding of the electroless Co plating process by serving as a rich source of information on all kinds of different chemical baths employed by previous researchers.

References

1. A Brenner, G Riddell. J. Res. Natl. Bur. Stand. 1947; 39: 385.
2. K Yatera, Y Morimoto, S Ueno, S Noguchi, T Kawaguchi, F Tanaka et al. J. UOEH. 2018; 40(2): 157–172.
3. IARC Monogr. Eval. Carcinog. Risks Humans, No. 100C. 2012.

4. EW Brooman, TA Naguy, A Force, W Air. Conf. Environ. Process Excell. 2004. AESF. 107–120.

5. EW Brooman. Nat. Assoc. Surf. Finish. Annu. Tech. Conf. 2005. SUR/FIN 2005; 6063: 164–184.

6. Y Yang, W Chen, C Zhou, H Xu, W Gao. Appl. Nanosci. 2011; 1: 19–26.

7. MG Miksic, A Arcus, RH Wright. J. Electrochem. Soc. 1966; 113(4): 360–362.

8. T Chen, DA Rogowski, RM White. J. Appl. Phys. 1978; 49: 1816–1818.

9. EL Nicholson, MR Khan. J. Electrochem. Soc. 1986; 133: 2342.

10. RD Fisher, WH Chilton. J. Electrochem. Soc. 1962; 109: 485.

11. RD Fisher, DE Koopman. J. Electrochem. Soc. 1964; 111: 263.

12. X Zhang, F Wang, Y Zhou, A Liang, J Zhang. Surf. Coat. Technol. 2018; 352: 42–48.

13. GO Mallory, JB Hajdu. Electroless plating: fundamentals and applications, William Andrew; NY. 1990.

14. R Tarozaite, M Kurtinaitiene, A Džiuve, Z Jusys. Surf. Coatings Technol. 1999; 115: 57–65.

15. AS Frieze, R Sard, R Weil. J Electrochem. Soc. 1968; 115: 586.

16. M Schlesinger, X Meng. Proc. - Electrochem. Soc. 1990; 90: 541–549.

17. SL Chow, NE Hedgecock, M Schlesinger, J Rezek. J Electrochem. Soc. 1972; 119: 1614.

18. GA Jones, BK Middleton. J Mater. Sci. 1968; 3: 519–523.

19. K Hono, DE Laughlin. J Magn. Magn. Mater. 1989; 80: L137-L141.

20. F Pearlstein, RF Weightman. J Electrochem. Soc. 1974; 121: 1023.

21. Y Shacham-Diamand, Y Sverdlov, V Bogush, R Ofek-Almog. J Solid State Electrochem. 2007; 11: 929–938.

22. XC Wu, AM Bittner, K Kern. Langmuir. 2002; 18: 4984–4988.

23. I Stankevičienė, A Jagminienė, L Tamašauskaitė-Tamašiūnaitė, Z Sukackienė, M Gedvilas, E Norkus. Mater. Sci. Eng. B Solid-State Mater. Adv. Technol. 2019; 241: 9–12.

24. R Tarozaite, A Sudavičius, Z Sukackiene, E Norkus. Trans. Inst. Met. Finish. 2014; 92: 146–152.

25. SS Djokić. J Electrochem. Soc. 1997; 144: 2358–2363.

26. SL Cheng, TL Hsu, T Lee, SW Lee, JC Hu, LT Chen. Appl. Surf. Sci. 2013; 264: 732–736.

27. T Homma, K Saito, T Osaka. Jpn. J Appl. Phys. 1990; 29: 1701–1704.

28. I Zyulkov, S Armini, K Opsomer, C Detavernier, S de Gendt. J Mater. Chem. C. 2019; 7: 4392–4402.

29. GS Alberts, RH Wright, CC Parker. J Electrochem. Soc. 1966; 113: 687.

30. J Kivel, JS Sallo. J Electrochem. Soc. 1965; 112: 1201.

31. E Rudnik, J Gorgosz. Surf. Coatings Technol. 2007; 201: 6953–6959.

32. A Rahaman, KK Kar. Fullerenes Nanotub. Carbon Nanostructures. 2011; 19: 373–397.

33. E Rudnik, P Skrzyniarz. Trans. Inst. Met. Finish. 2007; 85: 82–86.

34. WL Liu, SH Hsieh, TK Tsai, WJ Chen. J Electrochem. Soc. 2004; 151: C680.

35. M Aspland, GA Jones, BK Middleton. IEEE Trans. Magn. 1969; 5: 314–317.

36. H Einati, V Bogush, Y Sverdlov, Y Rosenberg, Y Shacham-Diamand. Microelectron. Eng. 2005; 82: 623–628.

37. H Matsuda, O Takano. J Appl. Electrochem. 1993; 23: 183–186.

38. H Honma, M Noguchi. V-I Electroless Cobalt Bath-Life Extension.1990.

39. EE Kalu. Plat. Surf. Finish. 1998; 85: 74–78.

40. F Pearlstein, RF Weightman. Electroless deposition of nickel and cobalt based alloys. 1968.

41. D Kim, K Aoki, O Takano. J Electrochem. Soc. 1995; 142: 3763–3767.

42. JPG Farr, A Abbas Noshani. Trans. Inst. Met. Finish. 1996; 74: 221–225.

43. IHM Aly, MM Younan, MT Nageeb. Met. Finish. 2003; 101: 37–42.

44. TP Xuan, L Zhang, QH Huang. Trans. Nonferrous Met. Soc. China (Eng. Ed. 2006). 16; 363–367.

45. Y Wei, W Meng, Y Wang, Y Gao, K Qi, K Zhang. Int. J Hydrogen Energy. 2017; 42: 6072–6079.

46. M Sheng, Q Wu, Y Wang, F Liao, Q Zhou, J Hou, W Weng. Electrochem. Commun. 2018; 93: 104–108.

47. A Kohn, M Eizenberg, Y Shacham-Diamand, Y Sverdlov. Mater. Sci. Eng. A. 2001; 302: 18–25.

48. WL Liu, WJ Chen, TK Tsai, SH Hsieh, SY Chang. Appl. Surf. Sci. 2007; 253: 3843–3848.

49. Y Sverdlov, Y Shacham-Diamand. Microelectron. Eng. 2003; 70: 512–518.

50. V Goel, P Anderson, J Hall, F Robinson, S Bohm. IEEE Trans. Magn. 2015; 2496315.

51. Q Zeng, Y Zhang, MJ Bonder, GC Hadjipanayis. J Appl. Phys. 2003; 93: 6498–6500.

52. TR Jayaraman, VK Venkatesan, HVK Udupa. Electrochim. Acta. 1975; 20: 209–213.

53. Y Gao, L Huang, ZJ Zheng, H Li, M Zhu. Appl. Surf. Sci. 2007; 253: 9470–9475.

54. D Seifzadeh, L Farhoudi. Surf. Eng. 2016; 32(5): 348-355.

55. ML Klingenberg, EW Brooman, TA Naguy. Plat. Surf. Finish. 2005; 92(4): 42-48.

Improved Strength of Cylindrical Joints through Adhesive Tailoring

Papai Biswas, Ishan Manoj, Atul Jain

Abstract

A study aimed at designing an axisymmetric finite element model for a tubular lap joint is presented in this paper. This axisymmetric model may consist of isotropic, orthotropic, anisotropic, and even layered composite materials. Special emphasis has been given to peel stress. A 3D solid continuum model was also developed to verify the axisymmetric model by analysing peel, shear, and axial stress. This axisymmetric study has shown a good agreement with the 3D model. Critical length analysis has been done through shear stress variation in the adhesive. Peel and shear stress variations with varying adhesive thickness also have been studied in the paper. Symmetric longitudinal tailoring has been performed to reduce peak stress (stress concentration) values at the overlapping end of the joint. Overall, this study helps to find out the optimum design of adhesive in cylindrical joints, optimum overlap length, Thickness of adhesive, and symmetric tailoring length may be calculated with the help of this study.

Keywords: Adhesive cylindrical joints; Symmetric tailoring; Multi-material interface; Stress concentration; Functionally graded material; Joint strength.

1. Introduction

As the use of composite material is increasing, conventional joining methods1, such as riveting, welding, and coupling of structures, are inversely decreasing due to their in-applicability in composite structures. Researchers are now interested in modelling composite joints and analysing the behaviour of adhesive joints, especially in aerospace structures. Adhesively bonded joints[1] can distribute stress more uniformly throughout the joint length, which is why one gets better mechanical performance compared to a conventional joint. The design of adhesive joints is greatly influenced by the adhesive interlayer's peak shear and peak peel stresses. Researchers are mainly focused on peel stress (*S11*), shear stress (*S12*), and axial stress (*S22*) of such types of adhesive joints.

Multi-layered cylindrical joints composed of similar or dissimilar materials will experience stress and strain concentration at the overlap ends. Particularly in the case of different materials and designs with various tailoring methods, this stress concentration will also appear at the interface area of the joints.[8]

Kumar et al.[2] showed the stress distribution in cylindrical lap joints for a single adhesive material of epoxy adhesive. The authors performed a detailed analysis of the stress profile

[8] ✉ Papai Biswas

papaibiswas587@kgpian.iitkgp.ac.in

Indian Institute of Technology Kharagpur, Kharagpur, West Bengal 721302 India

throughout the adhesive with the help of FEA and mathematical modeling. However, this study focused on stress distribution and did not address the multi-adhesives tailoring effect. Drastic changes in stress profile after implying bi-adhesive in joints have been observed, and it also shows the reduction of stress concentration at the overlap ends. It remains unclear what percentage of stress concentration[3] can be reduce in the adhesive at the end of the joint overlap.

To fill this research gap, a detailed numerical investigation of the adhesive tubular joint using the same model and loading condition has been conducted to get a better stress reduction at the ends of overlap joints.

In 1935, when Owens Corning[4] introduced the first glass fiber, The joining of two composite parts[1] became an exciting topic for researchers. In tubular adhesive lap joint (TLJ)[5], overlap ends point peel stress concentration is the main reason for failure. Researchers did not focus on it in a TLJ.

A lighter structure can be introduced with a more uniform stress distribution over the joint part of TLJ. The goal of this study is to reduce this ends peel stress concentration of TLJ. 2D-Diagrams of single adhesive and bi-adhesive TLJ models are shown in **Fig. 1** and **Fig. 2** respectively. To achieve our goal, finite element (FE) based research has been done. The most challenging part was making a FE model of our real-world problem (TLJ structure).

A study of the critical length has been done to achieve the modified stress profile with lower stress concentration at the overlapping ends of the adhesive joint. Analysis of the optimum thickness of the adhesive joint also has been performed. Step-wise functionally graded material (FGM) to reduce overlapping peak stress is also covered in the paper. To optimize the joint's strength, a study on the stiffness of the whole assembly also has been covered in the paper.

2. Axisymmetric Model Finite Element Model Formulation

2.1 Axisymmetric model

The tubular lap joint assembly is modeled as an axisymmetric model to reduce computational effort and simulation cost, utilizing a commercial finite element code, Abaqus/Standard FEA version 6.14[6]. The traction force of 100 MPa was applied to the shaft cross-section, in place of a concentrated far-field load of 38.01 kN along the axis of the shaft. The axisymmetric boundary condition is used along the center of the shaft, restricting rotation and radial and axial displacements. The Y-axis displacement of the tube has been restricted. This model has imposed no boundary condition on the adhesive, i.e. free to move in the plane. The free meshing has been done with 4-node bilinear axisymmetric quadrilateral elements (CAX4R) with two degrees of freedom per node, one in the radial direction and another in the axial direction for adherents and adhesives.

Elements at the adherent and adhesive surfaces are tied to each other with the help of a constraint manager. Fine meshing has been used near this interface and the end of the overlap region to capture steep stress gradients. Linear static analysis is performed with the help of linear elastic material.

Fig. 2 2D drawing of bi-adhesive TLJ model.

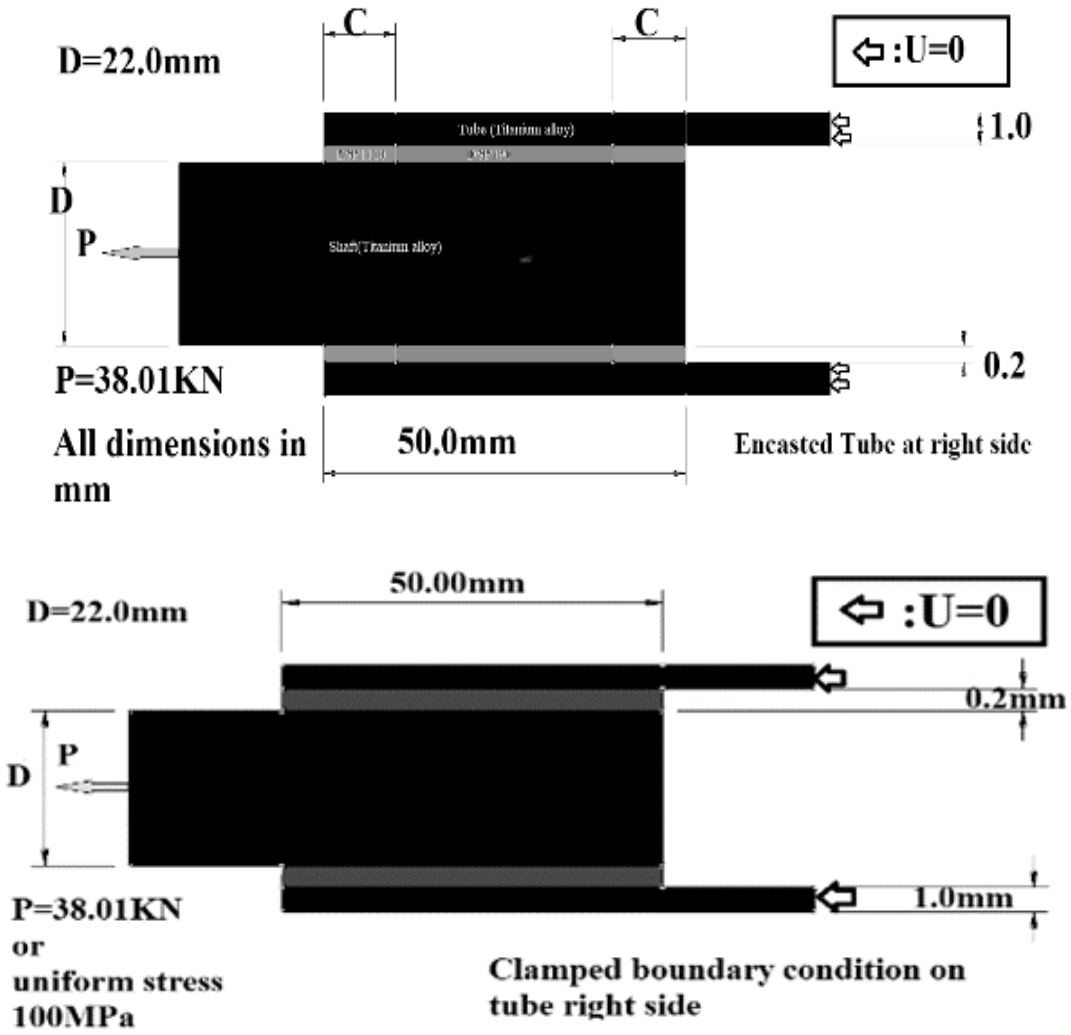

Fig. 1 2D drawing of single adhesive TLJ model.

Seeding of the geometry is such a) adhesive global uniform seeding size 0.01mm. b) tube inner surface seeding 0.01mm, outer surface seed size 0.25mm, and bias is used along the radius of 25. c) shaft outer surface seed size is 0.01mm, and the shaft center seed size is 0.5mm; somewhere, its size is 1.0 mm corresponding bias ratio of 25 and 10.

Moreover, stress singularity[7] arises at the free surface of the interface due to the lack of solution capacity of Abaqus software at the interface where a certain change of material properties is present. Therefore, we focused on a surface of 5.0 micrometers below the outer interface surface for adhesive stress analysis.

2.2 3D model

A general-purpose linear brick element with reduced integration, i.e. C3D8R of 3D stress family[8] (Linear hexahedral elements), was utilized to establish the 3-D model. A total number of 2220004 nodes & 2062880 elements have been constructed in the whole 3D model.

Adhesive seed size varies from 0.1 to 0.5 mm with a bias ratio of 5.0, starting from the edge of hollow cylindrical adhesive geometry and ending at the mid-position along the axis of adhesive. The overlap regions in all geometry, such as shaft and tube, meshed in structured form with the same seeding size used in adhesive. The non-overlap regions meshed in structured form with 0.25mm seed size. 0.01 maximum deviation is used in every case.

2.3 Validation of the axisymmetric model with the 3D model

As seen in **Fig 3**, the results of the 2D axisymmetric model and 3D model are in excellent agreement with each other. Along the analysis path, 200 & 1002 nodes have been utilized to plot peel, shear, and axial stress, respectively, in axisymmetric & 3D models. That is why a slight difference was found in maximum peak values at the ends of the overlapping zone, especially in axial and peel stress.

3. Material Properties & Loading

Saint Venant's principle[9] states that the stresses and strains in a body at points that are sufficiently remote from points of application of load depend only on the static resultant of the loads and not on the distribution of loads. According to this principle applied point load of 38.01 kN along the shaft axis at the center of the shaft circular cross section is considered uniform stress of 100 MPa distributed across the c/s of the shaft left end. Encased boundary condition was imposed on the tube end. The properties of the materials used in the investigation is shown in **Table 1**.

Table 1 Material properties used in the model

Members	**Shaft (S)**	**Tube (T)**	**ESP1110**	**DSP490**	**Epoxy**
E(GPa)	100	100	5.9	1.8	2.7
μ	0.342	0.342	0.4	0.4	0.35

4. Results and Discussion

4.1 Critical length analysis

In multi-material joints, critical length[10] is the minimum overlap length in the joint, which requires to transfer all tensile load purely through the shear mode from one adherend to another. Critical length analysis must be done through shear stress analysis in the adhesive bond length. Zero shear stress value at the mid-portion of adhesive indicates

critical length has been achieved (**Fig. 4**). Peel stress at the ends of the overlap increase proportionally with a decrease in the bond length, but shear stress decreases with the increase in overlap length. In the domain of $0<L<L_{CR}$, joints are more prone to peel stress failure due to a higher value of peel stress at the overlap ends compared to the $L>L_{CR}$ domain. Even though at $L=L_{CR}$, peel stress is much higher and failure happens due to this stress, we aim to reduce that overlap peel stress (**Fig 5**). **Fig. 4** shows shear stress distribution with various overlap lengths and $L_{CR}=50mm$ in the case of our model. L_{CR} also depends on loading and boundary conditions.

4.2 Peel and shear stress analysis due to the adhesive thickness variation

Peak peel stress at the ends of the overlap keeps on reducing with increasing the adhesive thickness to an approximate saturated value which is at 0.6 mm of adhesive thickness, as shown in **Fig 6**. It may be due to an increase in adhesive volume that results in less strain energy concentration in the adhesive bond.

4.3 Analysis of symmetric tailoring along the longitudinal direction

Peel & shear stress distribution along the bi-adhesive bond length of the tubular joint with different volume fractions under a quasi-static load of 38.01 kN is measured. DSP490 (E=1.8 GPa and μ=0.4) and ESP1110 (E=5.9 GPa and μ=0.4) have been used to analyze symmetric compliance tailoring (**Table 1**). Stress has been analyzed for 8 different volume fractions respectively 0, 0.2, 0.4, 0.5, 0.54, 0.6, 0.8, and 1.0.

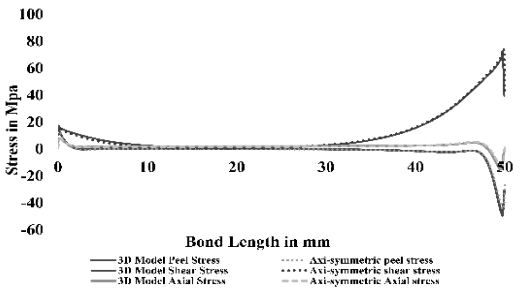

Fig. 3. 3D vs Axisymmetric model validation

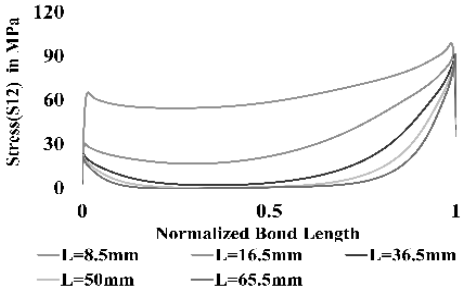

Fig. 4. S12 vs overlap length.

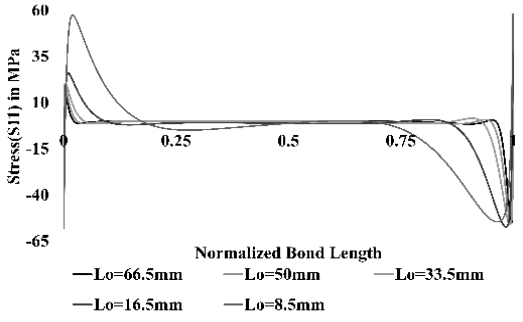

Fig. 5. S11 vs overlap length.

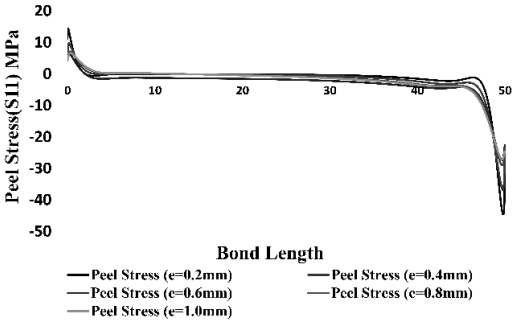

Fig. 6. S11 vs adhesive thickness(e).

In the case of a single adhesive joint, there are only two values of peak stress, but adding one more adhesive to that system introduced two more peak stress points at the adhesive interface because of certain changes in material properties. Distribution of peel stress in the case of bi-adhesive joint shows us a continuous decrement of peak stress value at both bi-adhesive joint interfaces with an increase in compliance value shown in **Fig. 7**. Still, at the overlap ends peak stress decrease initially up to Vc=0.4 beyond the point it has a constant value in the domain of 0.4<Vc<1.0 shown in **Fig. 8**. The peel stress profile for Vc=0.0 (full stiffer) and Vc=1.0 (full compliance) show us a sound reduction of 45.70% from 20.04 MPa to 10.88 MPa at the left end overlap and at the right end of the overlap a decrease of 61.01% from 47.15 MPa to 18.38 MPa. After reaching a volume fraction of 0.54, it has been observed that the interface peak stress reduction rate is insignificant.

Shear stress distribution along the bond length shows a similar monotonic decrement as in peel stress distribution but with a different curve pattern demonstrated in **Fig. 9**. Analysis shows us the amount of shear stress reduction of 27.40% at the left end of the tubular overlap joint from 83 MPa to 60.25 MPa & a decrease of 39.85% from 20.15 MPa to 12.12 MPa on the right side. Change in peak shear stress values at both end sides can be seen up to a compliance length of 10.0 mm or up to a volume fraction of 0.4; beyond that point, peak stress at both ends has got saturated with a constant value, but interface peak stress continuously degreasing in the whole domain expect at the Vc=0.2, there is a high jump of shear stress at the right side adhesive interface compared to the right end max shear value as shown in **Fig. 10**.

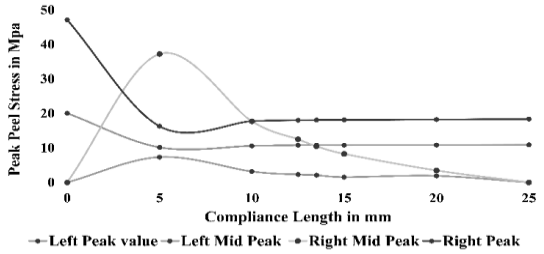

Fig. 7. Peak peel stress vs compliance tailoring.

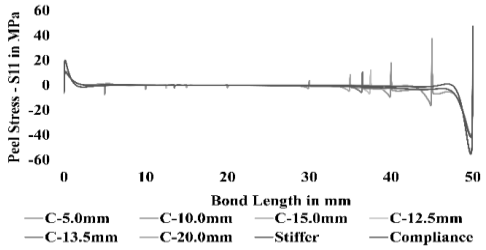

Fig. 8. Peel stress vs compliance tailoring.

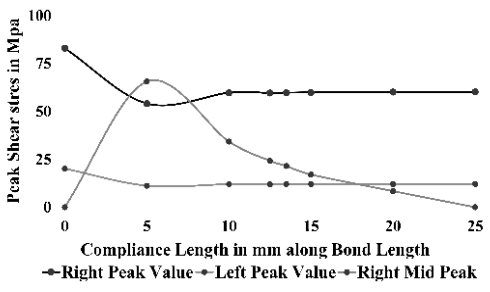

Fig. 9. Peak S12 vs compliance length.

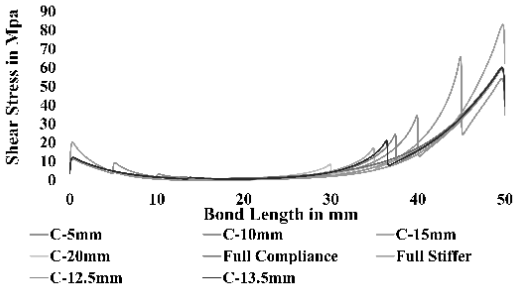

Fig. 10. S12 vs compliance length.

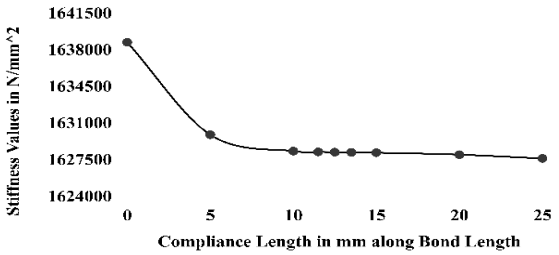

Fig. 11. Stiffness vs compliance length.

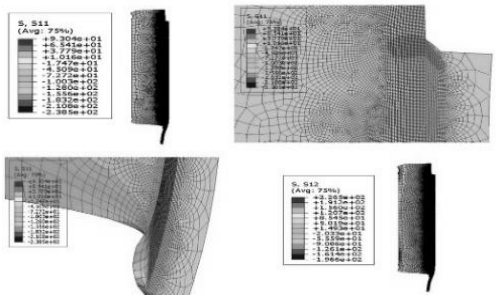

Fig. 12. Stress contour (S12 & S11).

According to Hook's law[11], force is required to deflect a spring-like material directly proportional to the stiffness value. Stiffness analysis shows us the joint strength of the bi-adhesive tubular joint, which is presented in **Fig. 11**. Strength is also a parameter that influences the toughness of the joint. The stress contour of the models is shown in **Fig. 12**.The stiffness value decreases exponentially from 1638721.63 N/mm to 1628311.73 N/mm with a percentage of 0.64% up to a volume fraction of 0.4 and within $0.4<Vc<1.0$ domain, Rate of decrement is meager, approximately it has got saturation with some constant value of 1627600 N/mm. Thus, from this stress and stiffness analysis, the joint, either with Vc=0.4 or with Vc=0.56, is predicted to be the highest performing across all of our essential bi-adhesive tubular joint models.

5. Conclusions

Multi-material joints, either in the composite world or in structural design with adhesive, are preferable due to the possibility of a uniform stress distribution within the adhesive joint. Especially in the composite world, it's not just preferable but a solution to overcome the difficulties of machining and joining by conventional methods.

Compliance tailoring of a tubular adhesive joint may not have enough shear stiffness at the joint but, tailoring can diffuse concentrated stress and strain from the overlapping end to somewhere else in the joint. On the other hand, a fully stiffer bond may have a sufficient amount of shear stiffness but it will turn into a high-stress concentration point at the overlapping end of a tubular joint. The mechanical performance of an adhesive tubular joint has been improved up to a certain level as compared to a fully stiffer or fully compliant adhesive joint. While implementing the compliance tailoring it has been observed that stress concentration has reduced significantly, even a small amount of reduction in stress concentration can be helpful in the aerospace and automobile industry. Reduction in stress concentration means a lighter-weight design which directly impacts on fuel consumption of vehicles. The use of 3D printed functionally graded material (*i.e.* discrete step function) can realize the predicted model.

References

1. C Worrall, E Kellar, C Vacogne. Joining of fiber-reinforced polymer composites - A Good Practice Guide. Composites UK Ltd. 2020.
2. S Kumar, MA Khan. Int. J Adhes. Adhes. 2016; 64: 142–152.
3. L Toubal, M Karama, B Lorrain. Compos. Struct. 2005; 68: 31–36.
4. R Reddy Nagavally. Int. J Curr. Res. 2016; 8: 37763-37768.
5. S Aimmanee, P Hongpimolmas, K Ruangjirakit. Int. J Adhes. Adhes. 2018; 86; 59–72.
6. Abaqus/CAE User's Manual Abaqus 6.11.
7. A Barroso, JC Marín, V Mantič, F París. Int. J Adhes. Adhes. 2020; 97: 102478.
8. P Liu, X Cheng, S Wang, S Liu, Y Cheng. Compos. Struct. 2016; 138: 30–39.
9. XS Xu, WX Zhong, HW Zhang. Int. J. Solids Struct. 1997; 34: 2815-2827.
10. S Kumar, BL Wardle, MF Arif, J Ubaid. Adv. Eng. Mater. 2018; 20(1): 1700883.
11. F Dell'Isola, G Sciarra, S Vidoli. Proc. R. Soc. Lond. A. 2009; 465: 2177–2196.

Recent Trends in Friction based Welding of Metal and Polymer

Pabitra Maji[a], Ranit Karmakar[b], Rahul Kanti Nath[a]

Abstract

Metal polymer welded structures are widely used in various sectors including automobile and aerospace industry with aim to weight reduction. Friction based welding of metal and polymer is one of the best alternatives which can be adopted for the dissimilar joining. Recent developments in the field of friction-based welding of metal and polymer as well as metal and polymer matrix composites are discussed here. The mechanisms associated with different approaches to the dissimilar welding are thoroughly evaluated. The weld appearances and microstructural modifications in different approaches are examined critically and are correlated with the mechanical performances of the joints. Finally, the article concludes with suggestions for future research works.

Keywords: Dissimilar joining; Metal; Polymer; Friction stir welding

1. Introduction

The new trend throughout the world is to use lightweight, high strength material for environment-friendly and safer application especially in the field of aerospace, automobile and military sectors. Likely, Polyethene (PE) has created its wide space application in the automobile industry owing to lighter, economical and eco-friendliness[1,2]. Similar to polymers, aluminum and magnesium alloys are also very much applied in these industries for their high weldability, good strength to weight ratio, corrosion resistance etc.[3–5]. It is frequently needed to use these two metals and polymers in the same structure, called a Hybrid structure. The hybrid structures are widely used in battery housing, automobile parts, outdoor applications of steels. For example, the new model Audi R8 included the Al alloy and polymers matrix composite in its body structure[6].

In a hybrid structure, the joining of metals and polymers is necessary. When it comes to the principle of making joint between metals and plastics, it is very interesting in nature. Several available techniques such as adhesive joining, mechanical fastening and conventional welding have their limitation when comes to hybrid structures. To counteract these issues only solution is the joining by frictional heat such as in Friction stir welding and Friction stir spot welding[7,8].[9]

These processes are very advantageous compared to conventional ones in respect to zero external heat, zero filler material requirements and its solid-state joining nature[9,10]. For the lap joint, the heat produced from the friction of rotating shoulder (of the tool) and

[9] ✉ Rahul Kanti Nath
riserrahul@gmail.com

[a] Regent Education and Research Foundation, Barrackpore, West Bengal, 700121, India
[b] Indian Institute of Technology Kharagpur, Kharagpur, West Bengal 721302 India

metal workpiece is responsible to melt the polymers by transferring from metal into that[11].

In this article, a detailed analysis on friction-based welding of metal with polymer/polymer composites is presented. The joining mechanisms associated with different welding techniques are carefully evaluated. Critical attention is laid on the microstructural appearances and failure of the joints.

2. Various Techniques

Most commonly used friction-based techniques for welding metal/metallic alloys with polymer/polymer matrix composites are spot welding and friction stir welding (FSW). Friction stir spot welding (FSpW) is one of the widely used variants for spot welding of metal and polymer. In this technique metal plate with a hole (preferably threaded) is placed upon the polymer. A pin less tool is plunged into the metal plate and the frictional heat generated between the tool shoulder and metallic plate gets transferred to the polymer plate. The resultant heat in the polymer softens/melts it and the semi-solid/liquid polymer moves upwards. Then the vertical movement polymer is restricted by the shoulder surface and consequently, the hole is filled by horizontal/downward/vortex flow and adhesive bonding between the metal and polymer completes the welding[12].

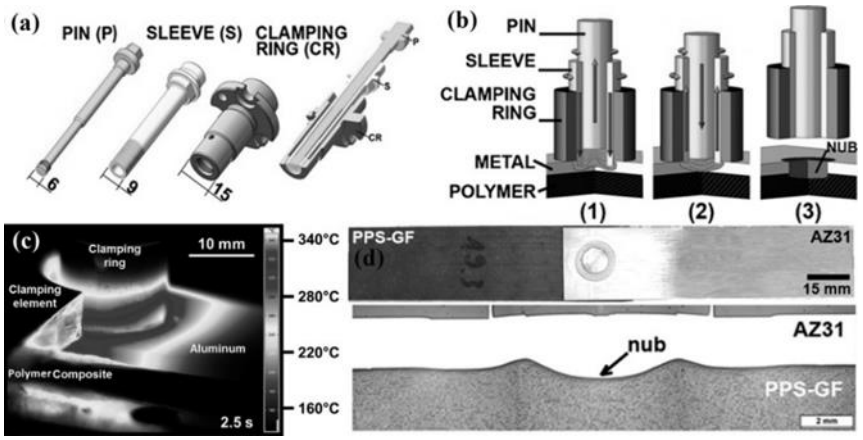

Fig. 1. a. Components of FSpJ tool, b. FSpJ process, c. Heat distribution during FSpJ, d. Top view and cross-sectional view of FSpJed aluminum-PPS composite[13,14].

Another popular approach for spot welding of metal and polymer termed as friction spot joining (FSpJ) is a modified version of FSpW as shown in **Fig. 1**. The tool used in this process consists of three parts namely Pin, Sleeve and Clamping ring (**Fig. 1a**) which are attached coaxially and are capable of relative motion among them. Between two variation of the process such as 'Pin plunge' and 'Sleeve plunge', 'Sleeve plunge' approach is mostly used and shown in **Fig. 1b**. In this process also, metal plate is kept above the polymer plate, but unlike FSpW, no hole is made in the metallic plate. The clamping ring holds the weld materials and the rotating sleeve is pushed nearly half into the metal plate while the rotating pin retracts from the metal surface. The frictional heat between metal

and sleeve plasticizes the metal and the plasticized metal squeezes in the cavity formed by the retracting pin. Thereafter, the sleeve retracts and the pin is pushed to fill the hole left by the sleeve with the entrapped material. Therefore, a 'metallic nub' is created over the polymer surface. Simultaneously, heat generated at the metal is transferred into the polymer and a thin layer melt at the upper surface. The molten layer is spread over the spot and creates adhesive bonding with the metal. Heat generation during FSpJ process and macrographic view of a joint is shown in **Fig. 1c** and **Fig. 1d**. Besides FSpW and FSpJ, other methods such as friction-based stacking (**Fig. 2**) and laser assisted FSpW also have been adopted by researchers to achieve metal-polymer welding. In friction-based stacking method, a hole with features such as cavity or thread is created in the metal plate and the polymer plate with a stud is kept below the metal plate with the stud being inserted in the hole of metal plate. The frictional heat generated between polymer and FSW tool softens the polymer and the semi-solid polymer fills the metallic hole and form joint by mechanical interlocking. In laser assisted FSpW, instead of through hole in the metal plate, micro holes/grooves are created on the metallic surface to be welded by laser surface treatment and the metal plate is placed above polymer plate. Then similar to FSpW, a FSW tool with or without pin is plunged in the metal plate and the frictional heat is generated. The heat is then conducted to the polymer plate and softens it. The downward force of the tool forces the soft polymer to move upward and fill the tiny grooves in the metal plate and mechanical interlocking results in joining of those.

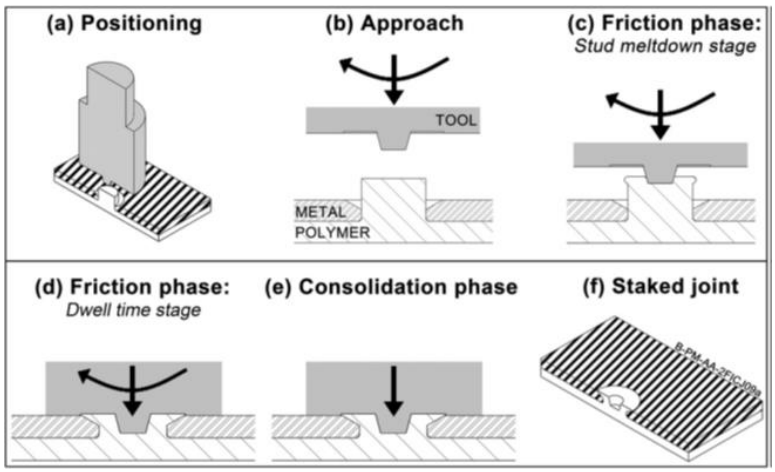

Fig. 2 Steps of friction-based stacking of metal and polymer[15].

In FSW, a rotating tool consists of a shoulder and a pin is plunged into the weld material and heat is generated due to the friction of weld material with the tool. The frictional heat softens the weld material and the rotating action of the pin stirs the material in a complicated manner. As the tool moves forward, the material is consolidated at the tailing end of the shoulder by downward force. Both butt joint and lap joint of metal-polymer have been done by the researchers. In butt joint as illustrated in **Fig. 3a**, the

metal plate is placed in the advancing side, whereas for lap joint (**Fig. 3b**) metal plate is placed above the polymer plate.

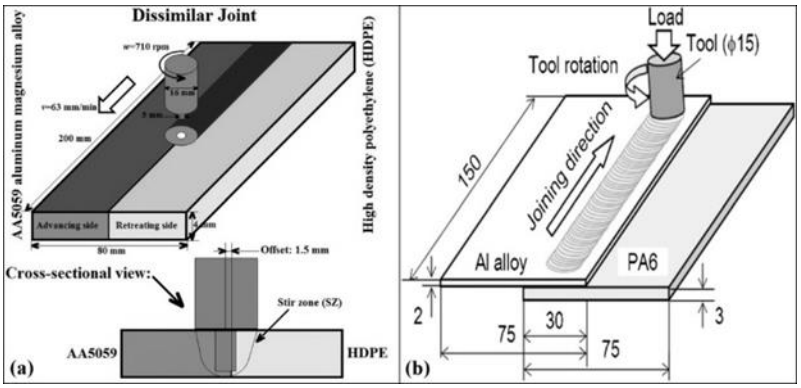

Fig. 3 FSW of metal and polymer in a. butt joint configuration, b. lap joint configuration[16,17].

3. Spot Welding

Pabandi et al.[18] adopted FSpW technique to weld AA5052 aluminum alloy and carbon fiber reinforced polypropylene composite. They used threaded hole in the aluminum alloy and observed filling of the hole by melted polymer after welding, which resulted in mechanical interlocking (**Fig. 4a**). Moreover, a 'reaction layer' of around 15 µm thickness consisting Al and C was formed between the aluminum alloy and polymer composite (**Fig. 4b**), while the amount of Al in the layer was directly proportional to the tool rotational speed. However, owing to difference in thermal properties, gap was created between the 'reaction layer' and the composite. The joint exhibited maximum of around 80% strength in shear-tensile test. The failure occurred at the interface of the joint for low heat input welds. Similar observation of failure at adhesive bonding in interface was made by Aliasghari et al.[19] in FSpWed AA5052 alloy and commercial polypropylene (PP). However, they also observed that Plasma electrolytic oxidation coating on aluminum alloy prior to welding resulted in ductile failure in PP as well as significant improvement in joint strength. Lv et al.[20] FSpWed AA6061-T6 and polypropylene (PP) and observed clear interface between the weld materials. They stated that the controlled axial force by FSW machine did not allow melting the PP. Therefore, clear interface without any gap was evident in the weld interface (**Fig. 5**). They also observed that under tensile shear load, the consolidated PP in the AA6061 hole was fractured. Two different crack generation and propagation such as along the metal polymer interface and in the consolidated polymer were evident leading to brittle and ductile failure respectively.

Goushegir et al.[21] joined AA2024-T3 alloy with carbon fiber reinforced poly phenylene sulfide (CF-PPS) through FSpJ approach. They observed that for higher frictional heat input the joint area was larger (**Fig. 6a, b**) and consequently, mechanical strength of the joint was higher. They divided that the joint area into four different regions namely 'the nub', 'partially deformed zone', 'transition zone' and 'adhesion zone' (**Fig. 6c, d**). They

also demonstrated that in the nub, carbon fibers of the composite were present along with aluminum. During welding, the downward axial force during welding enforced semi-solid aluminum to penetrate in the upper layer of the composite and a few carbon fibers got entrapped in the aluminum. Also, pores were created in the aluminum interface during welding which were subsequently filled by molten polymer and consolidated during cooling. Combined effect of those two phenomena resulted in good mechanical interlocking. During FSpJ of AA6181-T4 with CF-PPS, Esteves et al.[22] also observed similar joining mechanism. They also observed that slight penetration of nub in the polymer resulted in high strength of joint. They examined the effect of process parameters on the welded joint and concluded that tool rotational speed, plunging time, plunge depth and plunging force had significant effect on the joint properties in descending order. In lap-shear test of the joints, brittle failure with combination of cohesive and adhesive failure at interface was evident.

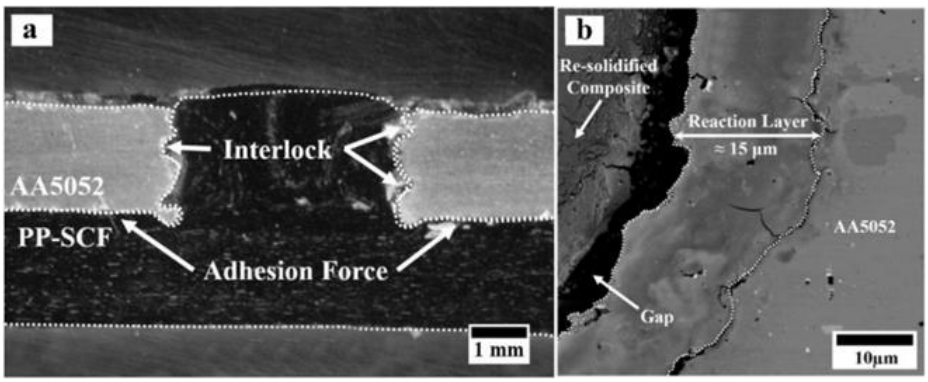

Fig. 4 Cross section of AA5052/PP-SCF joint a. stereograph image, b. scanning electron micrograph[18].

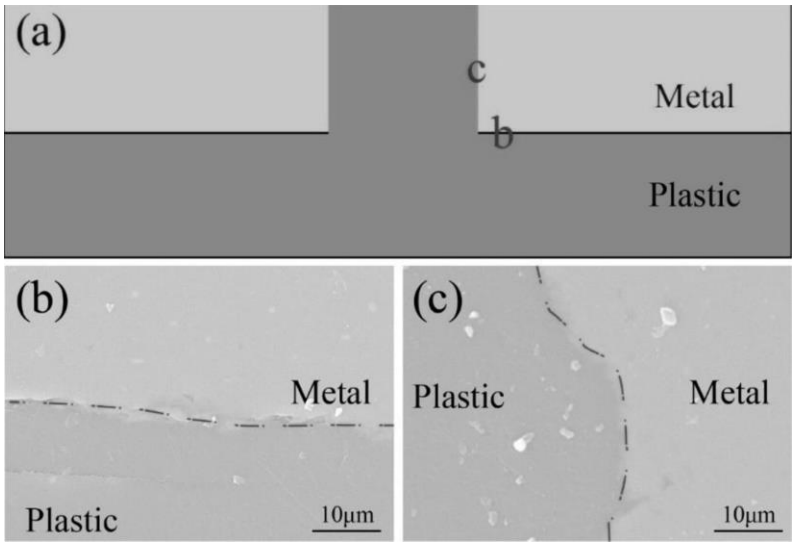

Fig. 5. a. Schematic representation of metal polymer joint, b., c. Micrograph of regions indicated in a[20].

In another work on FSpJ of CF-PPS with AA2024-T3 alloy, Andre et al.[15] examined the partially deformed zone and adhesion zone in the fracture surface of the joint. In the partially deformed zone, PPS matrix as well as carbon fibres is attached strongly with aluminium after mechanical test (**Fig. 7a**). Owing to the high temperature at the centre, the interlayer was melted and subsequently squeezed out from centre by the axial force. Therefore, a strong interlocking occurred between the weld materials. The adhesion zone on both metal and CF-PPS surface after lap-shear test (**Fig. 7b, c**) revealed presence of interlayer on both surfaces. This implied that the molten interlayer formed during welding was adhered to both the weld surface and created very strong micro-mechanical interlocking. Amancio-Filho et al.[14] FSpJed AZ31–O magnesium alloy with fibre reinforced PPS and correlated the microstructure of the joint with microhardness as illustrated in **Fig. 8**. The clapping ring used in FSpJ imposed work hardening in the alloy and enhanced the microhardness. The centre of the joint spot experienced dynamic recrystallization and yielded fine grains along with dispersion of precipitates. Therefore, higher microhardness than un-welded alloy was evident in weld centre. Away from weld centre thermos-mechanically affected zone (TMAZ), heat affected zone (HAZ) were also visible; where piling up of dislocation enhanced microhardness was evident.

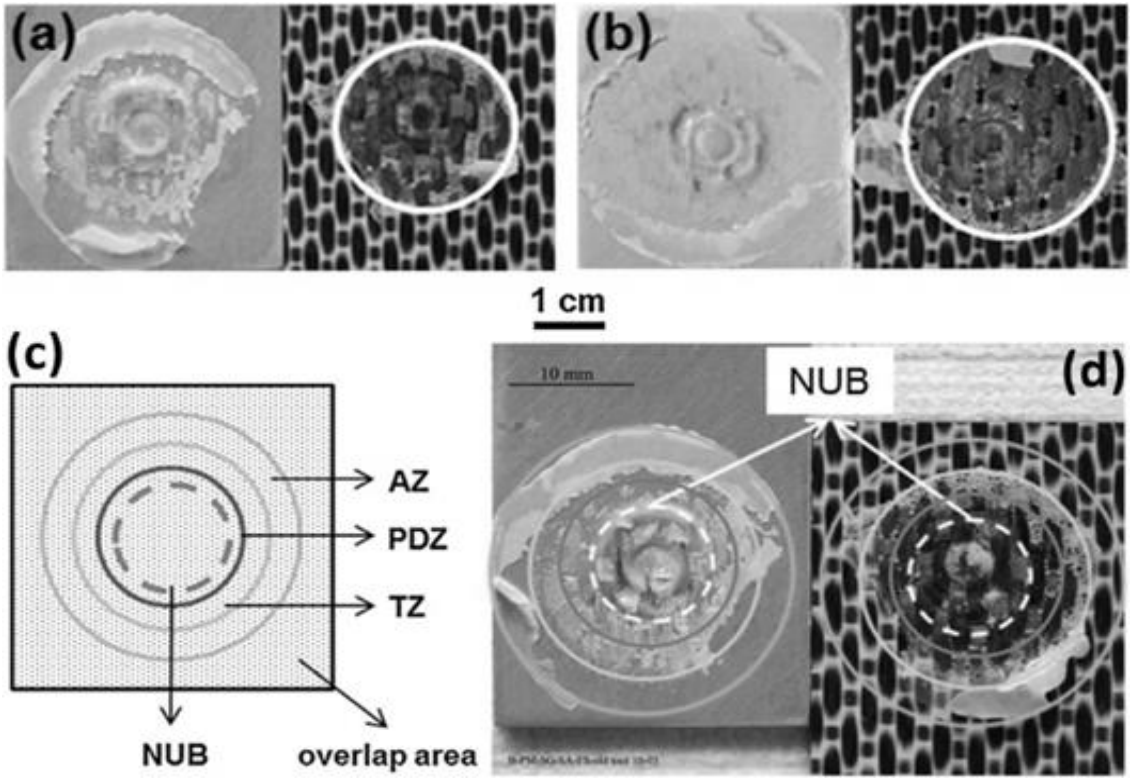

Fig. 6 After fracture view of metal polymer joints, a. Joint area at low heat input, b. joint area at high heat input, c. schematic representation of zones, d. zones in actual joint surface[21].

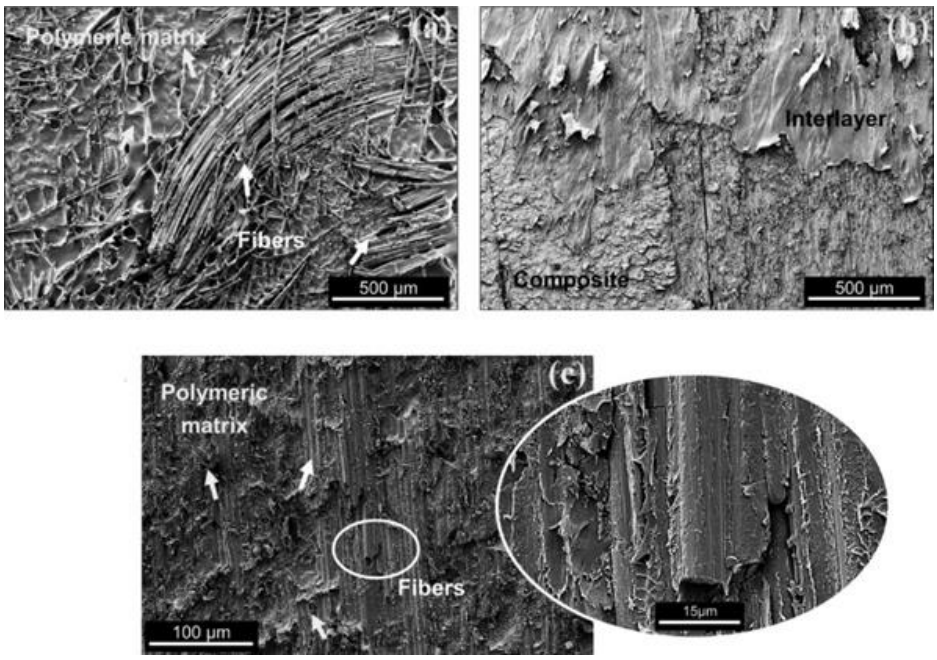

Fig. 7 SEM image of a. partially deformed zone, b., c. adhesion zone on aluminum surface and CF-PPS surface[14].

The friction-based stacking joint between AA 6082-T6 alloy and polyetherimide (PEI) by Abibe et al.[15] resulted in significant pores at TMAZ of polymer stack (**Fig. 9**). Under lap shear loading the joint failed by crack initiation from the pores as well as from the stack head and the stack root. Han et al.[23] claimed that using laser surface treatment on aluminum alloy before employing FSpW to join it with PP resulted in 100% joint efficiency.

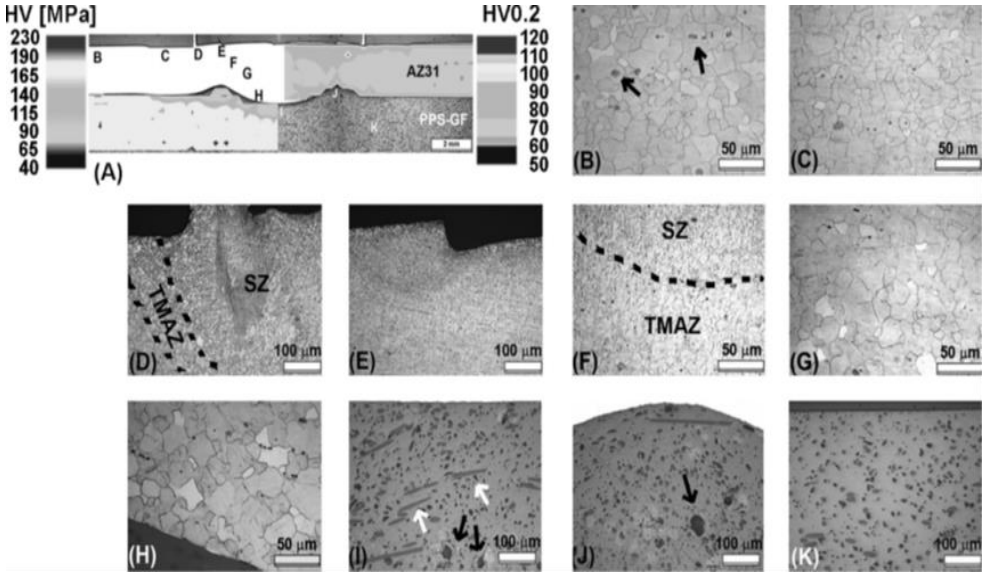

Fig. 8. a. Microhardness distribution in AZ31/PPS-GF joint, b.-k. microstructure of different portions in a[13].

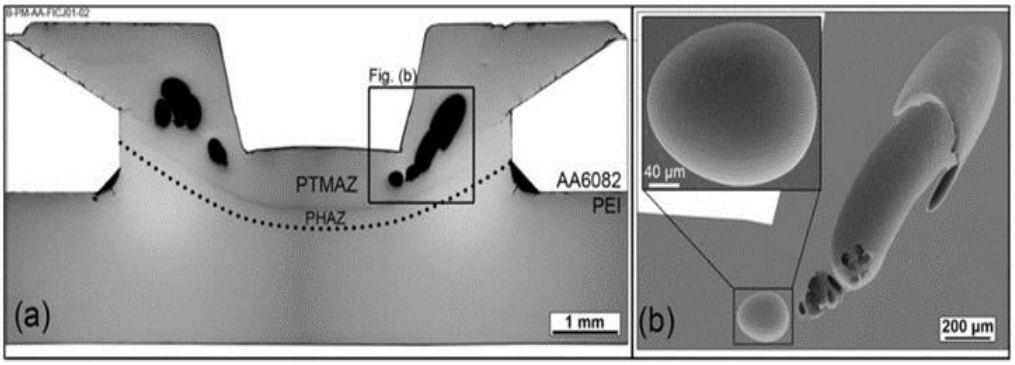

Fig. 9. a. Porosity in TMAZ of PEI, b. enlarged view of a pore[15].

4. Friction Stir Welding

The most common case of metal-polymer welding is lap joint using FSW which found in the literature. Shahmiri et al.[24] investigated the effect of heat on microstructure and mechanical properties of FSWed joint between AA-5052 alloy and PP-C30S polypropylene plate. The mechanism of joint formation while lapping between the polyphenylene sulphide and AA6111 was the solidification of molten plastics on and around the metallic chips formed during processing. For this bonding, no extra preparation of the surface was necessary. From **Fig.10**, the weld zone can be described as the composite of Al alloy chips and fragments into the polymer matrix and thus mechanical bonding was formed[25]. Nagatsuka et al.[18] successfully welded the polyamide 6 (PA6) with different grades of Al alloy with different Mg content like A1050, A3004, A5052 and A508. Except A1050, all Al alloy was bonding with PA6 by MgO while welding by friction stir lapping, which is shown in the TEM and its EDM images in **Fig. 11a** and also proved from the XPS narrow spectrum graph of MgO in **Fig. 11b**. Only A1050 was bonded with PA6 through the formation of Al_2O_3 as there is no Mg content in the alloy. Whereas a very interesting T-joint between AA5754 alloy and Poly methyl methacrylate (PMMA) has been made and analysed by Derazkola et al.[26]. AA6082-T6 plate and self-reinforced PP plastic plate was mechanically joined using a painless FSW tool in a little bit tricky way by Buffa et al.[27].

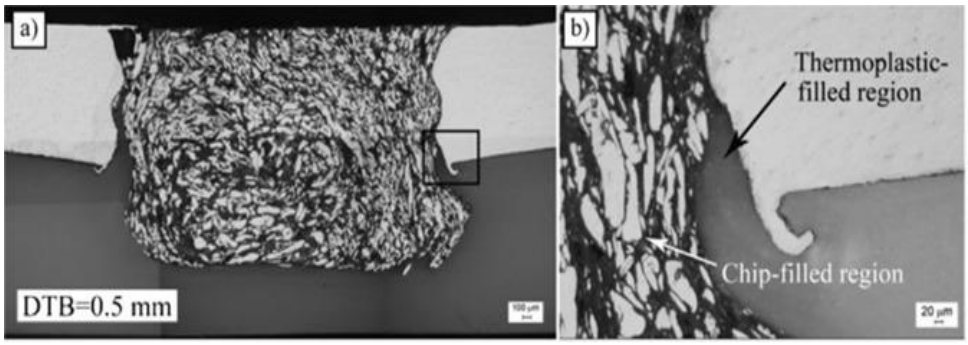

Fig. 10 Micrograph of aluminium-PPS joint with high backing distance and low traverse speed[24].

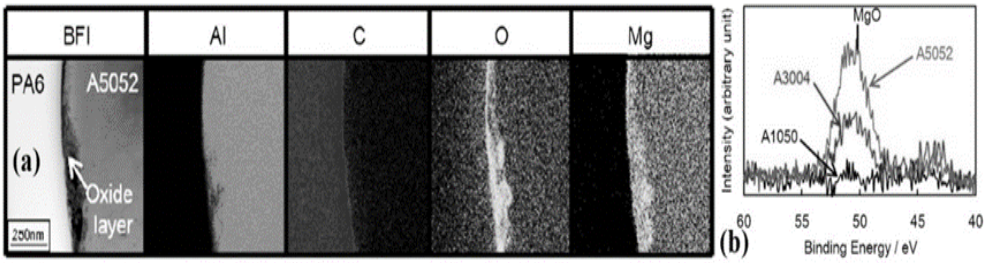

Fig. 11. a. TEM image and elemental distribution in aluminium-polymer joint, b. XPS of aluminium surface[16].

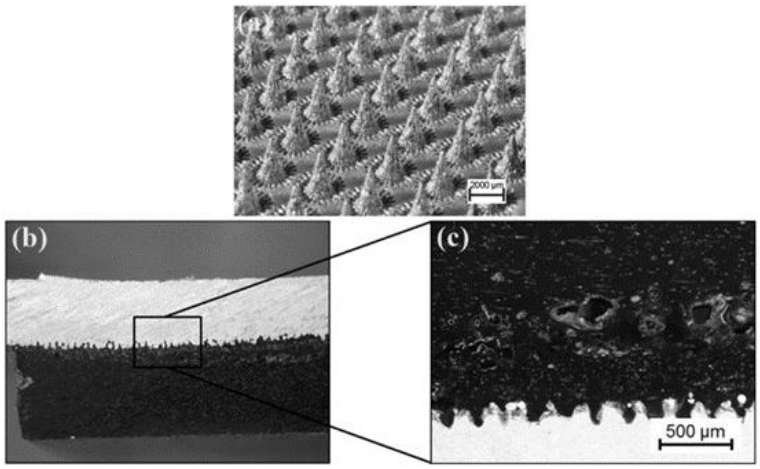

Fig. 12. a. Pin structured aluminium surface by laser treatment, b. FSW lap joint with the notch effect, c. Enlarged view of joint interface[28].

Wirth et al.[29] used a painless tool for lap joining of glass fiber reinforced PA6 and EN AW-6082 Al alloy and termed it as friction press joining (FPJ). They have found that the ideal temperature for obtaining optimum shear properties was 310 °C. Recently the use of laser source in manufacturing for precision and enhanced properties is very much adopted by modern researchers[30]. Moreover, when this punched with another technique, this hybrid one makes the process step up a new level. It was observed that if the laser pre-treated surface of Al alloy can be joined with glass fiber reinforced polyamide using FPJ, the shear strength can be increased by 40% compared to non-treated. Macroscopic pined surface structures were produced by laser as shown in **Fig. 12a**. It was found that the pin height controls the shear strength. But greater pin height can decrease the shear strength by notching effect (as shown in **Fig. 12b**)[28].

5. Conclusions and Future Research Directions

In this article, recent trends in friction-based welding of metal and polymer are discussed. Friction spot welding, friction spot joining, friction-based stacking are commonly used methods for spot welding of metal and polymer. Friction stir welding was also employed to great effect for both butt joint and lap joint of metal and polymers.

The bonding between metal and polymer by frictional heat is mainly by mechanical interlocking and adhesive joining. A few researchers also claimed to found chemical bonding or diffusion interlayer between metal and polymer. The frictional heat significantly contributes to the area of joining and consequently, controls the joint strength. In most of the spot-welding processes and lap joint with painless tool, as the heating source stays only on metal plate, low distortion of polymer structures is visible. In the welds, where polymers come in direct contact with FSW tool, distortion in crystallinity as well as porosities forms. Performing laser surface treatment of metal surface before welding results in excellent joining with high strength.

Literature on metal polymer welding by frictional heat indicates that majority of research on this topic is focused on lap joint and spot welding. Very limited literature is available on butt joint of these two pair. Also, the concept of pre-welding surface treatment may be explored largely as it showed great influence on joint properties. The available studies are majorly deals with aluminum and magnesium as metal alloys. However, welding of other pairs such as steel with polymers by frictional heat may be performed as this pair has great outdoor applications.

References

1. JM Garcés, DJ Moll, J Bicerano, R Fibiger, DG McLeod. Adv. Mater. 2000; 12: 1835–1839.
2. RK Nath, P Maji, JD Barma. J Braz. Soc. Mech. Sci. Eng. 2019; 41: 553.
3. I Eberl, C Hantrais, JC Ehrtsrom, C Nardin. Sci. Technol. Weld. Join. 2010; 15: 699–705.
4. PS De, RS Mishra. Sci. Technol. Weld. Join. 2011; 16: 343–347.
5. F Yusof, Y Miyashita, N Seo, Y Mutoh, R Moshwan. Sci. Technol. Weld. Join. 2012; 17: 544–549.
6. http://Altairenlighten.Com/2015/03/Audi-R8-Uses-Composites-Aluminium-to-Reduceweight-by-15/ [Accessed 06.15] (n.d.).
7. Y Huang, X Meng, Y Xie, J Li, L Wan. Compos. Part A Appl. Sci. Manuf. 2018; 112: 328–336.
8. HA Derazkola, F Khodabakhshi. Int. J Adv. Manuf. Technol. 2019; 100: 2401–2422.
9. HA Derazkola, A Simchi. J Manuf. Process. 2018; 34: 412–423.
10. P Maji, SK Ghosh, RK Nath, R Karmakar. J Brazilian Soc. Mech. Sci. Eng. 2020; 42: 191.
11. FC Liu, J Liao, Y Gao, K Nakata. Sci. Technol. Weld. Join. 2015; 20: 291–296.

12. A Weber. Assem. BNP Media. 2014.

13. ST Amancio-Filho, C Bueno, JF dos Santos, N Huber, E Hage. Mater. Sci. Eng. A 2011; 528: 3841–3848.

14. NM André, SM Goushegir, JF dos Santos, LB Canto, ST Amancio-Filho. Compos. Part B Eng. 2016; 94: 197–208.

15. AB Abibe, M Sônego, JF dos Santos, LB Canto, ST Amancio-Filho. Mater. Des. 2016; 92: 632–642.

16. F Khodabakhshi, M Haghshenas, J Chen, B Shalchi Amirkhiz, J Li, AP Gerlich. Sci. Technol. Weld. Join. 2017; 22: 182–190.

17. K Nagatsuka, T Onoda, T Okada, K Nakata. Weld. Int. 2017; 31: 9–16.

18. HK Pabandi, M Movahedi, AH Kokabi, Compos. Struct. 2017; 174: 59–69.

19. S Aliasghari, M Ghorbani, P Skeldon, H Karami, M Movahedi. Surf. Coatings Technol. 2017; 313: 274–281.

20. Q Lv, Z Liu, H Zhao, X Yu, Q Liu. J Manuf. Process. 2019; 43: 119–123.

21. SM Goushegir, JF Santos, ST Amancio-filho, Mater. Des. 2014; 54: 196–206.

22. JV Esteves, SM Goushegir, JF Santos, LB Canto, EH Jr, ST Amancio-Filho. Mater. Des. 2015; 66: 437–445.

23. SC Han, LH Wu, CY Jiang, N Li, CL Jia, P Xue et al. J Mater. Sci. Technol. 2020; 50: 103–114.

24. H Shahmiri, M Movahedi, AH Kokabi. Sci. Technol. Weld. Join. 2017; 22: 120–126.

25. W Ratanathavorn, A Melander. Sci. Technol. Weld. Join. 2015; 20: 222–228.

26. HA Derazkola, A Simchi. Thin-Walled Struct. 2019; 135: 376–384.

27. G Buffa, D Baffari, D Campanella, L Fratini. Procedia Manuf. 2016; 5: 319–331.

28. AN Fuchs, FX Wirth, P Rinck, MF Zaeh. Phys. Procedia 2014; 56: 801–810.

29. FX Wirth, MF Zaeh, M Krutzlinger, J Silvanus. Procedia CIRP 2014; 18: 215–220.

30. R Karmakar, SK Ghosh. in: Lect. Notes Mech. Eng. 2020; pp. 387–395.

Effect of Tool Incline Angle on Microstructural and Fracture Characteristics of Friction Stir Welded Pure Copper Butt Joints

Puspendu Chandra Chandra[a,b,c], Sabyasachi Mukherjee[a,b], Arpan Kumar Mondal[c], Yadaiah Nirsanametla[a]

Abstract

Defect-free FSW joints are produced in 2 mm pure Cu plates. Variations are done at tool incline angles of 1°, 2°, and 3° during the welding while other parameters are kept fixed. The morphology of the welded specimens is examined by an optical microscope and a Scanning Electron Microscope (SEM). Also, fracture morphology is shown using SEM. It is observed that the formation of the grains at the NZ is more refined and uniform during the welding at a 2° tool incline angle (specimen C2) other than 1° (specimen C1) and 3° (specimen C3) tool incline angle. It is evidenced that all fractures are done in ductile mode. The size of dimples present in the fracture surface of specimen C3 is big due to the slipping mechanism of fracture. Also, it is noticed that the many dimples on the fracture surface of specimens C1 and C2 are small compared to specimen C3 owing to the micro-void coalescence of the fracture mechanism.

Keywords: Pure copper; Friction stir welding; Tool incline angle; Microstructure; Fracture mechanism.[10]

1. Introduction

An ecologically friendly solid-state welding method called friction stir welding (FSW) was first created for welding aluminium alloys[1]. It enables the combining of materials that are comparable and unlike yet challenging to fuse using traditional fusion welding procedures. This method allows for the welding of materials with very differing melting temperatures since joining occurs in the solid state except the working metals being usually melted[2], or other issues with fusion welding, notably porosity, inadequate solidification, or even the generation of radiation or gases[3]. The technique is based on the idea that when a particular amount of pressure is applied to the material of the workpiece, a tool (not consumable) made up of a shoulder and pin revolves to generate frictional heat, which causes plastic deformation[4]. Without attaining its melting point, the revolving tool plasticizes the material as it moves along the joint line and physically combines the materials by stirring[5]. In recent years, some work has been done to expand the method's

[10] ✉ Puspendu Chandra Chandra

chandra18puspendu@gmail.com

a North Eastern Regional Institute of Science and Technology, Itanagar, Arunachal Pradesh, 791109, India

b Regent Education and Research Foundation, Barrackpore, West Bengal, 700121, India

c National Institute of Technical Teachers' Training and Research, Kolkata, West Bengal, 700106, India

use to heavier materials, including composite materials, carbon and stainless steels, titanium alloys, and copper alloys, amongst many others[6,7].

Copper has been widely utilized in the metallurgical, electrical, petrochemical, and transportation industries because to its various benefits, including outstanding conductivity of thermal as well as electrical, strength, superior corrosion resistance, beautiful ductility, and resistance to metal- to-metal wears[1,8-11]. With the right choice of process variables, FSW may produce non-defective welds in pure copper[12,13]. Teimurnezhad et al.[14] examined the impact of change in depth of plunge of the tool shoulder with a thread less pin to understand the formation of different zones and material flow pattern in the copper welded joint. They found that the material on the retreating side had a key role in creation of the weld. Khodaverdizadeh et al.[15] discussed the impact of rotational rate and traverse velocity on hardening under strain behaviour of copper joints as well as microstructural changes and mechanical features. They observed that increased of tool rotational rate and decreased of traverse velocity resulted in retrenchment of density of dislocation and growth of grains in the stirred region and heat affected zone. Heidarzadeh et al.[16] reported the influence of FSW variables on both the tensile and elongation properties of pure copper joints. They obtained a synergic increase of strength and ductility by optimum welding condition. Bakkiyaraj et al.[17] examined the impact of variation of tool offset of aluminium-copper (Al-Cu) dissimilar FSW joint. They reported that the tensile property was nearly same to the Al parent material and small number of dimples and very few micro-voids were present in the fracture surface. Raju et al.[18] discussed the impact of tool rotational rate and welding velocity on pure copper joint by FSW. They achieved good mechanical properties by rotational rate at 900 rev min^{-1} and welding velocity at 40 mm min^{-1} as compared to other welding situations owing to adequate heat creation as well as suitable material mixing in the stirred region. Salahi et al.[19] reported the effect of variation of tool rotational rate and welding velocity on fracture morphology in friction stir processed annealed pure copper. They discovered that heat input regulated grain formation and that cavity development was reduced by more substantial deformation due to plasticity. Salahi et al.[20] studied the impact of rotating rate as well as welding velocity of fatigue behaviour of pure copper FSW. Due to heat distribution in the flow line, they got refined and equiaxed grains in the nugget region whereas coarse grains were found in the HAZ.

2. Physics of Friction Stir Welding Method

FSW is an environment friendly welding technology. It is also called green welding technology, because of no gases generated during the entire process. The procedure has been a completely solid-state one. As several benefits including good weld quality, no requirement for protective gas and formation of minimal welding distortion and residual stress, FSW have widely used in variety of constructions. **Fig. 1** is showing an illustrative diagram of FSW. Materials are connected at the atomic level via diffusion in the process,

and the state of the material changes to a semi-solid medium during welding. During the welding operation, the tool is very important parameter. The joining phenomenon takes place across two stages. At the first stage, the rotating tool produce heat by the frictional action mid the tool shoulder (tool probe) in addition the material of the work-piece. It leads to regional material destruction by softening the material until it is turn into semi-solid. In the next stage, the tool begins moving in the weld join line, the deform material from both sides of the work-piece come together and make a bond between them. As the tool travel from one place to another, the temperature begins to drop, the material's condition change to solid and also change in phases and grain structure phenomenon. The extreme temperature at a welding site never exceeds the material's melting point. Maximum 70- 80% of heat is produced of material's melting point during the FSW process. The rotational rate and welding velocity are the key parameters in generating friction that also responsible for heat development. It is also essential that the tool material is harder than the working material and can maintain its hardness throughout a greater temperature range. The flowing direction of material during the FSW method depends upon the pin profile of tool, depth of plunge, tool incline angle, offset of the tool.

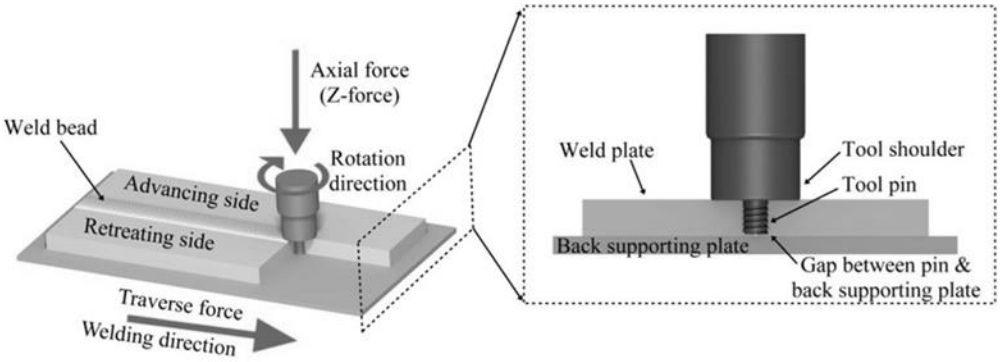

Fig. 1 Schematic representation of FSW[21].

3. FSW Experimental Details

In the FSW experiment, rolled sheets of pure copper (Cu) measuring 100 mm (length), 75 mm (breath), and 2 mm (thick) were used. The single pass butt weld joints were produced using a FSW tool which was not consumable manufactured of tungsten-carbide (WC) with a shoulder diameter of 16 mm and a non-threaded taper pin of 1.54 mm long, bottommost diameter of 5 mm, and top diameter of 4 mm. The FSW rotational rate, welding velocity, depth of plunge and offset of tool were fixed at 750 rev min^{-1}, 24 mm min^{-1}, 0.2 mm and 0 mm respectively. To fabricate the weld joints, three separate tool inclination angles of 1°, 2°, and 3° were employed. On a vertical milling machine, the FSW joints were manufactured. The experimental details have been shown in **Table 1**.

The welded joints were cut into pieces, which were then machined to the desired dimension. The samples for the metallographic investigation were cut perpendicular to the direction of welding, and they were polished using emery paper of a certain grade.

Polished samples were etched with 100 ml of H_2O, 25 ml of HCl and 5 gm of $FeCl_3$. Examination of the micro-structural characteristics was done using optical metallurgical microscope (Leica DM 2700M). The JEOL JSM IT500 SEM was used to examine the fracture surfaces and the welded nugget zone.

Table 1 Experimental Details.

Specimen No.	Tool rotating speed (rev min^{-1})	Welding velocity (mm min^{-1})	Offset of tool (mm)	Plunge depth (mm)	Tool incline angle (°)
C1					1
C2	750	24	0	0.2	2
C3					3

4. Results and Discussion

4.1 Microstructure analysis

Fig. 2 and **Fig. 3** shows the nugget zone (NZ) microstructure by optical microscope (low magnification- 100x) and SEM (high magnification- 2500x) of the friction stir welded joints of various tool incline angle and base metal.

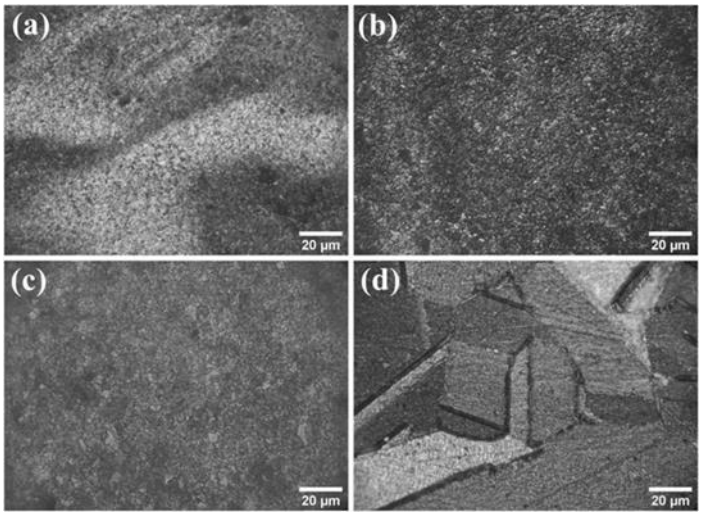

Fig. 2 Microstructure of NZ, a.-c. specimen C1-C3, d. base metal.

Due to dynamical re-crystallization and a cooler welding atmosphere, the NZ contained much less equiaxed grains compared to the BM (**Fig. 2d**). The microstructures of NZ are shown in **Fig. 2a – Fig. 2c** at different tool incline angles (1, 2, and 3). Furthermore, it is observed that grains development at the NZ are more refine and uniform during the welding at 2° tool incline angle.

Table 2 Grain size in NZ of FSW pure Cu.

Specimen No.	Grain size (μm)	
	NZ	BM
C1	3.818	19.60
C2	3.112	
C3	3.484	

At various tool inclination angles (i.e., 1, 2, and 3), **Fig. 3a – Fig. 3c** compared the SEM images of the NZ with those of the BM (**Fig. 3d**). In NZ, grain analysis has been carried out using ImageJ software. Table II shows the summary of grain size of various tool inclination angles (i.e., 1, 2, and 3) and BM. It is observed that from the **Table 2** that the average grain size is reduced when the tool incline angle rises from 1 to 2, but further increased of tool tilt angle from 2 to 3 the grain size increased. The average grain size of NZ of specimen C1, C2, C3 and BM are 3.818 μm, 3.112 μm, 3.484 μm and 19.60 μm respectively. From **Table 2**, it is observed that the average grain sizes at NZ are more refining compare to the BM. It is due to the stirring action of the tool pin at the NZ. Furthermore, it also seen that increasing tool incline angle of certain amount, the average grain refinement of the NZ is improved accordingly.

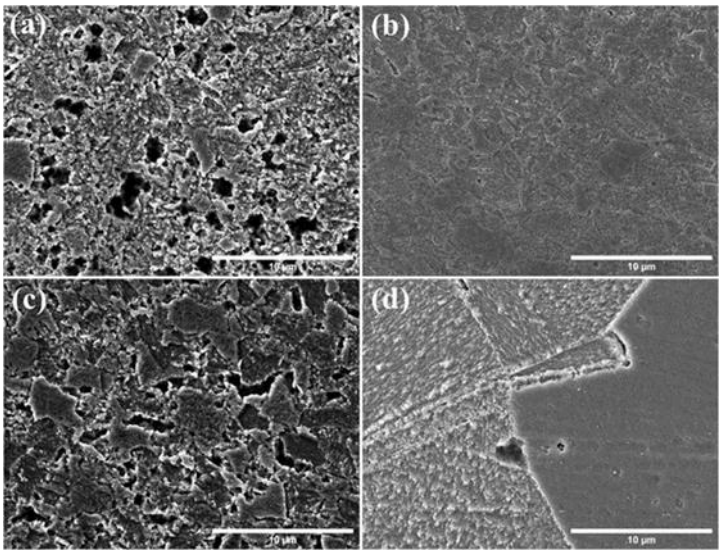

Fig. 3 SEM of NZ, a.–c. specimen C1-C3, d. base metal.

4.2 Fracture morphology

The SEM images of fracture surface with changed welding condition, such as tool incline angle 1, 2, and 3 are shown in **Fig. 4a**, **– Fig. 4c** correspondingly. From the **Fig. 4c**, it is found that fracture surface of weld specimen C3 (tool incline angle 3°) is similar to the BM (**Fig. 4d**). Also, the sizes of the dimples are higher comparing with the other welding

conditions. This directly indicates the modes of fractures are in ductile manner. It is owing to the heat generation at the stirred region with welding condition of 3 is comparatively maximum with the others welding condition. Furthermore, in the **Fig. 4a**, the size of the dimples is deteriorated which is clear evidence of lower and sufficient heat at tool incline angle (1). In addition, further increase in tool incline angle (2) the grain refinement is more superior (**Fig. 3b**). This leads to smooth and smaller dimples formation in fracture surface as shown in **Fig. 4b**. **Table 3** represents the fracture mechanism of the weld specimen at different weld conditions. The fracture of weld specimen C3 is caused by a sliding mechanism, whereas the fracture of weld specimens C1 and C2 is caused by Micro-void Coalescence.

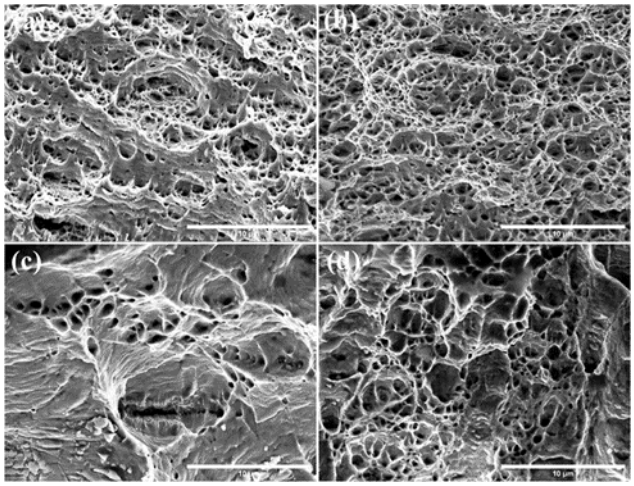

Fig. 4 SEM images of Fracture, a.–c. specimen C1-C3, d. base metal.

Table 3 Fracture characteristics and mechanism.

Specimen No.	Fracture Characteristics	Fracture Mechanism
C1	Small Dimples	Micro-void Coalescence
C2	Smooth and Small Dimples	Micro-void Coalescence
C3	Big Dimples	Slipping

5. Conclusions

The conclusions of above studies are follows:

1. The grains formation at the NZ are more refine and uniform during the welding at 2° tool incline angle (specimen C2) other than 1° (specimen C1) and 3° (specimen C3) tool incline angle.

2. The average grain size of NZ of specimen C1, C2, C3 and BM are 3.818 µm, 3.112 µm, 3.484 µm and 19.60 µm respectively.
3. The fracture characteristics of specimen C1, C2 and C3 are small dimples, smooth and small dimples and big dimples correspondingly.
4. The fracture of weld specimen C3 is caused by a sliding mechanism, whereas the fracture of weld specimens C1 and C2 is caused by micro-void coalescence.

Acknowledgement

Authors recognized and thank NERIST, India and NITTTR, India for necessary help in the present work.

References

1. DM Rodrigues, A Loureiro, C Leitao, RM Leal, BM Chaparro, P Vilaça. Mater. Des. 2009; 30: 1913–1921.
2. A Gerlich, P Su, M Yamamoto, TH North. J Mater. Sci. 2007; 42: 5589–5601.
3. RM Leal, C Leitão, A Loureiro, DM Rodrigues, P Vilaça. Mater. Sci. Forum 2010; 636–637: 637–642.
4. RK Nath, P Maji, JD Barma. JOM. 2021; 73: 1774–1785.
5. HA Derazkola, M Elyasi. J Manuf. Process. 2018; 35: 88–98.
6. Y Zhang, YS Sato, H Kokawa, SHC Park, S Hirano. Mater. Sci. Eng. A. 2008; 485: 448–455.
7. T Saeid, A Abdollah-zadeh, H Assadi, F Malek Ghaini. Mater. Sci. Eng. A. 2008; 496: 262–268.
8. CJ Kunding KJA, in: KM (Ed.). Mech. Eng. Handb. 3rd ed. Wiley, New Jersey. 2006; pp. 117–220.
9. H Lipowsky, E Arpaci, in: Copp. Automot. Ind. Wiley-VCH, Germany. 2007.
10. A Durocher, D Ayrault, C Chagnot, M Lipa, W Saikaly, J Nucl. Mater. 2007; 367-370: 1208–1212.
11. A Kumar, LS Raju. Mater. Manuf. Process. 2012; 27: 1414–1418.
12. GM Xie, ZY Ma, L Geng. Scr. Mater. 2007; 57: 73–76.
13. T Sakthivel, J Mukhopadhyay. J Mater. Sci. 2007; 42: 8126–8129.
14. J Teimurnezhad, H Pashazadeh, A Masumi. J Manuf. Process. 2016; 22: 254–259.
15. H Khodaverdizadeh, A Mahmoudi, A Heidarzadeh, E Nazari. Mater. Des. 2012; 35: 330–334.

16. A Heidarzadeh, ÖM Testik, G Güleryüz, RV Barenji. J Manuf. Process. 2020; 53: 250–259.

17. M Bakkiyaraj, SS Bernard, G Saikrishnan, S Guruyogesh, TG Guruprasanna, K Dineshkumar. Mater. Today Proc. 2020; 43: 824–827.

18. LS Raju, A Kumar, SR Prasad. Appl. Mech. Mater. 2014; 592–594: 499–503.

19. S Salahi, V Rezazadeh. World Appl. Sci. J. 2013; 23: 54–58.

20. S Salahi, GG Yapici. Procedia Mater. Sci. 2015; 11: 74–78.

21. RK Nath, V Jha, P Maji, JD Barma. Int. J Adv. Manuf. Technol. 2021; 113: 691–703.

Thermo-Fluid

Oil & Gas Facility Compressor Dry Gas Seal System Contamination Failure and its Mitigation

Dilip Kr Singh[a], Arpan Kr Mondal[b], Alice Atkins[c], Rashad Shikhalibayli[d], Priyanshu Singh[a]

Abstract

Dry gas seal system develops to solve the process contamination, catalyst poisoning with oil, loss of control of seal oil system or seal oil pumps driven failures and Lube oil contamination with process gas. Dry gas seal system installation ongoing with new project as well as old compressor modification to overcome the issues. But Dry seal gas also found startup and post operational challenges of seal gas contamination and condensations due contact with process gas. In this research and experimental work provide the mitigation by implementing API 692-part 4 standard. The dry gas seals reliability depends strongly on a system that assures a steady flow of clean and dry gas into the seals chambers. In this experiment performed isopropyl alcohol flushing of flash gas and gas injection compressor dry gas seal system by using 99% concentration Isopropyl alcohol (IPA) with newly developed flushing skid. The skid develops for high flammability liquid handling and flushing of compressor dry gas seal system. The maximum Reynolds number 44076 achieved at 250 liter per minute flow with dynamic viscosity 0.002381389 kg/m second at 20 °C ambient temperature. The velocity achieved 10.8 ft/sec at maximum pipe diameter and lowest pipe diameter achieved 47.9 ft/sec which three times higher than the operational velocity. The higher the turbulence has effect efficient cleaning. Isopropyl alcohol has properties to absorb moisture and its vapor has flash point temperature of 12 °C which release in atmosphere by mixing with nitrogen gas mixing to avoid the fire. The Isopropyl alcohol flushing validated by API 692 Part 4 standard.

Keywords: Compressor dry gas seal system; Isopropyl alcohol flushing; Cleanness; Reynolds number; Dryness; Dew point temperature.

✉ Dilip Kumar Singh

dilipkr21@gmail.com

[a] Maulana Abul Kalam Azad University of Technology, Kolkata, 700064, India

[b] National Institute of Technical Teacher's Training and Research, Kolkata, 700106, India

[c] Durham University, Stockton Road, Durham, UK

[d] Azerbaijan state oil and industrial university, Baku, Azerbaijan

1. Introduction

In oil and gas facility the centrifugal compressor most important equipment to processes the producing oil, petroleum, petrochemical, and natural gas processing. The compressor package highly expensive and keeping standby compressors have never been placed, even though its critical for smooth operation. The first compressor dry gas seal was developed and patented by Mr. Ring in 1951 and 9152 the first applications of dry gas seal was designs. In 1968, John Crane Inc. issued a patent and field applications began in 1975. Dry gas seal technology development has brought to avoid the wet seal problems experienced with centrifugal compressors, which are process contamination and catalyst poisoning with oil, Seal oil leakage cause loss of control of seal oil system or seal oil pumps failures and Lube oil contamination with process gas etc.

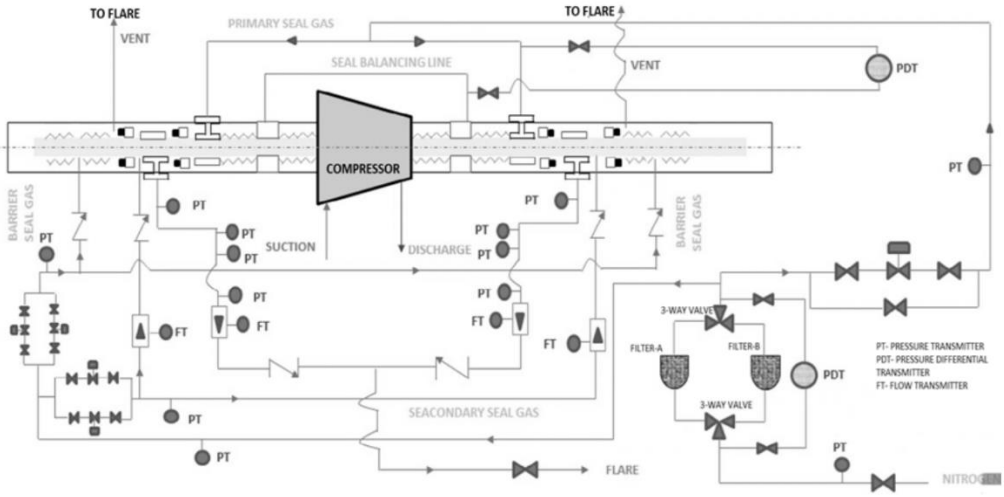

Fig. 1 Schematic of compressor primary and secondary seal gas system.

Now the dry gas seal technology is widely available on most of the manufacturers and implemented to both new installation and old compressor. The centrifugal compressors are equipped with dry gas seal system to seal the process gas within the compressor. Once the seal leakage monitored provide indication of high leakage which indicates the seal failure, with immediate effect shut down the compressor to avoid possible damage of equipment, environment, and personnel. It's becoming health and safety challenge. Manufacturer installed and located the monitoring device on both the driven and non-driven ends of the centrifugal compressor. Centrifugal compressor consists of a rotating hard face mating ring and a stationary primary ring in soft material. During the operating stage, the spiral grooves draw the seal gas towards the centre and create gas film pressure to separate the faces. There are three main types of dry gas seal system for turbomachinery applications, which are single, double, and tandem seals. The tandem seal is widely implemented in the turbomachinery compared to single and double seal in oil and gas industry. The tandem dry gas seal system consists of primary and a secondary seal with 3 μm cartridge filter unit as shown in the **Fig. 1.** The pressure breakdown occurs

on the primary seal faces and usually supplied from the discharge side of the compressor. The secondary seal normally operates at lower pressure than the primary seal and it's designed to control the full pressure when the primary seal gets failed. Even though a small amount of the sealing gas passes through the primary seal, and it's routed to the flare system. As per the **Fig.1**, secondary seal is supplied nitrogen gas as a separation gas. Dry gas seal system developed and utilized in both new installation and upgradation compressor to make the environment safe[1,2].

It's very known that oil & gas facility receive many harmful and dangerous gases with the sour gases or crude product from wellhead. Oil & gas refinery facility makes the various chemical process of these gases to remove the unwanted gases by using various equipment. Centrifugal compressors are used in petrochemical, chemical manufacturing processes and gas processing with transmission[1].

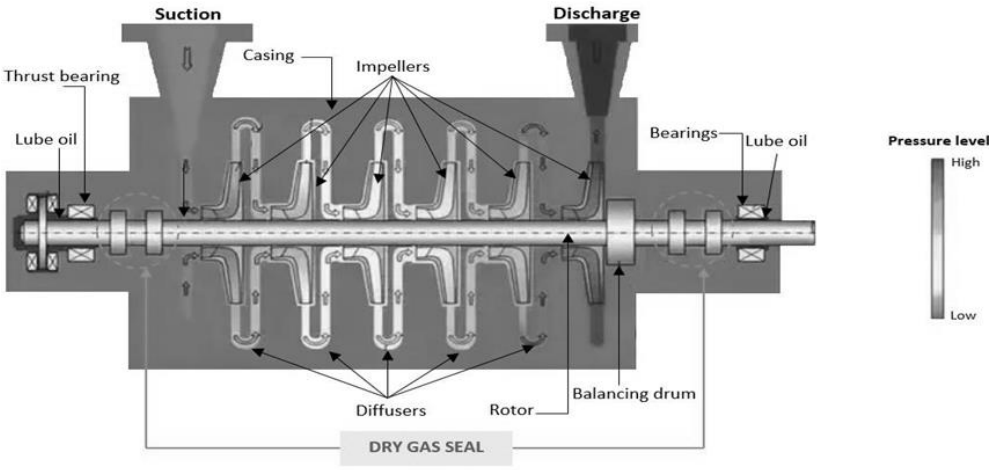

Fig. 2 Schematic of dry gas seal system.

The most important factor in ensuring dry gas seal reliability and avoiding situations that lead to high seal leakage is the high, it's about supplying quality gas to the seals. Many studies have been conducted on the causes of dry gas seal failure and all have identified that supplied gas get contaminated with the product as the primary cause[2]. The centrifugal compressor process with tandem dry gas seal setup shown in **Fig. 2**. If dry gas seals are failing well before their expected life, dirt or contaminants are the likely culprits. If the dry gas supply comes from the compressor discharge, look for a clogged filter. Inadequate seal gas filtration allowing particles smaller than 3 μm originating from the compressor casing will damage the seal faces. If your seal gas supply is nitrogen, which is typically clean and dry and doesn't require filtering, and maintenance has been done on the supply line, there's a small chance that dirt may have entered the piping and made its way to the seal. After any maintenance to a nitrogen supply line, personnel should ensure piping is cleared of metal bits, dirt, or other contaminants that could make their way into the seal chamber and damage dry seal faces[3,4]. We also recommend that the supply line be purged to atmosphere before supplying nitrogen gas to the seal.

In recent year, john crane sense developed for turbomachinery dry gas seal system monitoring and recording the data. The sensor connected with cloud servers for real time processing and provide alarm to the operation. John Crane Sense Turbo also developed digital solutions for industrial equipment to build a better understanding of asset health through the digitization of critical components. Many other manufacturers such as MAN ENEEGY and SEIMENS are developing the customize monitoring system by using pressure differential transmitter to confirm the gas leakage as shown in **Fig. 1**. Also, the customize equipment has mass flow meter, pressure control valve and other process instrument to monitored and the dry gas seal system health in DCS operation system. Apart of all monitoring devices the dry gas seal system gets failed due to contamination left into system or by process gas leakage[5,6].

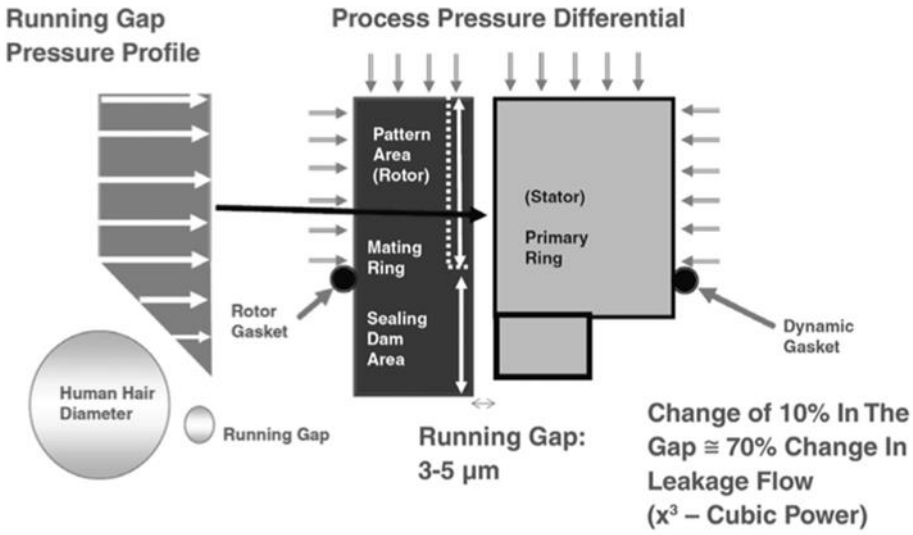

Fig. 3 Dry gas seal system contamination gap and leakage schematic.

The dry gas seal system contamination causes of dry gas seal failure by entering the foreign particle and passing into the seal running gap between the rotating and stationary rings causes the seal failure as shown in the **Fig. 3**. The seal gas supply through the filtration unit but due to start up cleanness process did not perform the inserted gas got contaminated[7,8].

The dry gas seal system affected mostly by contamination. The dry gas seals are worked by film of gas sealed the process product. The width of this film is few microns (0.000001 m), due to that gas filtering is utmost important. If a solid particle passes the filters and enters to the dry gas seal system, it will scratch the smooth surface. The gas pressure at seals is quite high and the gases can escape these scratches. As per API 614, The filters shall have a minimum efficiency of 98.8 % on particles less than or equal to 4 µm (beta ratio <= 85). The dry gas seal system cleaning is very important at pre-commissioning stage, otherwise contamination left into the system as shown in the **Fig. 4**. The **Fig. 4** contamination shows the pre-start up challenges found and recommend as per

API 692 Part 4 for isopropyl alcohol flushing. But the isopropyl alcohol is flammable liquid and flash point temperature 12 °C[9–12].

During a certain period of operation of compressor dry gas seal system, it's found slightly leakage of product gas and mixed with seal gas system due to foreign particle inters into primary seal and developed gap. After found these issues, the production facility shutdown for short period to perform the cleaning and maintenance. The post operational leakage confirmed during the cleaning of dry gas seal system and leakage shown in **Fig. 5**. The objective of this research work to developed equipment with safe methodology to perform the post operational and pre-start-up cleaning by using fluid medium isopropyl alcohol as per API 692 standard.

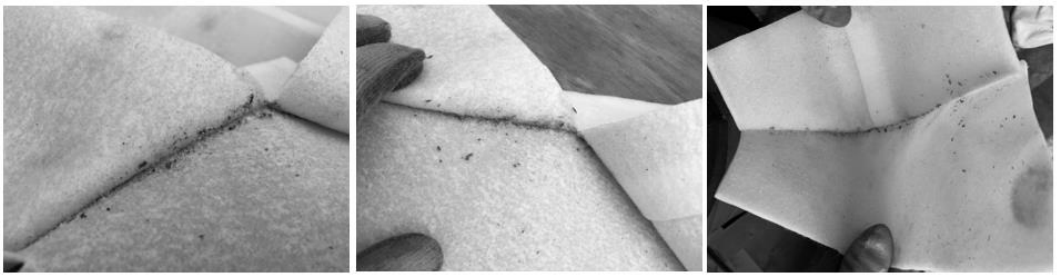

Fig. 4 Pre-start-up contamination of dry gas seal system.

Fig. 5 Post operational flushed filter bags bottom section.

The mitigation objective is very clear, and this research work provide the design of the skid and methodology to perform the isopropyl alcohol flushing safely. In this study safety of equipment, environment and people is very important due to fluid medium is highly flammable.

2. Experimental Setup

In this research work, design and developed the safe and compatible isopropyl alcohol flushing skid, which can handle flammable liquid. The skid made with 1000 litre capacity tank made of AISI 316 stainless steel grade with twin pot filter unit and flame proof centrifugal pump. The design model of the skid is shown in the **Fig 5**. The skid operates by variable flow device to control the flushing process parameters. The skid design including the safety devices such as Pressure safety valve, flame arrestor and pressure gauge etc.

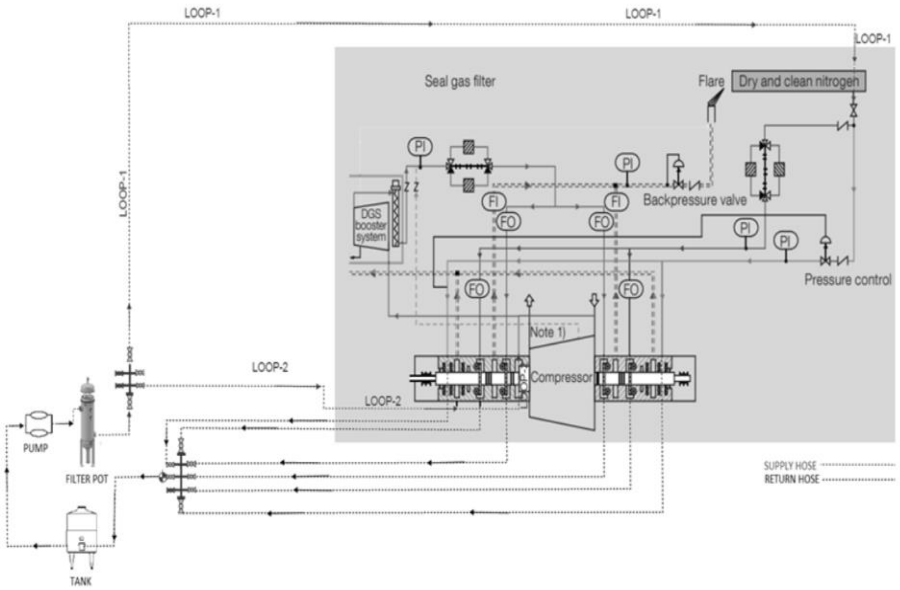

Fig. 6 Isopropyl alcohol flushing skid drawing.

The equipment design and developed as per the drawing shown in **Fig. 6** and perform the necessary testing to confirm the integrity. After successful development and testing, the necessary function test performed and confirm the compatibility.

The process parameter design based on the three variable parameters at three level, shown in the **Table 1**. The design of experiment developed based on Taguchi and creates L9 orthogonal array. The isopropyl alcohol properties shown in the **Table 2**.

Table 1 Design of experiment.

Parameters	Code	Level 1	Level 2	Level 3
Flow meter (m^3/ hr)	A	9	12	15
dynamic viscosity (kg/m hr)	B	11.678	9.98	8.573
density (kg/m^3)	C	795	791	786

Table 2 Isopropyl alcohol physical data at various temperature.

Temperature	Density	Specific heat (Cp)		Dynamic viscosity	
(°C)	(kg/m^3)	(J/kg.K)	(kcal/kg.°C)	(Pa.s)	(kg/m.h)
10	795	2443	0.584	0.003244	11.678
15	791	2502	0.598	0.002772	9.98
20	786	2562	0.612	0.002381	8.573

The experimental activity performed based on the Taguchi design of experiment shown in **Table 3**. The variable process parameters are flow, density and fluid viscosity. The isopropyl alcohol flushing performed based on the **Fig. 7** markup drawing. At first need to perform the temporary rig up with the newly developed flushing skid to the dry gas seal system and perform the gross leak test to confirm the system is leak free by snoop bubble test. This type of flushing should not have any temporary setup or and system joint leak due the high flammability flushing medium. After completion of Gross leak test proceed with nitrogen gas purging to confirm the system loop flow in correct direction. All the flange joint and temporary skid connect with earthing cable to avoid the electrostatic charge generation to develop any fire. Once nitrogen gas purging completed then depressurize the system at ambient condition and fill the isopropyl alcohol to the temporary skid and make circulation internally to confirm the cleanliness of the temporary skid and its connection. Start the dry gas seal system flushing as per the markup drawing shown in **Fig. 7**. Continue the flushing in closed loop circulation and monitor the flow, pressure, and maintain the velocity to achieve the desire Reynolds number (turbulence) to confirm efficient flushing[13-16].

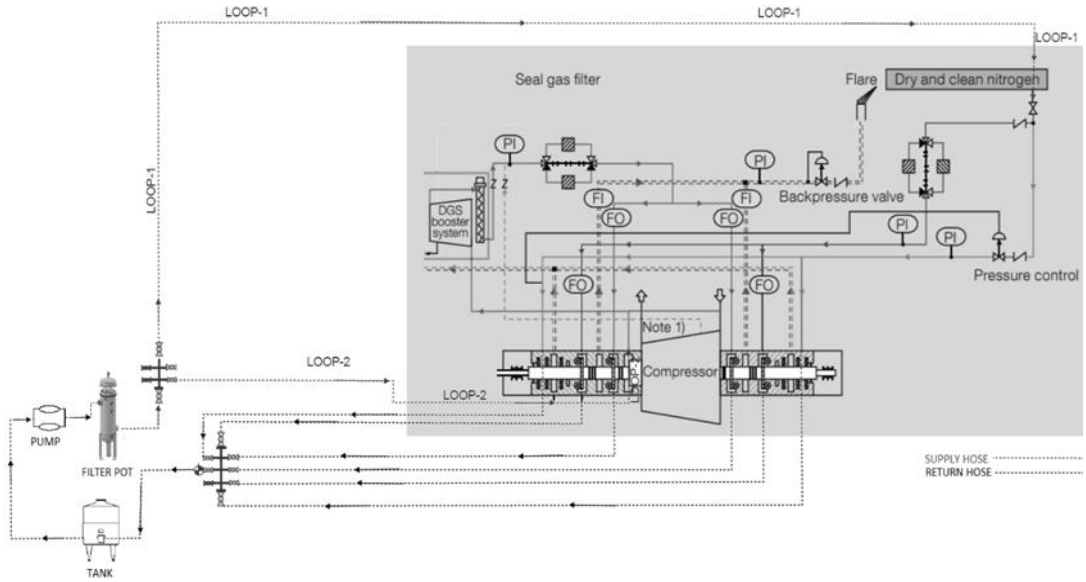

Fig. 7 Isopropyl alcohol flushing skid drawing.

The estimated Reynolds number based on the maximum pipe diameter shown in Table 3. The maximum flow can flow through the smallest pipe size (3/4") is 250 liter per minutes which developed 5.5 barg back pressure. The smallest pipe diameter not able to enhance the flow due to higher back pressure. In this experiment, the temporary skid has installed 1-micron polypropylene filter bag to perform the fluid filtration and remove the dirt's from the system. As per the API 692 standard, 99% concentrated isopropyl alcohol selected for the compressor dry gas seal system flushing and its physical properties shown in **Table 2**. In this experiment, isopropyl alcohol flushing performed for flash gas compressor and gas injection compressor dry gas seal system successfully. The experiment conducted based Taguchi L9 orthogonal array shown in **Table 3**.

After completion of flushing as per the above design of experiments, the dry gas seal system purge by nitrogen gas to remove the leftover alcohol and dry the system. The system dryness is very much important and must achieves -30-degree Celsius dew point with relative humidity less than 0.3, which is measured by Vaisala DM70 Handheld Dewpoint Meter for Spot-Checking Applications. In the experiment nitrogen gas purging perform by using potable nitrogen cylinder rack. Also, before the system start up, nitrogen gas purge and line up the dry gas seal system[17].

Table 3 Dry gas seal system isopropyl alcohol flushing L9 orthogonal array.

Run	**Control factors and level**			**Flow meter (LPM)**	**Dynamic viscosity ($\times 10^{-3}$ kg/m.sec)**	**Density (kg/m^3)**	**Pipe diameter (m)**	**Max. pipe area (m^2)**	**Velocity (m/sec)**	**Reynolds number (Output)**
	A	B	C							
1	1	1	1	150	3.243889	795	0.04	1.256×10^{-3}	1.9904458	19512.437
2	1	2	2	150	2.772222	791				22717.409
3	1	3	3	150	2.381389	786				26278.622
4	2	1	2	200	3.243889	791			2.6539278	25885.682
5	2	2	3	200	2.772222	786				30098.413
6	2	3	1	200	2.381389	795				3543.9363
7	3	1	3	250	3.243889	786			3.3174098	32152.570

8	3	2	1	250	2.772222	795				38053.815
9	3	3	2	250	2.381389	791				44076.314

3. Results and Discussion

The compressor dry gas seal system pre-startup flushing performed based on the plant operational team feedback due to dry gas seal failure. The operational input shows the dry gas seal contamination and condensation form due to process product contact. In similar way worldwide many oil & gas operations teams provide their feedback to American petroleum Institute for standard update which modified version is API 692 Part 4 standard[18]. In this experiment, we performed flushing to achieve highest level of turbulence to clean the system efficiently.

The compressor dry gas seal system cleaning performed based on the modified version of API 692 Part 4 standard[4]. In this experiment, we performed flushing to achieve highest level of turbulence to clean the system efficiently and the maximum turbulence achieved at maximum flow rate of 250 litre per minute. The velocity achieved 10.8 ft/sec at maximum pipe diameter and lowest pipe diameter achieved 47.9 ft/sec which three times higher the operational gas velocity 16 ft/sec[19-21]. The dry seal gas The Reynolds number estimation confirm the flow turbulences and efficient cleaning. Isopropyl alcohol is one of the moisture absorbents and make the system dry at the same time. The first cycle of flushing found dirt's which is collected on the 1 µm filter bags shown in **Fig. 8**.

After successful completion of second and third cycle of isopropyl alcohol flushing, filter bag inspected and found clean which shown in the **Fig. 9**. The objective of this research work to confirm the cleanness of the dry gas seal system to assures a steady flow of clean and dry gas into the seals chambers. After completion of draining, dry gas seal system piping and tubing purged by nitrogen gas to remove the left-over alcohol and dryness of the system achieved -30 °C dew point with relative humidity 0.2. The dew point measured on each flushed line by using potable Vaisala DM70 Handheld Dewpoint Meter.

The experiment of alcohol flushing validates and fulfil the dry gas seal system cleaning is based on API 692 Part 4 standard and achieved Velocity twice the maximum flow or turbulent flow. The achieved turbulent Reynolds number is 44076 which is higher than 3500 based on the API requirements. The filtration quality confirmed by the visual inspection of the filter gas shown in the **Fig. 9**. As per the API standard, the recommendation was to install a 400-mesh screen with 25 mesh backups in all seal gas, separation, and buffer gas supply lines, but we use 1-micron polypropylene filter bags which highly and better filtration capacity. The 400 mesh (0.037mm or 0.002 in.) screen

with 25 mesh (0.707mm or 0.003 in.) with screen images shown in **Fig. 9**[22-25]. The flushing activity validate the API standard.

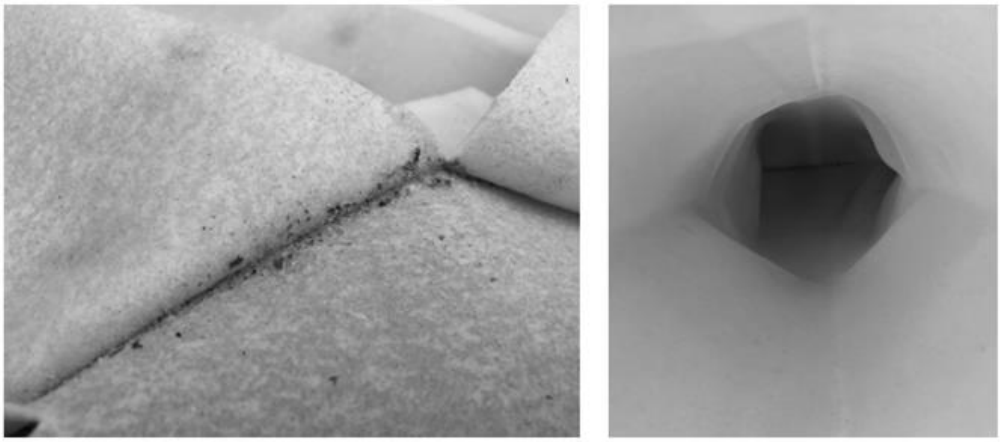

Fig. 8. 1st cycle flushing inspected filter bags condition.

Fig. 9. 2nd and 3rd cycle flushing Inspected Filter bags images.

4. Conclusions

From this research work shows the compressor dry gas seal cleanliness mitigation method. The 99% concentrated isopropyl alcohol flushing found successful. The experimental observations have been concluded below:

- The Isopropyl alcohol flushing of dry gas seal system cleanness achieved at maximum flow rate of 250 liter per minute and Reynolds number 44076.3.
- The selected 1-micron polypropylene filter bags found most suitable and high level of filtration quality to achieve the higher cleanliness in comparison of API 692 standard (400 mesh screen with 25 mesh).
- Based on the research, its recommended to install less 3-micron cartridge filter into the dry gas seal filter housing to avoid the contamination gap above 3 micron and make reliable trouble-free operation of dry gas seal system.
- For the start-up of dry gas seal system dryness achieved -30 °C with relative humidity 0.2 measured by Vaisala DM70 Handheld Dewpoint Meter.

Acknowledgement

The research work has been supported by Enermech OGP, Baku, Azerbaijan and thankful to Mr. Alan Newbigging and Mr. Anar Mehdiyev.

References

1. WE Forsthoffer. Forsthoffer's Best Practice Handbook for Rotating Machinery. Butterworth-Heinemann. 2011.
2. Z Guixiang, L Xiao, XX Yuan. Oil Gas Storage Trans. 2014; 3: 335-339.
3. M Lifang. Lanzhou Petrochem. Coll. Technol. 2010; 10: 7-9.
4. JS Stahley. Proc. 31st Turbomach. Symp. 2002; 145-152.
5. JS Stahley. 52nd Annu. Saf. Ammonia Plants Relat. Facil. Symp. 2001; 48.
6. American Petroleum Institute (API). Recommended Practice for Machinery Installation and Installation Design. API 686: 2nd Ed. 2009.
7. American Petroleum Institute (API). Dry Gas Sealing Systems for Axial, Centrifugal, Rotary Screw Compressors and Expanders. API 692: DRAFT.
8. DR Carter. Proc. 17th Turbomach. Symp. Turbomach. Lab. Tex. A&M Univ. Texas. 1988.
9. KE Atkins. RX Perez. Proc. 17th Turbomach. Symp. Turbomach. Lab. Tex. A&M Univ. Texas. 1988.
10. JR Dugas (Jr.), BX Tran, JF Southcott. Proc. 17th Turbomach. Symp. Turbomach. Lab. Tex. A&M Univ. Texas. 1991.
11. R FaneJli. Sulfur. Znd. Eng. Chem. 1949; 41(9): 2031-2033.
12. J Zaman, A Chakma. Fuel Process. Tech. 1995; 41: 159-198.
13. JS Chung, SC Paik, HS Kim, DS Lee, IS Nam. Catal. Today. 1997; 35: 37-43.
14. B Caudle, A Dyes. Improving Miscible Displacement by Gas-Water Injection. 1958.
15. A Davarpanah. Eur. Polym. J. 2018.
16. J Eastoe, MH Hatzopoulos, R Tabor. Microemulsions. In: Tadros, T. (Ed.). Encyclopedia of Colloid and Interface Science. Springer Berlin Heidelberg, Berlin, Heidelberg, 2013; 688-729.
17. Gas Processors Suppliers Association. Engineering Data Book, 10th Ed., Gas Processors Association, Tulsa, Oklahoma. 1987.
18. JS Stahley. Proc. 17th Turbomach. Symp. Turbomach. Lab. Tex. A&M Univ. Texas. 2001; 203-207.

19. SE John. Hal. 2002; 143-162.

20. RJ Latino, KC Latino. Root Cause Analysis Improving Performance for Bottom-line Results. 2nd Ed., CRC Press, Washington, D.C. 2002.

21. SO Uptigrove, PS Eakins, JE Sears. Dry Gas Seal Developments and Contamination Prevention. 1996; Vol. 2. IPC 1996-1986, International Pipeline Conference.

22. Flowserve Flow Division Solutions. Gaspac Compressor Gas Seals. Rev 11/99, Flowserve Corporation, Dortmund. 1999.

23. I Shahin. J Aeronaut. Aerosp. Eng. 2016; 5: 4.

24. W Yan, H Qiong, S Jianjun, W Da, Z Xiaoqing. Adv. Mech. Eng. 2019; 11(1): 1-12.

25. RJ Aimone, WE Forsthoffer, RM Salzmann. Dry Gas Seal Syst. 2007; 48(1): 20-21.

The adsorptive hydrogen storage in an activated carbon tank based on modified Dubinin-Astakhov model

Farheen Akhtar, Rajneesh Anand

Abstract

During adsorption cycles, the simulations of thermal effects play a significant role in designing adsorption-based systems such as gas separation, gas storage and heat pumps. This paper presents the two-dimensional axisymmetric model of a hydrogen storage tank on activated carbon at a particular temperature and pressure range using 'user defined functions' in Fluent (UDF). The adsorption model used for CFD analysis is based on mass, momentum and energy equations and the modified form of Dubinin-Astakhov model. The simulation is implemented through Ansys Fluent. The results are varied from pipe inlet to the tank wall based on mass flux at different flow times. The pressure and temperature profile inside the system for different inlet conditions is studied in detail. The contours of pressure and temperature profiles are plotted at different time intervals. The results obtained for the pressure and temperature profile show a good agreement with the other results available in the literature.

Keywords: Adsorption; Gas separation; User defined functions; Dubinin-Astakhov model

1. Introduction

An alternative source to the current fossil fuel-based energy system, a hydrogen energy vector, has been proposed to solve problems pertaining to environmental and energy distribution issues. A considerable amount of literature over the past few years deal with hydrogen storage, in which this remains an interesting research domain due to its low volumetric energy density under ambient conditions. Hydrogen can be stored in adsorbed/absorbed gas and liquid phases. So, there are four ways of storing hydrogen namely compression, liquefaction, adsorption in high surface nanoporous materials and metal hydrides[1]. Nanoporous materials which have high surface area such as activated carbon has been chosen as a storage media for hydrogen due to its light weight, reliability, safety, efficiency and low-cost adsorption material. Experimental and simulation studies have been carried out on the charging process of hydrogen storage tank in a packed bed of activated carbon at room temperatures. The adsorption of hydrogen on activated carbon in a steel container at a medium storage pressure of 10 MPa and room temperature of 295 K has been simulated by[2]. However, the discharging[11]

[11] ✉ Rajneesh Anand

rajneesh.1491981@gmail.com

National Institute of Technology Durgapur West Bengal, 713209, India

and dormancy process was not considered in their simulation. The design of efficient systems must take into account the heat generated and energy effects associated with the adsorption process.

The sorption characteristics in the micro-nanopores can be illustrated by the micropore filling theory. In a general perspective, it is credited that the pore size and the radius of curvature don't alter the sorption characteristics of gas molecules in relatively large pores. However, 'capillary condensation' transpires in gas molecules under supercritical conditions. In this case, the single-layer or multi-layer sorption theory cannot portray the existing state of gas in pores. Therefore, the shortcomings of the single-layer or multi-layer sorption theory can be concocted by the micropore filling theory[3,4]. The sorption characteristics of hydrogen and methane in high-surface activated carbon were deliberated by[5-7].

In order to define the adsorbed phases in energy and mass balance equations, a proper functional representation of the adsorption data of the system is necessary. The fitting of modelled data of adsorption isotherm to experimental data determines the pressure and temperature dependent operating parameters. Hence, the understanding of fitting accuracy is critical for adsorbate or adsorbent systems using thermodynamic simulations. The modelling of adsorption in microporous adsorbent at high ranges of pressure and supercritical temperatures has been thoroughly studied which is based on excess adsorption and Dubinin-Astakhov (D-A) model[8]. The energy and mass balance equations have been established for adsorption of hydrogen on activated carbon over a wide range of operating conditions in the supercritical region. The assumption of the perfect gas is discussed instead of a specific volume of the adsorbed phase for the evaluation of thermodynamic properties. The adsorption isotherms for gas as a function of pressure and temperature obtain the adsorbed phase distribution in the balance equations. For this purpose, the modelling of excess hydrogen adsorption isotherms has been adapted from the Dubinin-Astakhov (D-A) model at high pressure and over a wide range of supercritical temperatures. The excess adsorption data is converted to absolute adsorption by using a constant microporous (V_a) and adsorption volume[8].

The objective of this work is to simulate the hydrogen adsorption on activated carbon computationally from charging to discharging and research the variations of temperature and pressure at various time intervals. The CFD model is based on mass, momentum, and energy equations and adsorbed hydrogen in a steel tank wall. The adsorption model is based on a modified Dubinin-Astakhov (D-A) adsorption equation. User Defined Functions are hooked into the Fluent software to modify the energy and mass equations and to set the boundary conditions.

2. Computational Fluid Dynamics Model

The Dubinin-Astakhov (D-A) model has been particularly adapted to describe the subcritical gas pore filling in microporous adsorbents in activated carbons. The absolute adsorption isotherm is given by the following expression:

$$n_a = n_{\max} \exp\left[-\left[\frac{RT}{\varepsilon}\right]^m \ln^m\left(\frac{P_0}{P}\right)\right] \tag{1}$$

Where n_{max} is the maximum adsorption measured in mol.kg^{-1}, R is the universal gas constant and equal to 8.314 J mol^{-1} kg$^{-1,}$ the exponent m is preferentially set to 2 for most activated carbons, P_0 and P, are the saturation pressure (1470 MPa) and equilibrium pressure respectively. The temperature-dependent characteristic free energy term, ε is defined as the summation of an enthalpic factor, α (3080 J mole^{-1}), and of an entropic factor βT, (18.9 J mol^{-1}K^{-1}).

$$\varepsilon = \alpha + \beta T \tag{2}$$

The hydrogen is transferred from the gas phase to the adsorbed phase in the charging state while in the discharging state, these are transferred from the adsorbed to gas phase. So, the mass source term must be added to a mass conservation equation to define the change of phases. The mass source term is expressed as:

$$S_m = -\left(1-\varepsilon_b\right)\rho_p M\, \partial n/\partial t \tag{3}$$

where ε_b is the bed porosity, ρ_p is the activated carbon particle density (kg m^{-3}) and M is the molecular mass of hydrogen. The Linear Driving Force (LDF) model calculates the factor $\partial n/\partial t$. The rate of adsorption of LDF is given as:

$$\partial n/\partial t = k\left(n_a - n\right) \tag{4}$$

Where n_a is the absolute adsorption calculated by the D-A model and k is the mass transfer coefficient with a value of 0.15 s^{-1} and respectively. Then by substituting the value of $\partial n/\partial t$ from Eq. (4) into Eq. (3) we get:

$$S_m = -\left(1-\varepsilon_b\right)\rho_p M k\left(n_a - n\right) \tag{5}$$

Eq. (4) can be transformed into eq. (6) by finite difference method.

$$n_i = n_{i-1} + k\left(n_{a_{i-1}} - n_{i-1}\right)\left(t_i - t_{i-1}\right) \tag{6}$$

The energy source term of the energy conservation equation can be expressed as:

$$S_h = -\Delta H S_m / M \tag{7}$$

The following equation obtains the heat of adsorption:

$$\Delta H = \alpha \sqrt{\ln\left(n_{\max}/n_a\right)} \tag{8}$$

In this work, the entrance temperature of the hydrogen gas is kept at 301.5 K during charging. The initial pressure and temperature are set to 32000 Pa and 301.5 K respectively. The heat transfer coefficient is taken as 36 $Wm^{-2}k^{-1}$.

Geometry model and parameters

The geometry model and meshing of the hydrogen tank is shown in **Fig. 1a** and **Fig. 1b** respectively. The grey area corresponds to the pipe, while the tank is packed with activated carbon in a steel wall container. The grid of the hydrogen storage tank has 94105 nodes. The hexahedral mesh is considered here with a number of elements. The model dimensions are given in **Table 1**. The thermal properties of hydrogen activated carbon and steel is represented by **Table 2**.

Table 1 The model parameters.

Tank inner radius	46.9	Pipe inner radius	3.8
Tank length	350	Pipe length	50
Tank wall thickness	3.9	Pipe wall thickness	1

Fig. 1. a. The geometry and b. Mesh of the hydrogen storage tank.

Table 2 Thermal properties of hydrogen, activated carbon and steel.

Properties	**Hydrogen**	**Activated carbon**	**Steel wall**
Density (kg m^{-3})	Ideal gas	517.6	7800
Specific heat capacity (J kg^{-1} K^{-1})	14700	820	460
Thermal conductivity (W m^{-1} K^{-1})	0.2	0.646	13

3. Results and Discussion

3.1 Pressure analysis

The sharp rise of storage tank pressure is observed in **Fig. 2** and this pressure reaches the maximum at the end of charging. When the hydrogen is adsorbed and compressed, a considerable amount of heat is released, which leads to a quick rise in temperature and pressure. The pressure drops slightly during the stage of dormancy. This is due to the decrease in temperature as the heat is transferred between the outside and the hydrogen storage tank, which ultimately results in pressure reduction. During the dormancy stage, the pressure drops sharply and reaches the minimum value at the end of discharge. The rapid decline of pressure occurs due to a decrease in the amount of gaseous hydrogen and the absorption of a large amount of heat in the hydrogen storage tank.

The contours of the pressure plot from charging to discharging is shown in **Fig. 3**. At 3 seconds, the pressure inside the computational domain increases till the end of the charging process. During the dormancy, the pressure slightly decreases and it decreases further at the end of discharging reaching a minimal value.

3.2 Temperature analysis

The simulation of temperature at different points is shown in **Fig. 4**. The heat transfer in the central area is relatively slow because it is far away from the wall. Meanwhile, the tank temperature is somewhat higher than that of charging hydrogen, that is why the charging hydrogen have a cooling effect to some extent. A better cooling effect is observed at the entrance. At the end of the charging, the temperature at point 0.1 m from the pipe inlet is the highest, and its difference with point 0.06 m is quite small. The highest temperature at 0.1 m from the inlet is achieved at 301.722 K during the charging process (2 seconds). The lowest temperature is 301.693 which is found at the end of discharging (8 seconds).

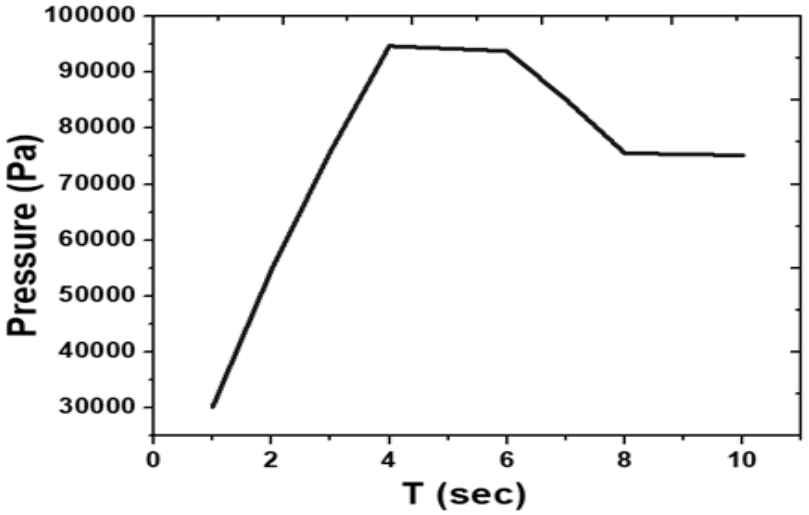

Fig. 2 Pressure simulation.

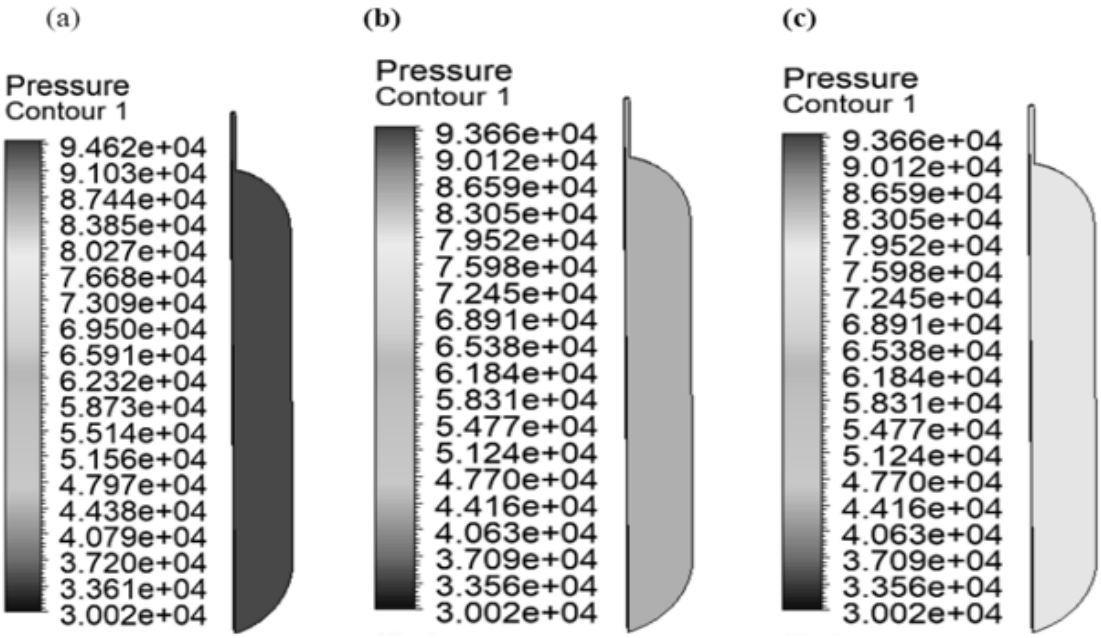

Fig. 3 Contours of pressure at a. 5 seconds, b. 8 seconds and c. 10 seconds.

With the adsorption and compression of hydrogen gas, a considerable amount of heat is released during the charging stage. The temperature rises at a distance of 0.06 m from the inlet is small because it is near the entrance and therefore, fresh filled hydrogen cools the area. The temperature at other points rises sharply during the process of charging. In the subsequent stages of dormancy, the temperatures at each point decrease sharply due to the large requirement of heat for the desorption and expansion process. The rise in temperature is observed which arises from a heat transfer between the hydrogen storage tank and outside after the discharging.

The addition of porous media into the tank leads to an increase in compression work and flow resistance especially at the charging stage. The amount of adsorbed hydrogen is more compared to that of compressed gaseous hydrogen.

The temperature at 0.1 m is more than at 0.06 from the inlet during the charging period due to the enhanced compression of the gaseous hydrogen. At a distance of 0.3 m from the pipe inlet, the temperature is almost close to the temperature at 0.1 m from the pipe inlet. This is due to the fact that both the points are close to the tank wall.

Fig. 5 reveals the contours of temperature variations at different time intervals. The temperature at the pipe inlet is small during the charging, and then it shows an increasing trend in the centre of the tank while the temperature reduces in the tank region at the end of discharging.

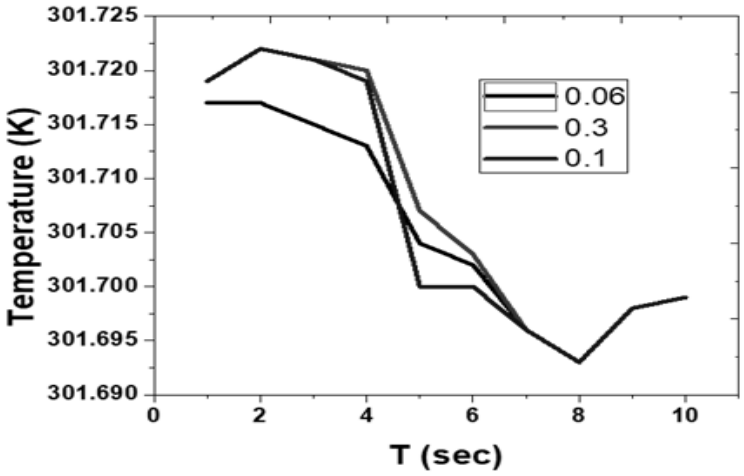

Fig. 4 Temperature simulation at different flow time.

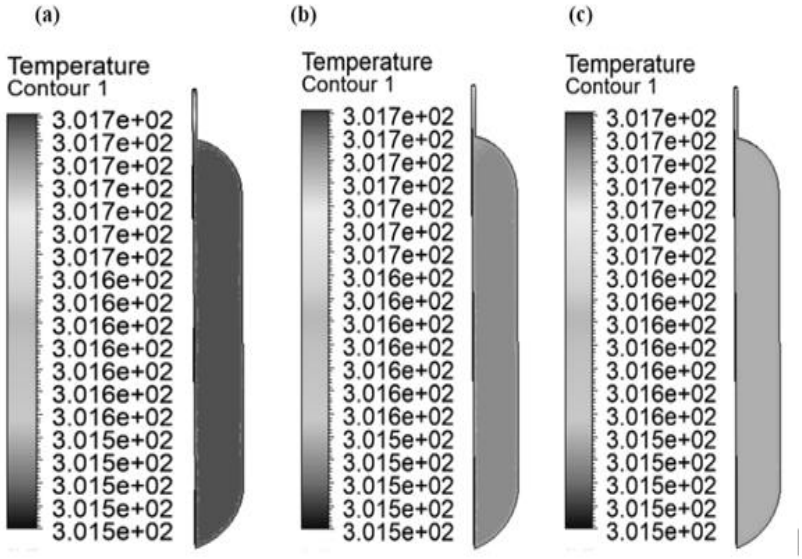

Fig. 5 Contours of temperature at a) 1 seconds b) 5 seconds c) 10 seconds.

4. Conclusions

The present work is based on the simulation of adsorption of hydrogen in an activated carbon tank. The geometric model is an axisymmetric one and the mass flux profile is established at the inlet with the help of User defined Functions. During the discharging process, the temperature at the central region is lower than that of the temperature of the central region during the charging process. During the charging period, the pressure increases sharply between one and four seconds then it drops slightly during the dormancy period. At the end of the discharging, the pressure reaches a minimum value. The adsorption amount is higher than that of the compression amount for gaseous hydrogen. The results for pressure and temperature profile are in a good approximation with the fluent data from the literature. Further work on this area will achieve great

progress by considering the effect of the porosity of packed bed during charging and discharging of adsorbed hydrogen.

References

1. G Hermosilla-Lara, G Momen, PH Marty, PL Neindre, K Hassouni. Int. J Hydrogen Energy. 2007; 32: 1542-1553.
2. JS Xiao, L Tong, CH Deng, P Benard, R Chahine. Int. J Hydrogen Energy. 2010; 35: 8106-8116.
3. MM Dubinin. Adv. Colloid Interface Sci. 1968; 2: 217– 235.
4. MM Dubinin, VA Astakhov. Russ. Chem. Bull. 1971; 20: 8– 12.
5. L Zhou, Y Zhou, M Li, P Chen, Y Wang. Langmuir. 2000; 16: 5955– 5959.
6. M Sudibandriyo. Int. J. Eng. Technol. 2011; 11: 79– 85.
7. BU Choi, DK Choi, YW Lee, BK Lee, SH Kim. J. Chem. Eng. Data. 2003; 48: 603– 607.
8. MA Richard, P Benard, R Chahine. Adsorption. 2009; 15: 43-51.

A Perspective on Energy Generation from Non-Conventional Sources

Uma Kumari, Pratibha Gupta

Abstract

Deterioration in fossil fuels is one of the pressing perturbations of the 21st century due to population explosion and high energy generation. In order to maintain such an imbalance between demand and energy supply resources has become a global perturbation and accordingly, the search for alternative fuel has been in research. Biofuels made from various lignocellulosic biomass could be valuable alternatives or complement fuel. The alteration of biomass to such pragmatic forms can be accomplished by number of physicochemical factors. The pretreatment aims to alter the physical and chemical structure of lignocellulosic biomass and enhance the conversion rate by evaluating various parameters. This review describes various a perspective on energy generation from non-conventional sources and a recent study reporting the use of these techniques to pretreat a variety of lignocellulosic biomass.

Keywords: Energy generation; Biofuels; Lignocellulose biomass; Pretreatment; Non-conventional energy source

1. Introduction

Population growth and mechanization have increased the demand for the use of petroleum products around the world. The search for surrogate fuels can offer a viable result to this global oil crisis[1]. Scientists from around the world have investigated various replacing energy sources that have the prospective to meet the growing energy hunger of today's population. Different categories and subcategories of biomass likely exist Varies in terms of energy production capacity[2]. The various biofuel energy sources investigated may be directly usable, whereas few needs to be formulated. Due to the widespread use of fossil fuels in different fields, the recent study focusses on evaluating the potential of using alternative fuels.

Overconsumption of petroleum resources as well as increasing demand for fossil fuels, there is a need of developing renewable resources for producing biofuels and biochemicals for sustainability and economic development. The lignocellulosic bioenergy industry has become a potential alternative to nonrenewable resources to offset the trend of increasing demand for petroleum fuel globally. This sort of bioenergy is the most abundant biopolymer present in nature. The global manufacturing of lignocellulosic[12].

biomass has been estimated at about 1.3×10^{10} tons/year[3,4]. The Lignocellulosic resources include (a) agricultural residues (palm stems, corn cobs, wheat straw, sugar cane bagasse,

[12] ✉ Pratibha Gupta
pratibhagupta2007@gmail.com

Department of Biotechnology, Radha Govind University, Ramgarh, Jharkhand, 829122, India

empty fruit bundles, corn straw, and coconut husks, etc.); (b) Forest residues (hardwood softwood, etc.); (c) Energy crops (switch grasses, lemongrasses, etc.); (d) Food wastes (e) Industrial waste and Municipal waste (waste paper and demolitions)[5]. Conversion of cheap biomass into value-added products by obtaining a 'carbon sink' from a 'carbon source' demonstrates that carbon may be fully utilized before releasing into the atmosphere. This technology is believed to convert the negative cost of biomass into a positive income[6]. The fractionation of lignocellulosic material into reactive intermediates such as glucose, cellulose, hemicellulose, and lignin are key procedure for development into biofuels, biochemicals, and other end products[7].

Conversion of lignocellulosic biomass to biofuels is more practicable option to improve energy reliability and reduce greenhouse gas emissions[8]. They burn cleaner and pure than fossil fuels and add no CO_2 to the atmosphere. As reported the greenhouse gas emissions can be reduced by 86%[9]. Lignocellulosic biomass such as agriculture wastes, forest wastes, and specialty crops are renewable energy sources. These Lignocellulosic raw materials are present in plentiful quantity and contains very low greenhouse gas emission. Plant materials stored in the form of cellulose, hemicellulose, lignin, and pectin is about 90% in dry weight. The lignin present in lignocellulose creates a protective barrier which can prevents fungi and bacteria from destroying plant cells for conversion to biofuel. The conversion of biomass into biofuel requires breaking down cellulose and hemicellulose to their corresponding monomers, so that they can be utilized by microorganisms. Hydrolysis process is commonly used to generate various sugars that are suitable for manufacturing ethanol[10]. Various microorganisms are used for the conversion of lignocellulosic biomass into sugar, but it requires a longer retention time. To overcome this problem Enzymatic hydrolysis process is widely used, which converts lignocellulosic biomass into sugar and then into ethanol[11].

In lignocellulosic material the digestibility of cellulose is hampered by physicochemical, structural, and compositional components. While converting biomass into biofuel, the lignocellulosic biomass must be treated to expose the cellulose of the plant fibers. Various techniques can be used in pretreatment process such as ammonia fiber blasting, chemical treatment, steam blasting, and biological treatment to change the structure of the cellulosic biomass and make the cellulose more attainable. Acids or enzymes may also be used to break down the cellulose into its sugar components. The pretreatment process aims to break down the lignin and crystalline structure of cellulose. After that acids or enzymes will hydrolyze the cellulose into sugar molecules and is further converted into biofuel[12]. The pretreatment process is a widely used and expensive process for the conversion of biomass into biofuel, but it increases efficiency by lowering the cost of production.

2. Structure of Lignocellulosic Biomass

Plant cell wall contain lignocellulose which is the primary building block. Plant biomass is commonly consisting of three polymers: Cellulose, hemicellulose, lignin (**Fig. 1**) and also contains small quantity of pectin, protein, extracts, and ash. Depending on plant species composition of these ingredients may vary. For example, hardwoods are high in cellulose, while straw and leaves are high in hemicellulose. On the basis of age, growth stage and other conditions in plants the ratios between various components may vary (**Table 1**)[13]. These polymers are associated with each other within the heterometric at varying degrees as well as relative compositions, depending on the type of biomass, species, and even source[14].

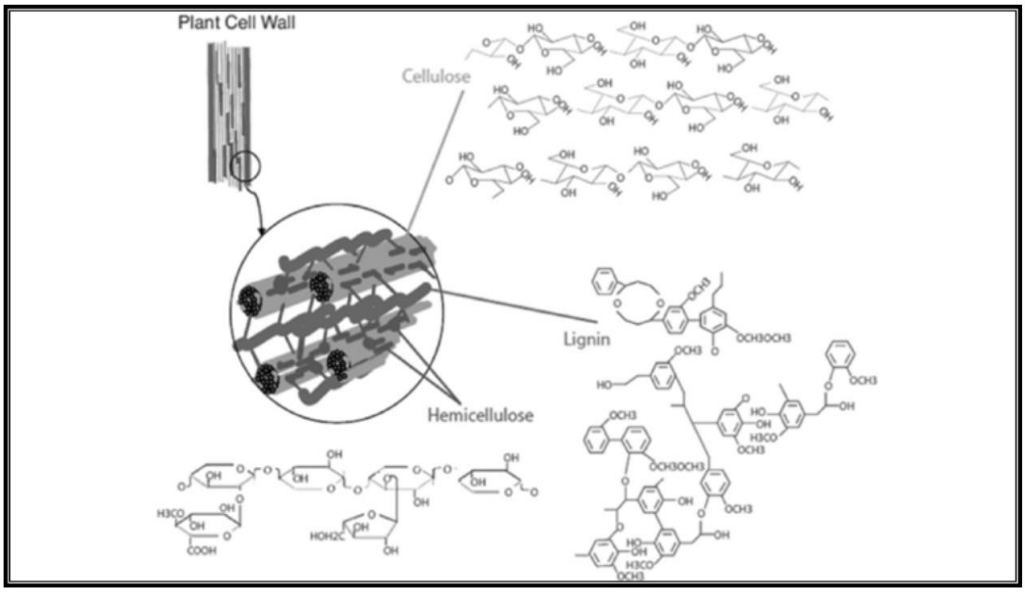

Fig. 1 Structure of lignocellulosic biomass[15].

Lignocellulosic materials require an aggressive pretreatment process to yield substrates that can be readily hydrolyzed by commercial cellulolytic enzymes or can also be hydrolyzed by enzyme-producing microorganisms to release sugars for fermentation. Cellulose is the main component of the plant cell wall to hold up their structure. When present as an unbranched homopolymer, cellulose is a polymer of beta-D-glucopyranose units linked in well-documented polymorphs by beta-(1,4)-glycosidic linkages[16]. Long-chain of cellulose polymers which are held together by hydrogen bond and van der Waals bonds. The microfibrils are wrap with hemicellulose and lignin. By the action of acids or enzymes on cellulose that disrupt beta-(1,4)-glycosidic bonds, the fermentable D-glucose is produced. Cellulose exists in both crystalline and amorphous forms in biomasses. Large fraction of cellulose chains forms microcrystalline cellulose but amorphous cellulose is formed from less fraction of disorganized cellulose chains[17].

The second most abundant polymer of plant cell wall is hemicellulose, comprising approximately 20-50% of lignocellulosic biomass. Chemically it is not uniform like cellulose and has branches with short side chains composed of distinct kind of monosaccharides. These sugars include pentoses, hexoses and uronic acids. The hemicellulose backbone can be either a homopolymer or a heteropolymer with short branches connected by beta-(1,4)-glycosidic bond or sometimes beta-(1,3)-glycosidic bonds. Hemicellulose may further exhibit some degree of acetylation, as with teroxylan. As compared to cellulose, hemicellulose has a low molecular weight and branches with short side chains that are susceptible to hydrolysis[18]. In agricultural biomass such as straw and grass, hemicellulose is mainly comprised of xylan, whereas in coniferous trees hemicellulose is mainly consist of glucomannan. Xylan is a heteropolysaccharide present in most of the plants with a backbone consist of 1,4-linked beta-D-Xylo pyranose units. Xylan can be easily extracted from an acidic as well as alkaline environment, whereas the glucomannan extraction requires a more alkaline condition. Amid the major constituents of lignocellulose, hemicellulose is thermochemically susceptible[19]. Hemicellulose is thought to "wrap" the cellulose fibers within the plant cell wall, and it is suggested that no less than 50 percent of the hemicellulose must be removed to remarkably enhance cellulose digestibility. Thus, for this purpose, stringent conditions of pretreatment are usually negotiated in optimizing sugar recovery. Based on different pretreatment process, hemicellulose conceivably obtained as a solid fragment or as an aggregate of both solid and liquid fractions[20].

Lignin is a third abundant complex molecular structure that contains cross-linked polymers of phenolic monomers. It is found in the primary plant cell wall and confers the structural support, impermeability, and resistance to attack from microorganisms. There are three phenyl propionic alcohols present as lignin monomers: coniferyl alcohol, coumaryl alcohol, and sinapyl alcohol. These phenolic monomers are linked together by alkyl-aryl, alkyl-alkyl, and aryl-aryl ether linkages[19].

Table 1 Biomass and its waste compositions[21].

Lignocellulosic materials	Cellulose	Hemicellulose	Lignin	Ash
Hardwoods				
Eucalyptus	43.25	22.5	25.0	1.6
Poplar	46.2	24.4	24.5	0.6
Softwoods				
Pine	43.6	24.9	25.6	0.7
Spruce	44.1	21.2	26.9	0.9
Forest residues				
Wood stems	42.6	22.3	37.7	
Bark, Pine	23.7	24.9	50.0	3.8

General residues	45.5	21.0	27.3	
Other lignocelluloses				
Corn stover	38.3	25.2	14.8	6.1
Sugarcane bagasse	37.3	35.8	20.1	5.7
Wheat straw	37.9	26.8	18.3	6.2
Switchgrass	37.1	31.2	8.5	6.3

3. Conversion of Biomass to Fuel

Primarily global energy consumption relies on conventional fossil fuels. However, such energy production has involved a spectrum of emissions that are linked with many human hazards[22]. Accordingly, energy generation from lignocellulosic biomass is an excellent option. Lignocellulosic biomasses available for energy production includes agroforestry wastes and residues, processed food waste, aquaculture, and industrial wastes, and other household wastes (**Table 2**). Lignocellulosic material has efficiency to generate energy that can be easily converted into any energy required by modern society. Biomass is estimated to be the 4th largest source of energy after nonrenewable energy (i.e., coal, natural gas, oil, etc.) and accounts for approx. 10 percent of the world's primary energy sources[23]. However, the succeeding potential of generating biofuel from biomass is highly dependent on the availability of growing areas.

Table 2 Classification of biomass[2].

Class	Category	Biomass
Woody biomass	Hardwood, softwood, branches, twigs, etc.	Alabama oak wood, Ailanthus, apple tree branches, olive twigs, etc.
Processed Waste	Trash, cake, bagasse, pod, etc.	Castor seed cake, pomegranate trash, potato peel, apple trash, cypress fruit press, orange peel, etc.
Grass		Wheatgrass, switch grass, esparto, sugarcane, switch grass pellets, cat grass, lemongrass, etc.
Leafy waste		Mango leaf, pine needle, potato plant trash, sugarcane leaf, tea leaf, tobacco leaf, etc.
Agricultural waste	Cob, pod, stalk, husk, plant trash, etc.	Barley straw, corn cob, maize cob, banana plant trash, corn straw, jawar straw, mustard stalk.

Today, only 0.19% of the world's 13.2 billion hectares of land is used to grow feedstocks for energy crops and biofuels. Meanwhile, only 0.5% to 1.7% of the world's crop land is used for growing resources for manufacturing of biofuel[24]. Biomass can be converted into biofuels by three major processes: Biochemical, Thermochemical, and Physicochemical. Anaerobic digestion (production of biogas and biomethane) and Fermentation (production of ethanol) is considered as a biochemical conversion process. Thermochemical conversion includes gasification, hydrothermal, incineration and pyrolysis treatment whereas extraction and esterification are considered under physicochemical transformations[25].

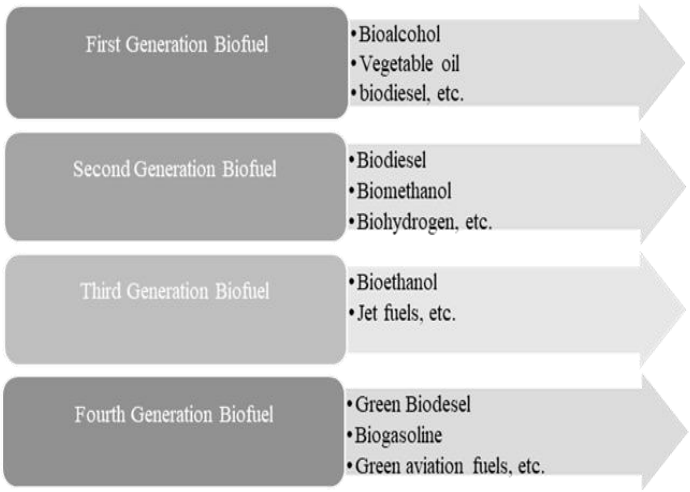

Fig. 2 Generations of biofuel[26].

Based on the type of raw materials available to produce biofuels, biofuels can be divided into three categories (**Fig. 2**). *First-Generation Biofuels* are related to biomass derived from comestible oils such as canola, soybeans, sunflowers, palm oil, coconut, and peanuts. Large-scale use of these feedstocks can have a significant impact on the world's food supply and is not considered sustainable or environmentally friendly[27]. *Second-generation biofuels* made from a variety of feedstocks that is from lignocellulosic feedstocks to municipal solid waste are called second-generation biofuels. In this sense, these biofuels are 'greener' as they can be produced and recycled from sustainable raw materials. At present, second-generation biofuels are in various stages of testing and are not widely available[27]. *Third-generation biofuels* refer to biofuels made primarily from algae. It has its high yield and low resource consumption compared to other commodities[27]. *Fourth-generation biofuels* aim to offer options by combining biofuel production and CO_2 capture and storage with the process of oxy-fuel combustion, or by applying genetic engineering and nanotechnology. The fourth-generation raw material contains modified organisms to strengthen biohydrogen production[28].

Depending on the chemical nature of bio-fuels, they are divided into different categories such as biodiesel, bioethanol, biohydrogen, and biomethane, etc. Biodiesel refers to

alternatives to diesel fuel made from renewable sources. A common method for the production of biodiesel is known as transesterification. *Biodiesel*s are made from variety of potential feedstocks such as recycled edible oils, microalgae, animal fats, and various oilseeds[29]. *Bioethanol* is emerging as a perspective source of biofuel production that have challenged the current energy insecurity and environmental security surrounding fossil fuels[30]. *Biomethane* is very famous for its high efficiency and clean burning properties as compared to all other biofuels available today. Almost any type of biomass can be used for manufacturing of biomethane. Feedstocks for biomethane production include manure from dairy and pig farms, residues from food processing and domestic organic waste, vegetable oil residues, etc.[31]. *Biohydrogen*- As we know hydrogen (H_2) is the most common as well as abundant element present in the universe. Although H_2 rarely occurs in nature as a free substance, it is readily found chemically bonded to any other elements. However, this conversion of biomass to hydrogen (H_2) is of particular interest because it is a way to use renewable energy to reduce greenhouse gas emissions[32].

4. Microbial Biofuel

Recently microbial biotechnology approaches are being explored to use microorganisms for producing different viable biofuels (i.e., alcohol, hydrogen, biodiesel, biogas, etc.) from different feedstocks, i.e., agricultural wastes, animal residues; another lignocellulosic biomass. Biodiesel production using microorganisms is considered a promising alternative to biodiesel production. Microorganisms such as microalgae, bacteria, fungi, yeast, etc. can incorporate intracellular lipids (primarily triacylglycerols) into a large proportion of lignocellulosic biomass. Oils from these oleaginous microorganisms are used as raw biomaterials for biofuel production using a transesterification process[33]. The fast-growing microbes are more potent and effective because they may use large types of feedstocks (such as sugarcane) that produce very high yields per hectare compared to canola seeds and biomaterials. Oleaginous microorganisms can also provide new lipid feedstocks for the biodiesel industry. Biofilm-forming microbes also play an important role in biofuel generation[34]. Oils are extracted from rapidly growing, stable microorganisms and transesterified with single-chain alcohols to produce high-quality biodiesel esters[35].

Biogas is formed from various metabolic pathways that are involved in anaerobic decomposition such as hydrolysis, acidogenesis, acetogenesis, and methanogenesis. Hydrolysis and methanogenesis are of great concern as they are related to the production of hydrogen and methane respectively. Hydrolysis of complex molecules occurs by the catalyzation of extracellular enzymes such as - cellulases, amylases, proteases, and lipases[36]. In general, the stabilization of organic residues occurs by hydrolysis, after which organic matter is simply converted into soluble forms that can further be utilized by microorganisms to produce H_2 and CO[37]. Although various group of microorganisms can be involved in the breakdown of organic substrates into volatile fatty acids

(*Actinomycetes*, *Thermonospores*, *Shewanella*, etc.), the major sources of methanogenesis come from *Methanbrevibacter* and *Methanosarcina*.

The biomass conversion into ethanol requires a microbial community that produces the enzyme cellulases to hydrolyze the lignocellulosic material. Enzyme-producing microorganisms for saccharification and fermentation of sugars are immobilized on stable surfaces to convert them to ethanol with high efficiency and low cost to generate large amounts of energy. By immobilizing enzyme-producing microorganisms on a stable surface, saccharification and fermentation of sugars to ethanol can be performed in a highly efficient and cost-effective manner. The microorganisms that play key role in ethanol-production can also perform major role in the decomposition of carcasses[38]. Like ethanol, butanol can be produced by microbial fermentation, through the fermentation of sugar, starch, or cellulosic feedstocks. Due to its benefits, biobutanol is an alternative to traditional fuels[39].

5. Pretreatment of Lignocellulosic Materials

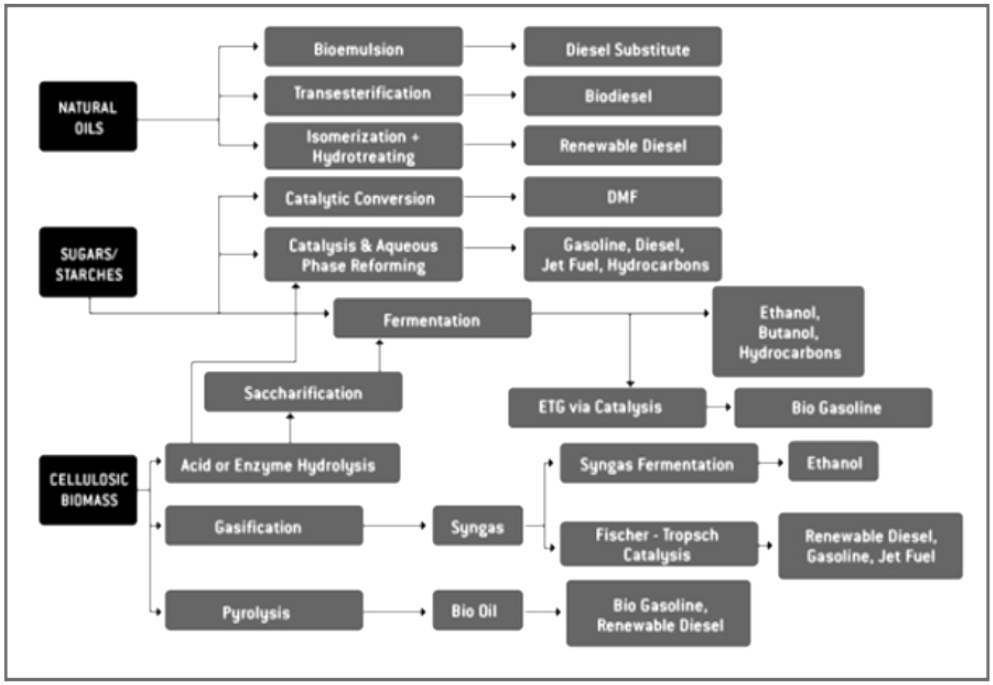

Fig. 3 Biofuel pathway[40].

The energy utilization from biomass requires a pretreatment process. It has been investigated previously that pretreatment can improve the energy utilization potential of biomass. It was also reported that physical or chemical pretreatments can have different effects on energy recovery (**Fig. 3**). Among many pretreatment methods, chemical pretreatment is said to have the most significant effect on increasing energy power generation potential[41]. Alkaline pretreatment causes swelling of biomass, causing depolymerization and degradation of structural bonds between lignin and cellulose.

Pretreatment under neutral conditions was also known to cause structural degradation of lignocellulosic materials[11]. Therefore, the pretreatment process significantly alters the elemental composition of biomass. However, the elemental composition is more significant for outlining the energy content of biomass and the potency of thermochemical conversion processes.

6. Conclusions

The present study formulates an innovative approach regarding the study of energy generation from non-conventional sources. As fossil fuel formation takes millions of years but biofuels made from lignocellulosic waste biomass can be formulated within a less period of time. Pretreatment of such non-conventional sources is needed for energy utilization. As the consumption of biofuels can reduce the use of fossil fuels as well as utilize the lignocellulosic waste biomass. These waste biomasses are more likely to be available at low cost and have a high sugar content that can be fermented into transportation fuels. The production of fuels derived from biomass such as biodiesel, biohydrogen, bioethanol, etc. using advanced conversion concepts is particularly promising as well as the use of residues in biofuel production helps reduce waste. Additionally, it destroys pathogens present in the waste. The main aspect of biofuels depends on their competitiveness against global agricultural policy and fossil fuels.

Acknowledgement

The authors acknowledge the Departments of Biotechnology and Research Cell of Radha Govind University, Lalki Ghati, Ramgarh, Jharkhand for providing the research facility.

References

1. MF Demirbas. Energy Convers. Manage. 2006.
2. R Roy, S Ray. Energy Sources Part A: Recover Util. Environ. Eff. 2019; 1-13.
3. JO Metzger, A Huttermann. Naturwissenschaften. 2009; 96(2): 279– 288.
4. GD Saratale, SE Oh. Afr. J Biotechnol. 2012; 11(5): 1002–1013.
5. Limayem, S. C. Ricke. Prog. Energy Combust. Sci. 2012; 38(4): 449–467.
6. WPQ Ng, HL Lam, FY Ng, M Kamal, JHE Lim. J Clean. Prod. 2012; 34: 57–65.
7. J Bozell, CJO Lenick, S Warwick. J Agric. Food Chem. 2011; 59(17): 9232–9242.
8. SC Yat, A Berger, DR Shonnard. Bioresour. Technol. 2008; 99: 3855–3863.
9. M Wang, M Wu, H Huo. Environ. Res. Lett. 2007; 2: 1–13.
10. J Iranmahboob, F Nadim, S Monemi. Biomass Bioenergy. 2002; 22: 401–404.
11. P Kumar, DM Barrett, J Delwiche, P Stroeve. Ind. Eng. Chem. Res. 2009; 48(8): 3713–3729.

12. M Galbe, G Zacchi. Adv. Biochem. Eng. Biotechnol. 2007; 108: 41–65.

13. CR Carere, R Sparling, N Cicek, DB Levin. Int. J Mol. Sci. 2008; 9: 1342–1360.

14. RP Chandra, R Bura, WE Mabee, A Berlin, X Pan, JN Saddler. Adv. Biochem. Eng. Biotechnol. 2007; 108: 67–93.

15. B Wang, YC Sun, RC Sun. J Leather Sci. Eng. 2019; 1: 5.

16. P Mckendry. Bioresour Technol. 2002; 83: 37–46.

17. L Laureano-Perez, F Teymouri, H Alizadeh, BE Dale. Appl. Biochem. Biotechnol. 2005; 121–124: 1081–1099.

18. BC Saha. J Ind. Microbiol. Biotechnol. 2003; 30: 279–2791.

19. AT Hendricks, G Zeeman. Bioresour. Technol. 2009; 100: 10–108.

20. GM Walkee. Ventus Publishing ApS. 2010; ISBN 978-87-7681-681-0.

21. Phyllis. ECN. 2012.

22. R Roy, D Debnath, S Ray. Arab. J Sci. Eng. 2022; 47(5): 5935-5948.

23. L Singh, ZA Wahid. J Ind. Eng. Chem. 2015; 21: 70-80.

24. A Faaij. Bioenergy. 2008; 32: 657-659.

25. N Paul, D Kemnitz. FNR. WPR Commun. Berlin. 2006; 43.

26. Vipparla, S Sarkar, B Manasa, T Pattela, DC Nagari, TV Aradhyula, R Roy. Springer, Singapore. 2022; 2: 239-257.

27. http://biofuel.org.uk .

28. K Goria, R Kothari, HM Singh, A Singh, VV Tyagi. Handbook of Biofuels. 2022; Ch. 20: pp 399-418.

29. J Sheehan, V Camobreco, J Duffield, H Shapouri, M Graboski, K Tyson. NREL, Golden, CO (US). 2000.

30. H Zabed, J Sahu, A Suely, A Boyce, G Faruq. Renew. Sustain. Energy Rev. 2017; 71: 475-501.

31. M Tabatabaei, A Sulaiman, AM Nikbakht, N Yusof, G Najafpour. Intech. Open. 2011.

32. N Gnanapragasam, B Reddy, M Rosen. Energy Convers. Manag. 2009; 50: 1915-1923.

33. X Meng, J Yang, X Xu, L Zhang. Renew. Energy. 2009; 34: 1-5.

34. UC Ghoshal, U Ghoshal, MM Rahman, A Mathur, S Rai, M Akhter et al. J Gastroenterol Hepatol. 2022; 37(3): 489-498.

35. G Vicente, LF Bautista, FJ Gutierrez, RA Rodríguez. Energy Fuels. 2010; 24: 3173- 3178.

36. RS Thompson. MS Thesis, USU, Utah. 2008.

37. L Nazari, Z Yuan, D Santoro, S Sarathy, D Ho, D Batstone et al. Water Res. 2016.

38. X Chen, Y Gu, X Zhou, Y Zhang. Bioresour. Technol. 2014; 164: 78–85.

39. H Alper, G Stephanopoulos. Nature Reviews. 2009; 7: 715-723.

40. http://advancedbiofuelsassociation.com/page.php?sid=2&id=24.

41. R Roy, S Ray. Arab. J. Sci. Eng. 2022; 47(5): 6311-6323.

Biomaterials

Methods and Techniques of Production and Environmental Impact of Biochar: A Review

Sambit Tarafdar[a], Sneha Paul[b]

Abstract

A variety of organic waste feedstock, including agricultural waste and sewage sludge, can be used to produce biochar, a carbon-rich material. Due to its large specific surface area, high cation exchange capacity, and stable structure, biochar has recently attracted the interest of scientists. This review will analyze how biochar can be applied, as well as the various ways it can be pretreated, focusing specifically on its application and the various pretreatments methods. Biochar's properties can be altered by treating them with different chemicals, including acids, alkalis, oxidizing agents, metal ions, steam, and purge gases. The modification or pretreatments methods mainly depends on the application of biochar. Composting of organic solid waste, water and wastewater purification, carbon sequestration, and soil remediation and amelioration are the main application of biochar. Plant biomass is abundant renewable biosource present on the earth. The main drawback of the plant biomass which hinder its use is its tight bonding that exist among its components, like cellulose, hemicellulose, and lignin. Before selecting a pretreatment method, the application should be considered. To effectively extract lignocellulosic biomass constituents, especially for biofuel production, several pretreatment techniques have been developed and implemented for efficient separation of these interrelated components. Physical, chemical, thermophysical, thermochemical, and biological procedures are the most common pretreatment strategies used for biochar.

Keywords: Biochar; Pretreatments; Acidic; Alkali; Application; Biomass

1. Introduction

The exponential growth of populations, coupled with rapid industrialization and urbanization, has resulted to an enormous rise in the production of organic wastes. A wide variety of wastes fall into this category, such as those produced in agriculture, industry, municipal, the sea, and forests. Composting, feeding cattle, and producing biogas are just some of the domestic and on-farm activities that make use of a small portion of the waste produced by agricultural and forestry operations[1]. However, a significant portion of it is disposed of by either burning it or dumping it in fields or landfills, both of which contribute to the pollution of the air, water, and soil. [13]

[13] ✉ Sambit Tarafdarsambit1992@gmail.com

[a]Amity Institute of Virology and Immunology, Noida, Uttar Pradesh, 2013131, India

[b]JIS College of Engineering, Kalyani, West Bengal, 741235, Indi

Consequently, different researchers suggest the composting of organic wastes[2,3]. Its laborious operation and the slow degradation rate at makes it non attractive choice[4]. Because of this, the exploitation of organic wastes to produce biochar might provide a solution to the existing problem. Because of the high value of the product, biochar production is a fast and cost-effective operation. In addition to this, it may also have other potential benefits, such as increasing the fertility of the soil, promoting the germination of seeds, enhancing the vegetative growth of plants, improving the soil's resistance to disease, absorbing harmful pollutants, and enhancing the land's capacity to retain water[5,6]. Furthermore, biochar can be utilized as a carbon sink and a fuel for energy production. Biochar, a solid by-product high in carbon, is made by pyrolyzing or degasifying organic material at high temperatures in an atmosphere with little or no oxygen to avoid combustion. The relative yield of product generation during pyrolysis is proportional to the temperature at which the reaction is carried out. Temperatures between 400 and 500 °C (752 and 932 °F) result in a greater production of char, whereas temperatures beyond 700 °C (1292 °C) result in a greater production of liquid and gas fuel components[7]. Gasification, also known as high-temperature pyrolysis (over 700 °C), is another method that can be used to produce biochar. However, it was discovered that the yield from gasification was not particularly high[8].

Farmers in India, Europe, China, Japan, and the United States still produce and use of biochar to increase fertility of the soil. Burning of agricultural waste in pits or trenches is the method that is being used to produce it[9]. They claim that increased soil fertility can be achieved through the use of biochar due to its ability to increase nutrient retention[10]. Several studies have demonstrated that biochar can improve soil fertility and agricultural yields, especially when used in combination with fertilizers[11,12]. The incorporation of atmospheric CO_2 also led to an increase in NPP (net primary production) accumulation over the course of a season after biochar amendment[13]. Phosphorus is essential for the vegetative growth of mosses, which are typically grow on peatlands. In most cases, peatland restoration will involve the application of phosphate rock fertilizations[14]. The usage of biochar, on the other hand, has the potential to considerably assist ecological restoration, which aids in the regeneration of an ecosystem that has been degraded, damaged, or destroyed. In addition, amending the soil with biochar increases the amount of nutrients that can be taken up by the plant. This reduces the plant's dependence on the chemical fertilizer, which is particularly significant in developing nations like India, where most farmers are unable to afford chemical fertilizers. Despite this, there have been a number of studies published in the most recent years which claim that adding biochar to soil has either no effect on plant development or has a negative effect on plant growth[15,16].

Pretreatment of the biomass must proceed before energy extraction. According to the published research, pretreatment considerably increases the energy recovery capacity of biomass[17]. Several reports indicated that physical and chemical pretreatments impacted

energy recovery in varying degrees. In most cases better results in terms of energy recovery were seen with the chemical pretreatments, hence they were preferred. It has been found that a number of the chemicals that are employed in the pretreatment of biomass can improve the amount of energy that can be recovered from the biomass[18]. The present study aims to assess various pretreatments methods and its impact on biochar.

2. Biochar

Pyrolysis, or the thermal decomposition of plant-derived biomass, is a process that can be controlled to generate CO_2, as well as other flammable gases (primarily H_2, CO, and CH_4), volatile oils, tarry fumes, and a solid carbon-rich residue known as char. Pyrolysis can occur with either a partial or complete absence of oxygen[19]. In contrast to char in general, biochar is said to consist of char that is formed from biomass and produced particularly for application to soil. Consequently, it encompasses the controlled production of similar substances, such as traditional charcoal, with or without the total removal of oxygen[20]. Even under favourable climatic and biological conditions, such as those that may occur in soil, the carbon in biochar is more likely to be found in stable aromatic forms of organic carbon than in a pyrolysis feedstock[21].

Biochar, a form of carbonaceous material and cost effective to be used. Biochar has promising environmental uses because of its low cost, wide availability of feedstock, large surface area, high porosity, and high ion exchange capacity[22]. In order to eradicate the contamination in the soil caused by organic pollutants and heavy metals, biochar has been widely used. A primary mechanism behind biochar's ability to improve soil quality is adsorption. Biochar’s adsorption mechanism involves a combination of surface complexation, hydrogen binding, electrostatic attractions, acid-base interaction, and pi-pi interaction[23]. Both biochar developed from Carya tomentosa and biochar derived from Carya illinoinensis have the ability to adsorb clomazone and bispyribac sodium in soil, which effectively reduced the amount of clomazone and bispyribac sodium that leached out of the soil[24]. However, Cederlund et al. found that the amount of glyphosate and chlorpyrifos that leached out was unaffected using biochar. This mismatch could be caused by the pollutant's various physiochemical characteristics. Polycyclic aromatic hydrocarbons (PAHs) were observed to be significantly reduced after biochar made from sawdust and biochar made from wheat straw were introduced. However, when sodium azide was added to the soil, there was a considerable reduction in the number of PAHs that were removed, which suggests that biodegradation played a major part in the breakdown of PAHs[25]. Soil microbial activity can be stimulated by adding biochar. When compared to low molecular weight PAHs, those having a higher number of rings (i.e., a higher molecular weight) were more resistant to biodegradation. And this held true for all PAHs[26]. In addition to organic contaminants, biochar possesses the ability to successfully adsorb heavy metal ions that are present in soil. Numerous mechanisms, including surface complexation, precipitation, cation exchange, chemical reduction, and

electrostatic attraction, contribute to the adsorption of heavy metals onto biochar[27]. The biochar showed varied degrees of metal adsorption capability. Among the several metals examined, lead (Pb) was most effectively adsorbed by biochar. It was also straightforward for other metal ions to replace the cadmium that had become adsorbed on the charcoal when the metals coexisted. Although water hyacinth biochar was effective at adsorbing almost 90% of As(V), Zn^{2+} was however the more effective was a biochar made from rice straw[28,29]. A change in the feedstock used or the experimental setup could account for this difference. Some of the factors that influence biochar's adsorption capacity are its pH, surface functional groups, porosity, surface charge, and mineral composition. In this section, we review some of the earlier research that looked into these issues[23]. Soil fertility enhancement, acidity, cation exchange capacity, and the presence of organic contaminants and heavy metals can all be reduced with the use of biochar. Moon et al. treated soil for one month with biochar made from soybean stover and biochar derived from oak and found that soil acidity increased by two units because of the treatment. Cation exchange capability was greatly enhanced by the use of just 5% biochar[30]. Biochar's addition to the soil enhanced its quality, which in turn promoted maize's development. In addition, the quantity of biochar that was used had a significant impact on the development of the maize. It was found that the optimal growth for maize occurred with 3% biochar. Adding biochar to the soil could improve its fertility. The paper mill's biochar had varying results on diverse crops[7]. The accumulation of biochar that was obtained from paper mills enhanced the radish's biomass, but it had no effect on the wheat or the soybeans. The use of biochar produced from bamboo increased both the growth and production of maize[31]. In conclusion, the incorporation of biochar could improve soil fertility due to the following factors: (1) an increase in water-holding capacity; (2) an increase in the stability of soil aggregates; (3) relief from soil compaction; and (4) a decrease in soil bulk density and an increase in porosity[32,33].

3. Pretreatment Methods

According to Roy and Ray since lignocellulosic biomass is abundant and carbon neutral, it has been the focus of research into energy recovery as a fossil fuel substitute. Chemical pretreatments were studied for their impact on waste biomass (rice straw) composition and energy recovery capacity. Analyses at both the intermediate and final stages showed that the pretreatments did significantly alter the composition of the waste biomass. The energy recovery potential dramatically rose as the acid pretreatments became more severe. Pretreatment of waste biomass (rice straw) with 30% sulfuric acid increased its energy recovery capacity by 15.67%. An increase in the calorific value of energy recovered can have a positive effect on the economy, as shown by the study. For rice straw that had been treated with 30% sulfuric acid, the calculated net economic benefit was 10.4%[34]. Choosing the right pretreatment method is essential since it affects the biomass's physical, biological, and chemical properties. Pretreatment makes lignocellulosic biomass more digestible and boosts product output by making it more

accessible to enzymes. This is because pretreatment loosens the internal cell-wall connectivity, removing the bond that the tight connection placed on growth[35]. The rate of enzymatic hydrolysis can be increased by a factor of three to ten times through the pretreatment of biomass before it is subjected to the process. For industrial processes, pretreatment of LCW is second only to power generation building in terms of cost. The pretreatment of crystalline cellulose serves three unique purposes: the breakdown of hydrogen bonds, the formation of a cross-linked matrix, and the creation of more porous and surface-active forms of the cellulose. Additionally, the consequence of pretreatment is not the same every time because of variations in the proportion of cell wall components[36,37]. When compared to sweet gum bark or cornstalks, poplar tree bark or corn responds better to the dilute acid pretreatment option. There are only few requirements that need to be met for a pretreatment process to be effective, efficient, and economically suitable. A cost-effective size reduction procedure, the creation of reactive cellulosic fibres, the use of inexpensive chemicals, minimal chemical consumption, the inhibition of hemicellulose and cellulose denaturation, and minimal energy requirements and consumption are a few of these. Different methods are used for pretreatment, the most commons are chemical, physical, and biological[38,39].

3.1 Physical pretreatments

Physical methods can be used to increase the surface area and pore size of lignocellulosic biomass while reducing the crystallinity and polymerisation degree of cellulose. This allows for greater flexibility in the final product. The processes of milling, sonication, mechanical extrusion, and pyrolysis are all examples of physical pretreatments[40].

3.2 Milling

Milling can be used to increase cellulase accessibility of lignocelluloses by altering their degree of crystallinity and altering the ultrastructure of the cellulose molecules. To Catalyze cellulose by cellulases enzymes, it is required to increase the availability of substrates. This will improve the efficiency of the enzymes[41]. Prior to LCW being hydrolyzed by enzymes, the lignocellulosic matter should be milled and reduced in size. Ball milling, colloid milling, vibro-energy milling, hammer milling, and two-roll milling are just a few examples of the many milling methods available. There are a few different types of wet-material mills, including the colloid mill, the dissolver, and the fibrillator. However, the hammer mill, extruder, cryogenic mill, and roller mill are all better suited for dry goods. Ball mills can be operated whether the material being processed is wet or dry[42]. Wastepaper can be pretreated in a number of ways, although hammer milling is the most efficient. Since milling reduces crystallinity and particle size, it facilitates enzymatic breakdown. The particle size of the processed material can be reduced by milling and grinding to as little as 0.2 mm. Pretreatment allows for a decrease in biomass particle size up to a certain limit; however, after that point, further particle size reduction has little effect. Smaller particle size corn stover, between 53 and 75 m, is more

productive than larger particle size corn stover, between 475 and 710 m. Different particle sizes show how productivity can have a major impact on the pretreatment stage. For saccharification of straw under mild hydrolytic conditions, whereby a higher yield of fermentable sugars is desired, ball milling is preferable to alternative procedures due to the dramatic fall in crystallinity index that it causes, from 4.9% to 74.2%[38,43,44].

3.3 Microwave irradiation

Irradiation with microwaves is usually employed for the processing of plant biomass. This pretreatment method offers a number of benefits, such that it is simple, having high heating capacity, short processing time, generates a low number of inhibitors, and requires less energy[45]. In 1984, a team of scientists from Kyoto University in Japan first reported using microwave irradiation inside a sealed chamber. Microwave heating of wet rice straw, rice hulls, and sugarcane bagasse yielded a variety of rice products. 50 mL glass jars, 2450 MHz energy, and 2.4 kW of irradiation are used in the microwave therapy[46]. High pressure and temperature were constant process requirements in conventional pretreatment methods. Heat breaks down the chemical bonds in lignocellulosic material, making more substrate available to the enzymes. Bringing lignocellulosic material to a high temperature, typically between 160 and 250 °C, is normally accomplished using high-pressure steam injection or indirect heat injection[42]. When lignocellulosic material is crushed into tiny particles, temperature gradients between different areas of the material are eliminated. To speed up the decomposition of lignocellulosic material into humic acid and furfural, conventional heating methods cause high temperature gradients; the microwave, on the other hand, evenly distributes heat. Effective degradation is achieved via microwave irradiation and a mild alkaline treatment. The combined use of alkali and irradiation as a pretreatment method on switch grass resulted in a sugar yield of between 70 and 90%[47]. Because microwave irradiation is carried out at high temperatures, it is necessary to use sealed containers in to achieve those temperatures. Microwaves could penetrate objects, reflect off surfaces, and absorb energy. Microwaves are passed through glass and plastic, but they are reflected by metals. Microwaves are absorbed by water and biomass. Based on these characteristics, microwave reactors can be roughly divided into two groups: those that transmit microwaves and those that reflect them. The first of which is composed of glass or plastic, and the other of steel[48]. A quartz window in the reactor lets microwaves in. An airtight, pressure-resistant glass tube container with a Teflon gasket is perfect for the high temperature, on the order of 200 °C, required for microwave irradiation pretreatment. Sensors within the microwave keep the temperature stable. Sensors with a Teflon covering are advantageous because to their resistance to high temperatures, absence of corrosion, and low absorption. Due to its beneficial features, some researchers prefer to use Teflon vessels in a microwave oven also[49]. In most cases, the size of the vessel might range from one hundred to several hundred ml. On top of the microwave that Chen and

Cheng designed, there is a vessel that has a capacity of 650 mL and measures 318 mm in length. Additionally, there is a connected nitrogen bottle, gauges, and thermometers[50].

3.4 Mechanical method

Materials having a definite profile can pass easily through a cross section die and the phenomenon is called as metal extrusion. The extrusion technique is well-known for its use in the recovery of sugar from biomass. The mechanical extrusion pretreatment method has several advantages over alternative approaches, including its flexibility to change, the lack of byproducts from degradation, the ability to maintain a consistent environment, and a high output rate. Extruders can be split into two distinct categories: both single-screw and twin-screw extruders can be used[51].

A single screw extruder consists primarily of a forward's screw, a kneading screw, and a reversing screw. A forward's screw element can be used to transport bulk materials with varying pitch and length with minimal shearing and mixing. Large-scale mixing and shearing necessitate the employment of material forced back by reverse screw elements, whereas the use of kneading screw elements with a weak forwards conveying effect provides a notable mixing and shearing effect[52]. A screw arrangement is characterized by its varying stagger angles, lengths, spacing, pitches, and placements. A twin-screw extruder can perform operations such as mixing, shearing, grinding, reaction, drying, and separation. One can speed up the enzymatic hydrolysis process by using either a single-screw or a twin-screw extruder. Other factors that can have a major impact on sugar recovery include compression ratio, barrel temperature, and screw speed. Extruders with a short time allow for a rapid transmission of heat, as well as accurate mixing and higher shear. The structure of the biomass is disrupted as the material travels through the extruder barrel, resulting in a greater surface area that is available for enzymatic hydrolysis[53,54]. To maximize sugar recovery, lignocellulosic material might be subjected to an alkaline or acidic treatment during the extrusion process. Because of the corrosion that acid might cause to the material of the extruder, an alkaline treatment is generally recommended over an acidic one. By employing AL6XN alloy for the manufacture of the barrel and the screws of the extruder, the corrosion problem can be eliminated[55]. Since alkaline treatment aids in delignification and causes less carbohydrate degradation, it is well-suited for lignocellulosic material. Dissolving lignins and hemicelluloses and breaking down ester bonds are two of sodium hydroxide's most common applications. The lignocellulosic material can be steeped in alkali at room temperature before being treated, or alkali can be pumped into the extruder using a volumetric pump[56].

3.5 Pyrolysis

Pyrolysis is the process that is used to convert biomass into bio-oil. The thermal breakdown of lignocellulosic biomass during pyrolysis takes place at very high temperatures and does not involve the presence of an oxidizing agent. The pyrolysis temperatures used was between 500 and 800 °C[57]. Byproducts including pyrolysis oil and

charcoal were created due to the rapid decomposition of cellulose[58]. There are two distinct types of pyrolysis pretreatment: rapid pyrolysis and slow pyrolysis. The qualities of the biomass, the reaction parameters, and the kind of pyrolysis all play a role in determining the final products. Pyrolysis is becoming widely attractive in the thermal industry as a result of the generation of energy-rich products with high value, the ease with which transport management, combustion, storage, and the flexibility with which it can be used and marketed[59]. The presence of oxygen and a lower temperature both contribute to an increase in this process's efficiency. In the presence of nitrogen and oxygen, a study was carried out to determine the rate of bond cleavage that occurs in cellulose. At a temperature of 25 °C, the pyrolysis process was seen to result in the breaking of 7.8×109 bonds/min/g of cellulose when oxygen was present, whereas the procedure resulted in the breaking of 1.7×108 bonds/min/g of cellulose when nitrogen was present. Due to the microwaves' ability to cause dielectric heating, microwave-assisted pyrolysis is the preferred method when seeking more effectiveness and output[60]. Gasification, pyrolysis, and direct combustion are the three methods that can be utilized to accomplish the thermochemical transformation of biomass into biofuels[61]. Pyrolysis can be done in a few distinct ways, each of which results in a somewhat varied yield of products. Water and polar chemical compounds are the primary components of bio-oil. When it is necessary to produce bio-oil, pyrolysis is mainly employed. The generation of liquid products is achieved through rapid pyrolysis carried out in a regulated atmosphere[62]. Torrefaction is a relatively new process that is also known as "mild pyrolysis". This thermochemical process is performed at lower temperatures (200-300°C) than pyrolysis. At lower temperatures, pyrolysis can take place. During this process, there is partial decomposition of the biomass present, and the final product that is obtained is called terrified biomass. In contrast, during the pyrolysis process, the biomass of plants is broken down into different components including vapor, aerosols, and char. Dry and moist torrefaction are the two categories that have been established to describe the process of torrefaction[63].

It takes an inert atmosphere, completely dry biomass, and normal atmospheric pressure to achieve torrefaction in the dry conditions. Most biomass that is subjected to this sort of processing ends up as biochar. Hydrothermal torrefaction, also known as wet torrefaction, is another name for the same process as hydrothermal carbonization. In contrast to dry torrefaction, the pretreatment process is carried out using a pressured vessel of water[64]. Even if the biomass that is utilized in wet torrefaction already has some moisture in it, it is still necessary to carry out a drying procedure following the torrefaction step in this method. In order to carry out wet torrefaction, a pressure ranging from 1 to 250 MPa is required. During the wet torrefaction pretreatment process, the primary product is hydro-char, which is made from biomass[65].

4. Chemical Pretreatment Methods

4.1 Alkaline pretreatment method

Alkali treatment requires far lower pressure, temperature, and ambient condition than other pretreatment processes; nonetheless, alkali pretreatment takes a long time (measured in days and hours). When compared to acid treatment, the amount of sugar that is degraded during the alkali treatment is significantly lower. Additionally, the removal and recovery of caustic salt are both possible and relatively simple during the alkali treatment process[66]. In alkaline pretreatment, sodium hydroxides are used more frequently than ammonium hydroxides, calcium hydroxides, or potassium hydroxides. Calcium hydroxide, on the other hand, is the most cost-effective of all the other alkali agents that can be used for pretreatment, despite being the least expensive. By reacting calcium with carbon dioxide, insoluble calcium carbonate can be recovered, making the process of calcium recovery simple. Use of lime kiln technology allows for the recycling of calcium hydroxide[67]. For alkali pretreatment, you'll need a tank, CO_2 scrubber, water jacket, water/air manifold, pump, tray, frame, temperature sensor, and heating element. The first thing that needs to be done in the pretreatment process is to mix lime powder and water into a slurry. After the spraying slurry of lime over the biomass, then store the biomass for a period that can range from a few hours to many days. Temperature increases have the potential to shorten the contact time[68-70].

Biochar produced by the pyrolysis of municipal solid waste had its surface area increased from 14.4 to 49.1 m^2g^{-1} and the number of oxygen-containing functional groups in the biochar rose after being treated with potassium hydroxide. In this way, the aspartic acid might be drained out of the body more quickly[71]. When wheat straw biochar was treated with potassium hydroxide, Sun et al. found that its porosity decreased (from 4.4 to 0.69 m^2g^{-1}). This suggests that, depending on the feedstock and production method, alkaline modification has a moderate impact on biochar's surface area[72]. In comparison to potassium hydroxide, sodium hydroxide is less expensive and less corrosive[73]. Adding sodium hydroxide to biochar made from coconut increased its surface area to a maximum of 2885 m^2g^{-1}, which was greater than the value attained by adding potassium hydroxide (1940 m^2g^{-1})[74]. Feng and Zhu changed biochar using a base after it was made with various feedstocks and heated to various degrees. Based on their findings, base modification of biochar may increase its sorption capacity for phenanthrene[75]. However, Fan et al. showed that bamboo biochar's surface area was unaffected by sodium hydroxide treatment[76].

The elimination of lignin and hemicellulose during lime pretreatment increases the crystallinity index. Lime pretreatment of biomass alters structural properties that influence hydrolysis. It was found by Chang and Holtzapple that enzymatic digestibility is proportional to lignin content, acetyl content, and crystallinity[77]. They concluded that high digestibility can be achieved with thorough delignification regardless of crystallinity

or acetyl concentration. Delignification and deacetylation work in tandem to remove parallel impediments to hydrolysis. However, crystallinity does play a role in the onset of hydrolysis, even if it has no effect on the final sugar output. An efficient pretreatment technique is required to lower the lignin concentration to 10% and eliminate all acetyl groups. Alkaline pretreatment is thus crucial in exposing cellulose to enzymes. Lignin removal can help boost enzyme efficiency by making cellulose and hemicellulose more accessible to the enzyme and getting rid of unproductive adsorption sites.

4.2 Acidic pretreatment method

Pretreating lignocellulosic biomass typically involves the use of acids. As a result of the development of inhibitory compounds during acid pretreatment, these techniques are less desirable. High levels of phenolic acid, aldehydes, 5-hydroxymethylfurfural, and furfurals (furfurals are a type of inhibitory chemical) are produced after acid pretreatment[78]. There are two main categories of acid treatments, distinguished by the end purpose of the treated material. The first kind of treatment lasts for only a few minutes (between one and five) but maintains a high temperature (above 180 °C). The second type of treatment lasts for a longer amount of time, from thirty to ninety minutes, but the temperature is kept below 120 °C. While the acid treatment eliminates the need for biomass hydrolysis, it must be washed to remove the acid before sugar fermentation[66,79]. Reactors that can endure highly corrosive, caustic, and poisonous acids are required for acid pretreatment to be effective. As a result of its high price, acid pretreatment is rarely used. Many other types of rectors, such as flow through, percolation, shrinking-bed, batch, plug flow, and counter current, have been developed by scientists in the past. The pretreatment's economic viability hinges on the capacity to recycle the concentrated acid created during the treatment[80].

To facilitate the adsorption of pentachlorophenol, the ash content of reed-derived biochar was decreased from 29.5% to 11.8% using 1 M hydrochloric acid[81]. Carboxylic, lactonic, phenolic, and carbonylic groups were added to the bamboo charcoal surface when nitric acid was administered at 2 millimolar concentrations[82]. Adding acid to biochar can change its surface area, with different effects depending on the acid used and its concentration. Reed-derived biochar, for instance, had an increase in its surface area from 58.75 to 88.35 m^2g^{-1} after being treated with 1 M hydrochloric acid[81]. The surface area of biochar made from rice straw decreased from 71.35 to 56.9 m^2g^{-1} when 2% sulfuric acid was added[83]. Phosphoric acid is one of the most often used chemicals in the laboratory. Both the surface area and total pore volume of the biochar made from rice straw were somewhat decreased after being treated with phosphoric acid, going from 522.5 to 517.1 m^2g^{-1} and 1.2 to 0.65 mg^{-1}, respectively. The amount of phosphoric acid present had a noticeable impact on the amount of adsorption capacity possessed by biochar[84]. To get the best results from employing phosphoric acid as a modification agent, you should choose the highest possible concentration of the acid. Weak acids, such as citric and

oxalic acids, can also help in the esterification process, which can add a carboxyl group to the charcoal surface. Oxalic acid and citric acid caused a little decrease in biochar surface area, from 1.57 to 0.69 and 1.21 m^2g^{-1}[85]. Biochar's surface area, on the other hand, grew considerably from 2.31 m^2g^{-1} to 571 m^2 g^{-1} after being treated with 30% sulfuric acid and oxalic acid[86].

In addition, concentrated acids are used in the processing of lignocellulosic biomass. Common acids include hydrochloric acid and sulfuric acid. The hydrolysis process utilized to extract fermentable sugars from lignocellulosic biomass could be enhanced by acid pretreatment. Pretreatment with sulfuric acid is standard practice for several wood species, including poplar, switch grass, spruce, and maize stover. When Bermuda grass and rye were subjected to acid pretreatment, reducing sugars were produced at rates of 19.71 and 22.93%, respectively[42]. The rice straw was subjected to a pretreatment process that consisted of two phases and was carried out in a percolation reactor using diluted sulfuric acid and aqueous ammonia. When ammonia is utilized, a yield of 96.9% of reducing sugar is obtained, however when dilute acid is utilized, a yield of 90.8% of reducing sugar is obtained. When treated with diluted sulfuric acid, the perennial grass Eulaliopsis binate produced sugars at a rate of 21.02%, lignin at a rate of 3.22%, and acetic acid at a rate of 3.34%. Additionally, inhibitors were produced but in very little quantities[87, 88]. Pretreatment is recommended when the concentration of sulfuric acid is 4 wt.% since it reduces expenses and improves the efficiency of the process. The hydrolysis of biomass that results from the application of dilute sulfuric acid is followed by the successful conversion of xylose into furfural. Hydrolysis is favored by diluted sulfuric acid when the temperature is high[35]. The removal of hemicellulose is an essential step in increasing the amount of glucose that can be extracted from cellulose, and dilute sulfuric acid is an extremely efficient for this purpose. It is not economically viable to convert biomass without first achieving a high xylan-to-xylose ratio. In lignocellulosic materials, xylan accounts for around a third of the carbohydrates. The high temperature, continuous flow approach with low solid loadings is one type of dilute acid pretreatment, while the low temperature, batch process with high solid loadings is the other. In the area of dilute acid pretreatments, these two methods are representative. One type has solid loadings of 5-10% and temperatures over 160 °C, while another type has loadings of 10-40% below 160 °C[89, 90].

5. Biological Pretreatment Method

Traditional approaches for chemical and physical pretreatments demand for relatively expensive reagents, pieces of equipment, and a significant amount of energy. In contrast, the treatment of lignocellulosic material by means of biological pretreatment involves the use of living microorganisms; this approach is better for the environment and needs less energy; also, it is more effective[91]. The natural environment is home having variety of microorganisms that are capable of cellulolytic and hemicellulolytic activity,

respectively. It is generally known that the fungi responsible for white rot, soft rot, and brown rot can degrade cellulose into its component parts hemicellulose and lignin without any difficulties. As a result of the presence of lignin-degrading enzymes such peroxidases and laccases, white rot is capable of lignin degradation. Among the elements that control the activity of these enzymes that degrade are carbon and nitrogen[92]. White rot, soft rot, and brown rot are all rots that affect the lignin and cellulose in plant biomass, although brown rot is the most common. *Ceriporiopsis subvermispora, Ceriporia lacerata, Pycnoporus cinnabarinus, Cyathus cinnabarinus,* and *Phanerochaete chrysosporium* are some of the most common white-rot fungi. The basidiomycetes *Bjerkandera adusta, Ganoderma resinaceum, Trametes versicolor, Fomes fomentarius, Irpex lacteus, Lepista nuda,* and *Phanerochaete chrysosporium* were all proven to have high efficiency for delignification in laboratory trials[92,93].

Hatakka examined how pretreatment of wheat straw affected its properties. Results showed that in 5 weeks, Pleurotus ostreatus converted 13% of wheat straw into sugars, while *Phanerochaete sordida* and *Pycnoporus cinnabarinus* converted almost same in less time[94]. Results showed that *Pleurotus ostreatus* turned 13% of wheat straw into sugars in 5 weeks, while *Phanerochaete sordida* and *Pycnoporus cinnabarinus* converted practically the same in less time. Fungus cellulase mutant the fungus *Sporotrichum pulverulentum* was bred specifically to degrade lignin in woodchips while keeping the cellulose intact[95]. The delignification of Bermuda grass was investigated, and it was found that the white-rot fungus *Ceriporiopsis subvermispora* and *Cyathus stercoreus* respectively improved delignification by 29-32% and 63%-77%. Due to carbon and nitrogen limitation, the fungus *P. chrysosporium* produces two lignin degrading enzymes during its secondary metabolism: lignin peroxidase and manganese-dependent peroxidase. These two enzymes are found in the extracellular filtrates of several different white-rot fungus[96].

6. Conclusions

Biochar's physiochemical characteristics can be altered for environmental use by employing a variety of pretreatment strategies. The surface area and functional groups of biochar can be modified with acid and alkali. The biochar surface area can be increased by modifying carbonaceous materials. It's possible that the hybrid composite of biochar obtained from various feedstocks can serve as a cheap modification of carbonaceous materials. Due to its ability to improve soil quality and mitigate climate change, biochar is a promising tool for long-term environmental preservation. Biochar has been shown to boost soil fertility, but its reason is unknown, and studies examining its impact on carbon sequestration have produced conflicting results. To accelerate their decomposition by microorganisms, organic wastes can benefit from biochar when composted. However, the optimal dose of biochar varied depending on the type of organic waste being treated. Soil and composting processes can provide valuable information for tailoring a biochar

application strategy. Adsorption capacity and biochar stability must be improved before biochar can be used for water and wastewater purification.

References

1. J Gabhane, A Tripathi, S Athar, S William, A Vaidya, S Wate. J Biofuels Bioenergy. 2016; 2(2): 122-131.
2. A Patle, S Williams, J Gabhane, H Dhar, P Nagamaik. Int. J Sci. Eng. Res. 2014; 5(5).
3. J Villasenor, L Rodriguez, F Fernandez. Bioresour. Technol. 2011; 102(2): 1447-1454.
4. J Gabhane, SPMP William, R Bidyadhar, P Bhilawe, D Anand, AN Vaidya et al. Bioresour. Technol. 2012; 114: 382-388.
5. DA Roberts, AJ Cole, NA Paul, R De Nys. J Environ. Manage. 2015; 161: 173-180.
6. CN Kelly, CD Peltz, M Stanton, DW Rutherford, CE Rostad. Appl. Geochem. 2014; 43: 35-48.
7. LV Zwieten, S Kimber, S Morris, KY Chan, A Downie, J Rust et al. Plant Soil. 2010; 327(1): 235-246.
8. G Guan, M Kaewpanha, X Hao, A Abudula. Renew. Sustain. Energy Rev. 2016; 58: 450-461.
9. D Solomon, J Lehmann, J Thies, T Schafer, B Liang, J Kinyangi et al. Geochim. Cosmochim. Acta. 2007; 71(9): 2285-2298.
10. M Ogawa, Y Okimori. Soil Res. 2010; 48(7): 489-500.
11. G Agegnehu, AM Bass, PN Nelson, B Muirhead, G Wright, MI Bird. Agric. Ecosyst. Environ. 2015; (213): 72-85.
12. J Matuštík, T Hnátková, V Kočí. J Clean. Prod. 2020; 259: 120998.
13. JM Kimetu, J Lehmann, SO Ngoze, DN Mugendi, JM Kinyangi, S Riha et al., Ecosystems. 2008; 11(5): 726-739.
14. ER Graf, V Valakh, CM Wright, C Wu, Z Liu, YQ Zhang et al. J Neurosci. 2012; 32(47): 16586-16596.
15. E Meschewski, N Holm, BK Sharma, K Spokas, N Minalt, JJ Kelly. Chemosphere. 2019; 228: 565-576.
16. M Bartoli, M Giorcelli, P Jagdale, M Rovere, A Tagliaferro. Materials. 2020; 13(2) 261.
17. R Kumar CE Wyman. Bioresour. Technol. 2009; 100(18) 4193-4202.

18. TAD Nguyen, KR Kim, SJ Han, HY Cho, JW Kim, SM Park et al. Bioresour. Technol. 2010; 101(19): 7432-7438.

19. JP Mehta, D Kapatel. NCRTTM. 2016; 74.

20. S. Shackley, S Sohi (Eds.). Department for Environment, Food and Rural Affairs, UK Government, London, 2010.

21. S Schimmelpfennig, B Glaser. J Environ. Qual. 2012; 41(4): 1001-1013.

22. M Ahmad, AU Rajapaksha, JE Lim, M Zhang, N Bolan, D Mohan et al. Chemosphere. 2014; 99: 19-33.

23. X Zhang, H Wang, L He, K Lu, A Sarmah, J Li et al. Environ. Sci. Pollut. Res. 2013; 20(12): 8472-8483.

24. X Gai, H Wang, J Liu, L Zhai, S Liu, T Ren et al. PLoS ONE. 2014; 9(12): e113888.

25. H Cederlund, E Börjesson, J Stenström. J Environ. Manage. 2017; 191: 28-34.

26. L Kong, Y Gao, Q Zhou, X Zhao, Z Sun. J Hazard. Mater. 2018; 343: 276-284.

27. X Xu, X Cao, L Zhao, H Wang, H Yu, B Gao. Environ. Sci. Pollut. Res. 2013; 20(1): 358-368.

28. F Zhang, X Wang, J Xionghui, L Ma. Environ. Pollut. 2016; 216: 575-583.

29. K Lu, X Yang, G Gielen, N Bolan, YS Ok, NK Niazi et al. J Environ. Manage. 2017; 186: 285-292.

30. DH Moon, I Hwang, YY Chang, A Koutsospyros, KH Cheong, WH Ji et al. Environ. Sci. Pollut. Res. 2017; 24(4) 4194-4199.

31. TT Doan, TH des Tureaux, C Rumpel, JL Janeau, P Jouquet. Sci. Total Environ. 2015; 514: 147-154.

32. V Nelissen, G Ruysschaert, D Manka'Abusi, T D'Hose, K De Beuf, B Al-Barri et al. Eur. J Agro. 2015; 62: 65-78.

33. LR Peake, BJ Reid, X Tang. Geoderma. 2014; 235: 182-190.

34. R Roy, S Ray. Energy Sources Part A Recover. Util. Environ. Eff. 2019; 1-13.

35. N Mosier, C Wyman, B Dale, R Elander, YY Lee, M Holtzapple et al. Bioresou. Technol. 2005; 96(6): 673-686.

36. MJ Taherzadeh, K Karimi. BioResour. 2007; 2(4): 707-738.

37. SH Mood, AH Golfeshan, M Tabatabaei, GS Jouzani, GH Najafi, M Gholami et al. Renew. Sustain. Energy Rev. 2013; 27: 77-93.

38. MJ Taherzadeh, K Karimi. Int. J Mol. Sci. 2008; 9(9): 1621-1651.

39. C Wyman. Handbook on Bioethanol: Production and Utilization. CRC press. 1996.

40. N Akhtar, K Gupta, D Goyal, A Goyal. Environ. Prog. Sustain. Energy. 2016; 35(2): 489-511.

41. U Mais, AR Esteghlalian, JN Saddler, SD Mansfield. Biotechnol. Fuels Chem. 2002; 815-832.

42. MN Aftab, I Iqbal, F Riaz, A Karadag, M Tabatabaei. Biomass Bioenergy: Recent Trends Future Challenges. 2019; 1-24.

43. S Bondy, S Guo-Ross, J Pien. Neurotoxicology. 1998; 19(1): 65-71.

44. J Walpot. Conserv. Recycl. 1986; 9(1): 127-136.

45. B Kumar, N Bhardwaj, K Agrawal, V Chaturvedi, P Verma. Fuel Process. Technol. 2020; 199: 106244.

46. JI Azuma, J Higashino, M Isaka, T Koshijima. Wood Res. Bull. Wood Res. Inst. Kyoto Univ. 1985; 71: 13-24.

47. Z Hu, Z Wen. Biochem. Eng. J. 2008; 38(3): 369-378.

48. T Komolwanich, P Tatijarern, S Prasertwasu, D Khumsupan, T Chaisuwan, A Luengnaruemitchai et al. Cellulose. 2014; 21(3): 1327-1340.

49. J Azuma, F Tanaka, T Koshijima. Hakko Kogaku Zasshi. 1984; 62(4).

50. WH Chen, YJ Tu, HK Sheen. Appl. Energy. 2011; 88(8): 2726-2734.

51. JO Otieno, FO Ogutu. Asian J Chem. Sci. 2020; 8(2): 34-54.

52. J Zheng, K Choo, L Rehmann. Biomass Bioenergy. 2015; 74: 224-232.

53. C Karunanithy, K Muthukumarappan. Ind. Crops Prod. 2011; 33(1): 188-199.

54. IA Kartika, PY Pontalier, L Rigal. Ind. Crops Prod. 2010; 32(3): 297-304.

55. SF Ahmed, M. Mofijur, SN Chowdhury, M Nahrin, N Rafa, AT Chowdhury et al. Fuel. 2022; 318: 123618.

56. J Zheng, L Rehmann. Int. J Mol. Sci. 2014; 15(10): 18967-18984.

57. T Kan, V Strezov, TJ Evans, Renew. Sustain. Energy Rev. 2016; 57: 1126-1140.

58. FJ Kilzer, A Broido. Pyrodynamics. 1965; 2: 151-163.

59. R. Kumar, V Strezov, H Weldekidan, J He, S Singh, T Kan et al. Renew. Sustain. Energy Rev. 2020; 123: 109763.

60. CO Kappe. Angew. Chem. Int. Ed. 2004; 43(46): 6250-6284.

61. C Yin, SK Kær, L Rosendahl, SL Hvid. Bioresour. Technol. 2010; 101(11): 4169-4178.

62. AV Bridgwater, D Meier, D Radlein. Org. Geochem. 1999; 30(12): 1479-1493.

63. MV der Stelt, H Gerhauser, J Kiel, K Ptasinski. Biomass Bioenergy. 2011; 35(9): 3748-3762.

64. Z Chen, M Wang, Y Ren, E Jiang, Y Jiang, W Li. IOP Conf. Ser. Earth Environ. Sci. 2018; 113(1): 012201.

65. QV Bach, Ø Skreiberg. Renew. Sustain. Energy Rev. 2016; 54: 665-677.

66. AK Kumar, S Sharma. Bioresour. Bioprocess. 2017; 4(1): 1-19.

67. CIS Rodrigues, JJ Jackson, MD Montross. Ind. Crops Prod. 2016; 92: 165-173.

68. AM Elshafei, J Vega, K Klasson, E Clausen, J Gaddy. Bioresour. Technol. 1991; 35(1): 73-80.

69. S Kim, MT Holtzapple. Bioresour. Technol. 2006; 97(4): 583-591.

70. D Lee, AH Yu, KK Wong, JN Saddler. Appl. Biochem. Biotechnol. 1994; 45(1): 407-415.

71. H Jin, S Capareda, Z Chang, J Gao, Y Xu, J Zhang. Bioresour. Technol. 2014; 169: 622-629.

72. H Sun, S Liu, G Zhou, HM Ang, MO Tadé, S Wang. ACS Appl. Mater. Interfaces. 2012; 4(10): 5466-5471.

73. AL Cazetta, AMM Vargas, EM Nogami, MH Kunita, MR Guilherme, AC Martins et al. Chem. Eng. J. 2011; 174(1): 117-125.

74. I Tan, A Ahmad, B Hameed. J Hazard. Mater. 2008; 154(1-3): 337-346.

75. Z Feng, L Zhu. Front. Environ. Sci. Eng. 2018; 12(2): 1-11.

76. Y Fan, B Wang, S Yuan, X Wu, J Chen, L Wang. Bioresour. Technol. 2010; 101(19) 7661-7664.

77. VS Chang, MT Holtzapple. 21st Symp. Biotechnol. Fuels Chem. 2000; 5-37.

78. G Brodeur, E Yau, K Badal, J Collier, K Ramachandran, S Ramakrishnan. Enzyme Res. 2011.

79. P Sassner, CG Mårtensson, M Galbe, G Zacchi. Bioresour. Technol. 2008; 99(1): 137-145.

80. S Kumar, RP Mahato, K Gupta, P Bardhan, MA Rather, M Mandal et al. Thermochem. Catal. Convers. Technol. Future Biorefineries; Springer. 2022; 53-78.

81. P Peng, YH Lang, XM Wang. Ecol. Eng. 2016; 90: 225-233.

82. Y Li, J Shao, X Wang, Y Deng, H Yang, H Chen. Energy Fuels. 2014; 28(8): 5119-5127.

83. SM Yakout, AEHM Daifullah, SA El-Reefy. Environ. Eng. Manag. J. 2015; 14(2).

84. N Zhou, H Chen, Q Feng, D Yao, H Chen, H Wang et al. J Clean. Prod. 2017; 165: 221-230.

85. B Lei, JI Fan. Int. Conf. Intell. Sci. Big Data Eng.: Springer. 2015; 300-309.

86. M Vithanage, AU Rajapaksha, M Zhang, S Thiele-Bruhn, SS Lee, YS Ok. Environ. Sci. Pollut. Res. 2015; 22(3): 2175-2186.

87. J Tang, K Chen, F Huang, J Li. Bioresour. Technol. 2013; 129: 548-552.

88. Y Kim, A Yu, M Han, GW Choi, B Chung. Appl. Biochem. Biotechnol. 2011; 163(1): 143-152.

89. A Esteghlalian, AG Hashimoto, JJ Fenske, MH Penner. Bioresour. Technol. 1997; 59(2-3): 129-136.

90. AH Brennan, W Hoagland, DJ Schell, C Scott. 8th Symp. Biotechnol. Fuels Chem.

91. H. Chen, J Liu, X Chang, D Chen, Y Xue, P Liu et al. Fuel Process. Technol. 2017; 160: 196-206.

92. P Kumar, DM Barrett, MJ Delwiche, P Stroeve. Ind. Eng. Chem. Res. 2009; 48(8): 3713-3729.

93. J Shi. PhD Thesis; Biol. Agric. Eng. Raleigh, North Carolina. 2007.

94. AI Hatakka. Eur. J Appl. Microbiol. Biotechnol. 1983; 18(6): 350-357.

95. P Ander, KE Eriksson. Physiol. Plant. 1977; 41(4): 239-248.

96. D Akin, L Rigsby, A Sethuraman, W Morrison, G Gamble, K Eriksson. Appl. Environ. Microbiol. 1995; 61(4): 1591-1598.

Recent Development of Biomass Torrefaction Process and its Challenges: A Review

Surajit Patra[a,b], Anurag Chakraborti[a,b], Amitava Ghatak[b]

Abstract

These days, biomass is a flexible, alternative source of energy that can be transformed into solid, liquid, and gaseous energy sources via thermochemical processes. The main drawbacks of natural biomass, such as its low bulk density, decreased energy density and hygroscopic behavior, can be reduced via torrefaction, a mild pyrolysis of biomass retreatment. Its primary goal is to manufacture solid biomass products with reduced moisture content and volatile matter. Torrefied biomass can be effectively used in co-firing power plants, which can change its chemical as well as mechanical features, such as energy density, better ignition, greater C/O and C/H ratio, improved grindability and combustion characteristics. This paper primarily focused on a thorough review of torrefaction technique and its fundamental attributes.

Keywords: Biomass; Torrefaction; Biofuel advancement; Torrefaction advantages; Palletisation

1. Introduction

The world is concerned that the supply of traditional energy sources like coal, crude oil, and natural gas will eventually run out, may be due to significant shift in global population[1,2]. According to India Energy Outlook 2021, due to growth of wage and living standards, India is currently the third largest energy user in the world[3]. The article also demonstrates 4% annual growth rate between 2010 and 2021. Since 21st century, use of energy has been increased in different sectors in India, hence 80% of the demand are still mitigating by coal, oil, and gas. To meet rest of the demand of energy and reduce environmental pollution in India, the renewable energy source such as torrefied biomass can be used in industry as well as in domestic sector also. Reduce reliance on fossil fuels, several studies have been conducted in the last few decades to identify substitute of fossil fuels[3,4].

In contrast to materials that requires numerous years to manufacture, such as coal or petroleum. Biomass is simply organic material that can be obtained from living things

✉ Surajit Patra

surajitpatra.nitd@gmail.com

[a]Techno Engineering College Banipur, North 24 Parganas, West Bengal, 743233, India

[b]Department of Mechanical Engineering, Techno India University Kolkata, 700091, India

like plants or animals[5]. Biomass can store chemical energy from sun very easily through photosynthesis[6], thus is a type of carbon-neutral fuel[7]. Since burning of fossil fuels increasing CO_2 emission day by day, hence, biomass is a sustainable energy source which can generate clean biomass energy during thermochemical process and reduce CO_2 emission[8]. Additionally, compared to fossil fuels, biomass often has lower nitrogen and sulphur concentrations which reduces NO_x and SO_2 emission[7,9,10]. However, it is important to take into account the carbon footprint created during the growing, harvesting, storage, transporting, and use of biomass while producing biofuel[11].

The key benefits to use biomass as a fuel compare to fossil fuels is due to its environment friendliness and abundant availability in nature[12]. During an application of biomass doesn't release any toxic substances into the environment. Hence, biomass may undoubtedly be utilized as a source of energy. Biomass may be converted into higher level energy carriers like bio-char, synthesis gas, and bio-oil via a variety of processes including pyrolysis, torrefaction, gasification, fermentation, and anaerobic digestion. According to Ministry of New and Renewable Energy, Government of India, approximately 32% of the entire primary energy supply in India derived from biomass energy[13], A part of fossil fuels, biomass have a possibility in near future as a prime source of renewable energy, since it can be thermochemically transformed into both liquid and gaseous fuel for use in mobility[14].

According to forest survey report 2021, about 25% of the geographical area of India is covered with forest and tree[15]. Hence, India has a plentiful biomass source with a quick life cycle. In contrast to solar, wind, hydro, and nuclear energy, bio-energy is a continuous energy source found in nature because biofuels made from biomass may be safely stored as solids, liquids, or gases. It suggests that bioenergy is a reliable emerging source of energy[16].

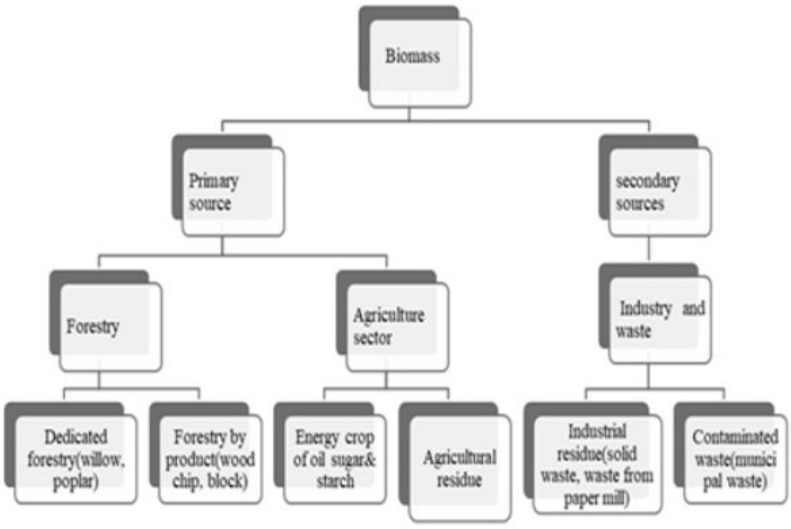

Fig. 1 Classification of biomass based on feedstocks[17].

Based on origin, biomass can be categorised as shown in **Fig. 1**. Forest leftovers and agricultural industry are the two primary sources of biomass[17]. And secondary sources are waste from industrial sectors and household waste. Since, wastes are particularly extracted from municipal areas, which are gathered in the form of biomass from primary sources[14]. **Fig. 2** shows the fuel properties as volatile matter (VC), fixed carbon content (FC), weight percentage of carbon, O/C ratio, H/C ratio, and high heating value (HHV) of raw, torrefied biomass and coal[18].

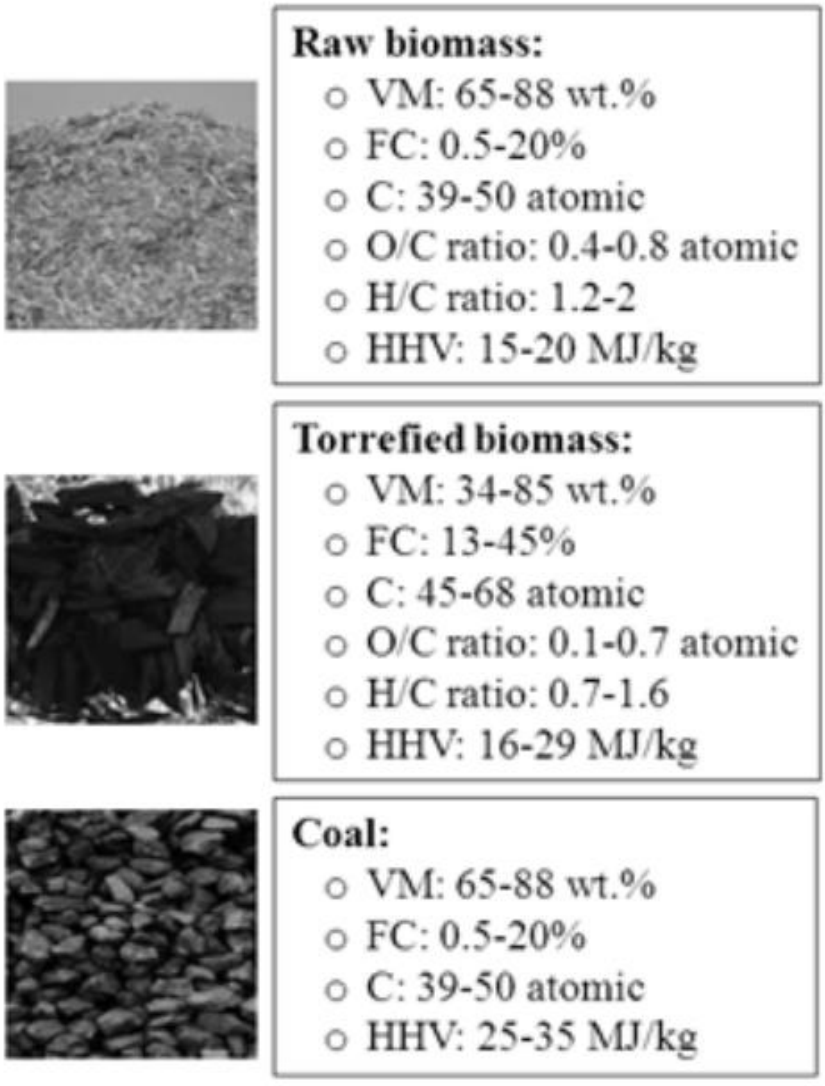

Fig. 2 Fuel properties of raw, torrefied biomass and coal[18].

Solid biomasses are hygroscopic in nature and absorb high amount of moisture from atmosphere. Some of the limitations of biomass are low bulk density and energy density (or calorific value), poor grindability, limited compositional homogeneity, and as well as lower resistance to biological degradation[19]. To overcome those drawbacks of biomass, recently some advance techniques has evolved to enhance the energy efficiency by

improving processing techniques[20,21]. Torrefaction is one of the pre-treatment techniques which modified biomass at lower temperature to obtain high efficient thermochemical energy. Detailed method of torrefaction and its effect on proximate and ultimate analysis and energy consumption of different feedstock biomasses are discussed in this review paper.

2. Torrefaction

Lignocellulosic biomass has few inherent properties like high moisture content, volume and volatile matter and less energy density and heterogeneous composition which makes biomass adverse for bulk energy conversion compared to solid fossil fuels[22,23]. Advancement of the limitations, a pre-treatment process of biomass is required to improve physico-chemical properties and fuel energy[24,25].

2.1 Torrefaction technique

Torrefaction is a technology by which biomass attain a thermochemical conversion[23,24]. During the torrefaction process, biomass heated at temperatures between 200 and 300 °C for 1h or longer under low or oxygen free environment. Biomass pyrolysis and decomposition or gasification are typically followed after torrefaction technique. Typical processing stages of moist biomass involved to prepare solid torrefied biomass product is shown in **Fig. 3**. At the temperature range 200-300 °C, the torrefaction decomposition reaction takes place, is explained in the figure. The torrefaction time (t_{Tor}) is divided in three periods. In the first period ($t_{Tor,H}$), biomass attained the elevated temperature from 200 °C, followed by the holding period (t_{Tor}) at the torrefaction temperature. Finally, attain a cooling period $t_{Tor,C}$of the decomposed torrefied biomass. Generally, the decomposition reaction takes place during t_{Tor}, hence, heating and cooling period also have an effect on the reaction.

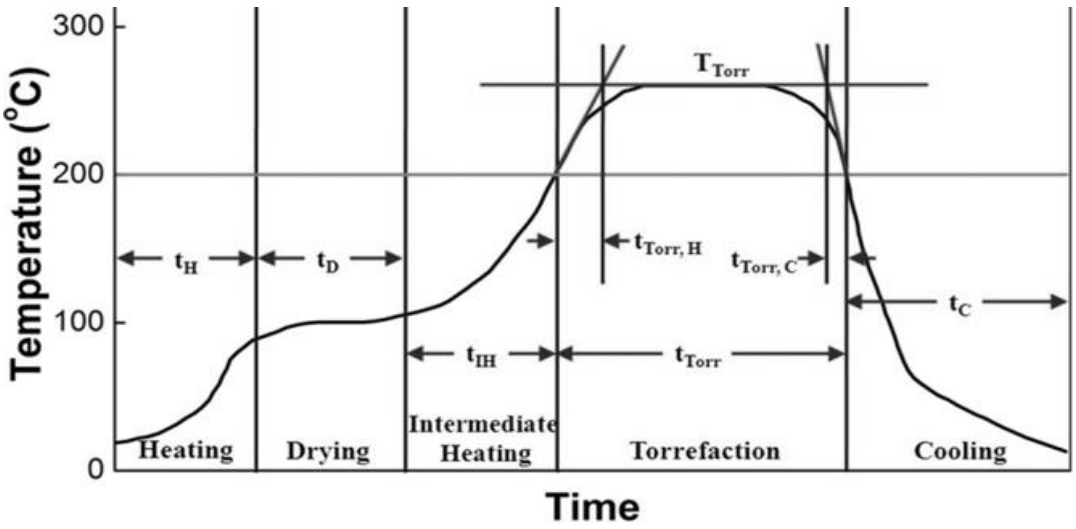

Fig. 3 Typical processing stages involved to prepare torrefied biomass product[26].

Table 1 Classification of torrefaction process and products formed during torrefaction[27].

Classification	Ultra-mild	Moderate	High
Temperature(°C)	200-230	230-270	270-300
Consumptions			
Hemicellulose	Mild	Moderate to high	High
Cellulose	Lesser	Lesser to moderate	Moderate to high
Lignin	Lesser	Lesser	Lesser
Product	Solid:	Ash and char	
	Liquid:	Water, alcohols, acetic acids, ketones and aldehydes	
	Gas:	Carbon monoxide, carbon di-oxide, hydrogen, toluene, methane, benzene and hydrocarbons.	

2.2 Classification and products of torrefaction

According to Chen et al.[27] based on process temperature, torrefaction of biomass can be classified into three i.e. ultra-mild, moderate and high, as shown in **Table 1**. The temperature ranges for the classifications are 200-230, 230-270 and 270-300 respectively. At ultra-mild temperature, both moisture and volatile matters of biomass feedstocks are released. Raw biomass is a combination of hemicellulose, cellulose and lignin. During torrefaction these three constituents thermally degrade and decomposed. Thus, both weight and energy of a biomass reduced whereas energy density of the biomass considerably increases.

Products obtained from torrefaction process are in the form of gas, liquid and solid, but solid fuel is the primary product for industrial applications. Carbon monoxide, carbon di-oxide, hydrogen, toluene, methane, benzene and some other hydrocarbons are non-condensable gas products. The condensable liquid torrefaction product includes water, alcohols, acetic acids, ketones and aldehydes. Whereas ash and char are the solid fuel obtained during torrefaction process. Depending on the torrefaction temperature, the colour of liquid product varies from brown to black.

2.3 Advancement of torrefaction technique

The development of torrefaction, can effectively replace biomass and improve the standard of solid biomass-derived fuel (biochar), has drawn an enormous contemplation in the past few years in an effort to overcome the antecedent limitations of natural biomass. Torrefaction has been researched and tried as a pre-treatment process to address these issues with woody biomasses, resulting in a high-quality, and easily grindable energy product for a variety of uses[28]. Torrefaction increases carbon content in biomass

and simultaneously reduces hydrogen and oxygen content[29]. As a result, some amount of volatile matter reduced which improve energy density of the biomass. Nowadays to obtain more fuel energy, natural biomasses such as saw dust, sugar cane bagasse, rice-wheat husk, bamboo dust etc. are replaced by solid torrefied biofuels[30-43]. Due to torrefaction, heating value of the biomass increased dramatically, composition improved and its properties can be comparable to coal. And torrefied biomasses may be used as a replacement of coal in various energy generation sectors. Torrefied biomasses are hydrophobic in nature, thus it loses the ability of water absorption during storage[44]. As a result of torrefaction, weight and combustion heat of a biomass reduced by 20 to 25% and increases about 25 to 30%, respectively. Improvement of combustion properties makes the biomasses more suitable for bio-fuel applications[17]. Recently torrefaction process design was investigated and advanced[45,46]. The woody biomass may be improved in terms of important solid fuel properties including heating value, powder flowability, grindability with an increase in torrefaction intensity (such as torrefied temperature and residence time)[6]. Number of studies are available in open source investigated the effect of various parameters such as different operating conditions, with or without oxygen, on torrefied biomasses using different types of feedstocks[47-52]. More research has recently studied on response mechanisms of torrefactionand its impact on biomass structures[53]. In a recent paper, Soria-Verdugo et al. proposed an extended 2-step first order kinetic mechanism which has an ability to predict kinetic mechanism of torrefaction process for biomass at inert and oxidative atmosphere[54]. However, still there is an inadequate result on application of torrefied biomass in industry.

3. Materials and Methods used for Torrefaction

3.1 Feedstock

Raw grass biomass, patula pine wood[55], saw dust[56-58], rice husk[36,37], sugarcane bagasse[35,59,60], fruit waste seed and shells[61-63], municipal solid waste[64-67] are generally used as feedstock for torrefied solid biomass. In the case of crop leftover like rice husk and wheat straw, sugar cane bagasse is mostly found as an agricultural residue in India. Whereas, plenty of raw grass, bamboo, wood, are also available in nature. Waste feedstock such as fruit waste seed and shells, municipal wastes.

3.2 Torrefaction process

Raw biomasses can be collected from various sources. To control the torrefaction reaction rate, large size biomasses are clipped into desired particle size (less than 2 mm) because the vapour generated during diffusion should get passage to escape through internal pores from the biomass pellet. To increase volumetric energy density, solid biomass particles are compacted using mechanical force (40-200 kg/m^3) to form pellets, briquettes or logs[68]. Generally, cylindrical pellets of maximum length 38 mm and 6-10 mm in diameter are used to prepare solid torrefied biofuel[69]. During biomass compaction temperature of the die should be maintained between 70 to 80 ºC. Low oxygen burner,

gas-to-gas heat exchanger, electrical immersion-type duct heater[70], microwave-assisted heating[71] or additional conventional heat sources are successfully used to prepare torrefied biomass. The seal reactors are continuously purged with inert gas, or nitrogen in case of non-oxidative torrefaction. During oxidative torrefaction process, oxygen gas is used and exothermic reaction takes place which accelerate torrefaction process due to higher decomposition rate[72-75]. To improve calorific value of torrefied biomass, wet torrefaction shows promising result at a low torrefaction temperature under high pressure. In case of wet torrefaction, feedstock biomasses are mixed with water, acids (acetic acid, citric acid, acrylic acid, sulphuric acid, etc.) or other materials (lithium chloride)[76]. Further, carbon content, hydrophobicity and calorific value as well as mechanical strength of torrefied biomass can be improved by pre-treating biomass using superheated steam[68]. It is required to cool the torrefied biomass immediately at room temperature to prevent oxidation with atmospheric oxygen[77].

4. Properties of Torrefied Biomass

4.1 Proximate and ultimate analysis

Proximate and ultimate analyses are required to study the variation of physico-chemical properties of torrefied biofuels. Typically, proximate analysis provides the information about volatile matter, ash, moisture and fixed carbon content of a biomass. Medic et al.[78] proposed an advance procedure of proximate analysis using thermogravimetric analyser based on modified ASTM D 5142-04[79]. Elemental composition of torrefied biomasses such as mass percent of carbon, hydrogen, nitrogen, sulphur, oxygen can be determined using ultimate analysis following the standard ASTM D5373-08[80]. **Table 2** shows proximate and ultimate analysis data of torrefied biofuels obtained from various literatures.

4.2 Heating value analysis

Friedl et al.[81] proposed a correlation between higher heating value (HHV) and weight percentage of elements obtained from ultimate analysis as shown in the following equation:

$$\text{HHV (kJ/kg)} = 3.55a^2 - 232a - 2230b + 51.2(a \times b) + 131c + 20600 \qquad (1)$$

where a, b and c are the carbon, hydrogen and nitrogen content respectively in weight percentage of dry torrefied biomass. Similarly, lower heating value (LHV) of torrefied biofuel can be correlated with HHV and moisture content and also expressed as:

$$\text{LHV (kJ/kg)} = \text{HHV} - 2260(9b + d) \qquad (2)$$

where d is the moisture content of torrefied biomass. Amount of moisture content can be obtained from proximate analysis. Generally, HHV is numerically determined with the product of water being in liquid state, whereas LHV is with the product of water in the steam state. HHV of torrefied biofuels obtained from various literatures are tabulated in

Table 2 Data of proximate, ultimate and high heating value analysis of torrefied biomasses.'

Sample	**Beech** [82]	**Eucalyptus** [83,84]	**Patula Pine**[85]	**Sawdust** [86]	**Willow** [87]	**Sugarcane bagasse**[88]	**Reed canary grass**[87]	**Wheat straw**[87]
Time (h)	1	1	0.5	0.5	0.5	1	0.5	0.5
Tempera-ture (°C)	240	280	250	250	250	250	250	250
Ultimate analysis								
C(wt.%)	51.70	63.5	51.46	47.16	51.7	50.6	50.3	49.6
H(wt.%)	5.40	5.3	5.86	5.01	6.1	5.6	6.3	6.1
O(wt.%)	42.90	30.9	42.02	35.52	38.7	43.5	37	35.6
N(wt.%)	0	0.2	0.14	0.55	0.2	0.3	-	0.9
Proximate analysis								
Volatile matter (wt.%)	80.60	53	82.52	64.79	79.8	65.49	80.3	77
Ash content (wt.%)	0.35	4.1	0.25	9.21	1.9	2.89	6.4	7.4
Fixed carbon content (wt.%)	19.20	42.9	17.24	23.74	18.4	26.82	13.3	15.6
High heating value (MJ/kg)	-	-	20.08	-	20.6	18.08	20	20.85

Prins et al.[89] proposed that if the content of xylan increase in hemicelluloses the rate of torrefaction reaction increases. HHV of biomass can be increased with increase in torrefaction temperature and residence time.

4.3 Grindability

Grindability of a biomass is an index which can be determined from the ratio between energy consumption during the experiment and quantity of the definite particle size distribution. Grindability of a torrefied biomass is also defined as a measure of its resistance during the crushing operation. Typically, grindability of a torrefied biomass

measured in a following manner. Laboratory cutting mill consist of cutting blade with a 0.5 mm sieve can be used to ground the torrefied biomass (standard mass 50 g). For grindability test, particle fraction size should be below 3 mm[90]. A digital wattmeter monitored power consumption during grinding. The grounded powder is sieved for a particular grade and weighed. The consumed specific energy for grinding of a torrefied biomass can be determined from the plot of power versus time by integrating the area under a curve with respect to required time for grinding for specific amount of biofuel. Grindability of a torrefied biomass can be expressed as the specific energy consumption per unit mass.

After torrefaction process, grindability index of a biomass improves due to increase in percentage of fine particles during torrefaction[91]. Grindability improves by weakening fibrous structure of a biomass[92]. Moisture and ash content is two primary factors by which grindability of torrefied biomass mostly affect[93].Wang et al.[94] describes energy required for torrefied pallet of wood, bark, and forest residues pellet as shown in **Fig. 4**. At low temperature and holding time the torrefied biomass shows higher energy consumption for grinding for all the three feedstock. Decrease in mechanical strength of torrefied biomass, results in decrease of grinding energy[90]. It indicates that the torrefaction temperature of biofuel increases grindability index[95].

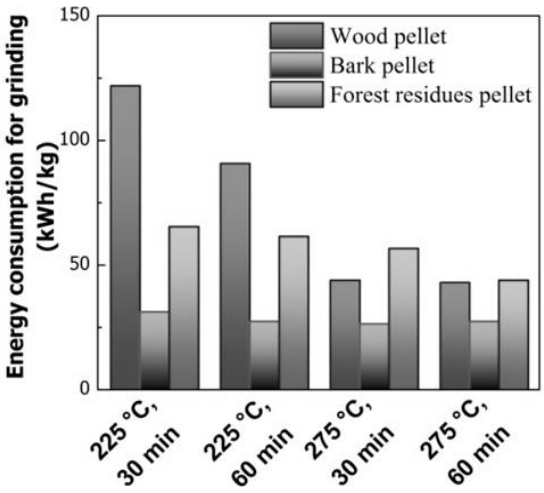

Fig. 4 Energy consumption for grinding of different biomasses[96].

To better understand the characterization of torrefied biomasses like wood dust[96], patula pine wood[55,97], rice husk[55], sugar cane bagasse[34], sawdust[98], municipal waste[64] and other materials, most frequently used techniques are derivative thermogravimetry (DTG), Scanning electron microscope (SEM), hydrophobicity test, x-ray diffraction (XRD), metallic elements, fourier transform infrared spectroscopy (FTIR) analysis, etc.

5. Conclusions

Biomass is not recognised as a worldwide resource like other fossil fuels because of inherent limitations including low bulk density, low energy density, stringy nature,

heterogeneity, hygroscopicity and other unavoidable causes. These limitations of biomass results some problems like transportation, storage and unsolicited putrefy. Those problems can overcome by the recent advancement in torrefaction process. With increase in torrefaction severity, overall phenomena and mechanical properties vary in an approachable manner. Till now extensive study on solid torrefied biomass has been done, whereas study on polymeric structure of biomass in torrefaction is inadequate. Similarly, investigation on by-product and torrefaction kinetics is also limited in open source. In addition, economic analysis must be included during assessing the unified torrefaction technique for commercialization of torrefied products.

References

1. F Manzano-Agugliaro, A Alcayde, FG Montoya, A Zapata-Sierra, C Gil. Renew. Sustain. Energy Rev. 2013; 18: 134–143.
2. CC Raj, R Prasanth. J Power Sources. 2016; 317: 120–132.
3. India Energy Outlook 2021. Energy report for India.
4. J Rockström, W Steffen, K Noone, A Persson, FS Chapin III, EF Lambin et al. Nature. 2009; 461: 472.
5. P Basu. Elsevier Inc., Burlington; 2010.
6. RS Carmona, DJ Matinez, FJ Perez. Ind. Crops Prod. 2018; 118: 302–310.
7. L Li, GK Liu, Y Li, Z Zhu, H Xu, J Chen, X Ren. ACS Omega. 2020; 5: 30001–30010.
8. KT Wu, CJ Tsai, CS Chen, HW Chen. Appl. Energy. 2012; 100: 52–57.
9. E Vainio. PhD Thesis. Åbo Akademi University; 2014.
10. S Kumar, R Seepaul, IM Small, S George, GK O'Brien, JJ Marois et al. Sustainability. 2021; 13:7355.
11. C Whittaker, I Shield. in: Greenhouse Gases Balances of Bioenergy Systems. Academic Press; 2018; 97–106.
12. A Demirbas. Biodiesel: A Realistic Fuel Alternative for Diesel Engines. Springer-Verlag London Ltd., London; 2008.
13. Ministry of New and Renewable Energy. Bio Energy Current Status for India, 2021.
14. JJ Chew, V Doshi. Renew Sustain Energy Rev. 2011; 15:4212–4222.
15. Ministry of Environment, Forest and Climate Change. India State of Forest Report 2021.
16. QV Bach, WH Chen. Bioresour. Technol. 2017; 246: 88–100.

17. DR Nhuchhen, P Basu, B Acharya. Int. J Renew. Energy. 2014; 2014: 1–56.

18. WH Chen, BJ Lin, YY Lin, YS Chu, AT Ubando, PL Show et al. Prog. Energy Combust. Sci. 2021; 82: 100887.

19. P Havlík, UA Schneider, E Schmid, H Böttcher, S Fritz, R Skalský et al. Energy Policy. 2011; 39: 5690–5702.

20. N Mosier, C Wyman, B Dale, R Elander, YY Lee, M Holtzapple et al. Bioresour. Technol. 2005; 96: 673–686.

21. TG Bridgeman, JM Jones, I Shield, PT Williams. Fuel. 2008; 87: 844–856.

22. JL Wen, SL Sun, TQ Yuan, F Xu, RC Sun. Appl. Energy. 2014; 121: 1–9.

23. TR Sarker, S Nanda, AK Dalai, V Meda. Bioenerg. Res. 2021; 14: 645–669.

24. TR Sarker, R Azargohar, AK Dalai, V Meda. Energy Reports. 2021; 7: 6338–6353.

25. TA Mamvura, G Danha. Heliyon. 2020; 6: 03531.

26. PCA Bergman, MJ Prins, AR Boersma, KJ Ptasinski, JHA Kiel, FJJG Janssen. Energy Research Centre of the Netherlands. 2004.

27. WH Chen, J Peng, XT Bi. Renew. Sustain. Energy Rev. 2015; 44: 847–866.

28. J Kemper. Int. J Greenhouse Gas Control. 2015; 40: 401–430.

29. B Acharya, A Dutta. Biomass. Conv. Bioref. 2006; 6: 139–149.

30. H Li, X Liu, R Legros, XT Bi, CJ Lim, S Sokhansanj. Bioresour. Technol. 2011; 103(1): 453–458.

31. AR Mohamed, NNA Nordin, NH Md Salle. J Adv. Res. Eng. Knowledge. 2019; 6(1): 7–14.

32. P Alizadeh, LG Tabil, PK Adapa, D Cree, E Mupondwa, B Emadi. Fuels. 2022; 3(1): 152–175.

33. K Manatura. Case Stud. Therm. Eng. 2020; 19: 100623.

34. Daniyanto, Sutidjan, Deendarlianto, A Budiman. Energy Procedia. 2015; 68: 157–166.

35. M Valix, S Katyal, WH Cheung. Environ. Technol. 2017; 38: 1638–1643.

36. A Irawan, H Alwan, D Satria, F Saepurohman, A Kurniawan. AIP Conf. Proc. 2019; 2085: 020021.

37. D Chen, A Gao, Z Ma, D Fei, Y Chang, C Shen. Bioresour. Technol. 2018; 253: 148–153.

38. SK Satpathy, LG Tabil, V Meda, SN Naik, R Prasad. Fuel. 2014; 124: 269–278.

39. OS Agu, LG Tabil, E Mupondwa, B Emadi. Front. Energy Res. 2021; 9: 699657.

40. AN Sakkour, AM Al-Abdullah. Am. J Eng. Res. 2020; 9: 185–190.

41. G Sridhar, DN Subbukrishna, HV Sridhar, S Dasappa, PJ Paul, HS Mukunda. in: 15th European Biomass Conference & Exhibition, Berlin, Germany; 2007.

42. M Alam, D Rammohan, A Bhavanam, NR Peela. Fuel. 2021; 285: 119188.

43. MF Li, Y Shen, JK Sun, J Bian, CZ Chen, RC Sun. ACS Sustain. Chem. Eng. 2015; 3: 2022–2029.

44. VF Kosov, JS Kuzmina, GA Sytchev, VM Zaichenko. J Phys. Conf. Ser. 2016; 774: 012139.

45. P Basu. in: Biomass Gasification, Pyrolysis and Torrefaction. 3rd Ed. Elsevier; 2018; 93–154.

46. JS Tumuluru, S Sokhansanj, CT Wright, RD Boardman, JR Hess. in: 2011 ASABE Annual Int. Meeting; 1110459: 1–39.

47. KM Lu, WJ Lee, WH Chen, SH Liu, TC Lin. Bioresour. Technol. 2012; 123: 98–105.

48. Y Uemura, W Omar, NA Othman, S Yusup, T Tsutsui. Fuel. 2013; 103: 156–160.

49. WH Chen, KM Lu, WJ Lee, SH Liu, TC Lin. Appl. Energy. 2014; 114: 104–113.

50. Z Wang, H Li, CJ Lim, JR Grace. Energy Convers. Manage. 2018; 174: 276–287.

51. C Zhang, SH Ho, WH Chen, Y Fu, JS Chang, X Bi. Appl. Energy. 2019; 235: 428–441.

52. D Chen, F Chen, K Cen, X Cao, J Zhang, J Zhou. Fuel. 2020; 275: 117936.

53. N Abdoulmoumine, S Adhikari, A Kulkarni, S Chattanathan. Appl. Energy. 2015; 155: 294–307.

54. A Soria-Verdugo, E Cano-Pleite, A Panahi, AF Ghoniem. Energy Convers. Manage. 2022; 267: 115892.

55. A Irawan, H Alwan, D Satria, F Saepurohman, A Kurniawan. AIP Conf Proc. 2019; 2085:020021.

56. H Li, X Liu, R Legros, XT Bi, CJ Lim, S Sokhansanj. Bioresour. Technol. 2012; 103(1): 453–458.

57. AR Mohamed, NNA Nordin, NH Md Salle. J Adv. Res. Eng. Knowledge. 2019; 6: 7–14.

58. P Alizadeh, LG Tabil, PK Adapa, D Cree, E Mupondwa, B Emadi. Fuels. 2022; 3(1): 152–175.

59. K Manatura. Case Stud. Therm. Eng. 2020; 19: 100623.

60. Daniyanto, Sutidjan, Deendarlianto, A Budiman. Energy Procedia. 2015; 68: 157–166.

61. YL Lin, NY Zheng. Energy. 2021; 225: 120226.

62. YY Gan, HC Ong, TC Ling, WH Chen, CT Chong. Energy. 2019; 170: 367–374.

63. E Bilgic, S Yaman, H Haykiri-Acma, S Kucukbayrak. Fuel Process. Technol. 2016; 144: 197–202.

64. KA Abdulyekeen, AA Umar, MFA Patah, WMAW Daud. Renew. Energy Rev. 2021; 150: 111436.

65. M Li, H Wang, Z Huang, X Yuan, M Tan, L Jiang et al. Energy Convers. Manage. 2020; 213: 112793.

66. YP Rago, FX Collard, JF Görgens, D Surroop, R Mohee. Fuel. 2020; 277: 118089.

67. KL Iroba, OD Baik, LG Tabil. Biomass. Bioenergy. 2017; 106: 8–20.

68. WH Chen, J Peng, XT Bi. Renew. Sustain. Energy Rev. 2015; 44: 847–866.

69. LJR Nunes, JCDO Matias, JPDS Catalão. in: Torrefaction of Biomass for Energy Applications: From Fundamentals to Industrial Scale. Elsevier; 2018. 125–141.

70. WB Teal, RJ Gobel, A Johnson. Biomass Torrefaction System and Method. US Patent US20130228444A1; 2013.

71. WH Chen, SC Ye. Bioresour. Technol. 2012; 118: 195–203.

72. MX Fang, DK Shen, YX Li, CJ Yu, ZY Luo, KF Cen. J Anal. Appl. Pyrolysis. 2006; 77: 22–27.

73. LF Calvo, M Otero, BM Jenkins, A Morán, I García. Fuel Process. Technol. 2004; 85: 279–291.

74. W Chiang, H Fang, C Wu, C Chang, Y Chang, J Shie. J Environ. Eng. 2008; 134: 316–325.

75. C Wang, J Peng, H Li, XT Bi, R Legros, CJ Lim et al. Bioresour. Technol. 2013; 127: 318–325.

76. JG Lynam, CJ Coronella, W Yan, MT Reza, VR Vasquez. Bioresour. Technol. 2011; 102: 6192–6199.

77. W Stelte. Best Practice Guideline-Storage and Handling of Torrefied Biomass, Danish Technological Institute, Denmark, 2015.

78. D Medic, M Darr, A Shah, BJ Potter. Fuel. 2012; 91: 147–154.

79. ASTM D 5142-04. ASTM Standards, vol. 05.06; 2008.

80. D5373-08. Annu. B ASTM Stand. 5:1–9.

81. A Friedl, E Padouvas, H Rotter, K Varmuza. Anal. Chim. Acta. 2005; 544: 191–198.

82. C Couhert, S Salvador, JM Commandré. Fuel. 2009; 88: 2286–2290.

83. B Arias, C Pevida, J Fermoso, MG Plaza, F Rubiera, JJ Pis. Fuel Process. Technol. 2008; 89: 169–175.

84. G Almeida, JO Brito, P Perré. Bioresour. Technol. 2010; 101: 9778–9784.

85. M Phanphanich, S Mani. Bioresour. Technol. 2010; 102: 1246–1253.

86. Q Chen, J Zhou, B Liu, Q Mei, Z Luo. Chin. Sci. Bull. 2011; 56: 1449–1456.

87. TG Bridgeman, JM Jones, I Shield, PT Williams. Fuel. 2008; 87: 844–856.

88. M Pach, R Zanzi, E Bjornbom. in: 6th Asia-Pacific International Symposium on Combustion and Energy Utilization. 2002; 25.

89. MJ Prins, KJ Ptasinski, FJJG Janssen. J Anal. Appl. Pyrolysis. 2006; 77: 35–40.

90. M Tymoszuk, K Mroczek, S Kalisz, H Kubiczek. Energy. 2019; 183: 116–126.

91. JJ Chew, V Doshi. Renew. Sustain. Energy Rev. 2011; 15: 4212–4222.

92. KS Kung, SK Thengane, AF Ghoniem. Fuel Process. Technol. 2020; 202: 106362.

93. SS Lam, WAW Mahari, YS Ok, W Peng, CT Chong, NL Ma et al. Renew. Sustain. Energy Rev. 2019; 115: 109359.

94. L Wang, L Riva, Ø Skreiberg, R Khalil, P Bartocci, Q Yang et al. Energy Fuels. 2020; 34: 15343–15354.

95. P Basu. in: Biomass Gasification, Pyrolysis and Torrefaction (2nd Ed.)-Practical Design and Theory. 2013; 353–373.

96. KH Wong, WT Chong, NL Sukiman, SC Poh, YC Shiah, CT Wang. Renew. Sustain. Energy Rev. 2017; 73: 904–921.

97. M Phanphanich, S Mani. Bioresour. Technol. 2010; 102: 1246–1253.

98. Q Chen, J Zhou, B Liu, Q Mei, Z Luo. Chin. Sci. Bull. 2011; 56: 1449–1456.

A Comprehensive Review of Biological Applications of Essential Oils

Pinku Chandra Nath[a], Rupak Roy[b], Dibyajit Lahiri[c], Moupriya Nag[c]

Abstract

Essential oils (EOs) are volatile organic molecules, having oily fragrances. The most reliable procedure for extracting EOs from various plants is the hydro distillation techniques which has been reported to be used friendly and economically sustainable. EOs are extracted from various plant parts including flowers, bark, leave, stems, and roots. EOs is used in almost every aspect of life, and the market demand for EOs is rapidly expanding as a result of these characteristics. Aromatherapy employs EOs, which act as anti-oxidants, anti-microbials, anti-fungals, pain relievers, anxiety relievers, and anti-depressants. EOs are also rapidly gaining popularity in the cosmetics, manufacturing, and perfume industries. In food preservation, EOs have notable cognizance. EOs have been involved in the improvement of mood and are used as an anti-depressant as per folk herbal medicines owing to their fragrances. The biological properties of EOs and their effectiveness in new applications that have recently been explored and developed, particularly in the food, cosmetics, and public health fields, are the focus of this study. Furthermore, the potential for EOs to be used in alternative treatments for a variety of infectious diseases has been portrayed in this study. Accordingly, the present scheme of study adopted in this review will be beneficial to various stakeholders and will open new avenues for research in this particular field.

Keywords: Essential oils (EOs); Food preservations; Anti-oxidant; Anti-microbial; Anti-fungal.

1. Introduction

The use of EOs has been used in folk medicine for ages. Mainly the EOs are derivatives of different lignocellulosic biomasses[1,2]. The production of EO involves different process parameters that require extensive process intensification and optimization for the maximized production of EOs[2]. Sometimes the extraction of EOs involves the application of various microorganisms and enzymes[3]. EOs are fragrant oils extracted from diverse sectional plants and used as common food aromas, known as ethereal or volatile oils. An EO is claimed to have the embodiment of various fragrances as well as the plant [14]

characteristics from which their origination occurs. Anti-bacterial, anti-oxidant, antiviral, insecticidal, and other biological activities were demonstrated in these volatile oils. These

[14] ✉ Rupak Roy

rupak@shrmbio.com

[a]Department of Bio Engineering, NIT Agartala, Tripura, 799046, India

[b]SHRM Biotechnologies Pvt. Ltd., Kolkata, West Bengal, 700155, India

[c]Department of Biotechnology, UEM Kolkata, West Bengal, 700160, India

oils are likewise used to treat disease, and some have been utilized in food safeguarding, fragrant healing, and the perfumery businesses[4]. EOs anti-microbial and anti-oxidant properties are utilized in an assortment of utilizations, including handled and new food conservation, regular treatments, drugs, and elective medication[5]. In view of the aromatic compounds present in EOs, they have been utilized in fragrance-based treatment as an elective wellspring of wound recuperating. It's also used for relaxation, but this evidence isn't taken into under concern. Various endeavors are being made to research the utilization of EOs as a treatment for an assortment of irresistible illnesses that are inert to drug medicines. Plants with therapeutic and fragrant properties are generally utilized as regular natural mixtures and as medications[6]. Beforehand, EOs was utilized to treat an assortment of irresistible infections from one side of the planet to the other. EOs are turning out to be progressively significant in this day and age, as they are utilized in the beverage and food industries, beautifying agents, and scent enterprises to make important fragrances, and have an assortment of natural exercises[7].

Different EOs have been utilized for insecticidal exercises against different vermin, however, definite investigations have uncovered that they need repellence, anti-fungal, phytochemistry, oviposition, and avicidal properties. The EOs don't have the attributes recorded above however, there is as yet a squeezing need to deal with these aspects of assessment and conduct both in vitro and in vivo experiments to prevent irritations, and the vast majority of the oils have demonstrated excellent cancer-prevention agent activity[8]. EOs with high anti-oxidant activity activates and acts as a defence against the unsaturation of lipids in animal tissue as well as serving as hepatoprotective agents in mammals[9]. Anti-oxidant compounds are generally significant for people since oxygen is a poisonous component that can change metabolic exercises into the most responsive oxygen type including superoxide, H_2O_2, hydroxyl free radicals, and singlet O_2, which are widely referred to as dynamic oxygen[10]. EOs is most popular for their anti-microbial, anti-viral moderators, anti-spasmodic, and carminative properties, and the EO's structure changes; they likewise show an assortment of exercises that are generally subject to the chemotypes[11].

2. EOs Sources and Isolation

Distinctive fragrant plants were utilized to separate EOs. These plants can be found in tropical and Mediterranean nations. These plants have acquired unmistakable quality because of the way that they are utilized to treat infections by the neighbourhood populace. EOs is delivered in all aspects of the plant, including the leaves, seeds, buds, stem, blossoms, and leaves. The epidermic cell, cavities, secretary cells, and channels accumulate Eos[12]. EOs is responsible for the odor produced by plants. EOs was extricated from plant materials that were dried, new, or part of the way dried out. The pace of extraction is dictated by dispersion through plant tissues, which straightforwardly include the surface from which the EOs was separated through different cycles. The solidness of

the EOs decides how well it tends to be extricated. As displayed in **Fig. 1**, the steam refining strategy and the hydro refining measure are the two most normal strategies for separating EOs. For extraction measures, these are the most proper and successful methods[13]. Other extraction techniques have been utilized; however; they are not truly appropriate for this interaction, like pressure (high and low) distillation utilizing heated water or steam water[14].

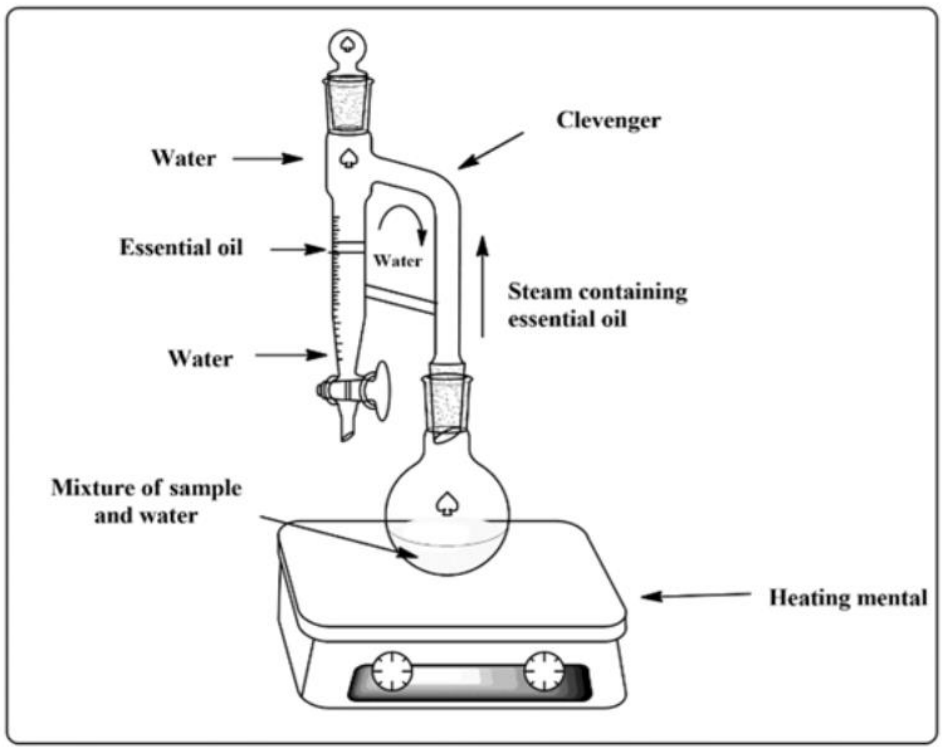

Fig. 1 Extraction of EOs using hydro-distillation equipment.

EOs extricated utilizing the steam distillation technique are, for the most part, utilized in pharmacological exercises and food things, while EOs utilized in the scent or fragrance industry are separated by utilizing lipophilic solvents and incidentally supercritical carbon dioxide to make them extra appealing[15]. The quality of water used for the preparation and extraction of EO is of immense importance[2]. The nature of the EOs was dictated by the age of the plants, the parts utilized for extraction, the phase of the vegetative cycle, the impact of the environment, and different elements. The spectroscopic and chromatographic procedures totally changed the synthetic investigation of EOs. UV-Vis spectroscopy, IR-spectroscopy, NMR spectroscopy, and gas chromatography were utilized to investigate the chemical composition of Eos[16]. The increased demand for EOs in a variety of contexts of life prompted us to seek out efficient techniques for evaluating them, and the technologies we employed were GC and GC-MS analyses[17]. The gas chromatography technique was used to characterize the EOs. The compounds found in the EOs were confirmed using GC and GC-MS methods[18].

Because EOs are dumped in oil glands in the organization of plant material, their yield and quality are also affected by their storage and handling[18].

3. Chemical Composition of EOs

EOs are extremely complex natural mixtures that can contain anywhere from 20-60 components in varying concentrations. They have a few major components that are present in relatively high concentrations (20 to 70%) contrasted with different components that are present in trace amounts. These significant segments, by and large, choose the natural.

properties of EOs. The components are divided into two groups based on their biosynthetic origin. The main group is made up of terpenes and terpenoids, while the other is made up of aromatic and aliphatic constituents, all of which have a low molecular weight **Fig. 2**.

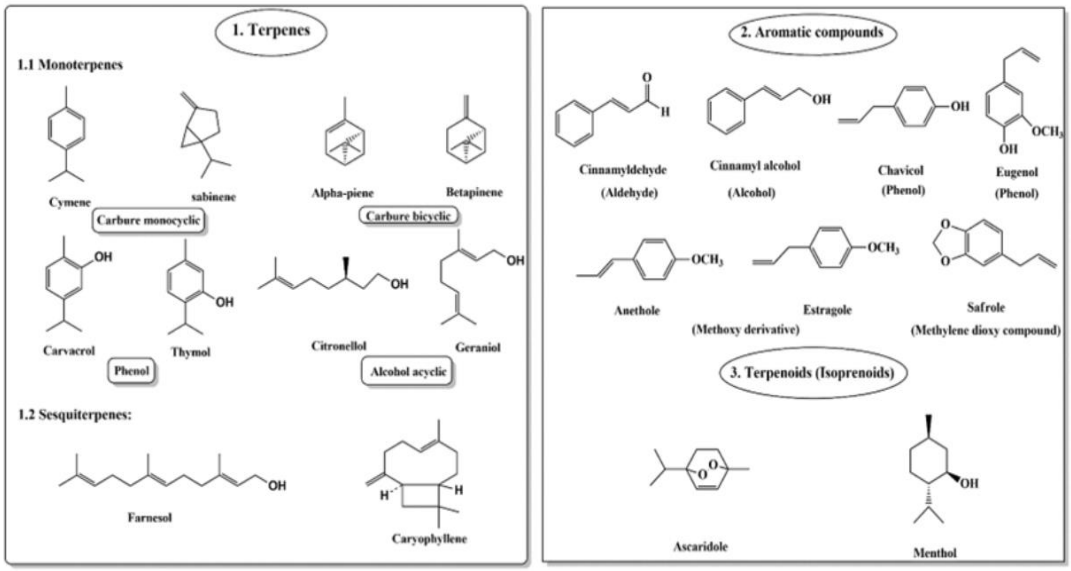

Fig. 2 Chemical structures of EOs components.

4. Biological Properties of EOs

EOs have been utilized as perfumes, and flavoring compounds in the perfume and culinary industries since ancient times[19]. EOs is utilized for hair care and skin in the cosmetics industry as well as perfumes because of their biological characteristics to protect our bodies against exogenous or hazardous specialists. Traditionally, they have been used in Chinese (Zhong Yo) and Indian (Ayurveda) medicines for pharmaceutical and medicinal purposes[19]. Glioma, colon and gastric malignancy, liver tumor, pneumonic tumor, bosom disease, and leukemia have all been connected to the biological properties of EOs. EOs is used in fragrant healing and back rubs for their potential anti-inflammatory behavior toward cardiovascular diseases, microorganisms and infections, oxidation, and diabetes[20]. They are likewise known for their additive and cancer

prevention agent properties, which ensure against an assortment of constant infections and can be utilized as a characteristic option in contrast to traditional treatment (**Table 1**).

Natural products are becoming increasingly interested in finding active ingredients that have both anti-microbial and anti-oxidant properties to increase food stability by inhibiting microorganism growth and protecting food from oxidation. EOs was tested as a substitute for synthetic food additives by several authors[21,22].

The variability of EOs (as a result of their chemical composition) has a significant impact on their unique physico-chemical properties. The natural impact of EOs is controlled by the focus utilized (by and large, a higher fixation has a more prominent organic impact), just as the microorganisms tried (contagious are more delicate than microbes), tests carried out, as well as information on the main components of the oil. Minor segments, then again, might be basic to the movement[23].

Table 1 Biological properties of different EOs and their uses

Essential oil	**Scientific name**	**Applications**	**Reference**
Black cumin	*Nigella sativa* L.	Breast cancer	(Periasamy et al., 2016)
Onion	*Allium cepa* L.	Antimicrobial	(Ye et al., 2013)
Rosemary	*Rosmarinus officinalis* L.	Antioxidant	(Nieto et al., 2018)
Savory	*Satureja hortensis* L.	Antifungal	(Razzaghi-Abyaneh et al., 2008)
Oregano	Origanum vulgare L.	Anti-inflammatory	(Ocana-Fuentes et al., 2010)
Lemon balm	*Melissa officinalis* L.	Antidiabetic	(Yen et al., 2015)
Cumin	*Cuminum cyminum* L.	Hepatoprotective	(Razzaghi-Abyaneh et al., 2008)
Lavender	*Lavandula angustifolia* Mill.	Analgesic	(Ghods et al., 2015)
Cinnamon	*Cinnamomum zeylanicum*Blume	Antimicrobial	(Unlu et al., 2010)
Tasmanian blue gum	*Eucalyptus globules* Labill.	Antioxidant	(Damjanović-Vratnica et al., 2011)

Apple mint	*Mentha rotundifolia* L.	Insecticidal	(Yakhlef et al., 2020)
Nazar Panra	*Skimmialaureola*Franch.	Antinociceptive and antipyretic	(Bhalla et al., 2021)
Spanish sage	*Salvia lavandulifolia*Vahl.	Treatment of neurodegenerative diseases	(Porres-Martínez et al., 2015)
Ginger oil	*Zingiber officinale*	Promotes sweating, expectorant, prevents vomiting	(Preethi et al., 2010)
Hyssop oil	*Hyssopus officinalis*	Nervous exhaustion and relaxing nerves	(Aćimović, 2021)
Root oil	*Angelica glauca*	Antioxidant, antifungal, antibacterial, and phytotoxicity	(Sowndhararajan et al., 2017)
Leaf oil	*Plectranthusrugosus*	Antifungal, antioxidant, antibacterial	(Aleksic & Knezevic, 2014)
Rose oil	*Rosa species*	Astringent, kidney tonic and blood tonic	(Ayati et al., 2018)
Mandarin oil	*Citrus reticulata*	Stress and wrinkles, acne, insomnia	(Patel & Gogna, 2015)
Plai oil	*Zingiber cassumunar*	Uterine relaxant, inflammatory	(Bhuiyan et al., 2008)
Elemi oil	*Canarium luzonicum*	Coughs, healing wounds, stress	(Worwood, 2016)
Carrot seed oil	*Daucus carota*	Detoxification, eczema	(Saleh et al., 2019)
Celery seed oil	*Apium graveolens*	Antifungal diuretic and blood pressure	(Kooti et al., 2015)
Geranium oil	*Pelargonium graveolens*	Acne, and menopause	(Kozlowska et al., 2017)
Myrtle oil	*Myrtus communis*	Sore throat, asthma, coughs	(Aleksic & Knezevic, 2014)
Vetivert oil	*Vetiveriazizanoides*	Insomnia, muscle aches, anti-depressant	(Bouaziz et al., 2009)

The possibility of a synergy between an EO and the components increases their action spectrum to improve the efficiency of EO[24-26]. In assessing its biological activity, such synergistic effects between minor and major substances in EOs must be considered[27]. When the combined effect is less than the individual effect, an antagonistic effect may be observed[28]. If the combined effect of EO compounds is the same as the sum of individual effects, an additional effect may be generated. The combined effect is greater than the sum of the individual effects of the substances. These consequences can depend on each EO component's composition and each EO concentration[29]. Synergism has the advantage of requiring significantly lower individual concentrations to achieve the same effect than combining two or more EOs. A significant decrease in undesirable sensory influence could be achieved by using certain oils because of their strong aroma. Thus, synergism and antagonistic connections between the EOs can influence their biological activity in positive and negative ways[30].

Previously Researched and demonstrated[28] the anti-microbial synergism of thyme and oregano essential oils[31] also demonstrated the synergy of *R. officinalis* and *O. vulgare* EOs against *Aeromonas hydrophilla, Yersinia enterocolitica,* and *Listeria monocytogenes* bacteria, as well as the combined anti-bacterial effect of these EOs against *Pseudomonas fluorescens* bacteria. Combination of cinnamon and clove EOs inhibited *Escherichia coli* growth[32]. These EOs, both individually and in combination, on the other hand, had the same activity against *E. coli* growth at higher concentrations. As a result, a concentration-dependent synergistic, antagonistic, or additive effect could exist. α-tocopherol and *Thymus numidicus* EO have a synergistic anti-oxidant interaction[33]. The synergistic effects of mixing components of different EOs as well as their anti-bacterial interactions with *E. coli* have been reported[34].

5. Modern Trends of EOs

EOs has a wide scope of uses in an assortment of items all throughout the planet, including frozen yogurts, scents, sponsored food, refreshments, and makeup. According to recent research, somewhere around 300 EOs out of 3000 are monetarily significant in an assortment of ventures like perfume and clean businesses, beautifiers, food, refreshment, agronomics, and drugs[35]. A portion of the bioactive parts found in EOs incorporate limonene, geranyl acetic acid derivation, carvone, and others, which are significant segments of sterile items and tooth glues. EOs is utilized to protect food added substances, treat normal sicknesses and people drugs, and is utilized by fragrance specialists. As a natural anti-oxidant, EOs is used. Natural anti-oxidants are commonly used in protective medicines and foods, and as a result, EOs is becoming increasingly popular[36]. Newly, there has been a surge in interest in the use of volatile EOs for restorative purposes and in the treatment of infectious disorders[37].

EOs are extensively used in textile, paint, plastics, and pharmaceuticals industry as well as in perfume, cleanliness, and aromatherapy; which includes inward breath, back rub,

and masking agents to avoid unpleasant odors[34]. Many types of cereals, anti-microbial food packaging, edible thin film, nano-emulsion, fruit and vegetable preservation, soft drinks, as flavor enhancers in carbonated beverages, key constituents in soda and citrus concentrates, and seafood preservation all use EOs[38,39].

6. Increasing EOs Adaptation Trends

EOs is plant extract-derived products that have been utilized for industrial and home-made items. Pest control solutions, cleaning acts, and anti-inflammatory are just a few of the products and personal care products that include EOs[40]. EOs can help with wound healing, regeneration, and relaxation, among other things. Alongside their applications in the improvement of medical problems, EOs fixes the most well-known medical problems like headaches and sickness[41]. It is also used in the food industry due to its preservative potential in comparison to food-borne pathogens, as well as its anti-microbial, anti-bacterial, and anti-fungal properties[42]. The utilization of fragrance-based treatment as orchestrating care is expanding because of its extraordinary qualities, which incorporate the capacity to adapt to a portion of the symptoms of disease and to advance injury recuperating[43].

7. Several Foremost EOs and their Applications

7.1 Carvacrol

Carvacrol is one of the most significant essential oils found in oregano and thyme oils. It contains a hydroxyl group on the phenolics ring, which is a phenolic compound[44,45]. Hydrophobic p-cymene, biological predecessor of carvacrol, induces a greater enlargement of the cytoplasmic membrane[46]. When used alone, p-cymene is ineffective as an antibacterial agent. The improved performance of p-cymene implementation into Bacillus cereus's lipid bilayer presumably enhances the transmission of carvacrol throughout the cytoplasmic membrane[47]. The anti-microbial activity of oregano, thyme, and savory is most likely due to the volatile terpenes carvacrol, p-cymene, and thymol. Carvacrol is considered as an important monoterpenoid with anti-bacterial action against Botrytis, which completely inhibits spore germination and the enhancement of mycelium in potato dextrose agar[48].

7.2 Eugenol

Clove oil (Approximately 85%) contains a significant amount of the compound eugenol. *B. cereus* amylase and protease production have been shown to be inhibited by eugenol concentrations below the lethal threshold[49]. Deterioration of the cell wall and extensive cell lysis has also been noticed. Eugenol's hydroxyl group binds to proteins, inhibiting *E. aerogenes* enzyme action. Two apple cultivars have been applied with various formulations that included eugenol oil (*Eugenia caryophylata*) and efficiently decreased disease severity following cold storage[50].

7.3 Bergamot

The bitter orange tree is the EO of bergamot extracted from the peelings of the *Citrus bergamia*. The bergamot concentrate is used to enhance Earl Gray tea, and the EO of this is also utilized for the similar reason. It's useful in the treatment of skin infections, lowers fever, heals stomach-related framework disorders, and clears chest congestion[51].

7.4 Clove

It's created from the *Syzygiumaromaticum L.* tree's fragrant flower buds, which are endemic to the Indonesian island of Maluku. Clove essential oil has a strong fragrance and is used to flavor foods; it is also used in medicine for pain relief, dental disorders, nausea treatment, inflammation reduction, digestive ailment treatment, and acne treatment[52,53].

7.5 Thymol

Thymol is structurally like carvacrol, with the hydroxil group on the phenolic ring in a different location. Zataria oil and thyme oil are two other EOs that have been discovered to be viable against microorganisms and parasites and are utilized to control plant sicknesses, for the most part on organic product[54].

7.6 Eucalyptus

It comes from the Eucalyptus genus and its numerous species. Every species has a distinct and unique application in each field. The most well-known EO extracted from *Eucalyptus globulus* smells minty. It's utilized as a decongestant chest rub, pain reliever, and antibacterial mediator. It's also used in aromatherapy to help with mental clarity, energy, and as a natural bug repellant[9].

7.7 Frankincense

The earliest known and the most useful essential oil is Frankincense and it is obtained from the resin of the four species of the generous *Bowwellia* and the most known from this genus is the *Bowsellia carterii* hard tree which grow in the arid land of Arabian Peninsula and north eastern[55]. The EOs of Frankincense was used in stringent and solemn services by the ancient Africans. The Frankincense EOs is one of a kind from any remaining got essential oils due to the ideal mix of wood, citrus, earth, and resin[56]. It is utilized as a mood enhancer, anti-bacterial, stress reducer, for quicker twisted recuperating, help in absorption, calming, blurs scars, diminishes growing of bug nibbles, for the treatment of skin illnesses, and facilitates tingling.

7.8 Lavender

English lavender, the most popular garden herb, contains the most potent EOs produced from *Lavandula angustifolia*[57]. It has the same sweet, floral, and green odor as the blossoms from which it is extracted and the health benefits are greater than the fragrance. The best use of lavender EOs is for its calming and sleep-inducing properties. It has anti-

oxidant, anti-bacterial, anti-inflammatory, and anti-fungal qualities, and it's applied to treat eczema, ringworm, and acne, among other skin disorders[58]. Lavender essential oils are used to aid digestion, reduce swelling in sore muscles, and alleviate pain. It is engaging smell draws in butterflies, honey bees, and a few pollinators, and it likewise goes about as a characteristic anti-agent for some flying insects[58].

7.9 Lemon

Lemon EOs is the most commonly used. *Citrus limon* EO is widely used around the world[59]. Lemon EO is used as an anti-microbial agent in a variety of household products, soaps, polishing items, furnishings, room spray, and cleaning items. Additional advantages of these EOs include pain relief, anti-fungal activity, aid in weight loss, and relief from nausea; Lemon EO is often used in aromatherapy to help alleviate stress and anxiety while also enhancing mood and concentration[60]. Additionally, it is outstanding for washing hair and encouraging natural hair growth.

7.10 Oregano

Origanum vulgare, a household spice, yielded oregano essential oil. It is the ideal blend of earthiness, spice, and warmth. The aroma of an EO bottle has an influence on the senses when it is opened. Oregano EO is becoming more popular, and it's usually used to treat skin conditions and also treat menstrual problems and painful menstrual cramps, as well as stomach problems, and to aid in the control of flu and cold infections[13].

7.11 Peppermint

Peppermint EO is extracted from the *Mentha piperita* plant and is used all over the world[61]. Among EO users and gardeners, this is the most popular mint hybrid. It is the most well-known form of EO due to its wide range of applications. It is widely used to prevent flu and colds, ease headaches, reduce muscular and joint discomfort, clear skin issues, alleviate nausea, and improve digestive system operations[61].

8. Conclusions

EOs is natural volatile compounds with a pleasant scent. To isolate the EOs, the hydro distillation technique is used, which is more appropriate for this procedure and easier to transport. Plant extraction involves the use of all plant parts. EOs is applied to treat a wide range of ailments, including infectious diseases, depression, and anxiety. These compounds are also utilized as anti-fungal, anti-cancer, anti-bacterial, and wound healers in cosmetics and fragrances industries. EOs is becoming more popular in the medical field, where they are generally applied to outer body parts to mitigate torment. EOs is used in the perfume industry due to their appealing odour. It is used all over the world, and as a result of increased usage, the global EO market is rapidly expanding and gaining importance.

References

1. R Roy, S Ray. Energy Sources Part A. 2019; 1.
2. R Roy, D Debnath, S Ray. Arab. J Sci. Eng. 2022; 47(9): 5935.
3. A Manipura, JR Duncan, HJ Roman, JE Burgess. Process Saf. Environ. Prot. 2005; 83(11): 472.
4. OY Celiktas, EEH Kocabas, E Bedir, FV Sukan, T Ozek, KHC Baser. Food Chem. 2007; 100: 553.
5. M Kelen, B Tepe. Bioresour. Technol. 2008; 99: 4096.
6. B Tepe, D Daferera, AS Tepe, M Polissiou, A Sokmen. Food Chem. 2007; 103: 1358.
7. JL Ríos, MC Recio. J Ethnopharmacol. 2005; 100: 80.
8. HJD Dorman, SG Deans. J Appl. Microbiol. 2000; 88: 308.
9. V Aleksic, P Knezevic. Microbiol. Res. 2014; 169: 240.
10. A Rahal, A Kumar, V Singh, B Yadav, R Tiwari, S Chakraborty et al. Biomed Res Int. 2014; 2014: 1.
11. N Mimica-Dukić, B Božin, M Soković, B Mihajlović, M Matavulj. Planta Med. 2003; 69: 413.
12. AH Gilani, A Khan, Q Jabeen, F Subhan, R Ghafar. J Ethnopharmacol. 2005; 100: 347.
13. T Kulisic, A Radonic, V Katalinic, M Milos. Food Chem. 2004; 85: 633.
14. N Bousbia, MA Vian, MA Ferhat, E Petitcolas, BY Meklati, F Chemat. Food Chem. 2009; 114: 355.
15. A Donelian, LHC Carlson, TJ Lopes, RAF Machado. J Supercrit. Fluids. 2009; 48: 15.
16. AI Hussain, F Anwar, STH Sherazi, R Przybylski. Food Chem. 2008; 108: 986.
17. P Bhalla, YC Tripathi, VK Varshney. J Essent. Oil Res. 2021; 33: 315.
18. SF Van Vuuren, AM Viljoen, T Ozek, B Demirci, KHC Baser. S Afr. J Bot. 2007; 73: 441.
19. MNI Bhuiyan, JU Chowdhury, J Begum. Bangladesh J Pharmacol. 2008; 3: 69.
20. B Damjanović-Vratnica, T Đakov, D Šuković, J Damjanović. Czech J Food Sci. 2011; 29: 277.
21. M Laranjo, AM Fernández-León, AC Agulheiro-Santos, ME Potes, M Elias. Food Process. Preserv. 2022; 46.

22. BK Singh, S Tiwari, NK Dubey. J Sci. Food Agric. 2021; 101: 4879.

23. N Djabou, V Lorenzi, E Guinoiseau, S Andreani, MC Giuliani, JM Desjobert et al. Food Control. 2013; 30: 354.

24. S Burt. Int. J Food Microbiol. 2004; 94: 223.

25. GA de Azeredo, TLM Stamford, PC Nunes, NJ Gomes Neto, MEG de Oliveira, EL de Souza. Food Res Int. 2011; 44: 1541.

26. P Goñi, P López, C Sánchez, R Gómez-Lus, R Becerril, C Nerín. Food Chem. 2009; 116: 982.

27. AC Souza, GEO Goto, JA Mainardi, ACV Coelho, CC Tadini. LWT Food Sci. Technol. 2013; 54: 346.

28. M Bouaziz, T Yangui, S Sayadi, A Dhouib. Food Chem. Toxicol. 2009; 47: 2755.

29. N Adrar, N Oukil, F Bedjou. Ind. Crops Prod. 2016; 88: 112.

30. S Chouhan, K Sharma, S Guleria. Medicines. 2017; 4: 58.

31. R Pei, F Zhou, B Ji, J Xu. J Food Sci. 2009; 74: M379.

32. F Fazlollahpour-Rokni, SA Shorofi, N Mousavinasab, R Ghafari, R Esmaeili. Complement Ther. Clin. Pract. 2019; 34: 201.

33. V Hajhashemi, A Ghannadi, B Sharif. J Ethnopharmacol. 2003; 89: 67.

34. N Mahato, K Sharma, R Koteswararao, M Sinha, E Baral, MH Cho. Crit. Rev. Food Sci. Nutr. 2019; 59: 611.

35. C Shi, X Zhang, N Guo. Microb. Pathog. 2018; 125: 262.

36. ZJ Ni, X Wang, Y Shen, K Thakur, J Han, JG Zhang, F Hu, ZJ Wei. Trends Food Sci. Technol. 2021; 110: 78.

37. CC Liolios, O Gortzi, S Lalas, J Tsaknis, I Chinou. Food Chem. 2009; 112: 77.

38. R Wang, R Wang, B Yang. Innov Food Sci. Emerg. Technol. 2009; 10: 289.

39. ME Guynot, AJ Ramos, L Seto, P Purroy, V Sanchis, S Marin. J Appl. Microbiol. 2003; 94: 893.

40. M Paw, T Begum, R Gogoi, SK Pandey, M Lal. J Essent. Oil Bear. Plants. 2020; 23: 337.

41. AB Hsouna, NB Halima, S Smaoui, N Hamdi. Lipids Health Dis. 2017; 16: 146.

42. Z Ayati, MS Amiri, M Ramezani, E Delshad, A Sahebkar, SA Emami. CPD. 2019; 24: 4101.

43. AA Ghods, NH Abforosh, R Ghorbani, MR Asgari. Complement Ther. Med. 2015; 23: 325.

44. K Can Baser. CPD. 2008; 14: 3106.

45. G Nieto. Medicines. 2017; 4: 63.

46. A Ocana-Fuentes, E Arranz-Gutierrez, FJ Senorans, G Reglero. Food Chem. Toxicol. 2010; 48: 1568.

47. S Patel, P Gogna. Ind. Crops Prod. 2015; 76: 1148.

48. VS Periasamy, J Athinarayanan, AA Alshatwi. Ultrason. Sonochem. 2016; 31: 449.

49. P Rattanachaikunsopon, P Phumkhachorn. Biosci. Biotechnol. Biochem. 2009; 73: 2085.

50. M Razzaghi-Abyaneh, M Shams-Ghahfarokhi, T Yoshinari, MB Rezaee, K Jaimand, H Nagasawa et al. Int J Food Microbiol. 2008; 123: 228.

51. H Kim, B Lee, KW Yun. Ind. Crops Prod. 2013; 44: 323.

52. L Kokoska, J Havlik, I Valterova, H Sovova, M Sajfrtova, I Jankovska. J Food Prot. 2008; 71: 2475.

53. R Singh, MAM Shushni, A Belkheir. Arab. J Chem. 2015; 8: 322.

54. M Unlu, E Ergene, GV Unlu, HS Zeytinoglu, N Vural. Food Chem. Toxicol. 2010; 48: 3274.

55. S Okano, Y Honda, T Kodama, M Kimura. J Oleo Sci. 2019; 68: 1003.

56. L Camarda, T Dayton, V Di Stefano, R Pitonzo, D Schillaci. Ann. Chim. 2007; 97: 837.

57. LAE Erland, SS Mahmoud. in: Essential Oils in Food Preservation, Flavor and Safety. Elsevier. 2016; 501–508.

58. K Sowndhararajan, P Deepa, M Kim, SJ Park, S Kim. Sci. Pharm. 2017; 85: 33.

59. M Zuzarte, L Salgueiro. in: Bioactive Essential Oils and Cancer. Ed. DP de Sousa. Springer Int. Publ, Cham. 2015; 19–61.

60. CL Ye, DH Dai, WL Hu. Food Control. 2013; 30: 48.

61. HF Yen, CT Hsieh, TJ Hsieh, FR Chang, CK Wang. J Food Drug Anal. 2015; 23: 124.

A Review on Biocomposites in Ancient Mortars through Material Characterization in Case Studies (Modern Reverse Engineering Technique)

Abstract

Lime mortars and plasters are commonly employed to preserve ancient structures. Utilizing biopolymers is one way to improve the durability and mechanical characteristics of lime mortars and plasters. Several biopolymers like jute, sisal, flax, millet grains, and bamboo were utilized as biocomposites in lime mortar throughout the ancient period. Bioorganic materials improved lime mortar's performance between the fourth and eighteenth centuries. This review demonstrates the availability, longevity, and accessibility of biopolymers. Also, it provides a state-of-the-art review of research into restoring historic structures and monuments using biopolymers like jute, sisal, flax, millet grains, and bamboo as bio-composite materials.

Keywords: Ancient Structures; Jute; Sisal; Flax; Millet Grains; Bamboo

1. Introduction

Biopolymers can be either plant, animal, or mineral-based[1]. Cellulose is the primary component of plant Polymers. Jute, flax, Sisal, Cotton, and Bamboo are the most popular Bio Polymers and are examples of common plant Polymers[2–4]. Cornhusk, palm, and pineapple husk are additional sources of plant fibers[5]. Biocomposite polymers offer a wide range of applications in practically every engineering industry. Because they are inexpensive, they are ideal for low-cost housing, construction, and renovation (panels, fake ceilings, and partition boards), packing, automotive interior decoration, and equipment for storing information. Furthermore, they have been proposed as adequate wood substitutes for use in furniture. Examples include ultra-light jute-polyester fibers that produce chair shells, doorways and partitions, home decor, and automotive body panels. Composites made of jute and polypropylene have also been used to make the insides of cars, shipping pellets, rollers and spindles, flower vases, accessories, polymer decking, fencing, household items, and handles[2].

Aside from that, geotextiles made from jute have been developed to combat leaching and soil erosion. Glass fiber composites, Wood polymer plastics, and mica or talc polypropylenes now have a severe alternative: natural fibers. Researchers are looking into the possibility of employing plant-based substances such as jute, sisal, flax, banana, and hemp as reinforcement in thermoplastics and thermosets to make composite materials [15]

[15] ✉ P. Maheswar Reddy

maheswarcivil.sch@nita.ac.in

National Institute of Technology Agartala, Tripura, 799046, India

that can be utilized to produce decking, window and door features, guardrails, allying, guardrails, furniture, marine components, and flooring. Thermoforming extrusion sheets, Compression molding, and the joining of polypropylene and plant fibers are these composites' main production methods. have a severe alternative: natural fibers. Researchers are looking into the possibility of employing plant-based substances such as jute, sisal, flax, banana, and hemp as reinforcement in thermoplastics and thermosets to make composite materials that can be utilized to produce decking, window and door features, guardrails, allying, guardrails, furniture, marine components, and flooring. Thermoforming extrusion sheets, Compression molding, and the joining of polypropylene and plant fibers are these composites' main production methods.

The ancient constructions were built by various cultures and techniques that were eventually systematized into unique architecture comprising temples, palaces, and churches. The structures serve as reminders of a wealthy, prestigious, and significant past, history, and prosperity. The mortar used in ancient buildings was held together with glue made from lime. Ancient mortars were composed of binder, aggregate, and biopolymer admixtures to increase structural endurance[6]. Because of their superior performance as moisture repellents and resistance to the effects of weathering agents, organic lime mortars like these were frequently utilized in the erection of ancient structures[7]. Lime mortars have been the subject of research on their binding capacity[8-10]. High-quality mechanical qualities can also be found in plant-based fibers like Jute, bamboo, flax, hemp, and sisal, low-cost compositional reinforcements. Even though Jute, hemp, bamboo, and flax fibers are stiffer than E-glass fibers[11-14]. Jute fibers, Rice husk, gum, glue, hemp, jaggery, and sticky extract from several plants are all mentioned as having been used in Indian plasterworks. These organic ingredients boost the plasters' binding ability and protect against cracking. Due to extensive personalization over time, the original character of organic extracts is sometimes obscured[15].

2. Case Studies

Case study on jute polymers: Jute is a biopolymer obtained from the Malvaceae genus Corchorus plants. As a lignocellulosic polymer, jute combines the properties of both textile polymers and wood polymers. In textile terminology, it is known as bast polymers (Bast polymers are polymers generated from bast or plant skin). These Cells comprise crystalline cellulose microfibrils bonded to an entire layer by hemicellulose and amorphous lignin. According to its elemental composition, jute fiber comprises hemicellulose 12%, lignin 11.8%, water 10%, water-soluble compounds 1.1%, cellulose 64.4%, wax 0.5%, and pectin 0.2%. Jute is a natural fiber composed of many different cells throughout its structure (**Table 1-3**)[2].

Fig. 1 In fields jute fibre[16].

Table 1 Jute polymer, mechanical and physical properties[2].

Diameter (μm)	Density (g/cm^3)	Modulus (GPa)	Ultimate Tensile Strength (MPa)	Tensile Strength (MPa)	Tensile modulus (GPa)	Elongation outbreak (%)
25–200	1.3–1.49	2.5–13	460–533	393–800	13–26.5	1.16

Table 2 Chemical composition of jute fibre[2].

Fibre	Cellulose (%)	Lignin (%)	Hemicellulose (or Pentosan) (%)	Pectin (%)	Ash (%)
Jute (Core)	41–48	21–24	18–22	0.0	0.8
Jute (Bast)	45–71.5	12–26	13.6–21	0.2	0.5–2

Table 3 Composite is made of natural fibres and polymers often use polymeric matrices[2].

Fibre	Thermosets	Thermoplastics
Jute	Epoxy, Polyester, Vinylester, Phenolic	Polypropylene, Polyethylene

The amount of cellulose present in the fiber and the helical angle formed by the microfibril band in the inner supplementary cell walls are the primary factors determining plant fibers' stiffness and strength. The total amount of cellulose contained within the fiber can be affected by the fiber's degree of crystallinity and the microfibrils' angle concerning the axis that runs through the center of the fiber because the axis is located directly in the middle of the fiber. The types of fibers that are the most durable are those that have a high concentration of cellulose as well as a high crystallinity index. These types of fibers have both of these characteristics in abundance. According to the findings of several studies, this fibers category is among those most resistant to damage. Besides,

natural fiber diameter, length, and diagnostic precision are a few experimental factors that might influence percentage elongation: tensile strength and modulus.

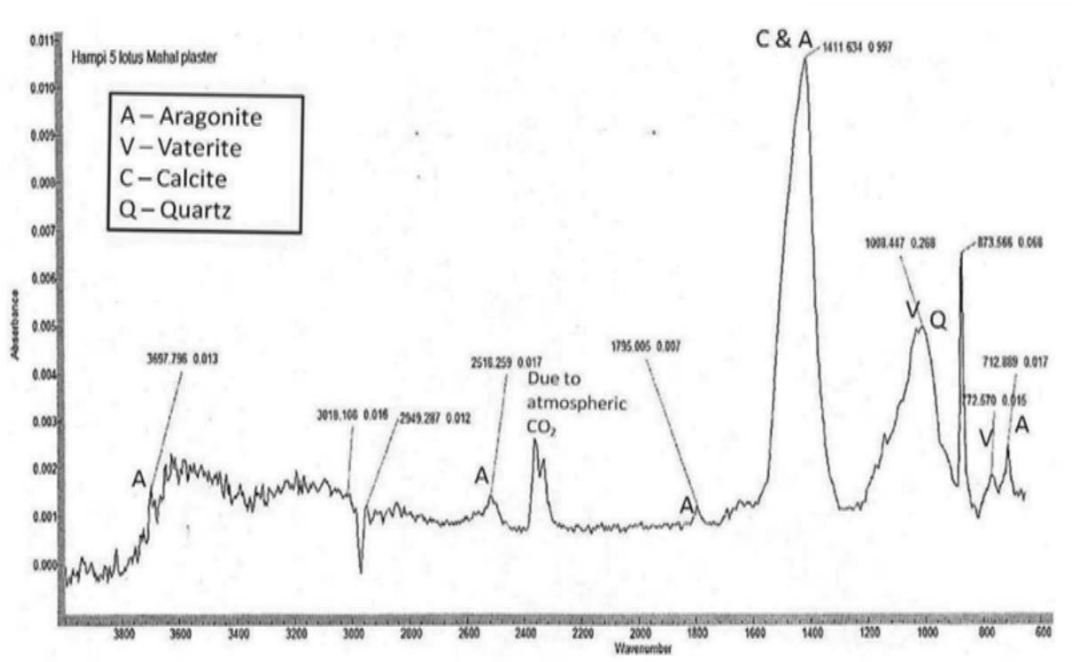

Fig. 2 FTIR spectra of the Hampi, India, lime plasters of the 14th to 16th century[17].

In order to manufacture cutting-edge composite materials, natural fibers are combined with thermosets such as unsaturated polyester, epoxy resins, phenol-formaldehyde novella-type resins, and phenol-formaldehyde. Resins of the phenol-formaldehyde novella type are included among these thermosets. Thermosetting resins typically impregnate the fibers in thermoset matrix composites before curing at ambient or increased temperatures. Vacuum infusion, Hand layup, press molding, and pultrusion are used to create high-performance composites using thermosetting matrices. Epoxy resin was used, which resulted in a better end product; however, unsaturated polyesters were more popular due to their low price and excellent adaptability for large-scale composite building projects because unsaturated polyesters were more adaptable for a broader range of applications. Epoxy resin was more challenging to work with, which was one of the reasons. Composites are robust when manufactured using treated naturally rather than untreated fibers[18]. Phenol formaldehyde matrix composites are more complex and have a greater modulus than epoxy composites when it comes to thermoset composites. Polyester composites are ranked second.

The Hampi, India, lime plasters of the 14th to 16th century CE was chosen as the case study, and plaster specimens were obtained for analysis[17]. In order to perform calculations, an XRD (a Phillips 2404 equipped with CuKα radiation and a graphite monochromator) was utilized to ascertain the mineral composition of the binding agent,

and the filler allowed for the execution of those calculations. The samples were examined at various angles between 5 and 120 degrees after 2 hours. A Zeiss scanning electron microscope analyzed the plaster samples to determine their content, microstructure, and texture. Micrographs taken with a scanning electron microscope ranged in magnification from 2,000 to 10,000 times. Plaster-like minerals such as calcite, dolomite, gypsum, aragonite, quartz, magnesium hydroxides, and calcium were analyzed qualitatively using FTIR. An Agilent 600 series spectrophotometer with an MCT detector cooled by nitrogen was used to collect the plaster's FTIR spectra. Producing KBr pellets from scratch requires only a few milligrams of material, making FTIR spectroscopy possible with little sample preparation. The moisture content of the plaster was measured at 105 °C, and as a direct consequence of this, the temperature at which the plaster lost its ability to ignite was reduced to 900 °C. Using the weight loss that the plaster experienced after being heated to 900 °C in a muffle furnace, an estimate of the amount of water bound up with organic matter and clay was created. This estimate was used to determine the amount of water in the plaster. Because of this, it was possible to arrive at a precise estimation of the quantity of carbon dioxide produced as a direct consequence of separating all carbonates. The collection of qualitative data regarding the primary components of the Hampi plaster was made possible through Fourier transform infrared spectroscopy. The powdered plaster was subjected to FTIR testing between the wavelengths of 550 and 4000 cm^{-1} by the requirements. Finally, (as shown in **Fig. 2**), FTIR was used to examine the aggregate after it had been sieved following processing in diluted HCl. In the spectra, there was a small peak at 2950 $cm^{-1.}$ It could have been caused by jute fibers or other organic materials in the plaster[17].

The Raja Ki Baoli, a brick-lime stepwell of the 12th century located in New Delhi, India, was chosen for the case study, and mortar specimens were obtained for analysis[19]. The chemical, microstructural, and mineralogical features of Raja ki Baoli's stepwell plasters were analyzed to find the polymer ingredients. All samples collected contained plant fibers as an organic ingredient (**Fig. 3**). There must be natural plant fibers somewhere, given how thick they were and how few scales they had. Under a scanning electron microscope, the fiber cells were observed to be polygonal and spherical, with a width of ≈ 20 μm. Bifurcated cells with bud-like projections and spherical fiber cells with gradually narrowing tips were also seen. As is characteristic of jute fiber, the detected nodes were very tiny, weak, and irregularly spaced. Sclerenchyma cells' nodes might not extend over their entire length[20]. The presence of vegetal fibers in all Raja ki Baoli plaster specimens was shown to be for strength and to avoid cracking while drying. The fiber was identified using scanning electron microscopy. After soaking in distilled water, fibers are brushed with a soft bristle brush and washed with distilled water until their textured surface is visible under a microscope. After washing, fibers were sputtered using gold utilizing the SPI-MODULE sputter coater, which was applied to the stubs. Carl Zeiss SMT EVO series device was used to snap photographs and evaluate the fibres[19].

Fig. 3 The Raja Ki Baoli, New Delhi, India Specimen contains jute fibres[19].

Case study on Sisal polymers: Sisal fiber comes from the leaves of Agave sisalana. Sisalana, Vergross, Istle, and Natale are the four species of sisal plants found in India. The amount of fiber produced by various plant species varies greatly. Fib fiber content disparity is also based on harvest time and plant origin. A leaf's chemical composition is 87.25 percent water, 4 percent fiber, 0.75 percent cuticle, and 8 percent miscellaneous dry matter. Fiber lengths range from 60 mm to 120 mm. The fibers have broad, rounded tips. Cells with angular shapes typically range in size from 500 to 6000 µm in length and 5–40 µm in width, with an aspect ratio length to the diameter of fiber of no more than 150.

There are a few different ways to get to the sisal fibers: microbiological retting, manual scraping, and raspador machines. Green leaves are crushed and battered by the wheel's blunt blades during the decortication process, at which point the cellulose material is removed. After the process of decortication, the fibers are washed, and then, depending on the method that was selected, they are either dried in the sun or by the use of hot air. Finally, the fibers are combed through a machine to remove any remaining debris. Fiber recovery occurs quickly after harvesting to preserve the natural gummy substance essential for producing high-quality fiber. Hardening makes fiber separation more challenging. The ease with which fiber can be extracted is improved by double retting. When the retting process is halfway done, the leaves are taken out of the tank, dried, and retted again a few months later. The procedure is continued until fibers of exceptional shine, pliability, and strength are produced. Brazil's share of the global sisal market is around 50 percent. On average, each Brazilian-grown sisal plant leaf finds 700–1400 technical fibers with a length of 50 to 100 cm and a horseshoe cross-section. A simple perique is used to remove the fibers from the plant. Sisal fibers have been shown to withstand temperatures up to 200 °C in thermogravimetric analyses (TGA)[2].

Table 4 Sisal fibre, mechanical and physical properties[2].

Diameter (μm)	Density (g/cm^3)	Modulus (GPa)	Ultimate Tensile Strength	Tensile Strength	Tensile modulus	Elongation outbreak
			(MPa)	(MPa)	(GPa)	(%)
50–200	1.45	9.4–15.8	468–640	468–700	9.4–22	3–7

Table 5 Chemical composition of Sisal fibre[2].

Fibre	Cellulose (%)	Lignin (%)	Pentosan (%)	Pectin (%)	Ash (%)
Sisal	47–78	7–11	10–24	10	0.6–1

Table 6 Composite is made of natural fibres and polymers often use polymeric matrices[2].

Fibre	Thermosets	Thermoplastics
Jute	Epoxy, Polyester, Novolac	Polypropylene, Polyethylene, Polystyrene

The Taj Mahal, Agra, in India, was chosen as the case study, and mortar specimens were obtained for analysis[20]. One of the world's most famous and revered buildings, the outside of the Taj Mahal is covered with white marble, while the inside is coated with lime plaster. Plaster was discovered to have cracked, flaked, and lost its adherence in certain areas after some time. Numerous groups from India and beyond have researched the monument and its environs. Plaster samples were collected at various failure locations around the structure and subjected to a battery of physicochemical tests to determine the cause of the damage. In addition to chemical, XRD, and FTIR analyses, significant supplemental data was gathered via petrographic and SEM examinations (For more sophisticated analytical details, follow 'Studies on Taj Mahal Plasters'[20]). XRD, SEM, and conventional petrography were employed in the mineralogical investigations. X-ray diffraction was used to get the results, and SEM tests were done on the broken surfaces of selected samples to confirm the results. Some of the thin pieces were petrographically examined using an Italian technique. Plaster samples reveal the presence of plant fibers. Primary fibers were sisal (Agave sisalana), hemp (Cannabis sativa), and jute (Chor-chorus). All the fibers that reinforce the plaster appear to be of Indian origin. One intriguing aspect is that these fibers have not degraded or been attacked by alkali after all these years[20].

Fig. 4 In fields Sisal fibre[21].

Case study on flax polymers: Flax is a plant in the Linaceae family that belongs to the genus Linum usitatissimum. Because of its historical importance as a grain crop, the word usitatissimum, which signifies most beneficial, has been used. Flax is cultivated because it is more productive than linseed, which has more robust and shorter stems and many more branches and grows to a greater height. As a self-pollinating plant, flax has been cultivated in temperate climates for millennia. There has always been a market for the plant's fibers and seeds. Because of their superior qualities, flax fibers are a crucial component of the textile industry. Together with hemp and jute, these are stem fibers.

Table 7 Flax fibre, mechanical and physical properties[2].

Diameter (μm)	**Density (g/cm^3)**	**Modulus (GPa)**	**Ultimate Tensile Strength**	**Tensile Strength**	**Tensile modulus**	**Elongation outbreak**
			(MPa)	**(MPa)**	**(GPa)**	**(%)**
40–600	1.5	100	1100	345–1500	27.6	2.7–3.2

Table 8 Chemical composition of Flax fibre[2].

Fibre	**Cellulose (%)**	**Lignin (%)**	**Pentosan (%)**	**Pectin (%)**	**Ash (%)**
Flax (Fibre)	71	22	18.6–20.6	2.3	–
Flax (Seed)	43–47	21–23	24–26	–	5

Table 9 Composite is made of natural fibres and polymers often use polymeric matrices[2].

Fibre	**Thermosets**	**Thermoplastics**
Jute	Epoxy, Melamine-formaldehyde	Polypropylene, Polyethylene

The non-cellulose parts of flax fibers are 30%, and the cellulose parts are 70%. Non-cellulose parts include hemicellulose, pectin, lipids and waxes, lignin, mineral salts, organic colorants, and water-soluble compounds (**Table 7-9**)[2].

The thermogravimetric curve of flax fiber reveals that it has undergone thermal degradation of its cellulose components and a water loss due to this process. Additionally, the curve reveals that this process has caused it to lose some of its water content[10]. Lignin decomposition occurs between 385 and 455°C, with the greatest occurring at 431°C[2]. Flax fibers are essential fibers bound by lignin or hemicellulose. The bulk fiber comprises 70 wt% cellulose, 18 to 19 wt% hemicellulose, 2 to 2.5wt% lignin, and 2 to 2.5wt% pectin. Crystalline and amorphous cellulose dominate the crude fiber. The fiber surface is likely to be reinforced with lignin, hemicellulose, and wax, which protects the plant stem from the environment. In addition to this composition, the fiber contains 5 to 10% water, which can enter along the fiber direction through the hollow interior of the plant's primary threads or be absorbed through the fiber surface. With dew-retting, plant fibers are removed by breaking down lignin, pectin, and hemicellulose more than cellulose[22–24]. Two additional peaks at 1228–1235 cm^{-1} and 1733 cm^{-1} In the infrared spectrum of both untreated and acetylated flax fibers, the presence of acetyl groups in the flax fibers and an ester link with the components of the flax fibers can be observed holds for both varieties of flax fibers. 1600 cm^{-1} is due to cryst alline cellulose a bsorbing water, suggesting that lignin, a material with many aromatic rings, is not present in the fibers at detectable concentrations[2].

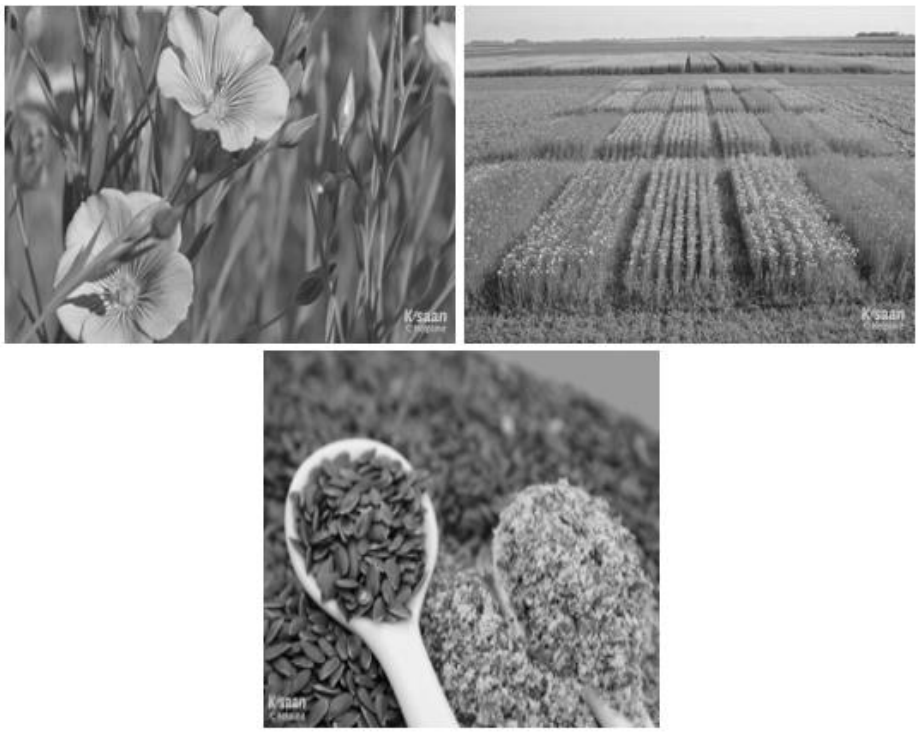

Fig. 5 In fields flax fibre[25].

Case study on millets: In structural and functional genomics research, foxtail millet has gained much attention as a model crop and in three of the most significant areas of stress biology[26]. Millet is a generic word for perennial grain crops that produce tiny seeds. For example, several different types of millet, Panicum miliaceum, Setaria italica, and Pennisetum glaucum are some examples.

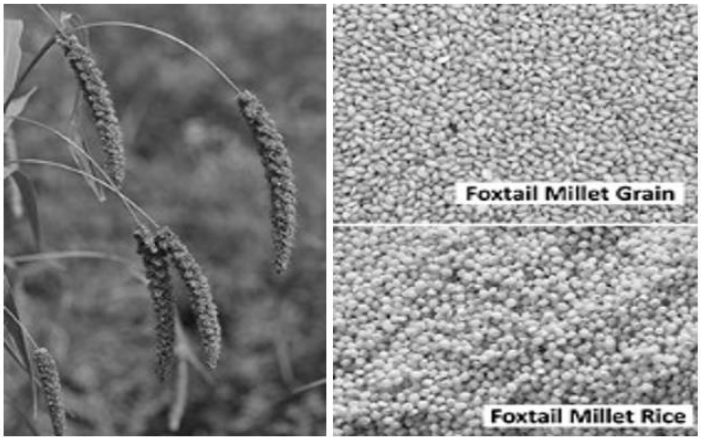

Fig. 6 Foxtail millet (Setaria italica) [29].

In India, Setaria italica is known as Kangni (Hindi), Shol (Kashmiri), Kang (Gujrati), Kangam (Oriya), corralu (Telugu), Navane (Kannada), Kaon dana (Bengali), Thina (Malayalam), and Kavalai (Tamil). Setaria italica is the second most-grown millet after Pennisetum glaucum[27]. The world produces 29.8 million tonnes of millet, with 10.3 million tonnes coming from India (FAOSTAT data from 2012; http://faostat.fao.org/). The grains might be elliptic, oblanceolate, conospherical, Sphere, hexagon, or spherical in form and yellow, grey in white color, creamy, pale blue, brown, creamy, violet, or grey. The Proximate composition of foxtail millet was calculated using the usual approach, and the findings are displayed in Table.7 and described further below[28].

Table 10 Foxtail millet (Setaria italica) proximate composition[28].

Moisture content (% w)	Carbohydrate (%)	Crude protein (%)	Crude fat (%)	Crude fiber (%)	Total ash (%)
10.77 ± 0.34	64.71 ± 2.34	12.82 ± 0.18	3.71 ± 0.15	6.15 ± 0.19	1.64 ± 0.05

Case study on bamboo polymers: The Poaceae family, the Bambusoideae subfamily, and the Bambuseae tribe are all responsible for the production of bamboo, which is a type of grass. Despite this, we refer to it as bamboo because it possesses characteristics of all three families. Fibrous cellulosic material held together by a lignin matrix makes up its structure. Sclerenchyma cells (enclosed in matrix tissue) and matrix tissue cells make up

bamboo (leptodermous). Bamboo is reinforced by vascular bundles composed of sclerenchyma cells. Many phloem fibers comprise a vascular bundle, each with several pillar fiber strata. Each pillar fiber layer's microfibres are arranged in a spiral, with the angle between adjacent spirals set at a different value for each pillar fiber layer. Bamboo's primary chemical ingredients are hemicellulose, cellulose, and lignin. More than half of the chemical elements in bamboo are made up of holocellulose, which is made up of hemicellulose and cellulose.

There are over 80 species in India, two of the most significant being Bambuseae bamboos and Dendrocalamus strictus. Bamboo's woody stems, known as culms, grow from subsurface woody rhizomes. Above ground, these shoots appear as delicate, sharp apexes encased in overlapping layers. They will reach their full height within two to four months due to their rapid growth. A number of factors, including the type of bamboo, the vigour and size of the clump, and the amount of rainfall, combine to determine the total number of culms produced. A fully developed, healthy clump will produce ten to twenty new culms annually. Excessive heat encourages blooming. Bamboo’s strength qualities are highly impacted by species, moisture content, age, and culm location, and the outside is rugged and durable. The outer layer of the cellulose-rich tissue in bamboo is considered more significant than the inner layer because the outer layer contains two times as much of the substance as the inner layer. Bamboo has a similar compression strength but far higher tensile strength than wood. The presence of wood-boring insects is a disadvantage of bamboo. Dry storage or the addition of preservatives is recommended. It is sensitive to temperature and Ultraviolet radiation and may absorb water. In addition, bamboo cultivation is invasive because it spreads by underground stems called rhizomes. It is difficult to wipe out a bamboo forest[2].

Table 11 Physio-mechanical properties of Bamboo fiber[2].

Ultimate Tensile Strength (MPa)	Elongation (%)
43–113	13–20

Table 12 Composite is made of natural fibers, and polymers often use polymeric matrices[2].

Fibre	Thermosets	Thermoplastics
Bamboo	Epoxy, Polyester	Polypropylene

Table 13 Bamboo fiber chemical composition[2].

Constituent	Lignin	Moisture	Ash	Hot water solubility
(%)	2.14	11.7	2.3	7.7

The culm (stem) of bamboo has a structure comparable to a unidirectional fiber-reinforced polymer due to multiple nodes throughout its span. It is made up of cellulose fibers arranged in a ligneous matrix along the length of a bamboo culm. However, only a few significant efforts have been undertaken to extract bamboo fibers. Natural fibers are in such short supply that only a limited amount of research has been done on the properties of natural fibers and their application as reinforcements in polymers since they are in such a short supply primarily attributable to the minimal supply of natural fibers that are currently available. Despite this, numerous thermoset and thermoplastic polymers may be reinforced with bamboo in different configurations, including natural bamboo, sections, strips, and fibers. Depending on the bamboo's height and cross-section, the proportion of cellulosic fibers ranges from 15 to 20% and 60 to 65%, whereas the tensile strength ranges 100Mpa to 600 MPa and the modulus ranges 3GPa to 15 GPa, respectively[30] is due to the specimen's relative proportion of fibers. It was discovered that bamboo fiber bundles with diameters ranging from one to two millimeters contained a comparable variation. Bamboo fibers have the potential to offer a significant amount of reinforcement, which opens up many doors for their use.

Fig. 7 General view of Bamboo trees[31].

Bamboo comprises the following chemical components: cellulose, lignin, hemicellulose, and water. Bamboo contains hemicellulose and cellulose in holocellulose, accounting for more than half of the total chemical components.

The Solapur fort in India was chosen as the case study, and mortar specimens were obtained for analysis[32]. Carl Zeiss JENAPOL petrological microscope was utilized in the

thin section analysis of samples. Images were taken at a 10X magnification using a Plane polarized light using crossed Nicol prisms. At the same time that photographs were taken, plant components embedded in the plaster were analyzed using a light microscope, a polarised optical microscope, and a scanning electron microscope. After being cleaned with distilled water, the samples were put through a treatment that included a mixture of glacial acetic acid and thirty percent H_2O_2 for two hours while they were immersed in a bath of boiling water was done so that the cement plaster adhering to the plant additives could dissolve. To ensure that the morphological structures were seen clearly under the microscope, the specimens were painstakingly cleaned regularly with a brush, and distilled water allowed the morphological structures to be observed more clearly. Selected samples were washed, rinsed, and air-dried before being examined by scanning electron microscopy and polarised light microscopy. In Granulometric analysis, plaster samples are dissolved at 15% diluted HCl and permitted to soak for the whole night. The aggregate was dried for 5–6 hours at 100 °C after being filtered using Whatman filter paper to remove the acid-insoluble fraction. The acid-insoluble portion was sieved for further investigation into the aggregate particle size and shape studied in the plaster. The plaster's minerals were determined using XRF, PAN Analytical Epsilon. Each powder sample was then attached to a crushed pellet with a size of 12mm to 13 mm in diameter and stored in a designated container. After the samples were set up, an X-ray beam was fired at them; subsequently, the fluorescence photons produced were collected and examined after they had been collected.

Because of this, a muffle furnace was utilized in the conventional chemical analysis to determine the loss of ignition (LOI) at 900 degrees Celsius was done in order to ensure accurate results. In order to investigate the mineral makeup of the plaster, a graphite monochromator and CuK radiation were utilized on a Philips 2404 XRD spectrometer was done so that the mineral makeup of the plaster could be determined. Two values were achieved by scanning the samples at temperatures ranging from 5 to 80 °C. At a frequency of 4000-400 cm^{-1}, powder samples were analyzed with FTIR, Bruker tensor by KBr pellets. In order to investigate the infrared spectrum of the plaster, the following parameters were utilized: a data interval of 0.5 nm, 20 average scans, and a resolution of 2 cm^{-1}. Plaster samples were characterized and photographed using SEM-EDX technology with a Carl Zeiss EVO 40 and a Bruker X flash detector. Photomicrographs were obtained at several magnifications from gold-coated samples to characterize the components of the plaster. Plaster samples were subjected to TG-DTA analysis. The results were analyzed utilizing diamond model equipment (Perkin Elmer, USA). The experiments were conducted with a Pt/Rh crucible, a temperature varying from 25 to 1000°C, a 40 ml/min flow rate, and alumina as the reference material. After being washed in distilled water, the samples were treated in a hot bath with a combination of 30 percent hydrogen peroxide and glacial acetic acid for 2 hours (H_2O_2). The samples were cleaned with a fine brush and distilled water regularly unless visible morphological

characteristics were detected under a light microscope. Once the samples were cleaned and dried, they were examined using SEM and polarised light microscopy. The bamboo leaves used as an organic component in the plasterwork of the Solapur fort were revealed by light microscopic research. Bamboo is a remarkable plant that can swiftly adapt to various environmental factors. It is one of the plants that grow the quickest, with a daily growth rate of between 30 and 100 cm, making it one of the fastest-growing plants. The epidermal structure is one of bamboo's anatomical features. Using microscopic evidence, we were able to determine the presence of silica particles, elongated cells, stomata, and micro-cells. The abaxial side has a rectangular form with a sinuous anticlinal wall separating the shore and inter-coastal zones.

Table 14 Thin section analysis, binding agents, and organic contents in Solapur fort, India lime plaster[32].

Sample Number	Percentage of Binding Agent by Weight	Percentage of Organic Content by Weight
1	30 – 35	2
2	30 – 32	0
3	25 – 30	2
4	34 – 39	0

All of the analyzed plaster samples showed small peaks at 2900 cm^{-1}, indicating the existence of natural materials like plant fiber. Peaks at 872, 1400, and 2850 cm^{-1} are characteristic of calcite and may be detected in most samples. In FTIR spectra, calcite and aragonite peaks at 712 cm^{-1} are mixed, whereas aragonite displays three separate peaks, which can be found at 850, 1420, and 1750 $cm^{-1,}$ respectively. Silicates and alumino-silicates have prominent bands between 1017 and 1020 cm^{-1}. Most samples show small, muted silicate peaks because of the presumably modest amount of plasterwork from the Solapur fort. Spectral bands at 1450 and 1650 $cm^{-1,}$ characteristic of primary amines, are discovered in every single one of the samples, and a spectrum of vegetable fiber shows the presence of proteinaceous additions. In plant fibers' FTIR, the calcium oxalate peak may be detected as a band at 1316 cm^{-1}. When this occurs, it indicates that the proteinaceous components of the plaster have been transformed into calcium oxalate.

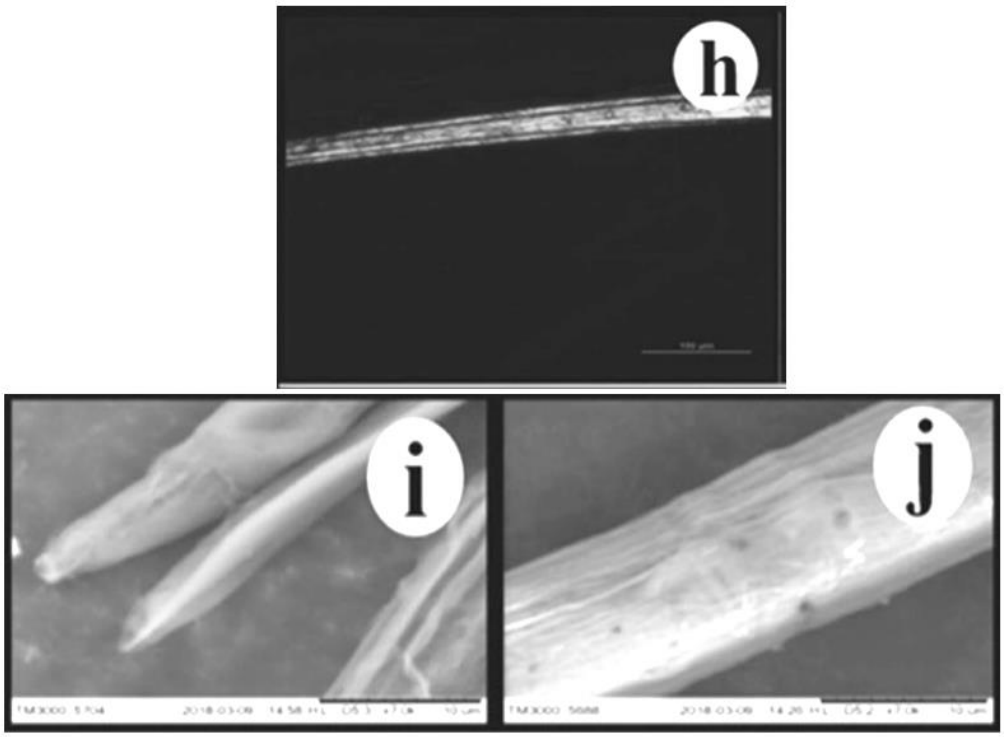

Fig. 8. h. the fiber has a twist in the shape of an "S" when viewed under polarised light microscopy (PLM). SEM images **i.** of the fiber's rounded and tapered ends, in addition to **j.** a kink (node) located on the interior of the fiber[32].

The FTIR analysis confirms the XRD and thin section findings on the plaster's mineralogical composition. Examination of the flax fibers themselves with a scanning electron microscope and a polarised light microscope provided conclusive evidence that the Solapur plaster contained flax fibres as an organic component, namely Setaria italica, lemma, and palea. Linum stems are processed to create flax fibers, among the most popular fibers in use today. Flax fibers, which are harvested from the stalks of the Linum plant, are among the most popular types of fibers. In cases where calcium oxalate crystals were absent, the flax fiber reportedly has an S-shaped twist (**Fig. 8**).

Flax fibers did not have any calcium oxalate crystals in their composition. SEM micrograph, the fiber's kink band structure is highlighted. Fibers with varying degrees of taper, both pointed and rounded, were discovered. Both sorts of edges can be found in large numbers across all samples. The sharp, diminishing ends of the cells the length of the fiber is estimated to be around 30 mm. Flax fiber has excellent flexibility and tensile strength. Cellulose and other plant fibers are superior to glass fibers in various structural applications due to the lower density of plant fibers, a higher stiffness-to-weight ratio of plant fibers, and other distinctive mechanical qualities of plant fibers. These advantages make plant fibers preferable to glass fibers in structural applications. In addition to this, glass fibers are more easily accessible than plant fibers. The technique results in cellulose

cottoned fibers with crystalline form, which are more durable, complex, and sharper than untreated fibers. The fiber's properties are determined by the presence or lack of cellular components such as cellulose, hemicelluloses, and lignin. The fact that humans use the cellulose fibers found in plants and trees to create things like rope, sails, tools, clothing, and homes is general knowledge. It would appear that the ancient Solapur architects were well aware of the many advantages of flax cellulose fibers, including their abundance, low manufacturing costs, lightweight, and rigidity comparable to cotton.

3. Conclusions

- Lime plasters of the 14^{th} to 16^{th} century CE in Hampi, India, and the Raja Ki Baoli, New Delhi, India, show that organic components are identified in lime plaster samples that are jute. Using jute in lime mortars and plasters reduces shrinkage and improves bonding in lime mortars and plasters.

- The Solapur fort in India shows that approximately 35 to 39% of binding agents and 2% organic components are identified in lime plaster samples: Bamboo foliage, Millet grains, and Flax fiber. The reason for using Bamboo foliage, Millet grains, and Flax fiber is to increase the silica content to attain more strength, to increase the thermal properties and elastic properties, for gelatinization, and to reduce the heat of hydration in lime mortars and plasters.

- To make plant fibers work with polymeric matrix, scientists intentionally altered them after extracting them. Sisal, cotton, jute, banana, hemp, and bamboo are all standard plant fibers known as lignocellulosic fibers. These fibers have qualities similar to synthetic fibers but have the added benefits of being biodegradable, inexpensive, and widely available. Another perk is that the extraction of fibers has developed into a full-fledged business, employing thousands of people in rural regions.

- In addition to the quality of the fibers themselves, their composition, and their properties, the mechanical qualities depend on the age of the plant from which the fibers are extracted. However, the quality of the fibers is independent of the age of the plant. As a direct result, achieving consistent results across all of the subsequent tests is challenging by replicating the same mechanical characteristics. There is a direct correlation between the amount of cellulose in plant fibres and the fibers' tensile strength and bending resistance. In addition, the spiral angle created by the bands of microfibrils located inside the secondary cells of the interior is very significant. About the axis of the fiber, this angle is the one that is measured. Two characteristics, namely the crystallinity index of the fiber and the microfibril angle concerning the principal fiber axis, can be utilized to estimate the total amount of cellulose present. It has been found that the mechanical properties of fibers can be improved by increasing their crystallinity and the

amount of cellulose they contain—a discovery made by scientists in the 1990s. Depending on the microfibril angle and cellulose content of the fibers, sisal has a tensile strength of 530 MPa and a modulus of elasticity in the range of 9–22 GPa. The modulus of elasticity can range anywhere from 9–22 GPa. Approximately 67% of the sisal fibers are composed of cellulose.

- In contrast, coir fiber has a tensile strength of 106 MPa and a modulus of elasticity of 3 GPa when its cellulose content is 43%, and its microfibril angle is 30–498%. Coir fiber also has a microfibril angle that ranges from 30–498%. Additionally, the microfibril angle of coir fiber can range anywhere from 30–498%. The probe's diameter, the test's length, and the speed at which it is moved all impact the modulus, the tensile strength, and the percentage of elongation of natural fibers. Limited literature is available on the current topic. These sophisticated analytical methodologies in reverse engineering will confirm any unknown materials to know earlier construction materials with practical technologies so that researchers might be able to make decisions at time restoration or conservation of heritage structures that either need to be used available materials or might search for alternate materials.

However, the researcher should be able to know that every time, there might be different situations that will challenge the restoration or conservation of heritage structures work based on ecological, topological, and environmental conditions of structural heritage sites. In this case, these modern reverse engineering techniques might contribute to knowing the outline of those heritage structures discussed earlier with proper background on why those biocomposites were utilized in those monuments.

References

1. LJ Shadle, DA Berry, M Syamlal. Coal Conversion Processes, Gasification. November. 2002.
2. N Chand, M Fahim. in Tribol. Nat. Fiber Polym. Compos. 2008; 1–58.
3. R Alavéz-Ramírez, P Montes-García, J Martínez-Reyes, DC Altamirano-Juárez, Y Gochi-Ponce. Constr. Build. Mater. 2012; 34: 296–305.
4. K Ghavami, RDT Filho, NP Barbosa. Cem. Concr. Compos. 1999; 21(1): 39–48.
5. N Chand, RK Tiwary, PK Rohatgi. J Mater. Sci. 1988; 23(2): 381–387.
6. A Moropoulou, A Bakolas, S Anagnostopoulou. Cem. Concr. Compos. 2005; 27(2): 295–300.
7. SQ Fang, H Zhang, BJ Zhang, Y Zheng. J Cult. Herit. 2014; 15(2): 144–150.
8. A Costigan, S Pavia. Proc. PROHITEC 09. 2009; 1609–1615.
9. C Groot. HERON. 1995; 40(1): 197.

10. JM Teutonico, I McCaig, C Burns, J Ashurst. APT Bull. 1993; 25: 32.

11. KVD Velde, P Kiekens. J Appl. Polym. Sci. 2002; 83(12): 2634–2643.

12. FT Wallenberger, NE Weston. (Ed.). Nat. Fibers Plast. Compos. 2004.

13. DN Saheb, JP Jog. Adv. Polym. Technol. 1999; 18(4): 351–363.

14. U Riedel, J Nickel. Angew. Makromol. Chemie. 1999; 272: 34–40.

15. M Singh, SV Kumar. Int. J Conserv. Sci. 2018; 9(4): 697–708.

16. http://www.jute.com/web/guest/picture-gallery/on-filed.

17. M Singh, SV Kumar, PD Sabale. Int. J Archit. Herit. 2019; 13(5): 725–741.

18. LU Devi, SS Bhagawan, S Thomas. J Appl. Polym. Sci. 1997; 64(9): 1739–1748.

19. SK Singh, B Dighe, MR Singh. J Archaeol. Sci. Reports. 2019; 29: 102063.

20. M Aslam. Stud. Conserv. 1990; 35(2): 102.

21. http://jafexpert.crijaf.icar.gov.in/sisal_info/sisal.aspx.

22. V Titok, L Khotyleva, V Leontiev, L Shostak. J Nat. Fibers. 2006; 3(1): 35–41.

23. RM Rowell, AM Tillman, R Simonson. J Wood Chem. Technol. 1986; 6(3): 427–448.

24. NE Zafeiropoulos, PE Vickers, CA Baillie, JF Watts. J Mater. Sci. 2003; 38(19): 3903–3914.

25. https://www.kisaanhelpline.com/crops/product/14_FlaxSeeds.

26. K Hariprasanna. in Millets Sorghum Biol. Genet. Improv. John Wiley & Sons. 2017; 112–149.

27. RK Singh, M Muthamilarasan, M Prasad. in Foxtail Millet Genome, Compend. Plant Genomes. 2017; 1–9.

28. GP Gouda, S Hiregoudar, U Nidoni, CT Ramachandra, N Naik, G Ganjyal et al. J Farm Sci. 2019; 32(3): 340–345.

29. https://www.millets.res.in.

30. S Amada, Y Ichikawa, T Munekata, Y Nagase, H Shimizu. Compos. Part B Eng. 1997; 28(1–2): 13–20.

31. https://nbm.nic.in/Photo-Gallery_bamboo.

32. B Dighe, M Singh, T Karche. Indian J Tradit. Knowl. 2021; 20(1): 106–116.